Structural Fire Engineering and Design of Filled Composite Plate Shear Walls (SpeedCore)

(CPF Research Grant # 03-18)

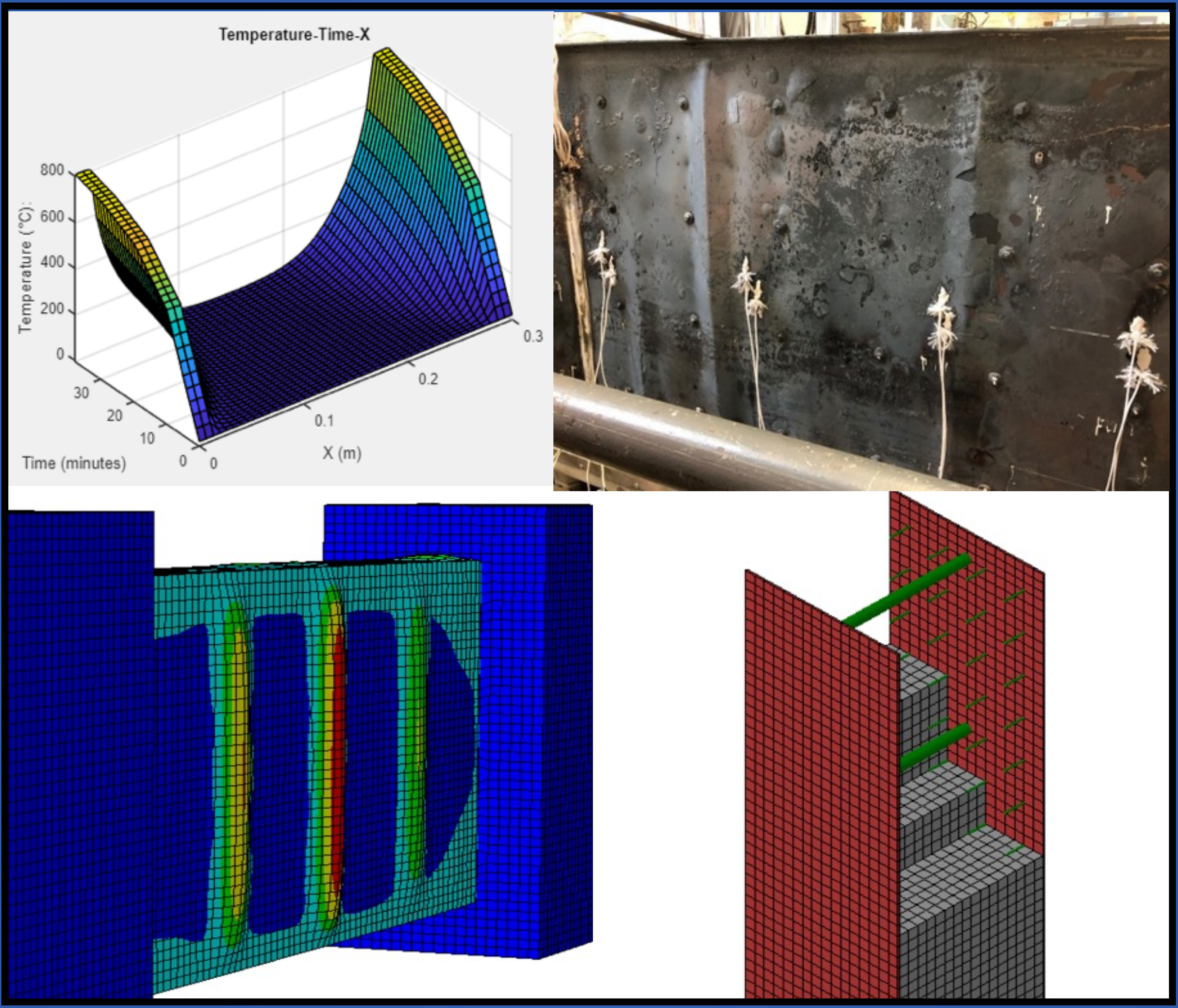

Ataollah Taghipour Anvari
Saahastaranshu Bhardwaj, PhD
Preshit Wazalwar
Amit H. Varma, PhD

Purdue University
Lyles School of Civil Engineering
West Lafayette, IN

Structural Fire Engineering and Design of Filled Composite Plate Shear Walls (SpeedCore)

(CPF Research Grant # 03-18)

Final Report

Ataollah Taghipour Anvari, Ph.D. Student
Dr. Saahastaranshu Bhardwaj, Postdoctoral Researcher
Preshit Wazalwar, M.S. Student
Dr. Amit H. Varma, Principal Investigator

Purdue University
Lyles School of Civil Engineering
West Lafayette, IN

March 2020

Sponsors:

Charles Pankow Foundation
Steel Institute of New York (SINY)
American Institute of Steel Construction (AISC)

Industrial Advisory Panel:

Farid Alfawakhiri, American Iron and Steel Institute
Robert Berhinig, Consultant
Rob Chmielowski, Magnusson Klemencic and Associates
Lisa Choe, National Institute of Standards and Technology
Gary Higbee, Steel Institute of New York
Ron Klemencic, Magnusson Klemencic and Associates
Larry Kruth, American Institute of Steel Construction
Jon Siu, City of Seattle

Acknowledgments

The research presented in this report was performed at Robert L. and Terry L. Bowen Laboratory for Large-Scale Civil Engineering Research at the Lyles School of Civil Engineering of Purdue University, West Lafayette, IN. The project was funded by Charles Pankow Foundation, Steel Institute of New York (SINY), and American Institute of Steel Construction (AISC). The authors are grateful to these agencies for financial support. The authors also acknowledge the technical inputs and review provided by the advisory panel.

Executive Summary

This report describes the experimental and analytical studies conducted to evaluate the performance of Composite Plate Shear Walls/Concrete-Filled (C-PSW/CF) subjected to fire loading, and to develop design guidelines and recommendations. The results from prior experimental investigations were compiled, and five additional fire tests were conducted to address gaps in the data. The tests were conducted on laboratory-scale specimens subjected to axial loading and simulated standard fire loading (heating). The parameters considered in the tests were axial loading magnitude (20 – 28% of section concrete strength, $A_c f'_c$), steel plate slenderness (24-48, tie spacing/plate thickness) maximum steel surface temperature (775 – 1043 °C), and uniformity of heating (all-sided vs. three-sided heating).

The analytical investigations were conducted using two independent numerical methods; Finite Element Analysis (FEA), and fiber-based analysis. The numerical models were benchmarked to test data, and the benchmarked models were used to conduct analytical parametric studies and expand the database. The thermal and structural material properties recommended by Eurocode standards were applied to the models. The parameters considered were the wall thickness (200 – 600 mm), wall slenderness (story height/thickness ratio, H/t_w= 5 – 20), axial loading ($P_u \leq$ 30% section concrete strength, $A_c f'_c$), heating uniformity (all-sided vs. three-sided heating), boundary conditions (pinned vs. fixed), steel plate reinforcement ratio (area of steel plates/wall cross-section area, A_s/A_g =1.3 – 5.3%), steel plate slenderness (tie or stud spacing/plate thickness ratio, s/t_p = 20 – 75), tie bar spacing to wall thickness ratio (s_{tie}/t_w = 0.5 – 1.0), and concrete strength (f'_c = 40 – 55 MPa). The range of the parameters was selected based on the range of typical parameters in design documents, literature, and current industry design practice.

Local buckling of faceplates between tie bars was observed in all walls. However, this did not cause significant degradation in structural performance or failure of the walls. The results from parametric studies indicate that wall slenderness ratio (story height/wall thickness), wall thickness, applied load ratio, and end conditions have significant influence on the fire resistance of walls. Higher wall slenderness ratios and load ratios have a detrimental effect on the fire resistance of walls. Walls with higher wall slenderness ratios failed due to global buckling of the wall. In thicker walls, the lower temperatures in the middle regions of the concrete core helped to improve the axial capacity of walls under fire loading. Limiting the plate slenderness ratio can slightly improve the fire resistance of unprotected walls by reducing the extent of local buckling between tie bars.

The results from the analytical parametric studies were simplified into Equation (1) for the design of C-PSW/CF. $P_n(T)$ is the axial load capacity of a unit width of the composite wall at elevated temperature. The total (linear) width of the wall is discretized into unit widths, where each unit width corresponds to a width equal to the tie bar spacing, s in the width direction. Thus, each unit width is like a column with steel plates on the surfaces, concrete infill, and tie bars distributed uniformly along the height. The temperature profile through the wall thickness can be calculated by discretizing the section into fibers (or elements). Since the temperature of the elements is uniform along the height and width of walls, 1D thermal analysis (through wall thickness) can be performed using heat transfer equations or the fiber tool developed in the study.

The section axial load capacity, $P_{no}(T)$, can be calculated using the temperature profile through the section, and the steel, $F_y(T)$, and concrete, $f'_c(T)$, fiber strengths at the applicable temperatures. The column elastic buckling capacity, $P_e(T)$, can be calculated as $\pi^2 EI_{eff}(T) \big/ L_c^2$, where the column flexural stiffness, $EI_{eff}(T)$, can be calculated using Equation (2) adapted from AISC 360-16, Section I2, for elevated temperature application. $E_s(T)$ and $E_c(T)$ are the steel and concrete fiber stiffnesses at the applicable temperatures. It is important to note that since temperature varies considerably through the section, the concrete contributions to strength, $A_c f'_c(T)$, and stiffness, $E_c(T)I_c$, have to be calculated as the sum of each concrete fiber's contribution.

$$P_n(T) = 0.32^{\left(\frac{P_{no}(T)}{P_e(T)}\right)^{0.3}} P_{no}(T) \qquad \text{Equation (1)}$$

$$EI_{eff}(T) = E_s(T)I_s + C_3 E_c(T)I_c \qquad \text{Equation (2)}$$

Equation (1) has the same format as the equation recommended in AISC 360-16, Appendix 4, for calculating the axial load capacity of steel columns at elevated temperature. The coefficients (0.32 and 0.30) have been calibrated to be conservative with respect to the results from analytical parametric studies. The axial (gravity) load capacity of C-PSW/CF wall can be estimated conservatively as the axial load capacity of the unit width strip calculated using Equation (1) multiplied by the linear width of the wall divided by unit width (tie bar spacing). This equation is appropriate for unprotected C-PSW/CF walls with the range of parameters described in the parametric studies. The wall slenderness ratio, H/t_w, has a limiting value of 20. Walls with wall slenderness ratios greater than 20 should be fire protected. The expansion of the material on the exposed surface of walls imposed moments to the wall cross section in nonuniform fire scenarios. This caused the early failure of walls (~40 mins) with wall slenderness ratios greater than 20.

The results from Equation (1) were used to develop a fire resistance rating equation for C-PSW/CF walls. This equation can be used to conservatively estimate the fire resistance rating (in hours) of unprotected C-PSW/CF walls exposed to standard fire time-temperature curve. In Equation (3), P_u is the applied axial loading, P_n is the axial load capacity at ambient temperature estimated using AISC 360-16 Section I2, H/t_w is the wall slenderness and t_w is the wall thickness in mm. As shown the fire rating depends directly on the applied axial load ratio, wall slenderness, and wall thickness. Equation (1) and (3) are limited to the range of parameters in the parametric study and should not be used for walls with a wall slenderness ratio greater than 20.

$$R = \left[-18.5 \left(\frac{P_u}{P_n} \right)^{\left(0.24 - \frac{H/t_w}{230} \right)} + 15 \right] \left(\frac{1.9\, t_w}{200} - 1.0 \right) \qquad \text{Equation (3)}$$

For example, unprotected C-PSW/CF walls with wall thickness of at least 300 mm, axial load ratio less than 10% of P_n, and H/t_w ratio less than 20, can achieve fire resistance rating of at least 3 hours. The fire resistance rating increases significantly with wall thickness (t_w). This is valid for C-PSW/CF walls that meet the steel plate slenderness requirements (tie or stud spacing/plate thickness, $s/t_p \leq 1.2\sqrt{(E/F_y)}$, tie spacing-to-wall thickness, $s_{tie}/t_w \leq 1.0$ and load ratio, $P_u/P_n \leq 0.2$.

Vent holes are recommended to relieve the buildup of steam or water vapor pressure as the moisture from the concrete evaporates at temperatures exceeding the boiling point of water. The report includes an equation that can be used to design the vent holes as a function of the maximum temperature and thermal gradient through the wall thickness, heating duration, moisture content, and acceptable level of pressure buildup on the steel plates. However, in typical cases, unprotected C-PSW/CF walls can be provided with 25 mm (1 in.) diameter vent holes spaced at 3.0 - 3.6 m (10-12 ft) in the horizontal and vertical directions to relieve the buildup of steam or water vapor pressure. These vent holes details can be improved using the equation and methodology discussed in the report. The water-to-cement ratio of the concrete mix design seems to have a minor influence on the pressure buildup but can also be controlled to improve the design of vent holes.

The project also led to the development and validation of a software tool that can be used instead of the design equations to more accurately model and calculate the thermal and structural performance of composite C-PSW/CF walls and rectangular concrete-filled steel tube (CFT) columns. This software tool, based on the fiber-based section and member analysis method, can be used to evaluate the performance and axial (gravity) load capacity of unprotected and protected composite members subjected to uniform or non-uniform (one-sided) heating. The analysis can be conducted by implementing standard (ISO 834 or ASTM E119), Eurocode parametric, or user input gas (or surface) time-temperature curves.

The proposed equations and the recommendations in this study can be used to develop design guidelines and specifications for fire design of C-PSW/CF under fire loading. A code change proposal will be proposed to the AISC 360 specification - Appendix 4 (Structural Design for Fire Condition).

Table of Contents

Chapter 1. Introduction

Examples of composite axial members include Concrete Filled - Composite Plate Shear Walls (C-PSW/CF) and Concrete Filled Steel Tube (CFT) columns. Composite Plate Shear Walls/ Concrete Filled (C-PSW/CF) are considered for commercial construction due to the advantages of modularity and expedited construction schedule. The C-PSW/CF system comprises of steel plates sandwiching plain concrete infill. The schematic cross-section of a C-PSW/CF is shown in Fig. 1-1. Steel faceplates running along the length of the wall filled with concrete, which together act as the web of the structure. Steel faceplates are connected through steel ties. These walls are typically reinforced by boundary elements towards their ends which act as flanges. The steel plates are analogous to the primary reinforcement bar in conventional reinforced concrete construction. Ties ensure the structural integrity of the system (Seo et al. 2016) and serve as out-of-plane shear reinforcement (Bhardwaj and Varma 2017a). Shear studs and/or ties provide composite action between steel plates and concrete infill. The research and design provisions have been discussed in detail by Bhardwaj and Varma (2017b).

Recent research projects have explored the commercial building application of C-PSW/CFs (Selvarajah 2013, Bruneau et al. 2013, Ji et al. 2013, and Varma et al. 2017). The current building codes, namely ASCE 7 (2016) and AISC 341 (AISC 2016) permit the use of C-PSW/CF, with and without boundary elements in seismic regions (Bruneau et al. 2013, Alzeni and Bruneau 2014, Epackachi et al. 2015, Kurt et al. 2016, Bhardwaj et al. 2018a). The lateral capacity of C-PSW/CFs for wind and seismic loads has also been investigated by Wang et al. (2018). C-PSW/CFs need to be designed for the limit state of local buckling of the faceplates (local instability). Local buckling of steel plates depends on steel plate slenderness, initial imperfections, and concrete casting pressure. Bhardwaj and Varma (2016, 2017) developed a procedure to incorporate the effects of initial imperfections and concrete casting pressure on the compression behavior of C-PSW/CFs. Bhardwaj et al. (2018b) also provided recommended steel plate (web plates and flange plate) slenderness criteria for C-PSW/CFs. The stability of empty steel C-PSW/CFs modules was evaluated by Shafaei et al. (2018a, 2018b).

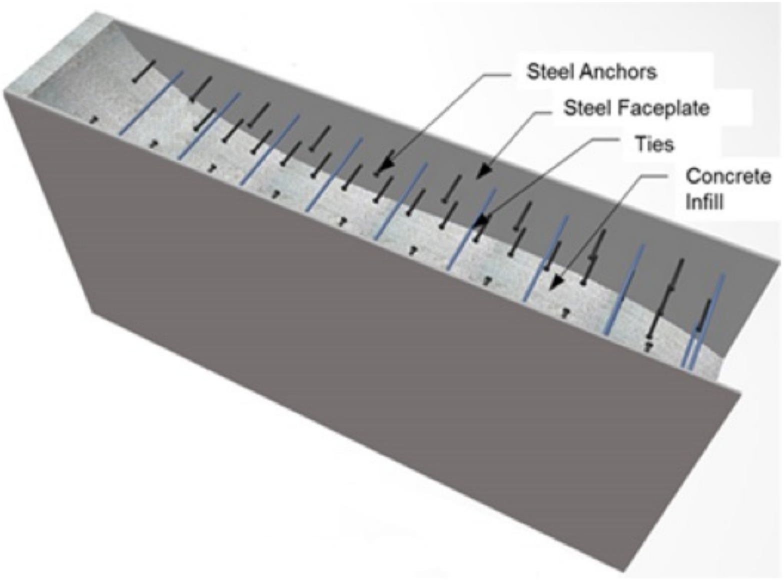

Fig. 1-1. Details of a Composite Plate Shear Wall/Concrete Filled (C-PSW/CF)

CFTs provide similar advantages to C-PSWs/CF, which are faster construction and improved material performance. CFT columns are typically made up of rectangular or circular hollow structural sections (HSS or steel tubes) filled with concrete. These columns are used in specialized construction as they combine the structural properties and advantages of steel and concrete. The steel tube acts as formwork and provides confinement to the concrete infill, thus improving the performance of concrete and cutting down the need to erect and demolish separate formwork. The concrete infill acts as a lateral support to the steel tube, delaying the local buckling of the steel tubes.

Extensive studies have been conducted on the behavior of CFTs, under various combinations of axial, bi-axial and seismic loading. Several researchers have compiled databases for experimental data on square, rectangular and circular composite columns (Bruneau et al. 2013, Kurt et al. 2016). The current AISC Steel Specification (AISC 360-16) provides design equations for composite structures (encased and filled) under axial, flexural and combined loading (AISC 360-16 Chapter I). Experimental and numerical research has also been conducted on C-PSWs/CF under various loading combinations to develop numerical models and propose design equations (Bhardwaj et al. 2018, Bhardwaj et al. 2019). However, these models cannot be extrapolated to elevated temperatures due to two main reasons: (i) non-linear material degradation of material properties at high temperatures and (ii) non-linear temperature gradient across the C-PSW/CF or CFT section.

Structures can occasionally be subjected to extreme loading events such as fire loading. In the case of a fire event, a structural column or wall may be exposed to elevated temperatures on all or some of its sides. These elevated temperatures cause a degradation of both strength and stiffness of the material. A column or wall carrying a constant axial load can thus fail when exposed to persistent heating. Composite members typically have a better fire resistance as compared to conventional steel members, due to the low thermal conductivity of concrete. When exposed to fire, CFTs and C-PSWs/CF develop a temperature gradient across the section, with the concrete core experiencing significantly lower temperatures. Hence, most of the load is carried by the core concrete.

1.1. Background and Literature Review

Several experimental as well as numerical studies have been conducted on C-PSW/CF and CFTs at elevated temperatures. These studies have focused on understanding different aspects of the fundamental behavior of composite members. The previous research on the composite members are discussed below.

1.1.1. Concrete Filled Composite Plate Shear Walls (C-PSW/CF)

Recently, Wei et al. (2017) conducted experimental studies on the fire resistance of Concrete-Filled Steel Plate Composite walls (CFSPC). The test results from Wei et al. (2017) provide significant data for the development of benchmarked models for current parametric numerical studies. The fire resistance of 12 CFSPC wall specimens was investigated. The specimens were subjected to combined gravity and fire loading. The tests were conducted in a gas furnace with the air temperature-controlled to follow the ISO 834 fire curve. The parameters considered by the authors were steel plate thickness, height, wall thickness, the spacing of shear studs, load ratio, and the fire scenario. Specimens with heights of 850, 1350, 1850 mm were used for uniform fire test scenarios, and 1000 mm height specimens were used for single-sided fire scenarios. The horizontal length of the specimens was maintained at 1000 mm. Stud and tie bars diameters were 2 and 10 mm, respectively. Shear studs at three different spacings (40, 60 and 80 mm) were welded to steel plate. The specimens were embedded in the loading beam and base beam at the top and bottom, respectively. Specimens were fixed to the base by the base beam, which was fixed to the strong floor. Eight specimens were exposed to fire at all the four sides of the specimens. The remaining four specimens were tested for single-sided fire scenarios with one side of the wall exposed to fire.

The results of the fire tests performed by Wei et al. (2017), indicated that the specimen slenderness ratio has a significant effect on the behavior of CFSPC walls. Specifically, as the slenderness ratio of specimens increases, the fire resistance of specimens decreases. Also, an increase in wall height can lead to global instability. The tallest specimen (1850 mm height) failed due to global instability. Tests showed that the composite action between steel plate and concrete deteriorates regardless of shear stud spacing. Therefore, the spacing of shear studs does not have a significant influence on the fire resistance of the wall. By comparing the fire resistance of specimens with various wall thicknesses, it was observed that the thicker specimens had a higher fire resistance. Specimens subjected to single-sided fire scenarios underwent insulation failure, with the earliest failure time being 166 minutes. The failure limit states are described in in section 2.6 of current report.

Moon et al. have conducted experimental studies on stiffened steel plate concrete walls (with ribs as stiffeners) subjected to fire loading (Moon et al. 2009). Moon et al. subjected 3000 ×3000×300 mm wall specimens to ISO 834 fire time-temperature curve (ISO 1975). The specimens were subjected to single-sided fire. The steel plates in these specimens were stiffened with ribs, which potentially improved the stability response of these walls. Axial load ratios of 40% and 63% of the design strength were applied in combination with fire loading. The fire rating of specimens with 40% and 63% of the axial load was 180 minutes and 89 minutes, respectively. The specimens initially experienced a lateral displacement towards the exposed surface. However; the lateral displacement towards the unexposed side began at later stages. The specimens failed due to local bulging of surface steel plates, spalling of concrete and stud / tie weld rupture.

Varma et al. (2013) investigated the local buckling behavior of SC Composite walls. The walls were analyzed at both ambient and elevated temperatures. Benchmarked FE models were used to assess the performance of the walls subjected to a combination of thermal and gravitational loads. A parametric study was also conducted to analyze the response of the wall specimens by varying the steel plate spacing-to-thickness ratio and the applied temperature (up to 350 °C). The researchers observed that the design provisions, for SC walls at elevated temperatures, in the existing codes are unconservative.

Booth et. al. (2007) conducted experiments to examine the out of the plane structural response of SC walls subjected to thermal and mechanical loads. Two full-scale specimens were tested with the temperatures rising to 300 °F. FE Models were also developed to obtain the results analytically. Hu et al. (2018) developed models to examine the response of SC walls under a combination of thermal and gravitation loads. These models were verified using the experimental data reported by Booth et al. (2007). Those models were then used to conduct a parametric study and equations predicting the out-of-plane stiffness of SC walls under fire loading were proposed. Hu et al. (2018) found that the out-of-plane stiffness of SC walls is greatly influenced by the fire exposure duration. Although several researchers have done extensive work, further investigation is required to evaluate the response of walls subjected to fire loading causing temperatures up to 1200 °C.

Liu et al. (2018) conducted an experimental and analytical study to evaluate the behavior of concrete-filled steel tubular (CFST) column-wall structures subjected to ISO-834 standard fire curves. The CFST column-wall had a non-linear temperature distribution through the thickness. The fire resistance of the CFST column walls ranged from 41 min to 63 min for load ratios of 0.3 and 0.45. The failure temperatures for CFST column walls varied from 772 °C to 880 ℃. Local buckling of the outer steel tube was observed, and the specimen failed due to bending under the compressive load. No welding failure was observed. Varma et al. (2013) conducted experimental studies to evaluate the behavior of CFT beam-columns under fire loading. The load -lateral displacement response and the moment-curvature response of the columns were reported. The specimens failed due to concrete crushing in the plastic hinge zones and local buckling of the steel plates. Equations were proposed to calculate the flexural stiffness and the moment capacity of a CFT beam-column at elevated temperatures.

1.1.2. Concrete Filled Steel Tube Columns (CFT)

The experimental studies involved heating CFT specimens in a specially designed furnace, the temperature of which was controlled to follow the standard time-temperature curve as specified in ASTM E119 or ISO 834. A constant or varying axial or lateral load was applied. These studies mainly focused on two things: the material properties and fire resistance rating.

Lie et al. (1995) tested 3 specimens of hollow structural steel filled with bar-reinforced concrete. Based on the results, they developed material models for steel and concrete at elevated temperatures and also proposed an analytical approach to calculate the axial capacity of reinforced square CFT members under standard (symmetric) fire conditions. Poh (2001) used experimental data from several tests to propose a new stress-strain-temperature relationship for structural steel. This material model is further discussed in Chapter 4.

Kodur and Mackinnon (2000) used data from 58 tests on plain, bar-reinforced and fiber-reinforced CFTs to develop empirical equations for prediction of fire resistance ratings. Empirical design equations were also proposed based on the tests and parametric studies. Yang et al. (2013) tested six full-scale square CFT specimens under non-uniform fire (one-sided and three-sided). They characterized various parameters influencing the performance of CFTs and also developed 3D numerical models for simulating the same.

A number of analytical and numerical studies have also been conducted on CFTs under fire loading. Numerical studies conducted on CFTs have focused on understanding their fundamental behavior under fire loading and development and benchmarking of finite-element models.

Hong et al. (2008) developed a 3D finite-element model using ABAQUS to simulate fire loading on CFTs. The models were verified and calibrated using test data and were used to predict CFT response at elevated temperatures. Detailed development and benchmarking of these models is given in Hong et al. (2008) and Hong (2007). Lie (1995) had proposed an analytical approach to calculate the axial capacity of reinforced square CFTs. Fischer and Varma (2015) developed a 3D FE model for composite beams and their connections subjected to gravity and fire loads. The models were used to provide additional insight into the axial forces developed in the connections, particularly during the cooling phase.

2D fiber-based models of CFTs have also been developed by Hong et al. (2009), which are simplified and quick to run. The simplifying assumptions include that the temperature along the length of the member was assumed to be constant, thus heat transfer was performed only in 2D (across the section). Detailed development and validation of the model is given in Hong (2007) and Hong et al. (2009). This model was found to be reasonably accurate in predicting key parameters of CFT behavior, when compared to experimental and finite-element data.

1.2. Current Research Motivation

Current AISC provisions (AISC 360-16, Appendix A4) provide equations to predict axial and flexural capacity for steel members at elevated temperatures. For composite members, a prescriptive approach is recommended which is based on empirical equations derived by researchers. While current building codes allow for performance-based design, it is not very common. The prescriptive approach involves using standard shapes and sections to attain a target fire resistance rating (FRR), which is defined as the time (in hours) to failure under standard (ASTM E119) fire loading. The FRR values can also be obtained experimentally, which require standard fire tests of the designed members.

An essential aspect of the applicability evaluation of C-PSW/CF systems and CFTs for commercial construction is the stability behavior of these walls under fire loading. These members, like other structural systems, must have the capability to endure the fire loading while maintaining the loadbearing capacity. They must have sufficient fire endurance so that they provide enough time for the dwellers to evacuate the building. As steel plates are on the surface of the C-PSW/CF and CFT, they are directly exposed to fire temperatures in the absence of fire protection. Fire loading will result in elevated temperatures in steel and concrete and causes non-linear thermal gradients through the cross-section of the walls. These elevated temperatures will result in the degradation of the mechanical properties of steel and concrete and may cause local or global instability. Finally, elevated temperatures in the members can lead to the collapse of the walls or columns at gravity load magnitudes lower than the compression strength of the members at ambient temperatures. Therefore, the stability of C-PSW/CFs and CFTs under fire loading needs to be evaluated experimentally and numerically.

The equations proposed in the literature, for the design of CFTs at elevated temperatures, are primarily empirical with very little theoretical basis supporting their development. As a result, they cannot be extended to generalized non-standard fire scenarios or structural designs other than those that were tested. This prescriptive design approach of composite structures (C-PSW/CF or CFT) for elevated temperature can limit innovation and optimization of designs. Therefore, a need exists for performance-based design methodologies of composite members under fire loading. The application of performance-based methodologies would allow for a more diverse range of structures to be designed using steel-concrete composite sections. Additionally, there is a need for more simplistic analytical models based on fundamental principles of mechanics that can predict the behavior of a broad category of structures under standard as well as non-standard fire loading scenarios with reasonable accuracy. These tools will further aid in performance-based design of composite structures and permit a greater scope for optimization and innovation.

The approach taken for this project for an analytical model to meet the needs described above was a fiber-based model/analytical tool. There are three main objectives of this fiber-based analysis method, they are:

(i) Develop a thermal and structural analysis tool for composite axial members at elevated temperatures. The tool would be based on fundamental principles of mechanics and thus would be applicable in all fire and axial load scenarios.

(ii) Conduct parametric studies on CFT columns, to study and quantify the effect various parameters have on CFT stability. An equation to estimate column capacity and fire rating would also be proposed based on the results

(iii) Analyze C-PSW/CFs by two methods: as a whole section and as discrete strips normal to its length, compare the analysis results to experimental and finite element data and validate the design equations proposed for C-PSW/CFs.

1.3. Current Research Undertaken and Report Layout

Five C-PSW/CFs specimens were tested at elevated temperatures. Fire tests were performed in Bowen Laboratory (Purdue University). Ceramic fiber heaters were used to heat the specimens. Specimens had different tie/stud spacing, loading ratio and they were exposed to two fire scenarios namely, all-sided and three-sided (one web and two flanges). The details of the experiments such as specimen design, instrumentation, test setup and results are provided in Chapter 2.

A parametric study focusing on the response of C-PSW/CFs subjected to axial compressive and fire loading was undertaken. The Finite Element (FE) method was used to simulate the thermal and structural response of the walls. The FE models were benchmarked based on the previous experiments conducted by Wei et al. (2017). Various parameters such as wall slenderness ratio, boundary conditions, load ratio, wall thickness, tie bar spacing, concrete strength, and plate reinforcement ratio were considered. The numerical results have been used to develop strength design and fire rating equations for C-PSW/CFs under fire loading. Chapter 3 describes the developed finite element models and proposed design equations.

A 2D fiber method-based tool has been developed to conduct a performance-based design of composite columns and shear walls. A simplified fiber model was developed as a tool to simulate the fire loading of composite axial members. The tool was used to conduct parametric studies on CFT columns to determine the effect of various parameters on CFTs. The tool was validated both at ambient and elevated temperatures using experimental data as well as 3D finite-element models. The section slenderness, column slenderness, fire protection and strength of the material were considered in the parametric study. According to the parametric studies, design equations were proposed. Details related to the fiber-based modeling are presented in Chapter 4.

The faceplate can trap the evaporated water from the concrete at elevated temperatures. The trapped water vapor builds up pressure between the faceplate and concrete infill. The built-up pressure increases further with an increase in temperature. Providing vent holes can enable vapor to escape and reduce pressure buildup. A rational method was developed to size the vent holes for C-PSW/CF. The details of the method with provided sample examples are provided in Chapter 5.

Chapter 2. Experimental Investigations

2.1. General

This chapter describes the fire testing of five C-PSW/CF specimens. The specimens had a cross-section dimension of 914.4 mm × 228.6 mm (36 in × 9 in) with 4.76 mm (3/16 in) thick faceplates. These specimens were previously tested by Wang et al. (2018) under combined axial and lateral cyclic loading to evaluate the response of C-PSW/CFs under lateral loading. The details of the tests and results are reported in Wang et al. (2018). Therefore, C-PSW/CF specimen were damaged at about 300 mm of the bottom of the specimens due to the formation of plastic hinges but the other parts of the specimens were undamaged. The damaged parts of the specimens were encased in reinforced concrete blocks to remove the damaged regions and prepare the specimens for fire tests. The details are provided in section 2.2 (Specimen Design) of current chapter.

Five fire tests were performed on C-PSW/CF specimens. The specimens were equipped with string potentiometers, and thermocouples to measure displacements and temperatures at various locations of the specimens. Ceramic fiber heaters were utilized to apply fire loading to the specimens. The specimens were subjected to axial loading equal to 20% - 28% of the compressive strength of concrete core at ambient temperature ($A_c f'_c$). The axial load was kept constant during the fire test. Four all-sided (heated two webs and two flanges) and a three-sided (heated one web and two flanges) fire tests were conducted. In the current chapter, the details of specimen design, test setup, instrumentation, and fire test results are presented.

2.2. Specimen Design

As noted previously, 5 total specimens were tested and Table. 2-1 presents the properties of all tested specimens denoted as CW1, CW2, CW3, CW4, and CW5. As shown in Table 2-1, specimens include steel tie bars and headed shear studs with a diameter of 9.5 mm (0.375 in). They also had tie bar spacings equal to 0.5 or 1.0 times the thickness of the specimen which results in steel plate slenderness ratios equal to 24 and 48, respectively. Specimen CW1 had tie bars at a spacing of 1.0 times wall thickness with headed shear studs between them. All sides (two webs and flanges) of CW1 and CW3-CW5 were heated during the fire test. However, only three sides of CW2 were heated in the fire test (one web and two flanges).

The specimens had previously been tested under combined axial and lateral cyclic loading (Wang et al. 2018). Plastic hinges had developed in the bottom 30 cm (1 ft) of the specimen. The remaining expanse of the specimens was undamaged. In order to reuse the specimens for fire tests, about 450 mm of the top and bottom of the specimens were embedded in reinforced concrete (concrete block) to eliminate the damaged parts at the specimen base that occurred during the cyclic tests.

Fig. 2-1 shows the detail of the steel reinforcement of concrete blocks and back-plate at both ends of specimens. Four rows of headed shear studs with a diameter of 9.5 mm (3/8 in) and spacing of 100 mm (4 in) were welded to the webs and flanges of specimens at both ends. Longitudinal and transverse reinforcement were provided to reinforce the concrete blocks. Deformed Bar Anchors (DBA) with a diameter of 15.8 mm (#5) were welded to a steel plate (back-plate) which play a role as longitudinal reinforcement in concrete blocks. Transverse reinforcement with a diameter of 12.7 mm (#4) was used at a spacing of 10.1 cm (4 in). Ten holes with a diameter of 14.3 mm (9/16 in) were made in the back-plate. Ten bolts were used at the end of concrete blocks to bolt the saddle at the end of specimens. Bolts had a diameter of 12.7 mm (½ in). The concrete block at the ends of specimens before and after pouring concrete are shown in Fig. 2-2 and Fig. 2-3(a), respectively. A schematic drawing of the specimens is shown in Fig. 2-3(b).

The heated region of the specimen had a width of 182.9 mm (72 in). A gap of 76 mm (3in) between the heated region and concrete blocks was provided to accommodate the axial shortening of the specimen and protect the fiber ceramic heaters during the fire tests.

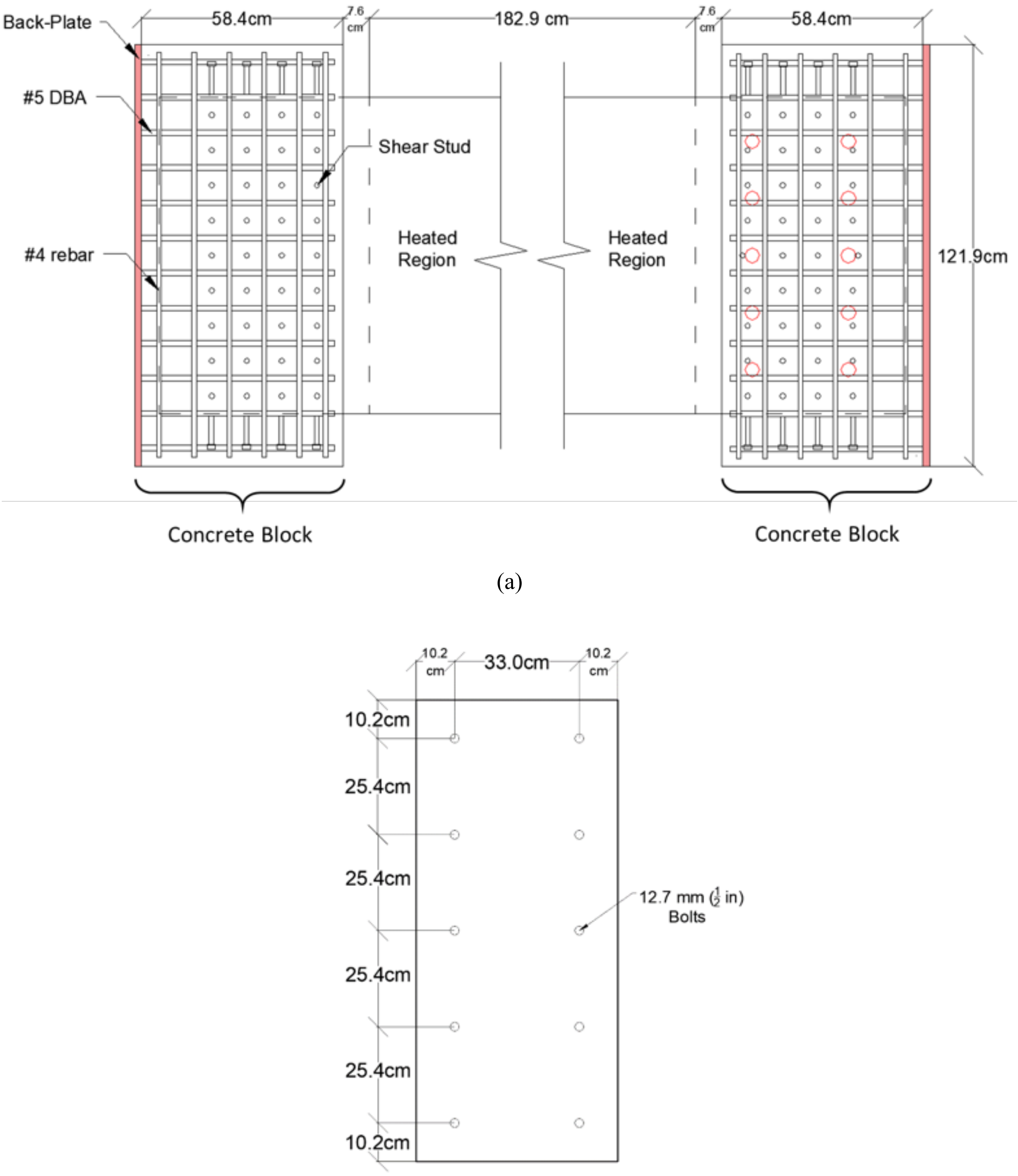

(a)

(b)

Fig. 2-1. (a) Foundation block design detail (b)The location of holes in the backplate

(a)

(b)

Fig. 2-2. (a) Specimen with welded headed shear studs (b) Concrete blocks steelwork

(a)

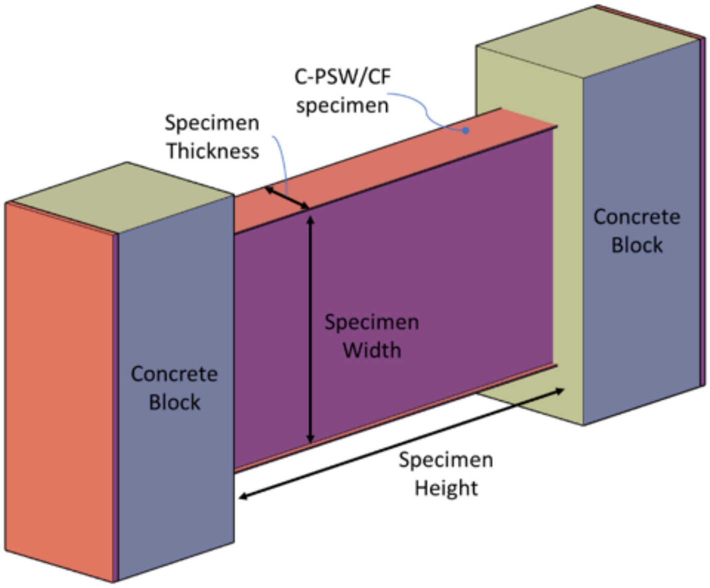

(b)

Fig. 2-3. (a)Specimen with concrete blocks after pouring concrete (b) schematic drawing of the specimens

Table 2-1. Specimen properties

Specimen	Plate thickness mm (in)	Shear stud diameter mm (in)	Shear stud spacing mm (in)	Tie bar diameter mm (in)	Tie bar spacing mm (in)	Steel plate slenderness	Load (%$A_c f'_c$)	Fire Scenario
CW1	4.76 (0.1875)	6.35 (0.25)	114.30 (4.5)	9.52 (0.375)	228.60 (9.0)	24	20	All sides
CW2	4.76 (0.1875)	6.35 (0.25) *	114.30 (4.5) *	9.52 (0.375)	114.30 (4.5)	24	20	Three sides
CW3	4.76 (0.1875)	6.35 (0.25) *	228.6 (9.0) *	9.52 (0.375)	228.60 (9.0)	48	28	All sides
CW4	4.76 (0.1875)	6.35 (0.25) *	114.30 (4.5) *	9.52 (0.375)	114.30 (4.5)	24	20	All sides
CW5	4.76 (0.1875)	6.35 (0.25) *	114.30 (4.5) *	9.52 (0.375)	114.30 (4.5)	24	28	All sides

* There shear studs were welded to flanges only.

2.3. Test Setup

Fig. 2-4 shows the schematic 3-D drawing of the test set up. The test setup included a self-reacting frame with two reaction steel blocks at ends to support the applied axial loads, two tension rods and a hydraulic jack. The test setup was supported by four concrete blocks which were located at the ends of the test setup and tied to the strong floor using threaded steel round bars. Two guide frames were provided near the hydraulic jack to limit the movement of the loading beam to the axial direction of specimens. Two steel beams with half-cylindrical bearings were provided at both ends of the specimen to allow rotation in the specimen about the weak axis of the specimen. Steel plates with welded saddles on one side of them were bolted to the backplates to complete the bearing arrangement. The axial displacement of the specimens was not restrained. An axial load was applied to the specimen. The specimens were allowed to expand and contract during the fire tests. The assembly process of the first specimen and assembled test setup (after placing the specimen) are shown in Fig. 2-5 and Fig. 2-6.

Fig. 2-7 shows the arrangement of the heaters around the specimens its position in the setup. Fourteen ceramic fiber heaters with the heating area size of 914.4×406.4 mm (36×16 in) and 914.4×203.2 mm (36×8 in) were used for all-sided heating tests. The heaters on sides (heating the web of the specimen) were supported by steel stands to position them at 2.54 cm (1 in) from the surface of specimens. The surface temperature of the heater can reach a maximum of 1100°C. Fig. 2-8 shows CW1 with the heaters before the fire test.

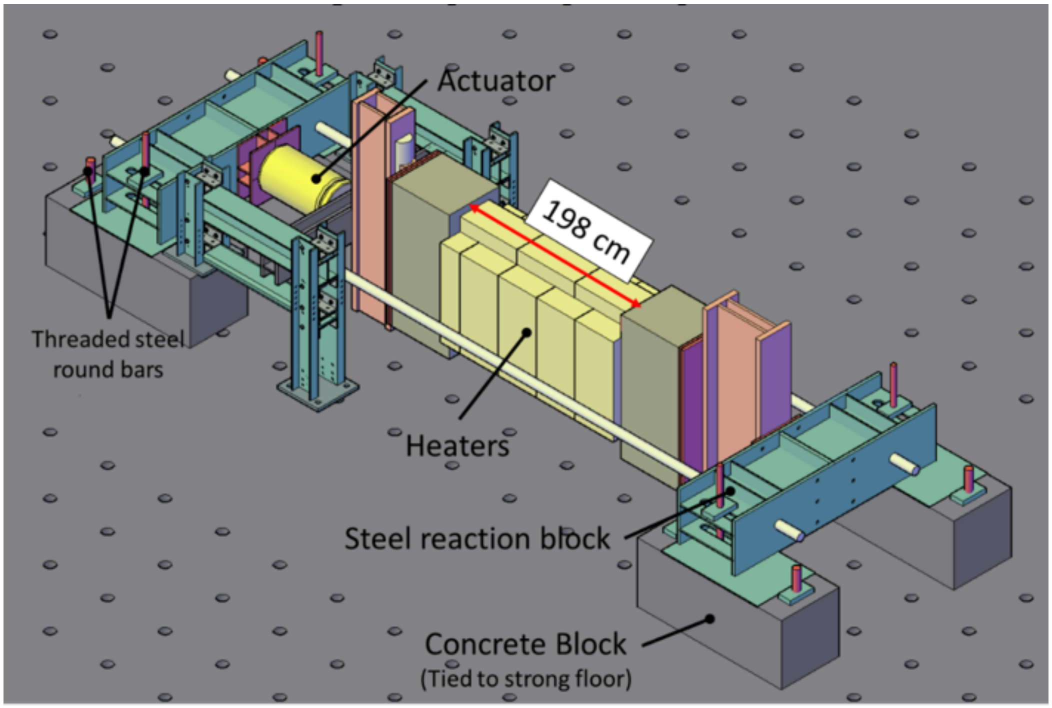

Fig. 2-4. (a) 3D schematic drawing of the test setup

Fig. 2-5. Placing CW1 in the test setup

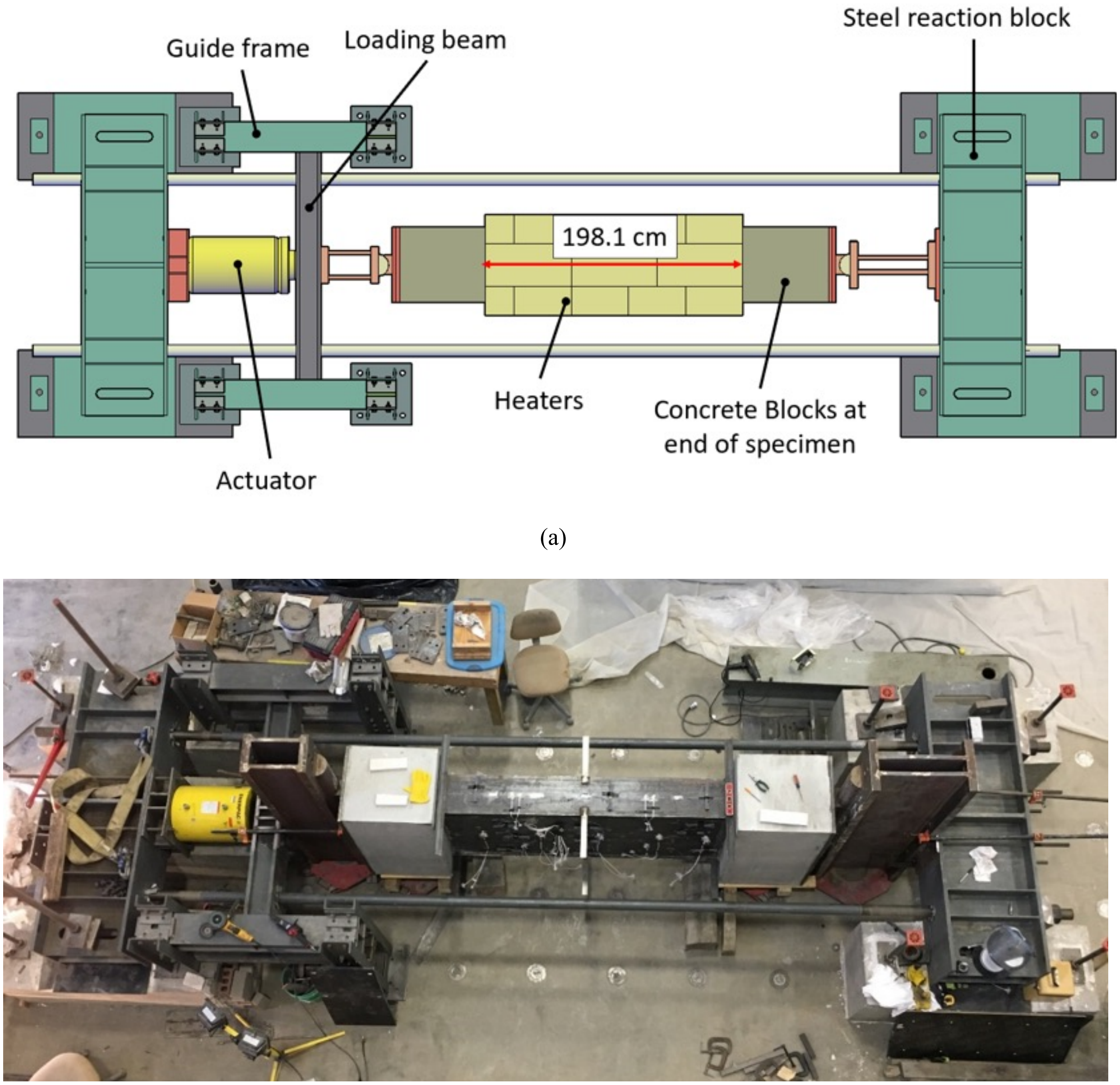

(a)

(b)

Fig. 2-6. (a) Schematic top view of test setup (b) Top view of the test setup

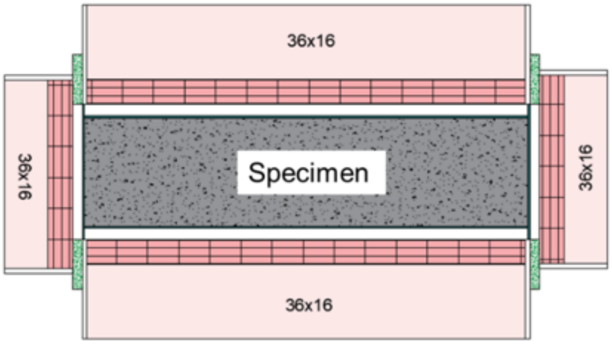

(a)

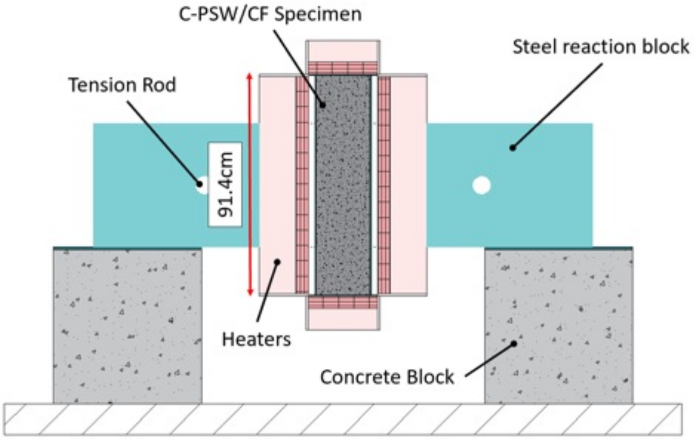

(b)

Fig. 2-7. (a) Arrangement of heaters (b) Placement of specimen and heaters in the test setup

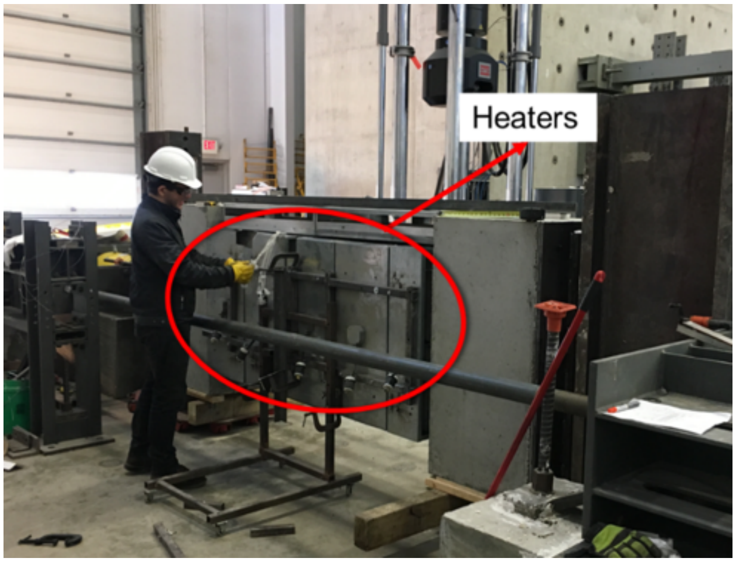

Fig. 2-8. CW1 located in the test setup ready to test

2.4. Instrumentation of Test Specimens

Strain gauges were used to measure the strain at different locations of the specimens. Strain gauges were installed on the exterior face of the specimen to assess and improve the eccentricity of loading within the specimen. In Fig. 2-9 the layout of the strain gauges is presented. The specimens were instrumented with string potentiometers and thermocouples to monitor the behavior of specimens during fire tests. Instrumentations were connected to the data acquisition system (DAQ). National Instruments's Lab View (V8.6) was used for data acquisition. Specimens were loaded at ambient temperature in several cycles to ensure the alignment of the specimen in the test setup.

A total of 14 ceramic fiber heaters were used to heat the specimens (all-sided heating). Two thermocouples were welded to the surface of specimens at the center of the covered area by each heater. All thermocouples were covered by high-temperature cement to avoid direct exposure to heaters and improve the attachment of thermocouples to the faceplate. A thermocouple (per heater) was connected to the data acquisition system to record the surface temperature of the specimen and the other thermocouple was connected to the heater's Control Panel (CP). The layout of the thermocouples is presented in Fig. 2-10. In order to measure the temperature through the thickness of CW1, nine thermocouples were embedded within the thickness of the specimen. A hole with a diameter of about 7.5 cm was cored in CW1 to place a thermocouple. The hole was filled with mortar and the faceplate was welded after ten days to let the mortar cure. High-temperature cement was applied to thermocouples to ensure the attachment of the thermocouples to the thermocouple tree. The location of thermocouples on the thermocouple tree is shown in Fig. 2-10(c). The temperatures were recorded at 1-sec intervals.

Four string potentiometers were installed in height of the specimens to measure the axial deformations (SP1-4). The string potentiometers were fixed on angle steel shape sections that were extended horizontally. The angles were welded to the specimen's flanges. String potentiometers were protected against heat exposure by covering them with autoclaved concrete panels. The out-of-plane deformation of the specimen was measured by four string potentiometers located at the East and West side of the specimen (SP5-8).

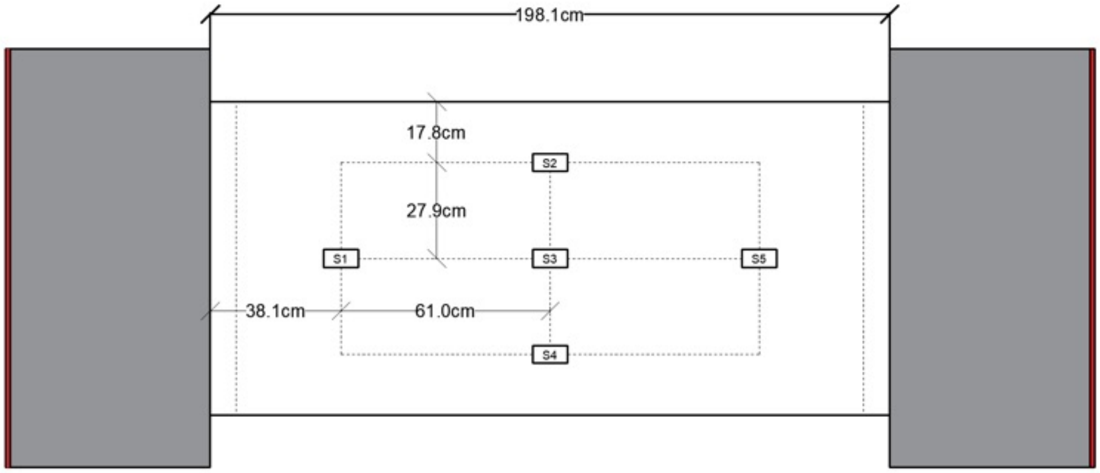

(a) On the web of the specimen

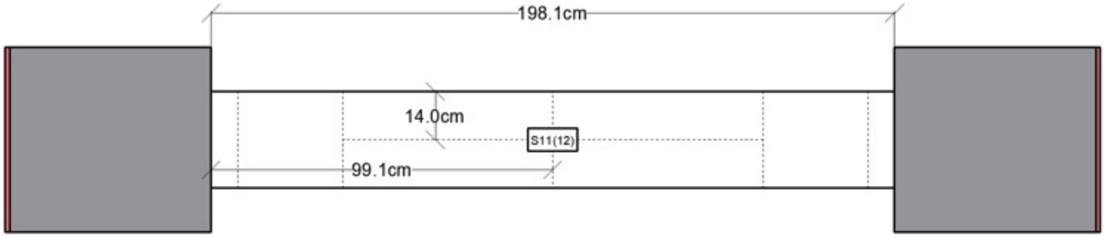

(b) On the flange of the specimen

Fig. 2-9. Layout of ambient temperature strain gauges

Four flat steel bars (with rectangular cross-section of 38 mm × 12 mm) were welded to the flanges at mid-height of the specimen. The steel flat bars were extended horizontally to pass through the heaters. String potentiometers were connected to the end of the flat bars to measure the out-of-plane displacement of the specimen. SP 9-10 were attached to the loading beam on the test setup to monitor uniform displacement of the loading beam during loading the specimen. Since the setup is allowed to move, SP11 and SP12 were used to measure the displacement of the test setup. By subtracting the displacement of the setup from measured displacement by SP5 to SP8, the out of plane displacement of specimens were corrected. SP13 was supported by welded vertical angles to the top of the specimens. SP13 was used to measure the axial displacement along the mid thickness of specimens. The displacements were measured at 1-second intervals. The layout of string potentiometers is shown in Fig. 2-11.

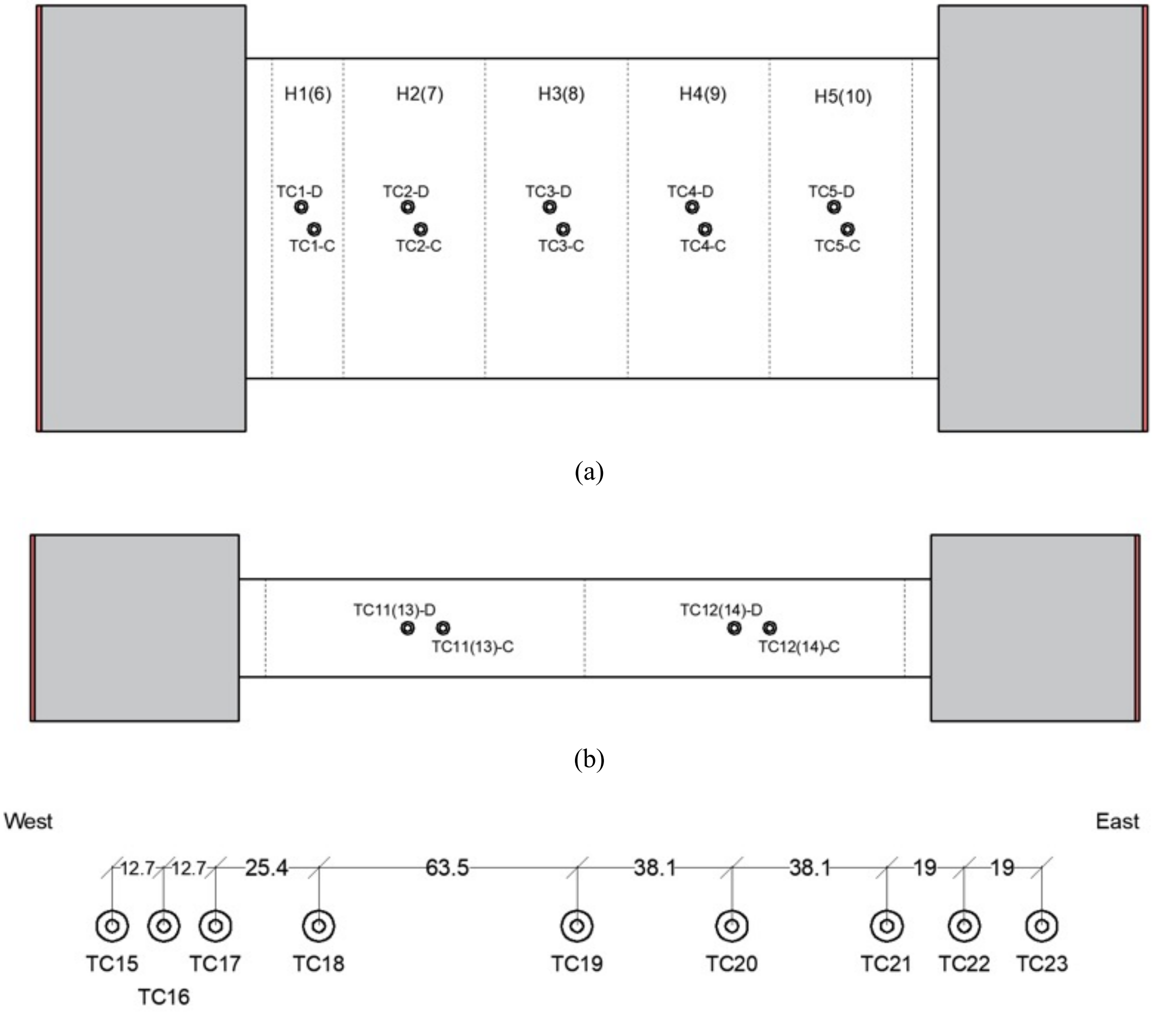

(a)

(b)

(c)

Fig. 2-10. (a) The layout of thermocouples installed on the West web (East) (b) the thermocouples installed on the Top flange (Bottom) (c) Layout of thermocouples placed within the thickness of the specimen (Dimensions are in mm).

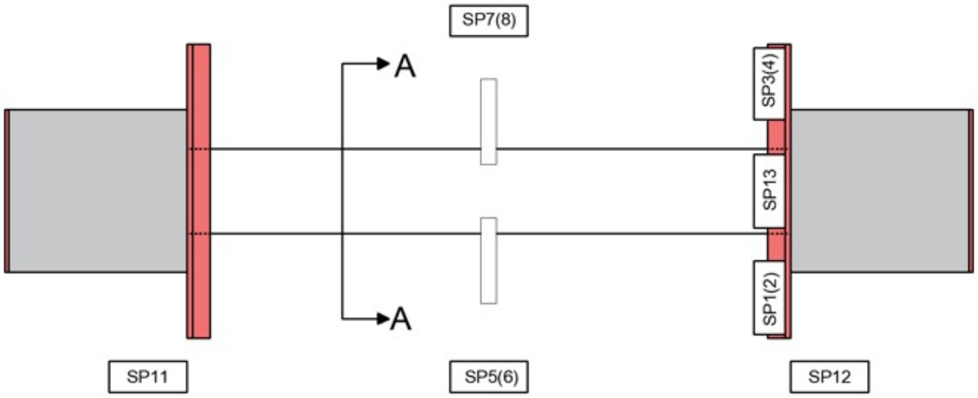

(a) Top view

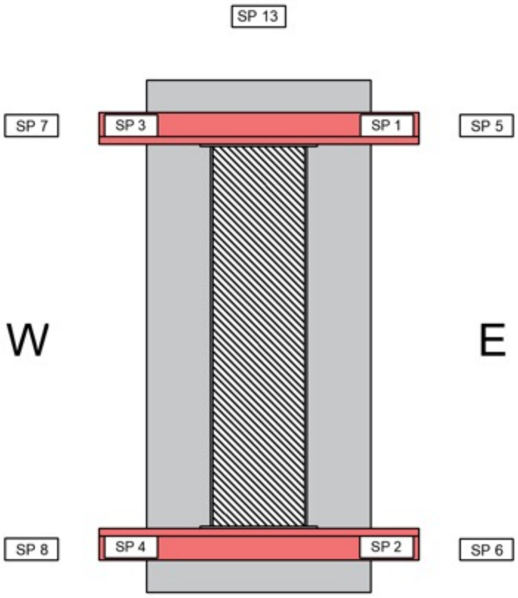

(b) A-A section

Fig. 2-11. The layout of the string potentiometers

2.5. Loading Protocol

Specimens were loaded axially to 20% or 28% of the compression capacity of the concrete core on the day of the test (*20%* $A_c f'_c$ *or 28%* $A_c f'_c$), where A_c is the area of the concrete and f'_c is the compressive strength of the concrete on the day of the test. The axial load was applied gradually at ambient temperature and the load was kept constant until the displacements were stabilized. The load was held constant while the specimen subjected to fire load. The loading system was monitored to maintain the load by adjusting the input voltage to the hydraulic ram when deformations take place in the specimen during fire tests.

2.6. Failure Criteria

Loadbearing and insulation failure criteria (per ISO 834) were investigated in uniform and three-sided heated specimens, respectively. The loadbearing failure of the specimen would occur when the axial contraction of walls exceeded $H/100$ (mm), where H is the height of the specimens. The wall would lose its separating function if the temperatures on the unexposed surface of the wall exceed the following limits:

(i) The average temperature rise (the average of measured temperatures on the unexposed surface) should be less 140 °C.

(ii) The temperature rise in any individual thermocouple should be less than 180 °C.

2.7. Trial Fire Tests and Heating Protocol

The standard time-temperature curves such as ISO 834 and ASTM E119 provide the gas temperature (temperature of air exposed to the surface of the specimen) versus time. The temperature of the gas in the furnaces can be controlled to follow a selected time-temperature curve. During fire tests (using ceramic fiber heater), the heaters can be controlled based on the surface temperature of the region covered by a heater. The surface temperatures are different than the gas temperatures due to the effect of convection and heat loss. The comparison of surface temperatures can help to evaluate the agreement of the temperatures in both techniques. A trial fire test was conducted to compare the measured surface temperatures of specimens tested in furnaces (the literature) with the measured surface temperature of the material (steel and concrete) heated by ceramic fiber heaters (at Bowen Laboratory).

Fig. 2-12(a) shows the setup and heaters used in the trial fire test. Three ceramic fiber heaters were used to heat the surface of a steel plate and concrete beam. The steel plate (thickness = 4.8 mm (3/16 in)) was placed on top of the concrete beam. The beam had a width of 305 mm (12 in) and a height of 356 mm (14 in). As the goal of this trial test was to compare the surface temperatures, only thermocouples on the surface of the steel plate and concrete were used. Fig. 2-12. (b) shows the comparison of the measured surface temperatures with the measured surface temperature of specimens heated in furnaces by Wei et al. (2017), Zheng and Hou (2008), Hou et al (2015) and Rodrigues et al. (2014). The results show a good agreement between the measured temperatures in fire tests performed by using ceramic fiber heaters and furnaces. The measured surface temperatures (heated by heaters) are very close to the reported surface temperatures reported in the literature.

This was achieved by keeping the heaters' power on and assure that the temperatures of the heaters are increasing throughout the fire test. The rate of temperature rise can vary for some heaters due to differences in the covered area by each heater. To heat the specimens uniformly, the target temperature of the heaters was increased at several steps. The target temperature (for all heaters) was increased when the surface temperature of the covered area by each heater got close to the target temperature. The general heating protocol of the specimens is as follows. (The steps may vary slightly for some test.)

- Set the target surface (steel) temperature to 260 °C (500 °F) on the control panel at the beginning.
- Set the target surface (steel) temperature to 538 °C (1000 °F) on the control panel when the surface temperatures of the covered area achieve 232 °C (450 °F).
- Increase the target surface (steel) temperatures at intervals of 38 °C (100 °F) when the temperatures achieve 510 °C (950 °F).

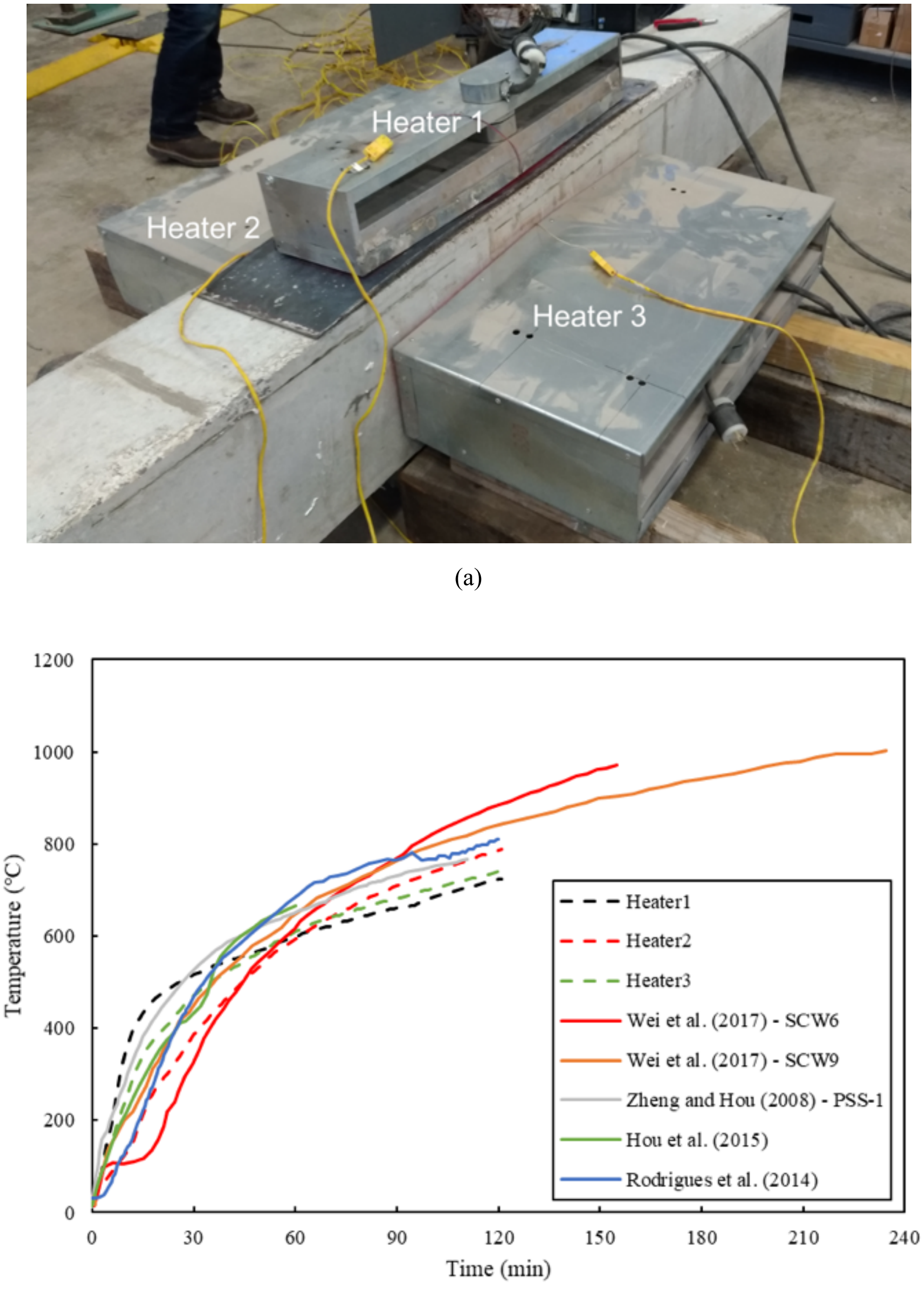

(b)

Fig. 2-12. (a) Test setup used for trial fire test (b)Comparison of measured surface temperatures in fire tests using ceramic fiber heater and furnaces

2.9. Concrete Mixture

Table 2-2 presents the concrete mix design for the specimens. Self-consolidating concrete with a spread of 660 mm (26 in) was used. The compressive strengths of the concrete infill on the test day is presented in Table 2-3.

Table 2-2. Concrete mix used for specimens (Self Consolidated Concrete-SCC)

Design Slump		26.00 +/- 4.0”		
Design Air		Entrapped		
Design Strength		5000 psi (27.6 MPa)		
Material		**S.G.**	**Weight (lb. / yd^3)**	**Vol (cf)**
Cement	Type I Cement	3.15	700	3.56
Fine Aggregate	Sand Natural	2.65	1533	9.40
Coarse Aggregate	3/8” PEA Gravel	2.70	1550	9.20
Water	MWater (Pounds)	1.00	276.5	4.30
Admixture	Mastermatrix VMA 358		4 oz/cwt	0.00
Admixture	Masterglenium 7511		7 oz/cwt	0.00
Air	Air (Entrapped)			0.54
W/C Ratio		0.40		
Fine aggregate to Total aggregate ratio		0.50		

Material Suppliers & Specifications

Material	Standard	Source
Type I Cement	ASTM C150	Buzzi
Sand Natural	INDOT	US Agg. Swisher RD
3/8” PEA Gravel	INDOT	US Agg. Swisher RD
Air (Entrapped)		Entrapped

Table 2-3. The compressive strength of concrete on the fire test day

Specimen	Concrete compressive strength	
	(MPa)	(Psi)
CW1	51.64	7490
CW2	61.25	8884
CW3	41.80	6064
CW4	51.49	7468
CW5	44.03	6386

2.10. Fire Test Results

Wei et al. (2017) tested 12 concrete-filled steel plate composite (CFSPC) specimens (analogous to C-PSW/CF). Wall thickness (150 - 200 mm), wall height (850 – 1850 mm), steel plate reinforcement ratio (3.4 - 8.5%), and fire scenario (uniform and single-sided) were the main parameters considered in the study. Specimens had a shear stud spacing of 40 to 80 mm which results plate slenderness ratios of 13 to 27, respectively. The shear studs were 2 mm in diameter and 20 mm long. Both load bearing and thermal failure criteria (ISO 834, 1975) were investigated. The walls had a fire resistance rating of more than 2 hours. The specimen with a wall slenderness ratio more than 12 failed due to global buckling while weld cracking or crushing were observed in other specimens a failure. A steel plate reinforcement of 5% was recommended. No recommendations were made for shear stud or tie bar spacing and size.

The results of the previous study (Wei et al. 2017) were studied and five additional C-PSW/CF specimens were tested in the current study. Steel plate slenderness ratios (24 – 48), load ratios (20 – 28% $A_c f'_c$) and fire scenario (all-sided and three-sided) are the parameters considered in the design of the specimens. Shear studs with larger size and length (than prior specimens) were used in a specimen (CW1) to study the behavior of using shear stud. The insulation capacity of walls was studied by heating a three-sided of specimen CW2. The effect of plate slenderness ratio (tie bar spacing) can be studied by comparing the response of CW3 and CW5. Specimen CW4 and CW5 were tested under 20 and 28% of the compressive capacity of the concrete core.

The current section describes the testing procedure of each wall followed by a discussion and comparison of the data. A constant axial load equal to a certain percentage of the compressive capacity of the concrete core was applied to the specimens (see Table 2-1). The specimens were heated using ceramic fiber heater as described in section 2.7. Axial displacements and surface temperatures of the specimens were measured during the fire test. The layout of the instrumentation (to measure temperatures and displacements) is provided in section 2.4. The load bearing and thermal failure criteria were investigated (see section 2.6). The measured data were used to study the effect of the considered parameter and also benchmark the developed numerical models (Chapter 3 and 4).

2.10.1. CW1 Fire Test - Test 1

The first test of CW1 was performed on April 11, 2019. The specimen was heated for 40 mins. The specimen was loaded to 2157 kN (485 kips - $20\% A_c f'_c$). This specimen had tie bar spacing equal to the thickness of the specimen with shear studs welded between the tie bars. The specimen had a steel plate slenderness of 24 which is less than $1.2\sqrt{E/F_y} \approx 28.9$. The load was kept constant with small variations (±90 kN or ±20 kips) during heating the specimen. After about 10 mins of heating the specimen, a significant amount of water was coming out of the specimen. Most of the water was dripping to the bottom heaters. The top surface of Heater 13 was filled with water after about 15 mins due to the evaporation of water from concrete infill. The evaporation of water can build pressure inside the specimen. The vapor can be trapped between faceplate and concrete if inadequate vent holes were provided. Noises could be heard from the specimen during heating the specimen due to the evaporation of water. The test was stopped after 40 mins when whistling noise exceeding about 80 dB was heard.

The measured surface temperature and displacements of the specimen are shown in Fig. 2-13 and Fig. 2-14, respectively. The wires of SP1 and SP3 melted during the fire test due to exposure to heat. Also, SP6 malfunctioned at the beginning of the fire test. The specimen was investigated when it was cooled down the next day. Previously, a hole had been made in the steel plate for the thermocouple tree. The thermocouple tree hole was acting as a vent hole during the fire test. Some small local buckling between the tie bars and shear studs occurred (Fig. 2-15). To prepare the specimen and test set-up for the second test, 25 mm (1 in) deep holes were drilled into the concrete at the center of vent holes. Also, the welded angles supporting the string potentiometers were extended further away from the specimen to be protected against heat during the test.

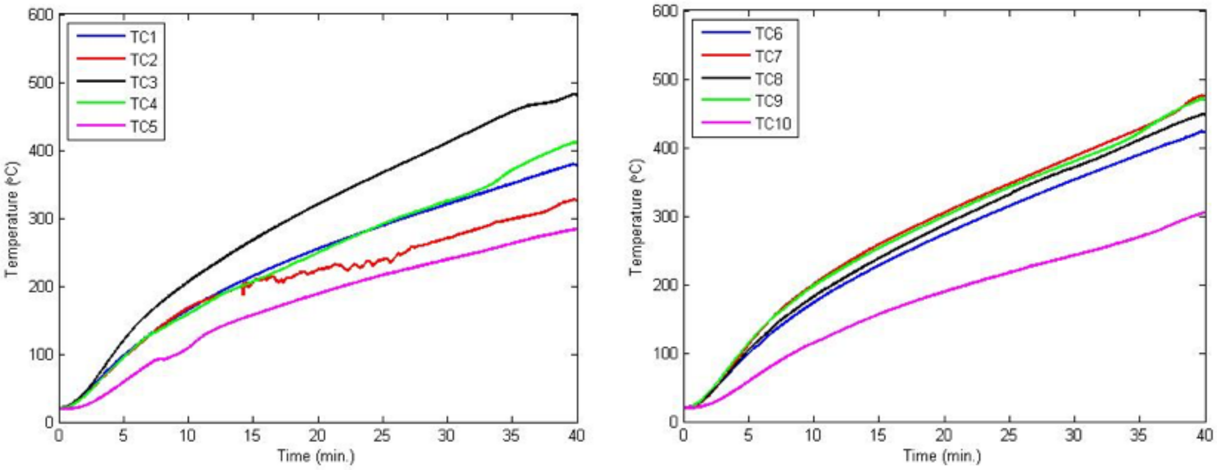

(a) East web

(b) West web

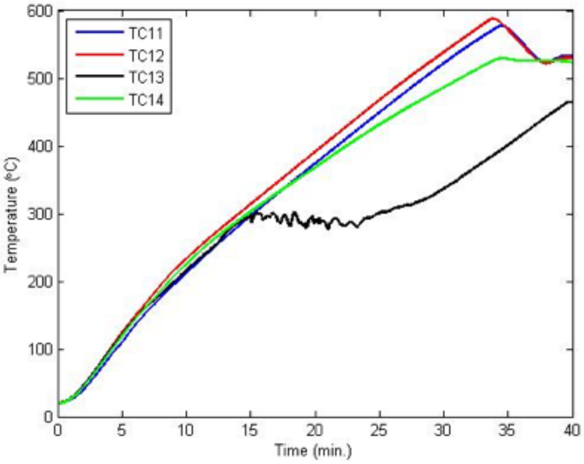

(c) Top and bottom

Fig. 2-13. The surface temperature of CW1 (Test 1)

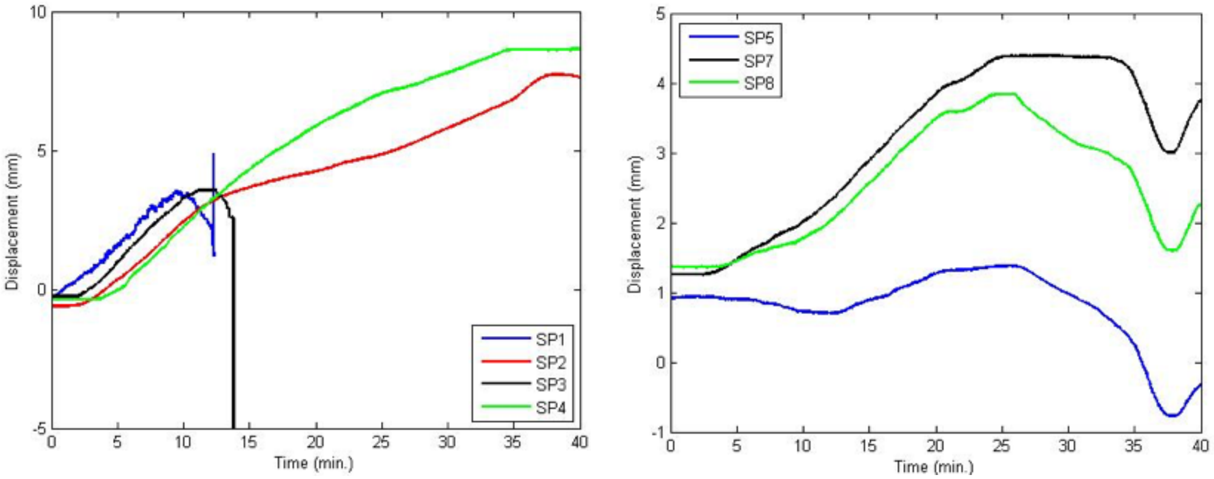

(a) Axial displacement

(b) Out of plane displacement

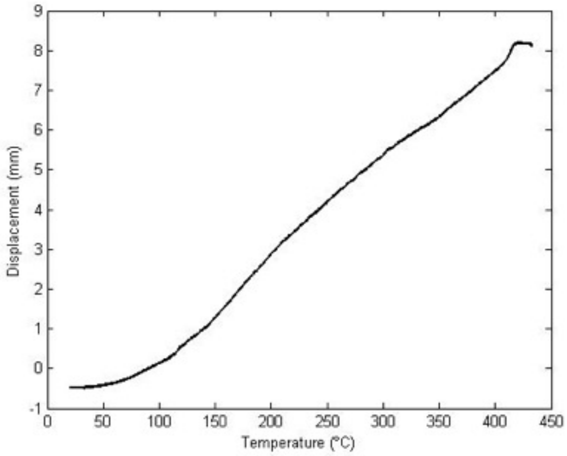

(c) Surface temperature against axial displacement

Fig. 2-14. Measured axial and out of plane displacements of CW1 (Test 1)

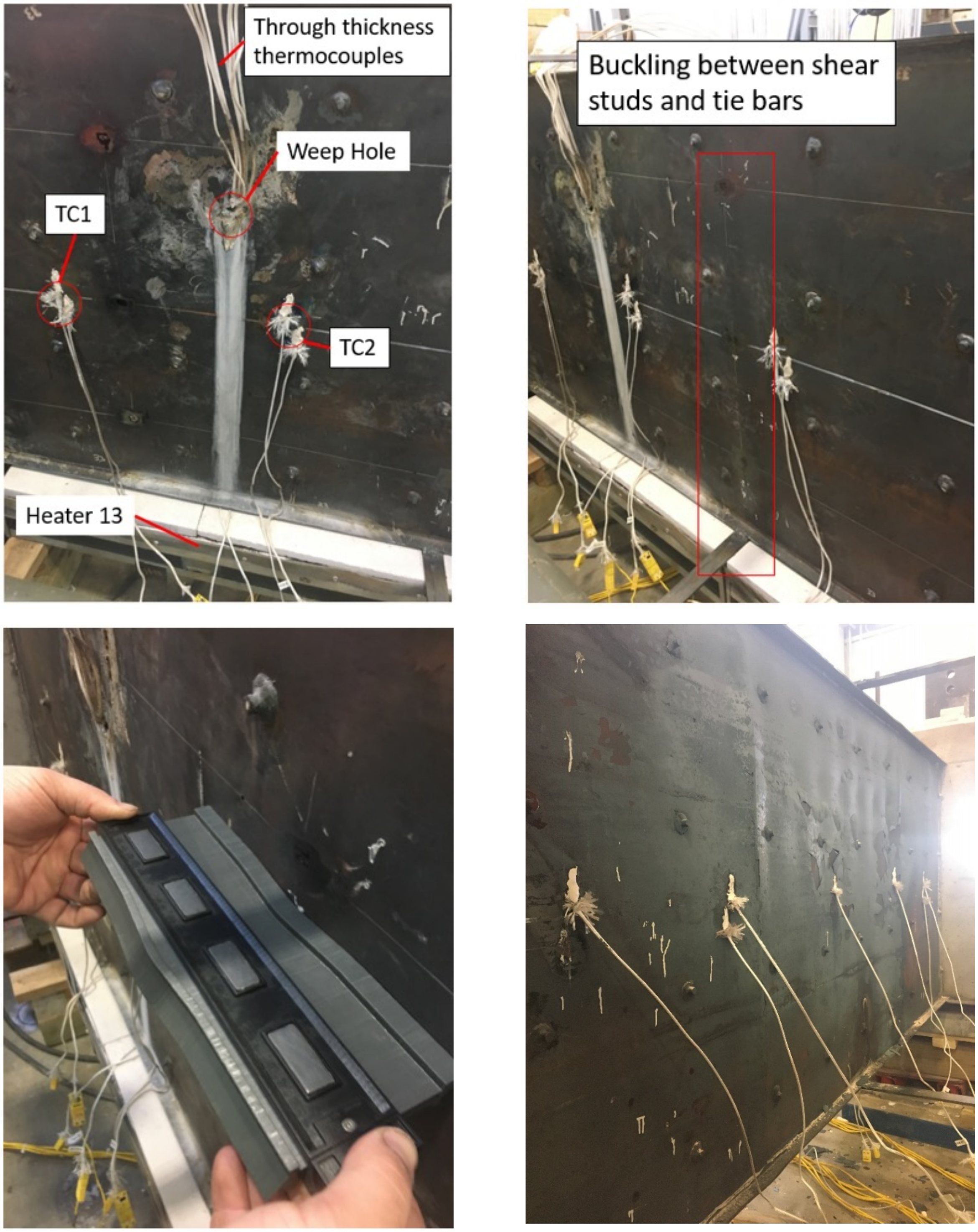

Fig. 2-15. Local buckling in CW1 specimen after the fire test

2.10.2. CW1 Fire Test - Test 2

The second fire test of CW1 was performed on April 16, 2019. The specimen was subjected to fire loads for about 180 minutes. The specimen was loaded to 2157 kN (485 kips - $20\% A_c f'_c$). The load was kept constant with small variations (±90 kN or ±20 kips) during heating. A decibel meter was installed close to the specimen to measure the noise level. The specimen started making noises (water evaporation) after about 10 minutes of heating. The noise level was about 55 dB at the beginning of the test. The noise level went up to a maximum of 68 dB at 95 mins and then decreased to about 62 dB at the end of the test.

The specimen had six vent holes on webs and three vent holes on the flanges. The vent hole diameter was 3.2 mm (1/8 in). At the beginning of the test, the heaters' target temperature was set to 537 °C (1000 °F). After 25 mins when the surface temperature of most parts of the specimen achieved to above 500 ℃, the target temperature of heaters was increased to 815 °C (1500 °F). The surface temperature of the webs was less than the top and bottom flanges. Therefore, the heaters' target temperatures were increased at 93 °C (200 °F) intervals to heat the specimen uniformly. Due to high surface temperatures, some of the thermocouples were separated from the specimen during the test. The Control Panel's thermocouples were switched with DAQ's thermocouples to keep the heaters working in case of thermocouple separation. Control Panel's thermocouples for heaters 4, 7, 8, 11, 12, 13 were switched with DAQ's thermocouples in the test. The surface temperature of the specimen against time is shown in Fig. 2-16.

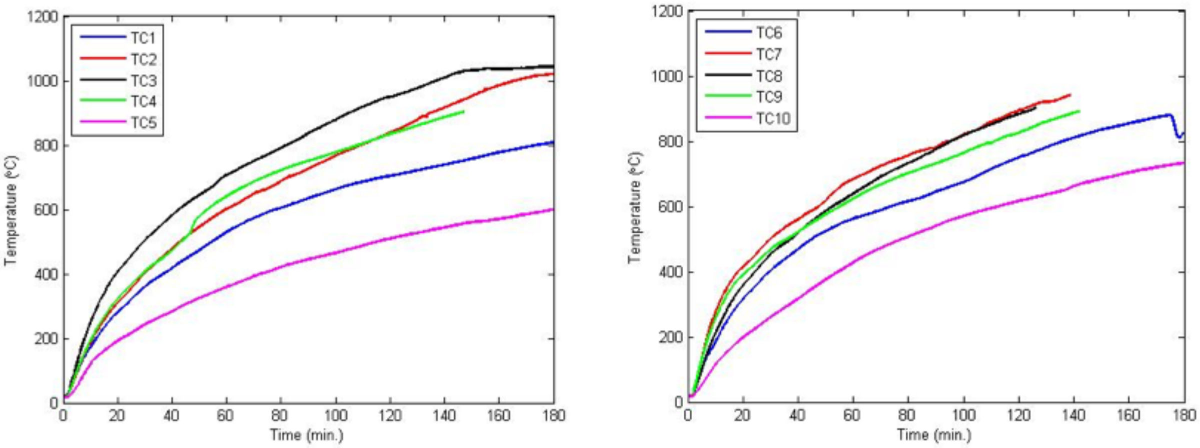

(a) East web

(b) West web

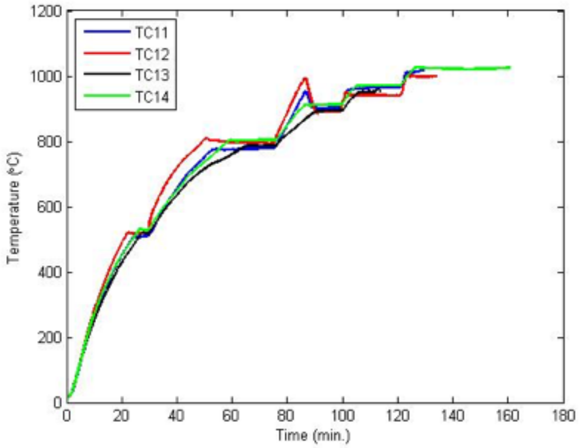

(c) Top and bottom

Fig. 2-16. The surface temperature of CW1 (Test 2)

CW1 expanded for about 40 mins due to the thermal expansion of faceplate. The difference in the magnitude of peak axial displacement (and the time at which the displacement was reached) can be due to slight differences in the temperature of different parts of the specimen (Fig. 2-16(a)). After the specimen reached the maximum axial displacement expansion, the specimen began to shorten for about 20 mins. This reduction in axial displacement can be a result of the deterioration of mechanical properties and local buckling of steel at elevated temperatures. In the next stage, the specimen did not experience any significant shortening in the axial direction for about 80 mins while the temperature was increasing within the specimen. The shortening of the specimen got faster after about 140 mins. The test was stopped after 180 mins of heating the specimen due to an increase in the rate of axial displacement reduction in the specimen. The axial displacement of the specimen is shown in Fig. 2-17(a).

The out-of-plane displacement of the specimen was measured through the flat bars welded to the flanges of the specimen and extended through the heaters to the sides. The specimen was bent slightly to the West during the mechanical loading of the specimen before the fire test. Slight out-of-plane displacement in both directions (toward both East and West directions) was observed at the beginning which can be due to thermal expansion in flanges of the specimen. However, after 40 min of heating, the specimen started to bend to the west up to about 8 mm (5/16 in) at the end of the test. The measured through-thickness temperature is shown in Fig. 2-17(d).

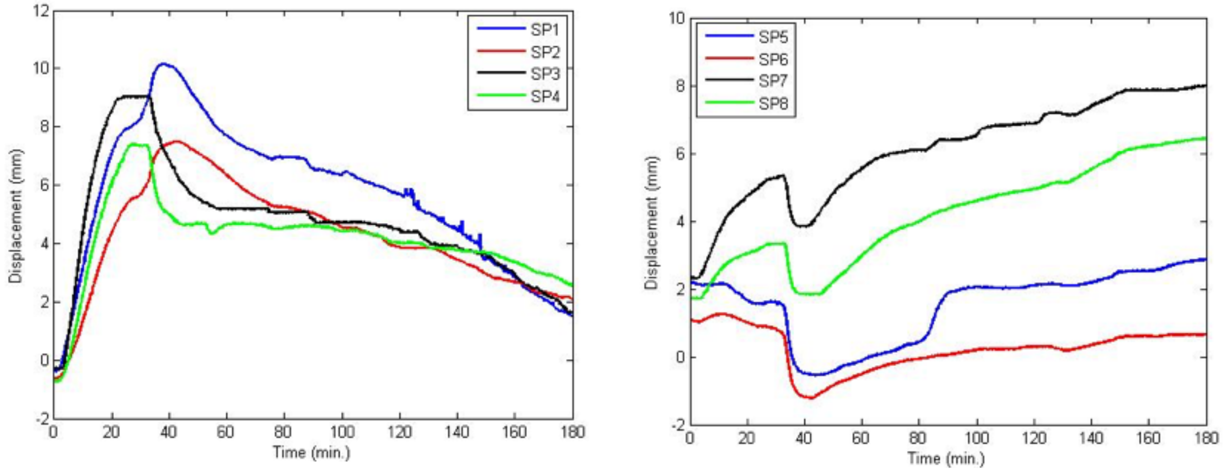

(a) Axial displacement

(b) Out of plane displacement

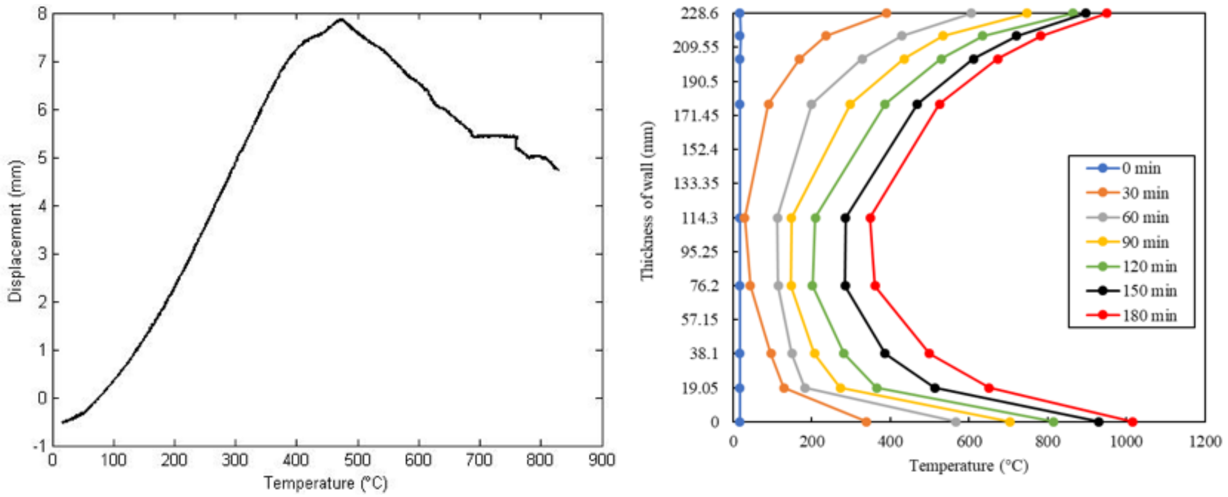

(c) Temperature against axial displacement

(d) Through thickness temperatures

Fig. 2-17. Measure displacements and through-thickness temperature of CW1 (Test2)

The temperature through the thickness of the specimen increased symmetrically about the centroidal axis. The concrete surface temperature increased faster than the mid-thickness of the specimen due to the low thermal conductivity of concrete. At 30 min, the temperature in the middle of the specimen was about 29 ℃ when the concrete surface temperature reached 340 ℃. At the end of the fire test, the temperature in the middle of the specimen was 350 ℃ and the concrete surface temperature reached 780 ℃. Fig. 2-16(d) shows the surface temperature of steel, which correspond to depths of 0 mm and 228.6 mm in the cross-section. Local buckling was observed between the tie bars and shear studs as shown in Fig. 2-18. The faceplate was removed from the specimen to check the condition of shear studs and tie bars as shown in Fig. 2-19. Some of the shear studs had undergone weld failure (to the plate) where local buckling occurred in the steel plate (faceplate).

(a) East web

(b) West web

Fig. 2-18. Local buckling in CW1 specimen after fire test (Test 2)

Fig. 2-19. Failed shear studs after the fire test

2.10.3. CW2 Fire Test - Test 1

CW2 was first tested on May 29th, 2019 for about 25 mins. This specimen had a tie bar spacing equal to the half of the thickness of the specimen (steel plate slenderness = 24). Three sides of CW2 were heated. Top, bottom and the east web of the specimen were exposed fire and the west face was unexposed. A constant axial load equal to 2557 kN (575 kips - *20%* $A_c f'_c$), was applied to the specimen. On the unexposed surface, one thermocouple was welded to the center of each quarter of the specimen, and one thermocouple was welded at the center of the surface. In Fig. 2-20, the location of the thermocouples welded to the unexposed surface of the specimen is shown. The measured temperatures are presented in Fig. 2-21.

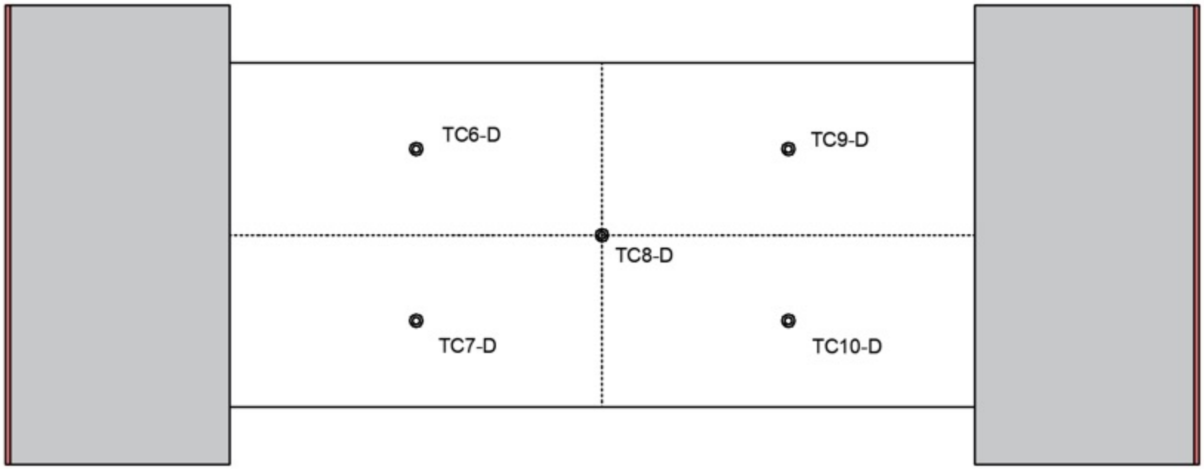

Fig. 2-20. The layout of thermocouples on the unexposed surface of the specimen

The specimen experienced bending toward the East (exposed web). The axial displacement of the specimen was measured at about 45.7 cm (18in) away from the specimen as described in previous sections. Due to their location, the sensors experienced a rigid body rotation and, accordingly, the deformations measured by these sensors were not the actual axial deformations experienced by the specimen.

Fig. 2-22. qualitatively shows the influence of the rigid body rotation on measured displacements compared to the actual axial displacements experienced by the specimen. The correction of the measured axial displacement is presented in Appendix B. The actual axial displacements were calculated using the measured displacements by string potentiometers and are shown in Fig. 2-23.

The overall bending of CW2 caused the movement of the test setup and due to this displacement, some of the thermocouples on the exposed web (East web) were touched the heaters' surface (Thermocouples were disconnected). The test stopped after 25 mins to replace the thermocouples and add more protections to the thermocouples. Two string potentiometers (SP11 and SP12) were added to monitor the test setup movement. Also, SP13 was added to measure the axial displacement of the specimen along the mid thickness of the specimen (as shown in Fig. 2-11).

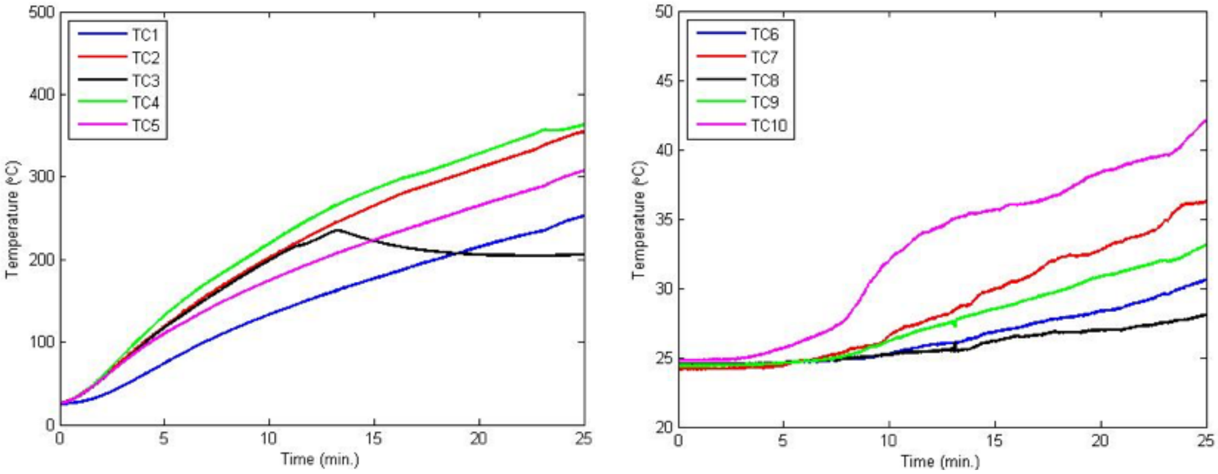

(a) East web

(b) West web

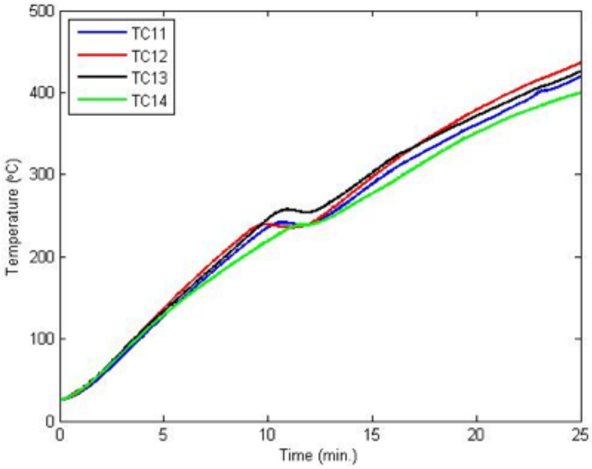

(c)Top and bottom flanges

Fig. 2-21. Measured temperatures - CW2 (Test1)

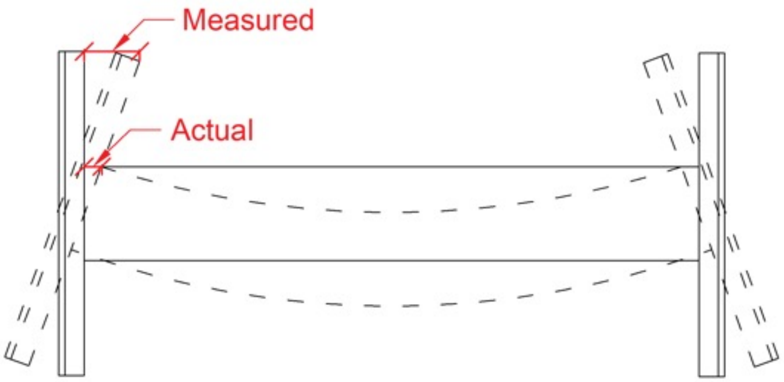

Fig. 2-22. Measured and actual axial displacement of the specimen (plan view)

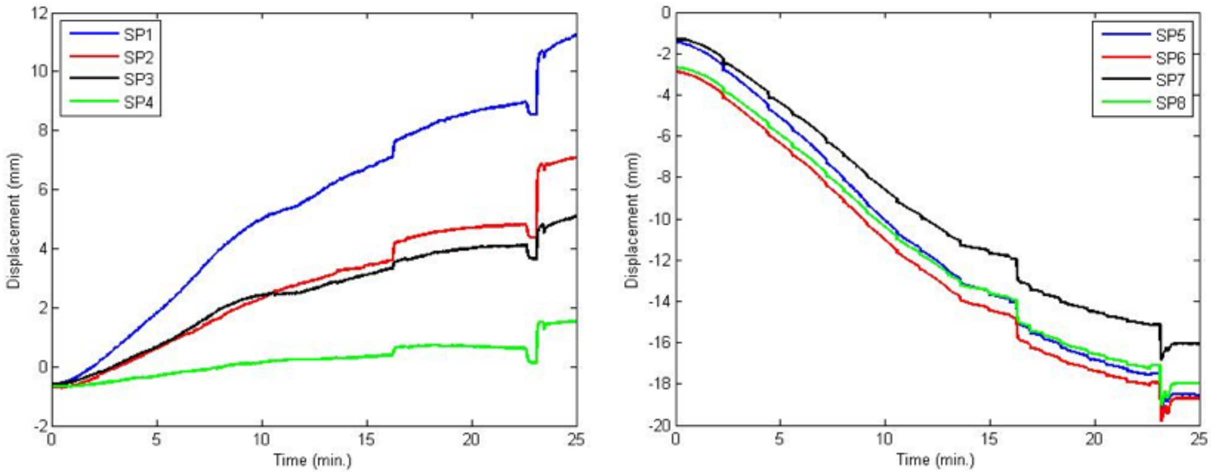

(a) Axial displacement

(b) Out of plane displacement

Fig. 2-23. Measured displacements CW2 (Test1)

2.10.4. CW2 Fire Test - Test 2

CW2 was tested again on June 6, 2019, at Bowen Laboratory. The noise level was about 55 dB at the beginning of the fire test. After about 40 mins, the noise level due to the water boiling noise reached a maximum of 66 dB. The measured temperatures on the exposed and unexposed surface of the specimen are shown in Fig. 2-24. During the test, the water was oozing out of the specimen. This caused an error in the measured temperatures by TC8. TC8 was used to measure the surface temperature on the unexposed web of the specimen (Fig. 2-20). The average temperature on the unexposed surface reached 103℃ with the maximum temperature at TC10 (130°C). According to ISO 834, insulation failure criteria of walls, the average temperature rise

(Average of measured temperatures on the unexposed surface) should be less 139℃. Also, the temperature rise on any individual thermocouple should be less than 181℃ for any thermocouple. Therefore, the specimen satisfies the thermal protection failure criteria after 140 min of exposure to fire.

Due to the bending of the specimen, the string potentiometers were measuring higher displacements in the axial direction. The axial displacement of exposed and unexposed surfaces of the specimen was calculated based on the measured displacement by SP2 and SP4. This method is presented in Appendix B. SP1 was disconnected due to the heat effect during the test. The measured axial displacement of the specimen is shown in Fig. 2-25(a).

The test setup is designed in a way that it can move slightly to the sides. A string potentiometer was installed at each end of the specimen (on concrete blocks) to measure any displacements due to the movement of the test set-up. The average of the measured displacements by SP11 and SP12 was deducted from SP5 to SP8, to get the accurate out-of-plane displacement of the specimen. The out of plane displacement of the middle of the specimen is shown in Fig. 2-25(b). SP5 and SP6 were connected to the exposed side of the specimen and SP7 and SP8 were connected to the unexposed surface of the specimen. The specimen was bending toward the exposed surface until 40 mins after heating the specimen. However, after 40 mins the out-of-plane displacements reduced, and the specimen was straightening gradually until the end of the test. The difference in the measured out-of-plane displacement between the string potentiometer connected to the exposed and unexposed surfaces can be due to the thermal expansion of the specimen flange and the flat bars.

A motion capture system was used for CW2 fire test to measure the displacement of targets located on the unexposed surface of the specimen. Optical tracking is one of the dominant technologies currently being used for motion capture especially in computer gaming and cinema industries. Optical tracking is based on monitoring a defined measurement space with two or more infrared-equipped cameras. Objects that need to be tracked are equipped with radio-reflective markers. In an optical motion capture system, multiple synchronized cameras are installed around the target and 2D images are captured from each camera to perform position calculations. Subsequently, the overlapping position data are compared to compute the 3D positions via triangulation. A total of 17 targets were attached to the unexposed surface of the specimen as shown in Fig. 2-26.

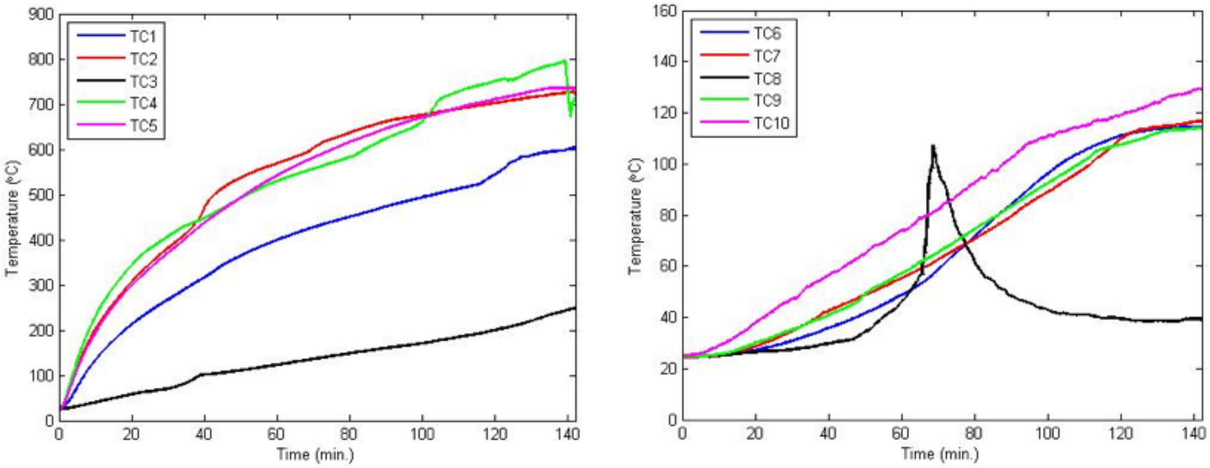

(a) East web (b) West web

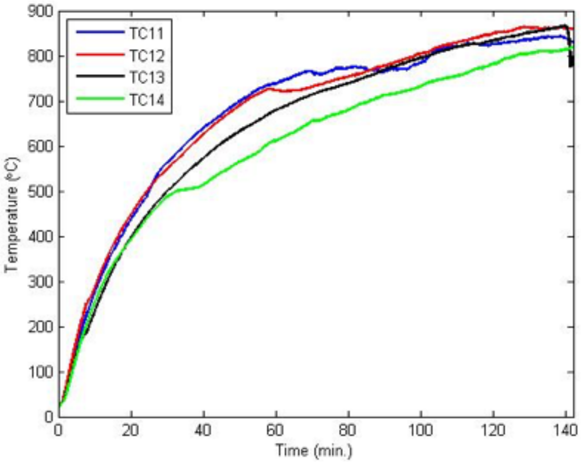

(c) Top and bottom

Fig. 2-24. The surface temperature of CW2 specimen

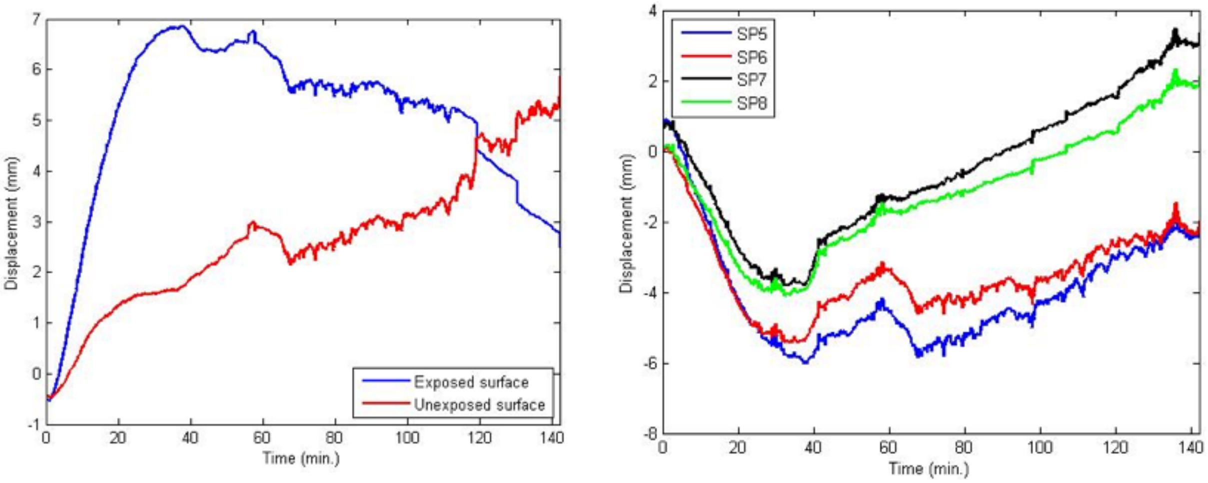

(a) Axial displacement (b) Out of plane displacement

Fig. 2-25. Measured displacements CW2 (Test2)

The displacement of the targets in the middle of the specimen was compared with the corresponding string potentiometers. High temperatures caused the loss of the targets on the specimen. By using the displacements measured by OptiTrack, the movement of the whole test setup and the specimen movement was measured during the fire test. The comparison of measured displacements by string potentiometers and OptiTrack is shown in Fig. 2-27. In Fig. 2-28, the position of the specimen at different time steps after the beginning of the fire test is shown. Target 1 and 7 are on the north and south concrete blocks, respectively.

Local buckling on the exposed surface of the specimen between the tie bars occurred at different locations as shown in Fig. 2-29. Twelve vent holes with 3.2 mm (1/8 in) diameter were drilled on the unexposed surface. Vapor and water were coming out of the specimen through the vent holes during the fire test.

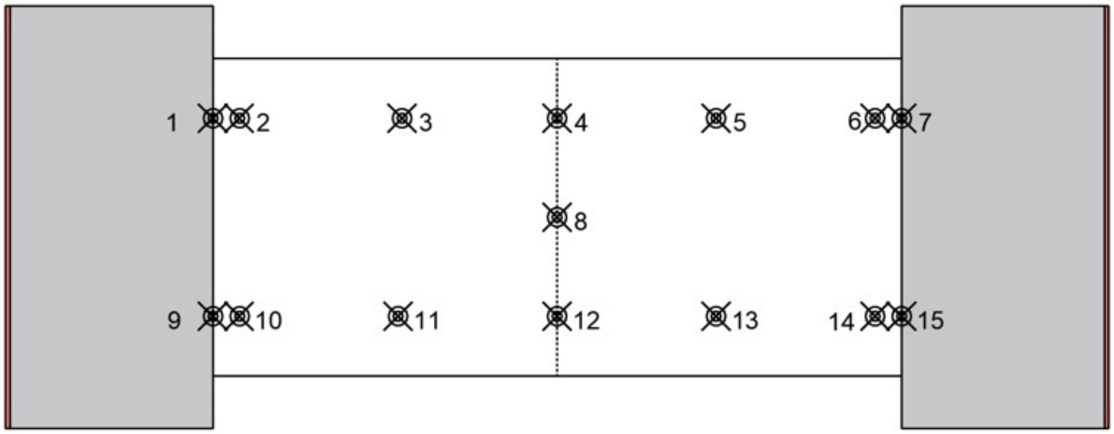

Fig. 2-26. The layout of the OptiTrack targets

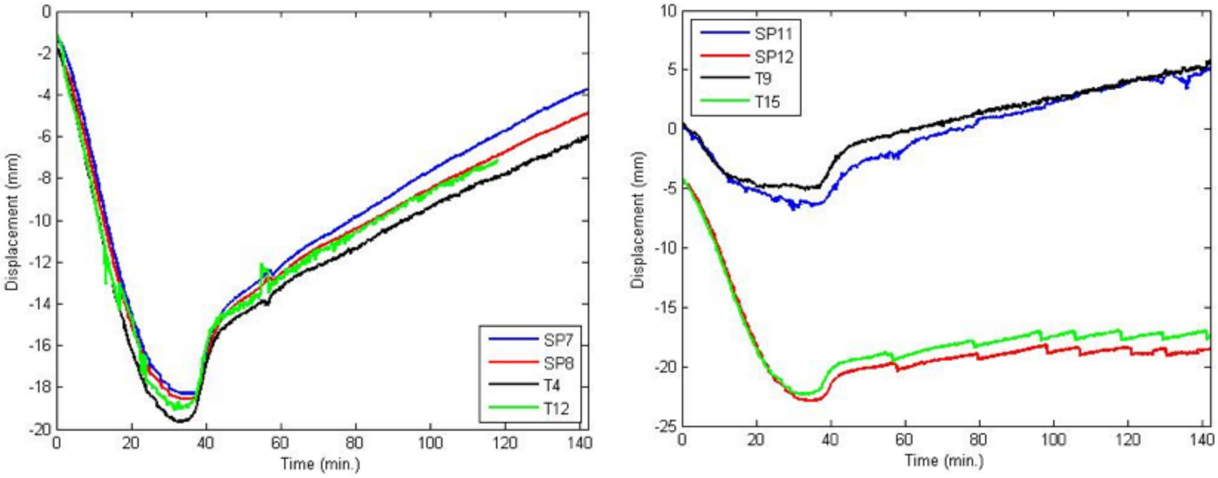

(a) Out-of-plane displacement

(b) Test setup movement

Fig. 2-27. Comparison of measured displacement by string potentiometer and OptiTrack.

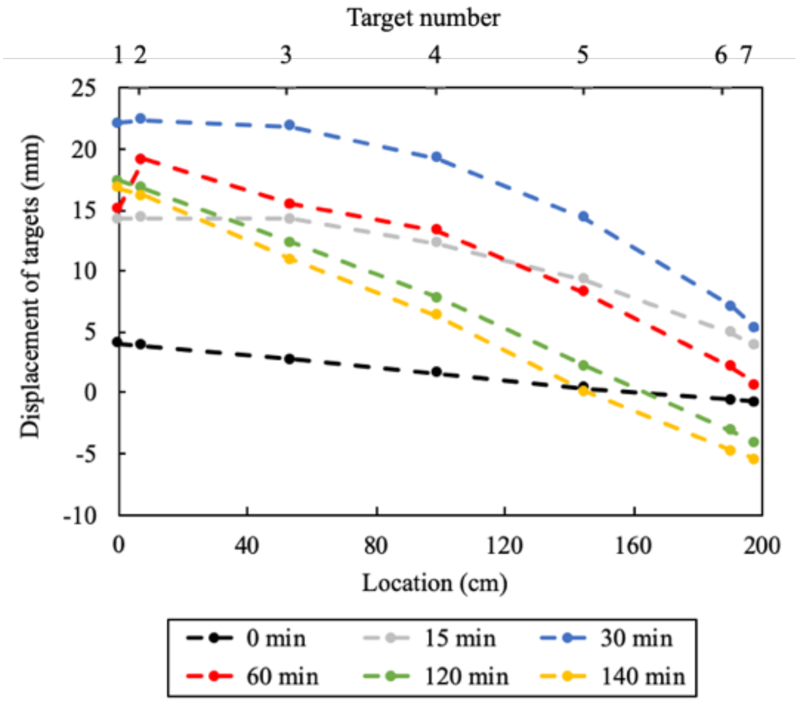

Fig. 2-28. Movement of the specimen within the test setup at different time points

(a) East web of the specimen after the fire test

(b) Local buckling in the specimen

Fig. 2-29. Local buckling on the exposed surface of CW2

2.10.5. CW3 Fire Test

CW3 was tested on July 19th, 2019 at Bowen Laboratory. All sides of the specimen were heated. This specimen had tie bar spacing equal to the thickness of the specimen that results in steel plate slenderness of 48 which exceeds the provided limit ($1.2\sqrt{E / F_y} \approx 28.9$). The vent holes were provided based on a developed vent hole design method (Chapter 5). Four vent holes with 12.7 mm (1/2 in) diameter were drilled on the webs of the specimen with a maximum spacing of 914.4 mm (3 ft) away from each other. The location of the provided vent holes on the specimen is shown in Fig. 2-30. 3/16 in diameter holes were drilled into the concrete with 25.4 mm (1 in) length at the center of vent holes. The noise level at the beginning of the test was about 56 dB which increased to a maximum of 69 dB at the end of the test.

The heaters' target temperature was set to 260 ℃ (500 °F) at the beginning of the test. After 24 mins the target temperatures were increased to about 815 ℃ (1500 °F). Fig. 2-31. shows the surface temperature of the specimen. Heater 13 was damaged after about 60 min of heating the specimen. The replacement of the heaters in the middle of the test was not safe. Therefore, to avoid heating the specimen non-uniformly, all the heaters were turned off and the test was stopped at 80 mins. Since large local buckling had occurred in the faceplate (as shown in Fig. 2-33) no further tests were conducted on this specimen.

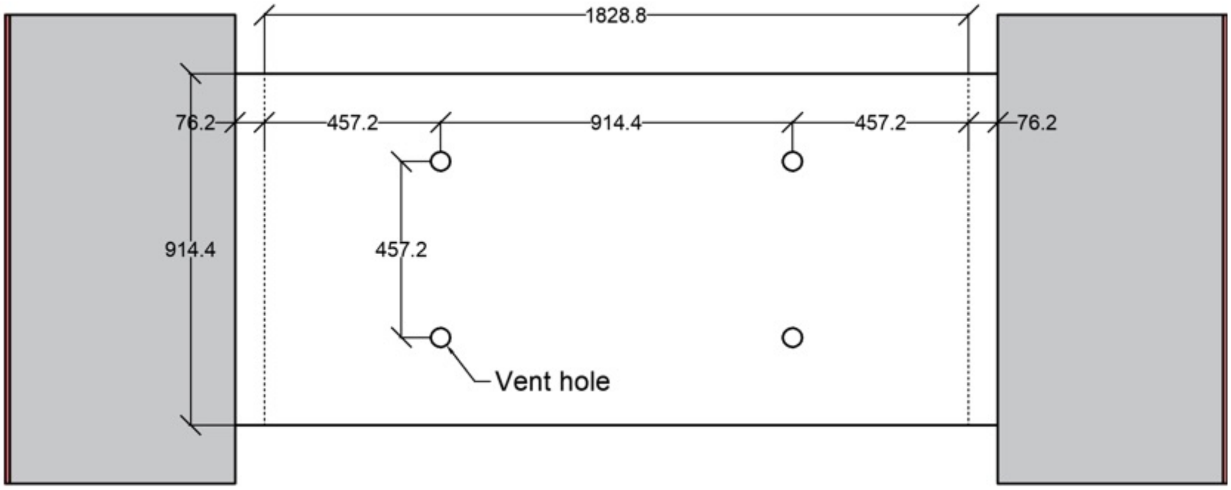

Fig. 2-30. Location of designed vent holes on CW3. All dimensions are in mm.

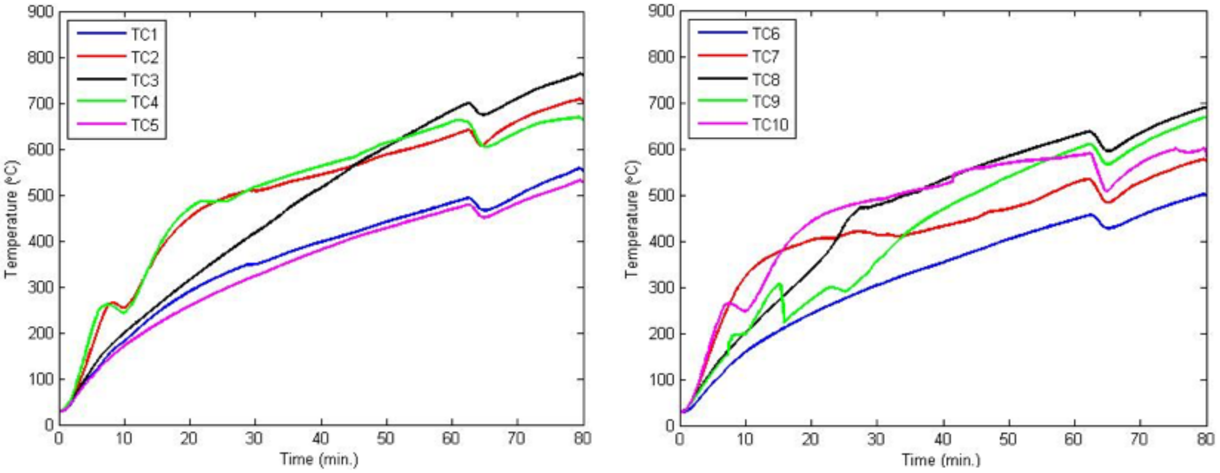

(a) East web

(b) West web

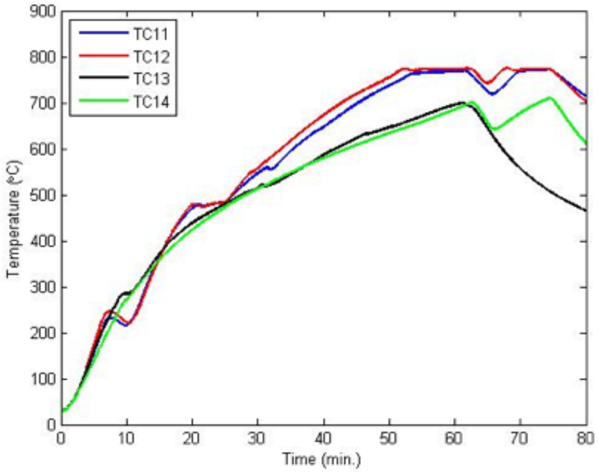

(c) Top and bottom

Fig. 2-31. The surface temperatures of CW3

A constant axial load of 2491 kN (550 kips - *28%* $A_c f'_c$) was applied. In Fig. 2-32(a), the measured axial displacement of the specimen is shown. The specimen was expanding for about 17 mins. The axial displacement of the specimen was stabilized until 60 min after heating the specimen. At about 60 min, the heaters were turned off for about 1 minute to fix Heater 13. Therefore, the axial displacement of the specimen dropped and all the heaters at the top and bottom of the specimen were turned off at 75 mins. The out-of-plane displacement of the specimen is presented in Fig. 2-32(b). The specimen started to bend toward the East and after 50 mins the out-of-plane displacements were stabilized. Fig. 2-33 shows the condition of CW3 after 80 mins of fire exposure.

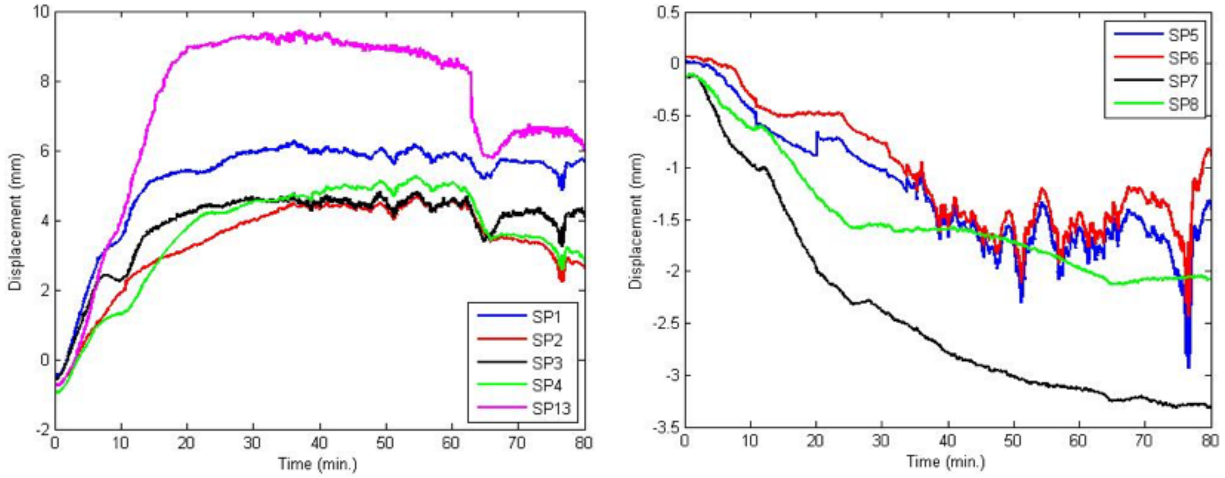

(a) Axial displacement (b) Out of plane displacement

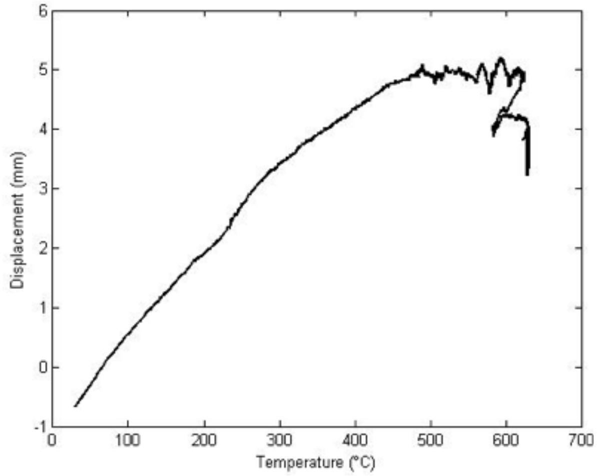

(c) Surface temperature against axial displacement

Fig. 2-32. Measured axial and out of plane displacements of CW3

(a) East web

(b) West web

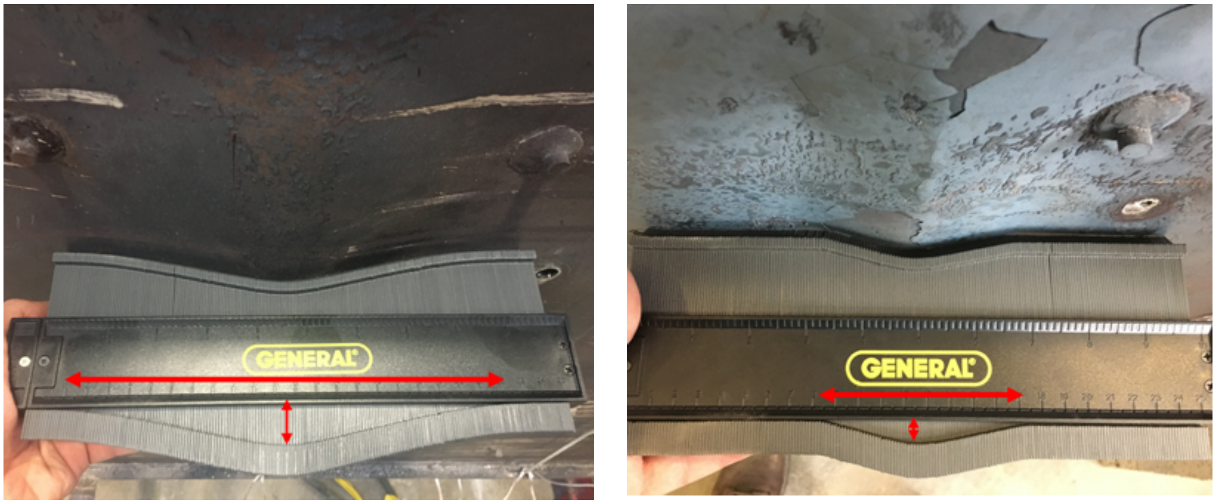

(c) Size of local buckling in CW3 with steel plate slenderness of 48

(d) Size of local buckling in CW1 with steel plate slenderness of 24

Fig. 2-33. Local buckling in the specimen between tie bars and comparison with CW1

2.10.6. CW4 Fire Test - Test 1

The fire test of CW4 was performed on September 10th, 2019 at Bowen Laboratory. All four sides of the specimen were heated. The specimen had a tie bar spacing of 114.3 mm (4.5 in), equal to half of the specimen thickness. The specimen had steel plate slenderness of 24 which was less than the recommended steel plate slenderness ($1.2\sqrt{E/F_y} \approx 28.9$). Four vent holes were provided on both sides of the specimen (webs) with a maximum spacing of 914.4 mm (3 ft) as shown in Fig. 2-30. Vent holes had a diameter of 12.7 mm (1/2 in). A hole with a diameter of 4.7 mm (3/16 in) and a width of 25 mm (1 in) was drilled into the concrete at the center of vent holes.

The target temperature of heaters was controlled to heat the specimen uniformly. The heaters were set to a target temperature of 260 ℃ (500 °F) at the beginning of the fire test. The target temperatures were increased to 537 ℃ (1000 °F) and 815℃ (1500 °F) after about 14 mins and 47 mins from the beginning of the fire test. The measured surface temperatures of specimen against time are shown in Fig. 2-34. The noise (water evaporation) started at about 14 mins after heating the specimen. The noise level at the laboratory before the beginning of the test was about 56 dB and it reached 84 dB at the end of the test. The specimen was heated for about 53 mins. Because whistling noise was heard, the test was stopped for safety measures.

An axial load of 2152 kN (484 kips - $20\% A_c f'_c$) was applied to the specimen before heating the specimen and it was kept constant (within ±20 kips) during the fire test. In Fig. 2-35 (a) the measured axial displacement of the specimen is shown. The string of SP13 and SP3 melted after about 11 min and 50 min of heating the specimen, respectively.

The specimen was expanding for 50 mins. Slight out of plane displacement was measured during the fire test as shown in Fig. 2-35 (b). The average axial displacement against the average surface temperatures is shown in Fig. 2-35 (c). The specimen experienced expansion until the surface temperature reached to about 470 ℃ (878 °F). Local buckling had occurred between tie bars during the test on both sides of the specimen. In Fig. 2-36, the statues of CW4 after the fire test is shown.

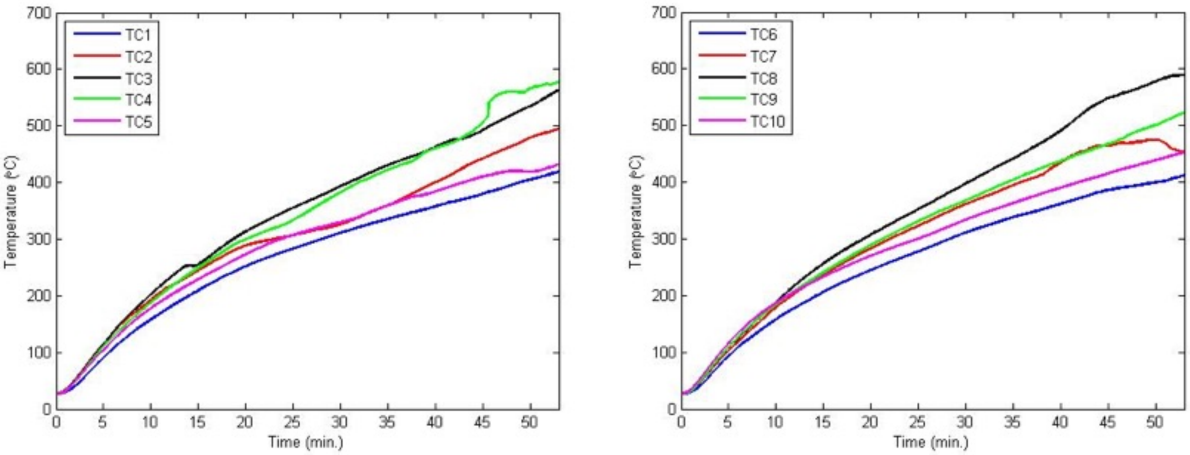

(a) East web

(b) West web

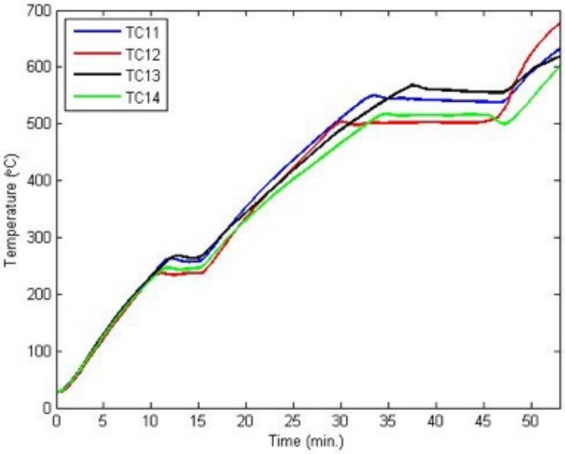

(c) Top and bottom flange

Fig. 2-34. The measured surface temperature of CW4 (Test1)

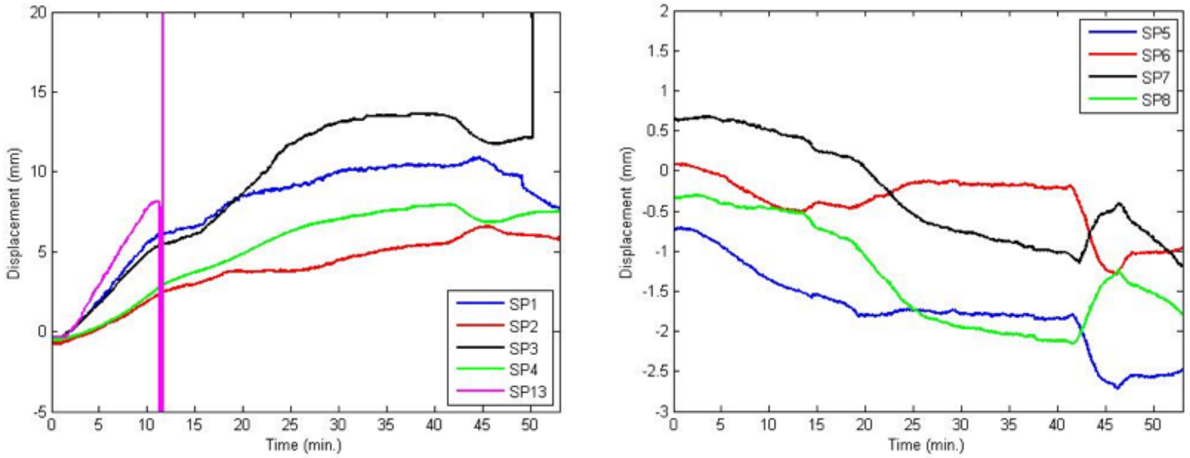

(a) Axial displacement

(b) Out of plane displacment

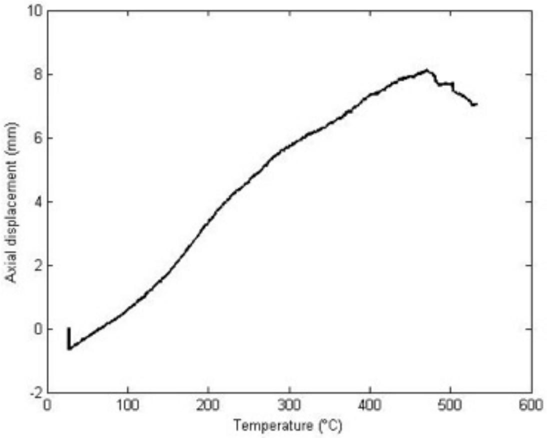

(c) Axial displacement against surface temperature

Fig. 2-35. Measured axial and out of plane displacements of CW4 (Test1)

(a) East web

(b) West web

(c) Local buckling between tie bars

Fig. 2-36. Local buckling in the specimen between tie bars after the fire test CW4 (Test1)

2.10.7. CW4 Fire Test - Test 2

The second test of specimen CW4 was performed on September 17, 2019. By inspecting the specimen after the first test, it was found that the heaters were impeding the vapor ejection. More vent holes were made in the specimen at both ends of the specimen (where it was not covered by heaters) on the web to let vapor discharge without any obstruction. The locations of the vent holes are shown in Fig. 2-37. Vent holes' size was 12.7 mm (1/2 in) diameter and a 4.7 mm (3/16 in) diameter hole (25 mm deep) was drilled into the concrete at the center of vent holes.

The heaters' target temperature was set to 260 ℃ (500 °F) at the beginning of the test. The heaters' target temperature increased to 537 ℃ (1000 °F) after 10 mins of heating. The target temperature increased gradually at 38℃ (100 °F) intervals at 47, 52, 69 and 89 mins of heating. Some of the thermocouples were separated from the specimen during the test due to high surface temperatures. The control panel's thermocouples were switched with DAQ's thermocouples to keep the heaters working in case of any thermocouple separation. Control panel's thermocouples for heaters 4, 5, 6, 7, 8, 9, 10, 11 were switched with DAQ's thermocouples during the test.

The surface temperature of the specimen against time is shown in Fig. 2-38. The noise started at about 35 mins of heating the specimen. The noise level in the laboratory before the beginning of the test was about 57 dB. The noise level reached to 68 dB at 68 min and reduced to 63 dB at the end of the test (150 mins).

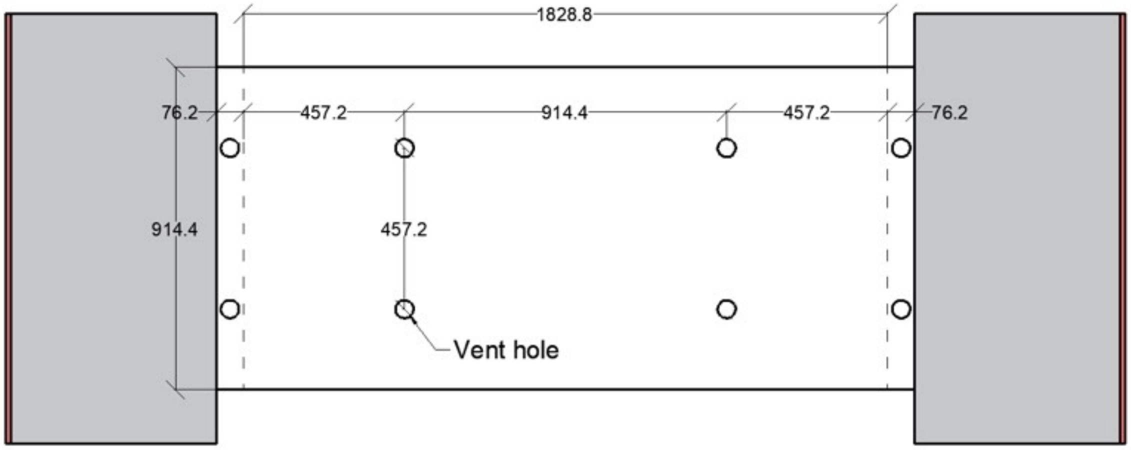

Fig. 2-37. Location of vent holes in CW4 (Test2). Dimensions are in mm.

An axial load of 2153 kN (484 kips - *20%* $A_c f'_c$) was applied to the specimen before heating the specimen. The axial load was kept constant (within ±90 kN or ±20 kips) during the fire test.

Because the string of SP1, 3 and 13 were affected by heat during the test, the measured axial displacements by SP 2, 4 were considered. The specimen expanded for 30 mins and then it shortened, gradually. The reduction in axial displacement of the specimen can be due to local buckling of the faceplate and deterioration of material mechanical properties at elevated temperatures. The fire test was stopped after 150 mins of heating the specimen since some the thermocouples stopped working and it was not possible to control the heaters. The measured displacements are shown in Fig. 2-39. Local buckling of faceplate had occurred between tie bars/shear studs at multiple locations. Fig. 2-40 shows the condition specimen after fire exposure.

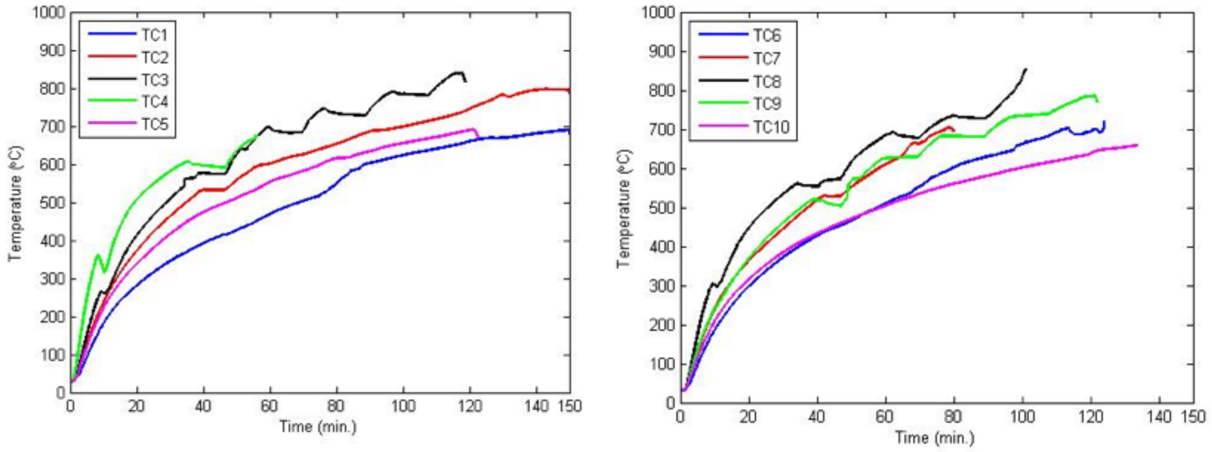

(a) East web (b) West web

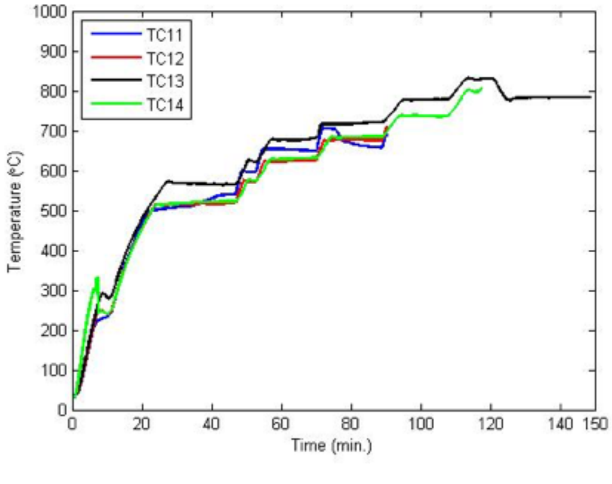

(c) Top and bottom flanges

Fig. 2-38. The measured surface temperature of CW4 (Test2)

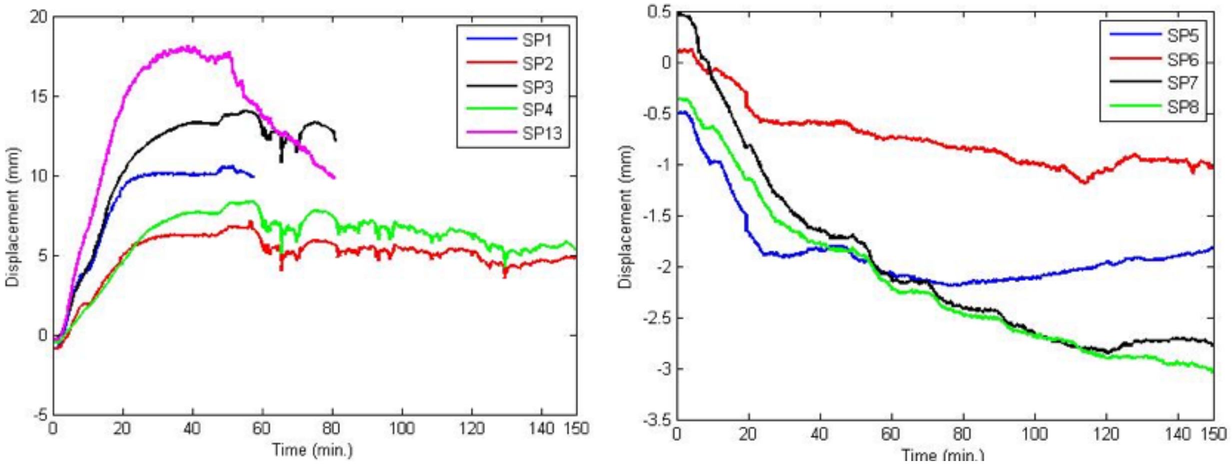

(a) Axial displacement

(b) Out of plane displacment

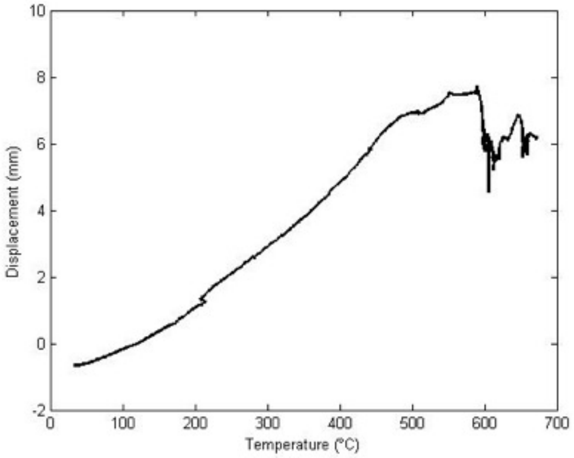

(c) Axial displacement against surface temperature

Fig. 2-39. Measured axial and out of plane displacements of CW4 (Test2)

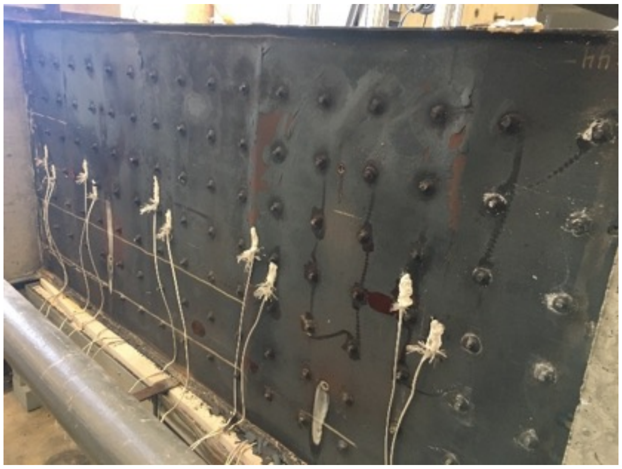

(a) East web

(b) West web

(c) Local buckling between tie bars

(d) Local buckling between shear studs at the top flange

Fig. 2-40. Local buckling in the specimen between tie bars/shear studs after fire test (CW4-Test2)

2.10.8. CW5 Fire Test

The fire test of CW5 was performed on November 5th, 2019 at Bowen Laboratory. All four sides of the specimen were heated. The specimen had a tie bar spacing of 114.3 mm (4.5 in), equal to half of the thickness of the specimen. The specimen had steel plate slenderness equal to 24. Six vent holes were provided on both sides of the specimen (webs) with a maximum spacing of 1016 mm (3.33 ft). Three vent holes were drilled at the top and bottom flanges. The location of vent holes is shown in Fig. 2-41. Vent holes' size was 15.9 mm (5/8 in) in diameter. A 4.7 mm (3/16 in) in diameter hole was drilled into the concrete at the center of vent holes. A gap with a width of 50.8 mm (2 in) was provided in front of the middle row of vent holes to avoid obstructing the vapor ejection by the heaters.

The target temperature of heaters was controlled to heat the specimen uniformly. At the beginning of the test, the heaters' target temperature was set to 260 °C (500 °F). The heaters' target temperature increased to 537 °C (1000 °F) after 20 mins of heating. The target temperature increased gradually at 38°C (100 °F) intervals at 54, 91, 96 and 120 mins. The measured surface temperatures of specimen against time are shown in Fig. 2-42. The noise (water evaporation) started at about 9 mins of heating the specimen. The noise level at the laboratory before the beginning of the test was about 58 dB. The noise level reached to 78 dB at 55 min and reduced to 69 dB at the end of the test. The specimen was heated for about 150 mins.

An axial load equal to 2655 kN (579 kips - $20\% A_c f'_c$) was applied to the specimen before heating the specimen. The axial load was kept constant (within ±90 kN or ±20 kips) during the fire test. The specimen expanded for about 38 mins and it began bending toward East. The bending of specimen increased for about 10 mins and it stabilized for about 54 min. However, the bending of the specimen kept increasing from102 mins after the beginning of the fire test until the end of the fire test. The heating of the specimen stopped after 150 mins due to excessive movements in the test setup. The measured displacements and the axial displacement at the center of the wall cross-section (average displacements of SP1-4) are shown in Fig. 2-43. Local buckling of faceplate had occurred between tie bars/shear studs at multiple locations. Fig. 2-44 shows the condition specimen after the fire test.

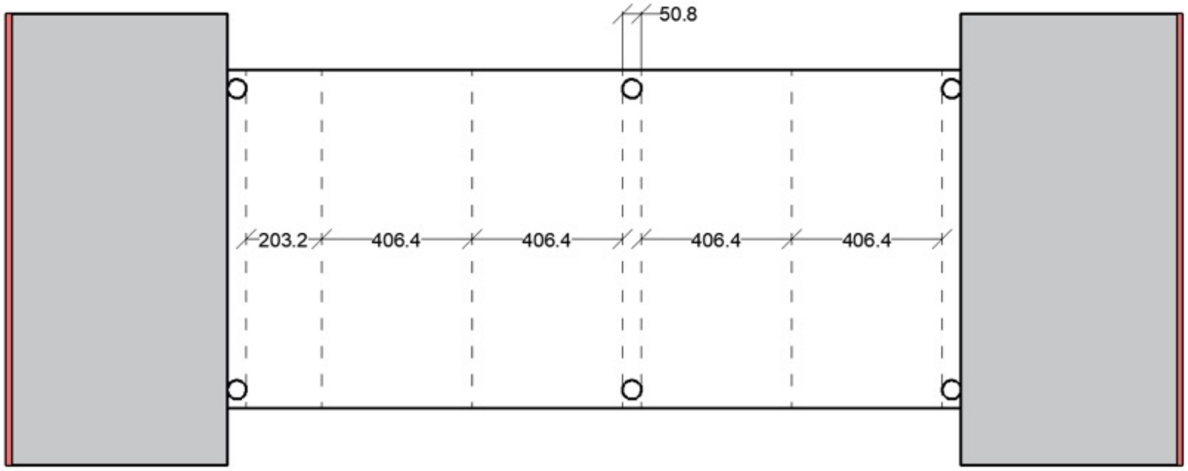

a) Webs

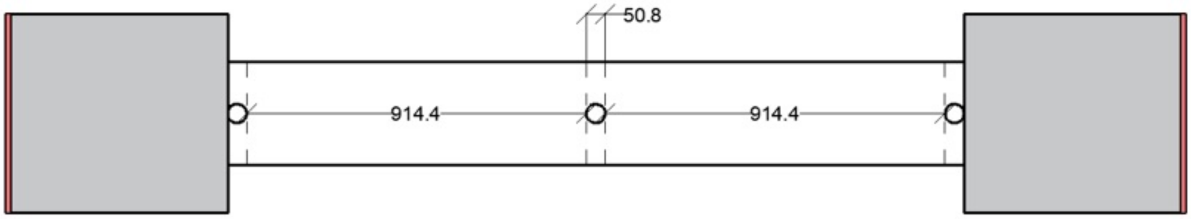

b) Flanges

Fig. 2-41. Location of vent holes on the specimen. All dimensions are in mm.

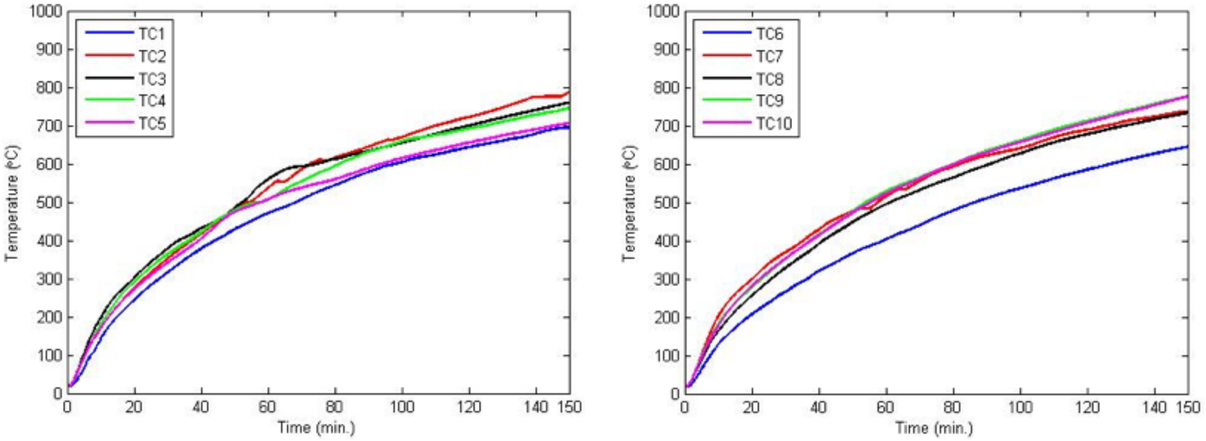

(a) East web (b) West web

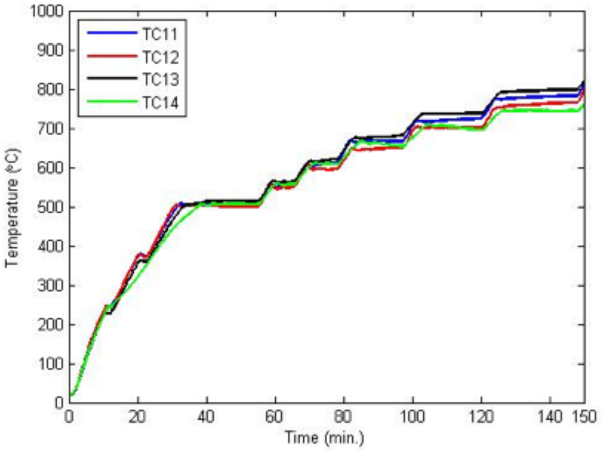

(c) Top and bottom flanges

Fig. 2-42. The measured surface temperature of CW5

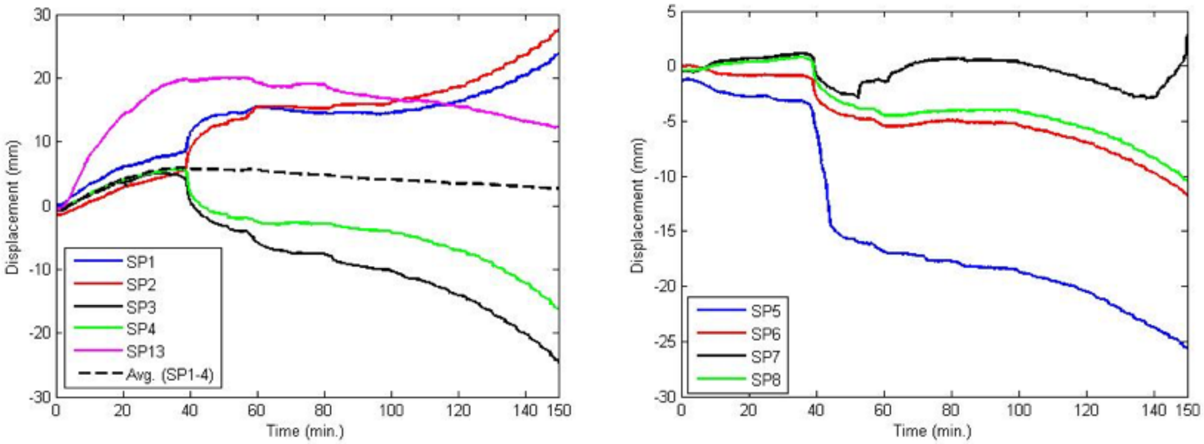

(a) Axial displacement

(b) Out of plane displacement

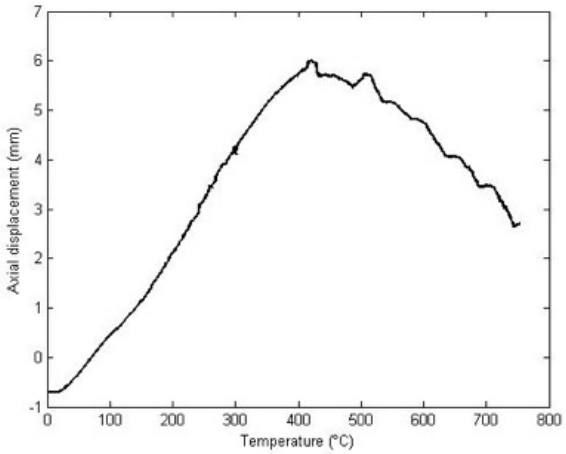

(c) Axial displacement against surface temperature

Fig. 2-43. Measured axial and out of plane displacements of CW5

(a) East web

(b)West web

(c) Local buckling between tie bars

(d) Local buckling between shear studs at the top flange

Fig. 2-44. Local buckling in the specimen between tie bars/shear studs after fire test (CW5)

2.11. Summary and Conclusions

Five C-PSW/CF specimens were tested under combined axial and fire loading. Specimens had different varied parameters such as tie bar spacing, shear studs, loading ratio and fire scenarios (uniform and three-sided heating). The test setup was designed for C-PSW/CF specimens' fire tests. Two steel beams with half-cylindrical bearings are provided at both ends of the setup to allow rotation in specimens about the weak axis. Various instruments were provided to measure the temperatures, strains, and displacements of the specimens. Four all-sided and one three-sided fire tests were performed.

Fire tests were conducted to study the behavior of walls under fire loading with various plate slenderness ratios and applied load ratios. Also, the fire test data were used to benchmark the models in addition to the fire tests conducted by other researchers (Wei et al., 2017).

The loadbearing capacity and insulation failure criteria (ISO 834, 1975) were investigated. Failure to support the load was considered to occur if the axial contraction of the specimen exceeded $H/100$ (mm), where H is the height of the specimen. The axial displacement in none of the specimens exceeded the loadbearing failure criteria's limit. A wall would be considered failed if the average temperature increase on the unexposed surface exceeds 140 °C or temperature increase at any point on the unexposed surface exceeds 180 °C (ISO 834, 1975). The temperatures on the unexposed surfaces of CW2 remained below the specified limits.

CW1 was heated for 180 mins from all sides. Local buckling between tie bars and shear studs occurred and some of the shear studs in the buckled region failed away from the faceplate. Three sides of CW2 were heated for 140 mins. The specimen bent globally toward the heated web, initially. However, the specimen began to straighten after about 40 mins. Local buckling between tie bars was observed on the exposed surface. Since one side of the specimen was unexposed, the motion capture system was used to measure the displacement of CW2. All sides of CW3 were heated for about 80 mins and the test stopped due to the failure of one of the heaters. The size of local buckling in CW3 (steel plate slenderness = 48) was larger than CW1 (steel plate slenderness = 24). All sides of CW4 and CW5 were heated for 150 min. Local buckling of faceplate was restrained by tie bars, similar to the previous specimens.

The local buckling of the faceplate (steel plate) between the tie bars occurred in all specimens. The local buckling in specimens was due to the degradation of the material mechanical properties and thermal expansion of faceplate at elevated temperatures. Numerical analysis showed that walls with higher plate slenderness ratio lose load bearing capacity of faceplate at earlier stages of heating. This also led to a lower expansion of walls at the early stages of heating and earlier failure of walls.

The axial displacement against the average surface temperature of all-sided heated specimens is compared in Fig. 2-45. The averages of the measured displacements by all string potentiometers (SP1-4) are used to develop Fig. 2-45(a). Because SP1 and SP3 were lost during the fire test of specimen CW4, the averaged axial displacements based on measured displacements of SP2 and SP4 are compared in Fig. 2-45(b). CW1 experienced higher thermal expansion than CW3 at similar temperatures. Comparing the response of CW1 and CW3 shows that limiting the steel plate slenderness can improve walls' axial capacity at the early stages of fire exposure by delaying the local buckling occurrence. CW1 and CW3 had steel plate slenderness equal to 24 and 48, respectively. Comparing the axial displacement of specimens with the same steel plate slenderness and different load ratios (e.g. CW1 and CW5) shows that increasing the load ratio results in lower thermal expansion and more reduction in axial displacement of walls.

More fire tests on specimens with various wall slenderness ratios and wall thickness a different configuration (T or C shape walls) can give more insight into the behavior of C-PSW/CF.

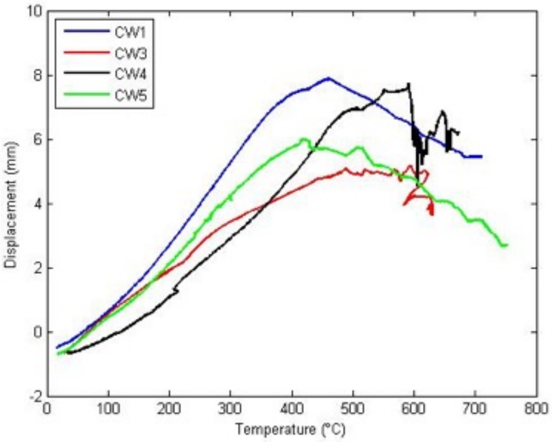

(a) Based on the average of all string potentiometers (except for CW4)

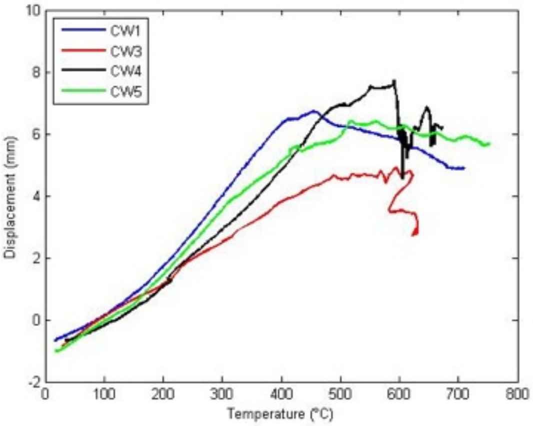

(b) Based on the measured displacments by SP2 and SP4

Fig. 2-45. Axial displacement against surface temperature of all-sided heated specimens

Chapter 3. Analytical Studies (Finite Element Analysis)

3.1. General

Limited experimental investigations have been conducted to evaluate the response of C-PSWs/CF exposed to fire loading. However, reviewing the existing work and data allows for benchmarking the advanced modeling techniques utilized in this project. A summary of available research is presented in Chapter 1 for concrete filled-steel plate composite wall (C-PSW/CF). Two numerical analyses conducted to simulate the response of C-PSW/CFs under combined axial and fire loading namely Finite Element (FE) analysis and fiber method analysis. This chapter presents detailed 3D thermal and stress FE models developed using commercial FE software (ABAQUS). The details and results of the fiber method analysis are presented in Chapter 4. The temperatures calculated through FE thermal analysis used as input in stress analysis to account for the material properties degradation at elevated temperatures. These models were benchmarked according to the prior (Wei et al. 2017) and current (Chapter 2) experimental studies' data. Analytical parametric studies were conducted to explore the influence of various parameters in design of C-PSW/CF under fire loading as discussed in section 3.3. Also, the obtained results from the parametric study were utilized to develop equations to calculate the axial capacity C-PSW/CFs at elevated temperatures and estimate the fire resistance rating.

3.2. Benchmarked Finite Element Models

The finite element method was used to numerically investigate the behavior of C-PSW/CFs under a combination of fire and gravity loads. The FE models are developed and benchmarked to the experimental studies conducted by Wei et al. (2017) and current tests as presented in Chapter 2. Three-dimensional FE models were developed in commercially available software, ABAQUS (Simulia 2016). The finite element models and subsequent numerical studies provided insights into the material and the structural-level response of the walls subjected to fire loading.

The developed models were based on sequentially coupled thermal/heat transfer and stress analyses within the finite element software. Three-dimensional FE models of the walls were developed to obtain the temperatures within the walls. The model consists of concrete infills, which are enclosed by steel plates (consistent with the specimens tested by Wei et al. 2017). The thermal properties of steel and concrete are defined as per Eurocode (2005).

The next step was the coupling of the thermal analysis to a 3D stress model. The specimens tested by Wei et al. (2017) were modeled, including the studs and tie bars. The 3-D view of the model is shown in Fig. 3-1. The shear studs and ties are both modeled as beam elements in the stress model. The concrete core is modeled using 3-D solid elements whereas the steel flange, web, and inner plates are modeled as shell elements. Since the thickness of steel plates is much smaller than the thickness of the concrete core, shell elements are appropriate for modeling steel plates. Additionally, sequentially coupled thermal-stress analyses are more computationally expensive and the use of shell elements makes them more computationally efficient.

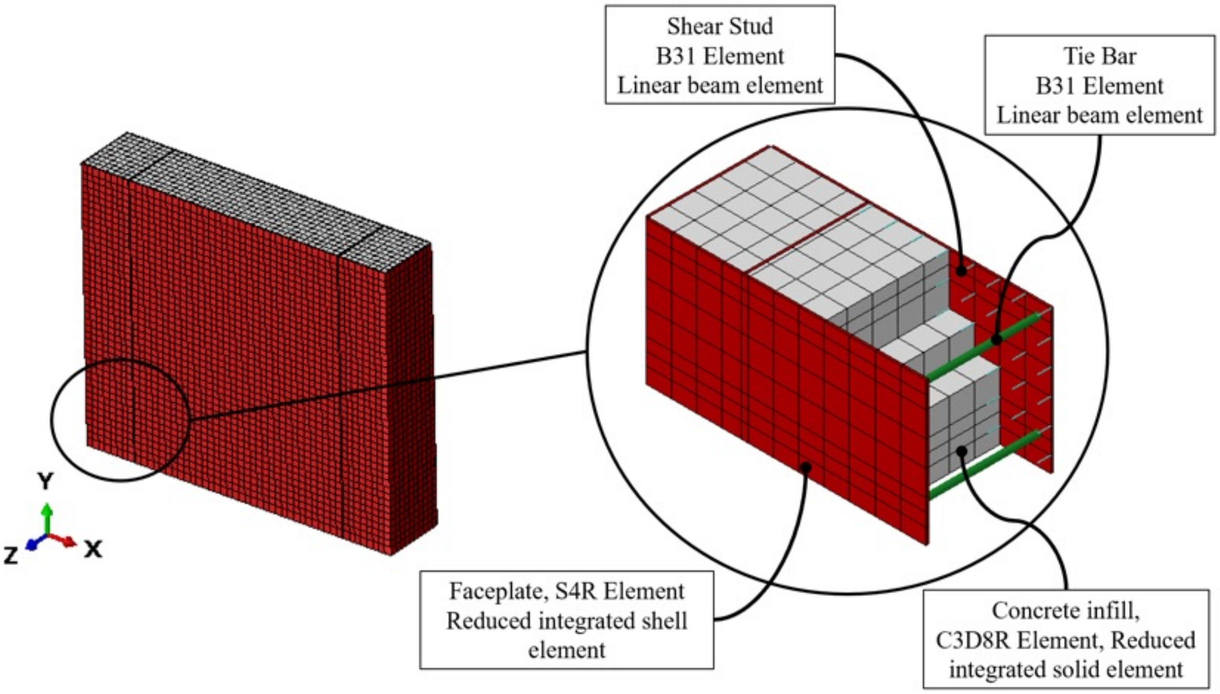

Fig. 3-1. 3-Dimensional model of the Concrete Filled Composite Plate Shear Walls

3.2.1. Material Properties for Finite Element Analysis

The thermal properties of steel and concrete are defined as per the Eurocode (2005). According to calibration studies for heat transfer results, a moisture content of 3% (for concrete) was selected and the specific heat (c) was chosen accordingly. The average of upper and lower limit values of thermal conductivity (k) specified by the Eurocode is used for concrete. The thermal expansion (α) values of siliceous aggregate concrete are applied.

The mechanical properties of steel and concrete at elevated temperatures are also defined per the Eurocode and adapted for the developed finite element models. The load-deformation response of a member varies significantly with temperature and needs to be considered when defining the mechanical properties. Fig. 3-2(a) and Fig. 3-2(b) show the temperature-dependent stress-strain curves for concrete (cylinder strength of 50 MPa) and steel (yield strength of 500 MPa), respectively. Concrete material behavior was modeled using the 'Concrete damaged plasticity' model in ABAQUS. This model is based on plasticity and continuum damage mechanics that considers the tensile cracking and compressive crushing of concrete as two main failure mechanism (Lee and Fenves, 1998). The steel material was modeled as 'elastic-plastic'. ABAQUS provides different options for conducting the thermal-stress analysis and as noted previously the sequentially coupled thermal-stress analysis technique was employed for this study. The technique involves conducting a heat-transfer analysis for the models and resulting nodal temperatures from that analysis serve as inputs for the stress analysis model.

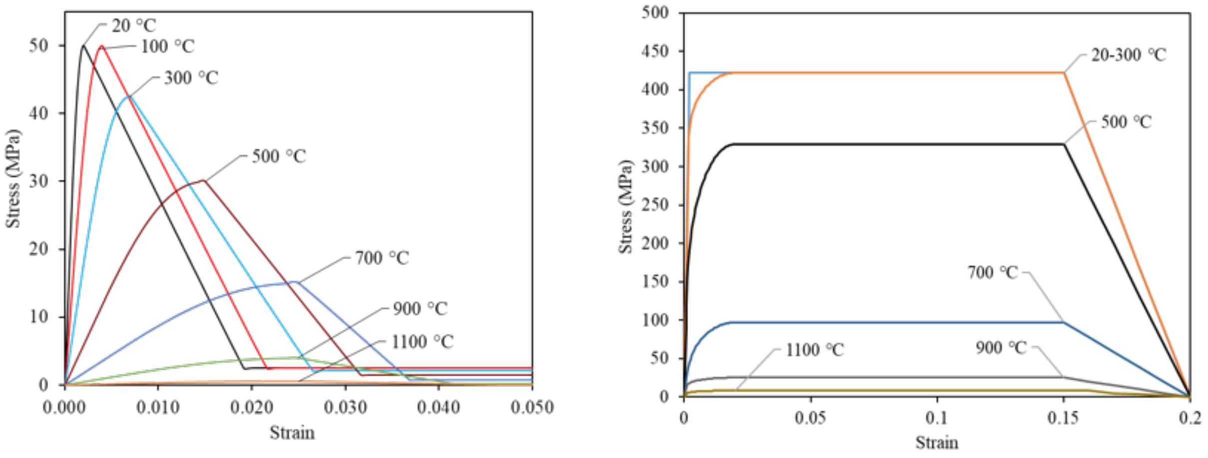

(a) (b)

Fig. 3-2. Stress-strain relation of concrete (a) and steel (b) at elevated temperatures per Eurocode 3

3.2.2. Finite Element Heat Transfer Analysis

The model consisted of concrete infill and the steel faceplates as shown in Fig. 3-1. The concrete is modeled using DC3D8 element, which is an 8-node linear heat transfer brick element, and the steel plates are modeled using DS4 element. The steel plates are tied to the outer surface of the concrete to facilitate heat transfer between steel and concrete. The inner steel plates are also tied to the concrete. This approach is conservative as it does not consider the energy loss at the steel-concrete interface and may result in cross-section temperatures marginally higher than those observed experimentally. The ambient temperature is assumed to be 20 °C, and the specimens are subjected to ISO-834 standard fire curve. The heat flow between the burning gases and the steel surface is simulated using a subroutine in ABAQUS. This subroutine provides the temperatures at the outer surface of the specimen (the surface exposed to fire) by accounting for the radiation and convection modes of heat transfer between the surface and the gas temperatures. For brevity, the details of this subroutine are not discussed here and are reported by Cedeno et al. (2009).

3.2.3. Finite Element Stress Analysis

The stress analysis models were built with the same mesh size used in heat transfer models. Additionally, the stress model includes shear studs and tie bars. The concrete is modeled using C3D8R elements which are 8-node linear brick element with reduced integration. The steel plates are modeled using S4R elements which are 4-node general-purpose linear shell elements. These reduced integration elements are used to increase the computational efficiency of the analysis. The shear studs and the tie bars are modeled using B31 element, a 2-node linear beam element. Fire analysis may result in the failure of stud/tie welds as observed by Wei et al. (2017). Cartesian type connector elements were employed to simulate the temperature-dependent force-slip behavior of studs and ties. The force-slip relationship for the connectors was based on Ollgaard et al. (1971) and was modified to consider temperature-dependent properties as discussed by Selden (2014).

The models have all the degrees of freedom restrained at the bottom surface. Gravity loading is applied to the top surface. The tie bars and shear studs are embedded in the concrete infill. The ambient temperature of the specimen is taken as 20 °C and the temperatures at any other time are interpolated from the nodal temperatures from heat transfer analysis. Hard contact and tangential behavior with a friction coefficient of 0.55 was used to define the contact properties between the faceplate and concrete-infill of the models. The stress analysis is a 2-step process. In the first step, an incremental axial compressive load is applied to the specimen. The magnitude of the load increased from zero to the maximum value in an hour. In the second step, the axial load is maintained constant, and nodal temperatures based on the heat transfer analysis are applied. The second step continued for 4 hours or more (Based on the failure time of the wall). The run times for thermal and stress analyses were scaled down by accordingly scaling up the thermal conductivity of steel and concrete that a time unit in FE models was corresponding to 1 hour of fire exposure.

3.2.4. Comparison of Numerical and Experimental Analysis

The numerical models were employed to obtain the stability response of the specimens tested by Wei et al. (2017) and specimens tested in Chapter 2. The summary of the results for specimens [tested by Wei et al. (2017)] is described in Table 3-1. This section compares the results of thermal and stress analysis with the experimental results. For brevity, thermal analysis for only three specimens namely, SCW 7 and CW1 (uniform fire specimen) and SCW12 (a single-sided fire specimen) are discussed.

Typical temperature distributions for uniform fire and one-sided fire conditions are shown in Fig. 3-3(a) and Fig. 3-3(b), respectively. The figure shows temperature profiles at 4 hours after the beginning of the fire exposure. Uniform fire resulted in a rise of steel temperature (up to 1010 °C), with a minimum temperature of 720 °C in the concrete infill. Single-sided fires result in surface temperature increase on the exposed side. A thermal gradient through the cross-section develops when the unexposed side temperature approaches 250 °C.

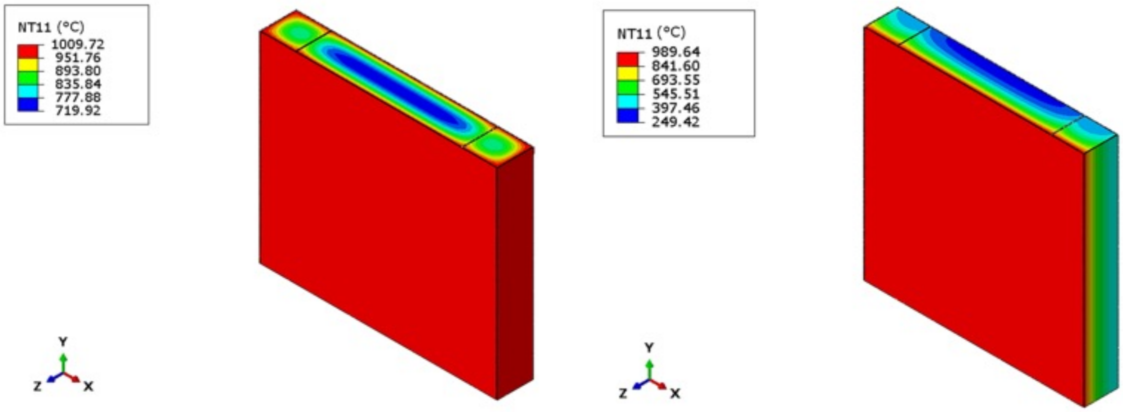

(a) (b)

Fig. 3-3. Temperature distribution for (a) Uniform fire and (b) One-sided fire conditions after 3 hours of fire exposure

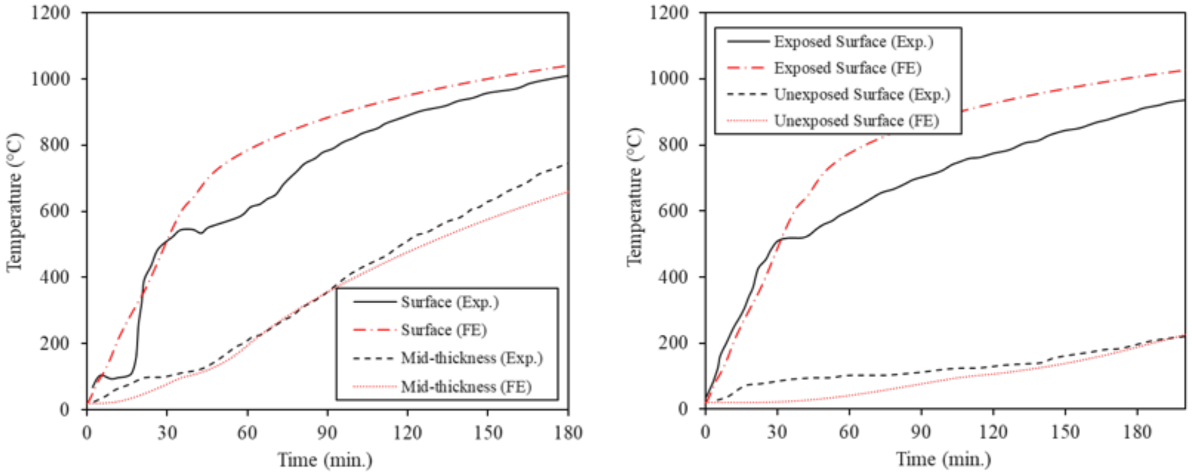

(a) (b)

Fig. 3-4. Comparison of predicted temperatures from the FE analysis with the experimental (Exp.) data at different sections for SCW7 (a), SCW12 (b)

Fig. 3-4. presents the comparison of temperature obtained numerically with those observed experimentally for SCW7 and SCW12. The experimentally observed surface temperatures indicate a plateau in the first 30 minutes of the heating. Wei et al. (2017) attribute this plateau to the latent heat associated with the loss of moisture content from the concrete infill. To investigate this, concrete specific heat values corresponding to different moisture content were used in the FE models. However, no significant difference in the surface temperature evolutions was observed. The change in moisture content affected the evolution of temperature at the mid-thickness of the cross-section. The plateau observed in experimental measurements could be due to some heat loss or inconsistencies in the measurements. The experimental surface temperatures are reported at 2 mm from the concrete surface, and the steel surface temperatures are not reported. The plateau observed after 30 minutes may be due to an air gap between steel and concrete as the plate buckling initiates. Additionally, the FE models incorporate thermal ties (no heat loss at the interface) at the steel-concrete interface.

The numerically observed mid-thickness temperature for uniform fire specimens (SCW 7), unexposed-side temperature for single-sided fire specimen (SCW 12) compare well with the experimental results. However, the outer surface temperature or exposed-side temperature values obtained from the FE models were higher than the experimental values in some regions of the curve. This may be due to the air gap between the faceplate and concrete surface upon initiation of the local buckling of the faceplate. FE models do not account for any heat loss at the steel-concrete interface. The higher surface temperature in FE analysis can decrease the failure time of the specimens. However, considering potential variability in experimental observations, using the ISO 834 fire curve is a more reliable and conservative approach to determine the failure time and surface temperature for C-PSW/CFs.

Wei et al. (2017) observed that fire loading resulted in the failure of the specimens due to local buckling of the steel plates, weld cracking, and concrete crushing. Consistent with experimental observations, the FE models exhibited extensive buckling of the steel plates (both web and flange) at failure. The axial deformation response of the FE models can be compared with experimental results. Fig. 3-5(a) presents the axial deformation versus time for SCW7. In the initial stages (up to 30 minutes), the uniform-fire specimens underwent a thermal expansion. This stage was followed by a stage of axial compression, which lasted for 60 minutes. Material strength degradation occurs as the steel and concrete temperatures increase. Therefore, the axial compressive deformation overcomes thermal expansion. The axial compression deformation was increased initially, but eventually, the specimen failed due to rapid axial shortening. Similar behavior was observed on the exposed side of the single-sided fire specimen as shown in Fig. 3-5(b). However, the unexposed side kept expanding throughout the fire, before specimen failure.

The axial displacements versus time response obtained from the FE models (applied ISO 834 time-temperature) compares reasonably with that observed experimentally as shown in Figs. 3-5(a) and (b). However, the FE failure time is lower than the experimental failure times. This difference is the result of higher surface temperatures for FE models (as discussed previously) or some variability in the recorded experimental measurements. The axial displacements of the specimens (SCW4, SCW7) are plotted against the surface temperature in Figs. 3-5(c) and (d). The FE model surface temperature at failure agrees well with the experimentally observed surface temperature at failure. Therefore, the surface temperature may be a better indicator of specimen failure for FE models. The failure time can then be calculated using heat transfer equations and surface temperatures.

FE analyses directly using experimental surface temperature data, instead of ISO 834 standard time-temperature curve inputs, were also conducted for specimens with available measured surface temperatures from Wei et al. (2017). These analyses resulted in a failure time that was closer to experimental observations. However, considering potential variability in experimental observations, using the ISO 834 standard time-temperature curve is a more reliable and conservative approach to determine the failure time and surface temperature for C-PSW/CFs. Fig. 3-5(e) and 3-5(f) compare the axial displacement of SCW7 against time and surface temperature where measured surface temperatures were applied in the heat transfer analysis.

Similarly, the FE models were benchmarked to current experimental investigations presented in Chapter 2 of the current report. The measured surface temperatures were applied as input to the thermal analysis. The temperature profile through the thickness of CW1 is compared in Fig 3-6 (a) where the measured surface temperature was applied to the model. There is a reasonable agreement between the estimated (FEA) and the measured temperature. The difference in the temperatures within the 0 to 75 mm of wall thickness is attributed to the moisture migration within the wall thickness. To pass the thermocouples through the steel faceplate a hole was provided in the steel faceplate (at wall thickness = 0 mm in Fig. 3-6(a)). During the fire test, water was escaping from the hole. The water migration was not simulated in the models and this caused a difference in the measured and estimated temperatures within the wall thickness around the hole (0 to 75 mm).

The axial displacements of CW1 and CW3 are plotted against the surface temperature in Fig. 3-6 (b) to (e). The CW1 expanded for about 45 mins when the surface temperature reached about 450 °C. However, due to degradation of mechanical properties of material at elevated temperatures began to contract. The duration of CW3 fire test was 80 mins as discussed in section 2.5.10. The specimen expanded for about 20 min. The axial displacement was reduced gradually until the end of the test. Based on the presented comparison of data Fig. 3-6, there is a reasonable agreement between the measured axial displacements and the obtained displacements from the developed finite element results. The deformed faceplate due to local buckling of steel plate between the tie bars in CW3 is compared with the deformed shape of CW3 model at failure in Fig. 3-7. The local buckling of the steel faceplate had been arrested by tie bars in the test and FE model.

Table 3-1. Summary of finite element and experimental results (specimens tested by Wei et al. 2017)

Specimens	H (mm)	t_w (mm)	t_p (mm)	Shear stud	Tie bar	Load ratio	Failure Time (min)			Failure Surface Temp. (°C)	
							Test	FE	FE**	Test	FE
Uniform fire tests											
SCW1	850	150	3	Φ2@40	Φ10@160	0.34	161	125	-	900-1000*	950
SCW2	850	150	3	Φ2@60	Φ10@160	0.34	178	110	-	900-1000*	875
SCW3	850	150	3	Φ2@80	Φ10@160	0.34	174	120	-	900-1000*	940
SCW4	1350	150	3	Φ2@40	Φ10@160	0.34	156	75	155	840	780
SCW5	1850	150	3	Φ2@40	Φ10@160	0.34	133	60	-	900-1000*	700
SCW6	850	200	4	Φ2@40	Φ10@160	0.34	212	150	197	870	1000
SCW7	850	150	2	Φ2@40	Φ10@160	0.40	178	120	166	930	950
SCW8	850	150	5	Φ2@40	Φ10@160	0.26	166	135	##	940	950
Single-sided fire tests											
SCW9	1000	150	3	Φ2@40	Φ10@160	0.34	191	180	##	1000	1000
SCW10	1000	200	4	Φ2@40	Φ10@160	0.34	>207	#	##	#	#
SCW11	1000	150	5	Φ2@40	Φ10@160	0.26	185	200	##	945*	1020
SCW12	1000	150	3	Φ2@40	No tie bars	0.34	166	196	##	950*	1015

* Failure temperature not reported, estimated based on reported data

** Measured surface temperatures applied to the surface of the heat transfers models

specimen did not undergo failure for subjected fire curve

specimen did not undergo failure for subjected measured surface temperature until experimental failure

All dimensions in mm, unless noted otherwise.

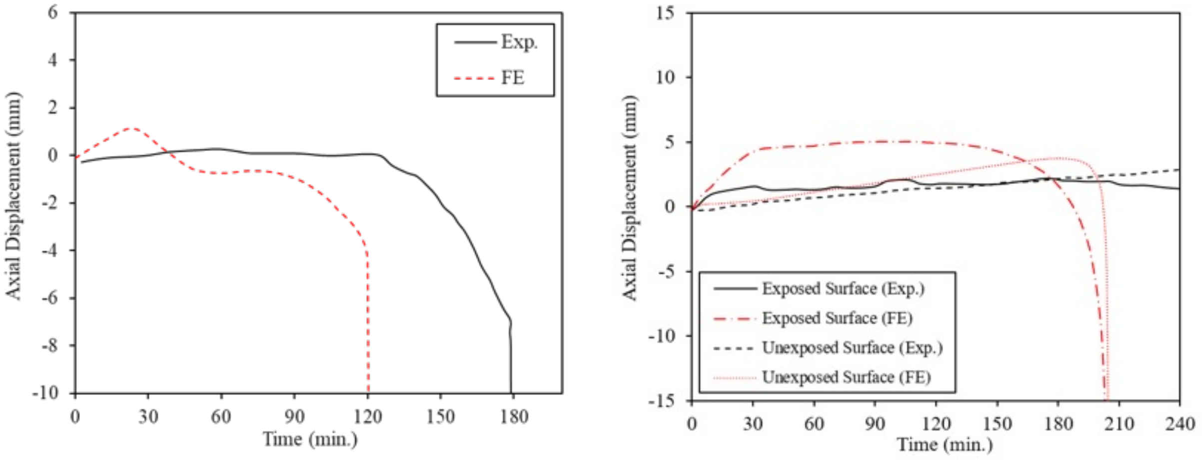

(a) SCW7 (b) SCW12

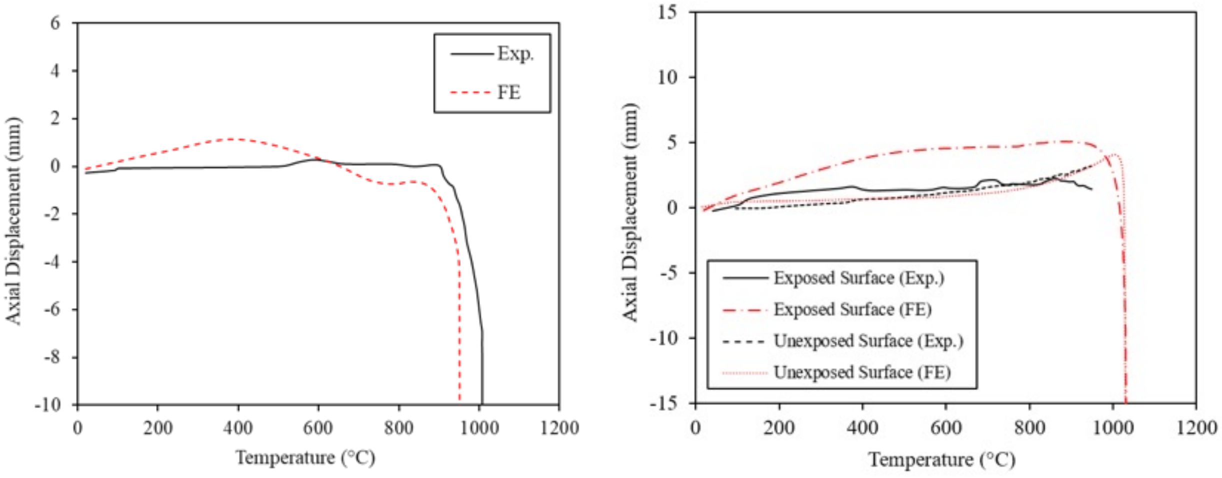

(c) SCW7 (d) SCW12

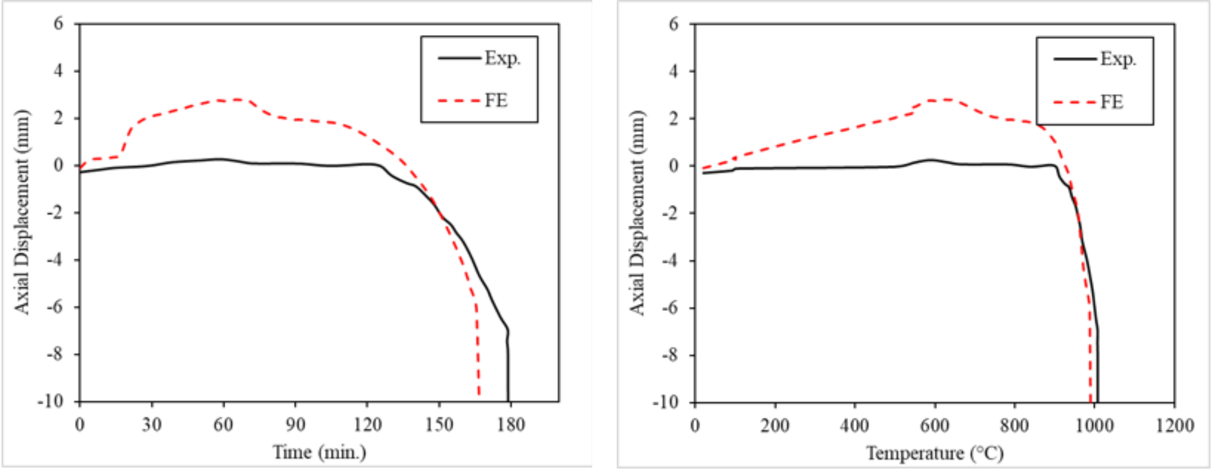

(e) SCW7- Applied measured surface temperatures (f) SCW7- Applied measured surface temperatures

Fig. 3-5. Comparison of axial displacement against time or surface temperature for SCW7 and SCW12

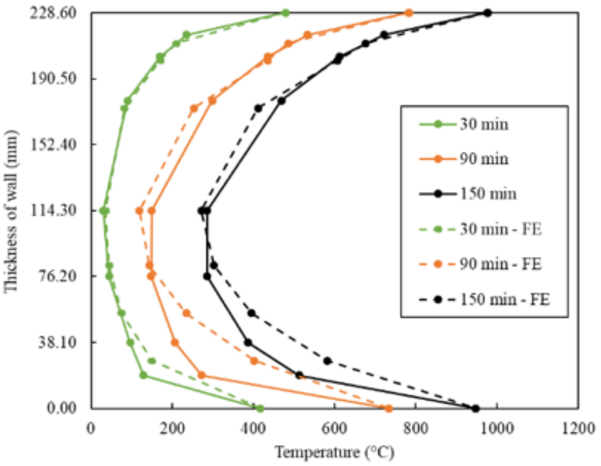

(a)

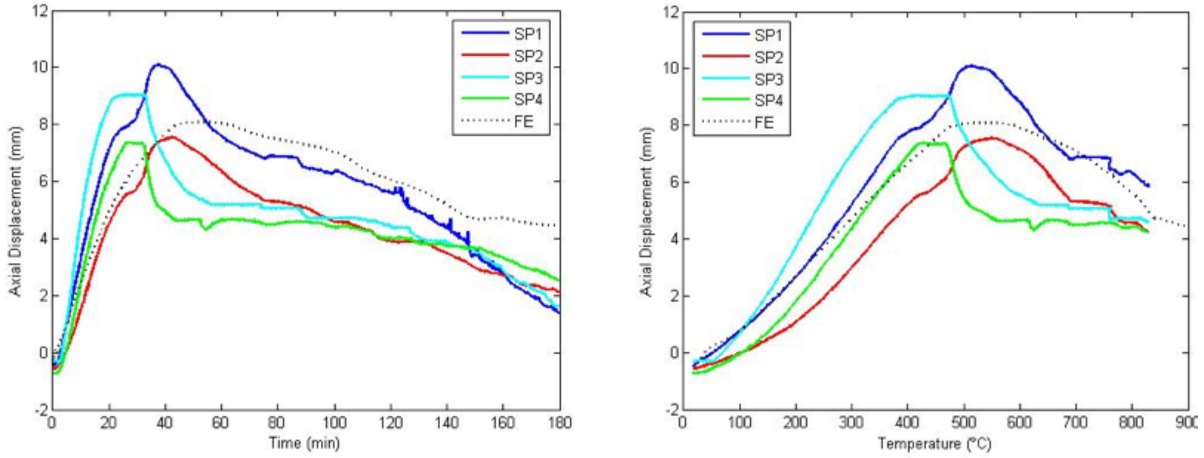

(b) CW1

(c) CW1

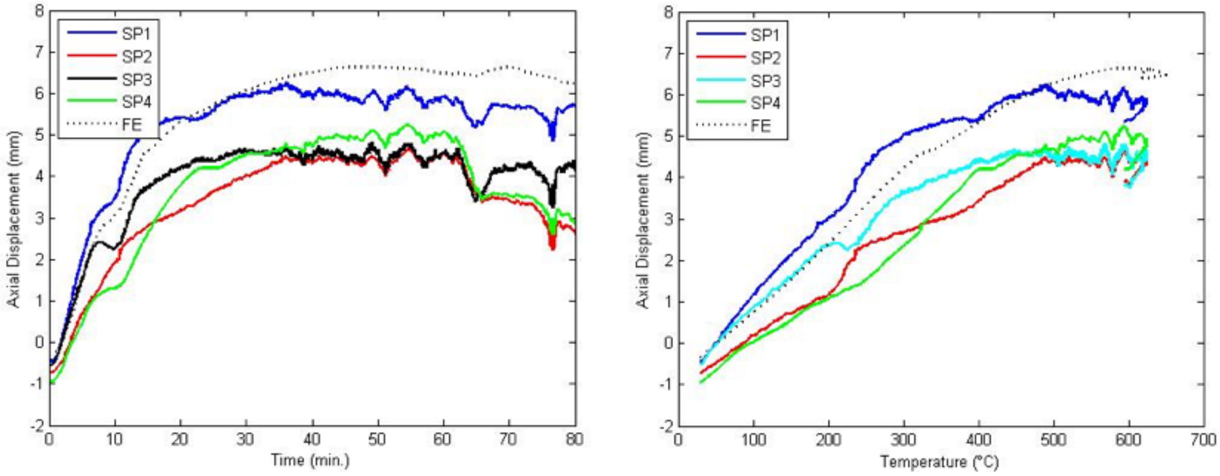

(d) CW3

(e) CW3

Fig. 3-6. Comparison of axial displacement against time for CW1 and CW3

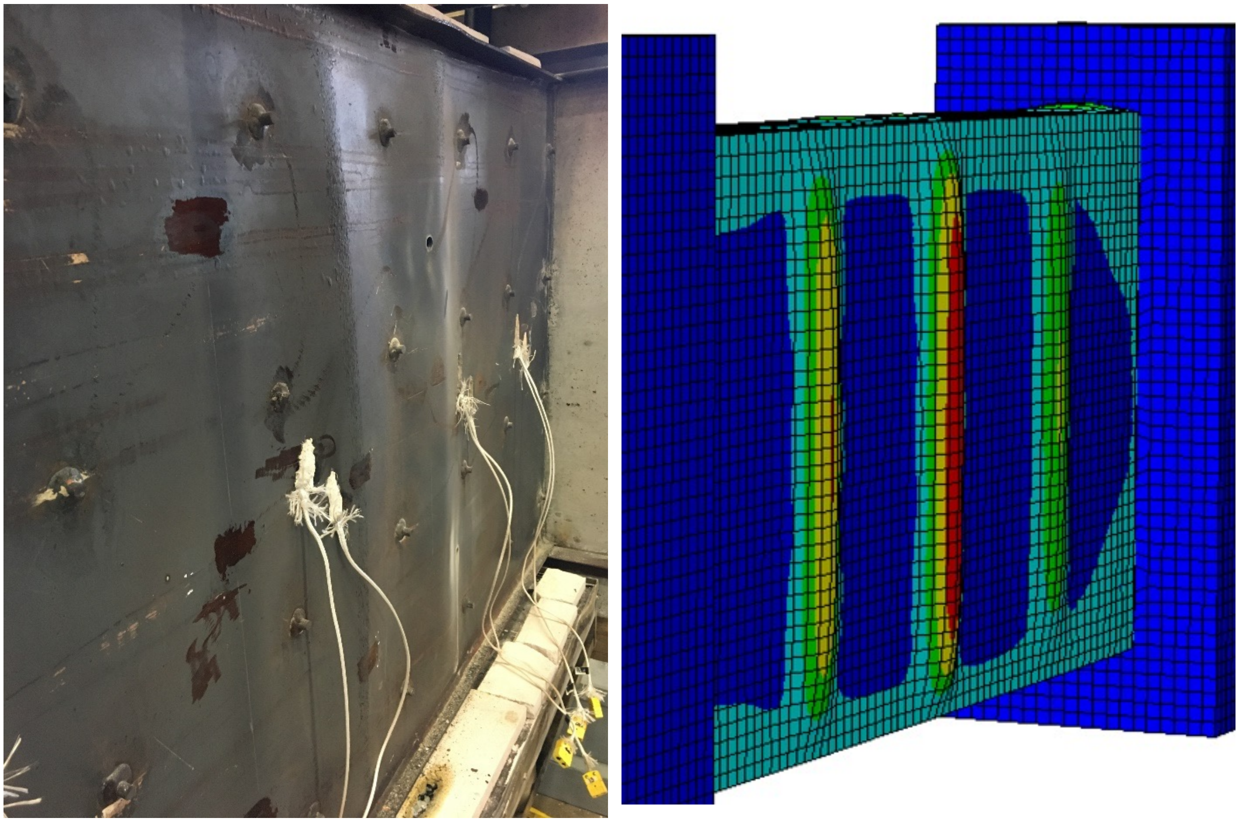

Fig. 3-7. Local buckling of faceplate in CW3

A summarized comparison of experimental and finite element results for all 12 specimens (Wei et al 2017) is presented for specimens in Table 3-1. The table presents the specimens properties and the experimental and numerical failure time and failure surface temperature. The failure times obtained from the FE analyses are conservative with respect to experimental failure times. Table. 3-1 also indicates that the experimentally observed surface temperature at failure is in better agreement with the numerical results in comparison to failure times. Therefore, the surface temperature at failure is recommended to be used to determine the fire resistance of C-PSW/CFs. However, the FE models are expected to be conservative in comparison to experimental results due to the inherent limitations of the material stress-strain curves at extreme temperatures and the assumption of no heat loss at the steel-concrete interface.

3.3. Analytical Parametric Study

The previous sections in this Chapter described the process to develop a benchmarked finite element modeling technique for C-PSW/CF systems. With the modeling technique verified, an analytical parametric study was conducted to study the influence of different parameters on the fire resistance of C-PSW/CFs. The analytical parametric matrix developed takes into consideration the typical range of parameters considered in the design documents and the current industry design practices as per AISC 341-16, section H7 and Varma et al. 2014.

The studied parameters are the wall slenderness, wall thickness, axial load ratio, boundary conditions, steel plate slenderness (tie bar spacing), steel plate reinforcement ratio and concrete strength. Table 3-2. presents the detailed properties of the studied walls. Table 3-2 presents the wall slenderness (H/t_w), wall thickness (t_w), wall width (W), wall height (H) , faceplate thickness (t_p), steel plate reinforcement ratio ($\rho = 2t_p/t_w$), tie bar diameter (d_{tie}), tie bar spacing to wall thickness ratio (s_{tie}/t_w), tie bar reinforcement ratio [$\rho_{tie} = \pi d_{tie}^2/4(s_{tie}^2)$], applied axial load as a function of compressive capacity of concrete core ($P/A_c f'_c$) and concrete compressive strength (f'_c) of the models.

The designation of the models' name follows as wall thickness, wall slenderness, the applied load ratio, steel plate slenderness, steel plate reinforcement ratio, concrete strength, and the type of boundary condition at the bottom and top of models. For example, CW-200-05-20P would indicate a wall with thickness of 200 mm, a wall slenderness of 5, an applied load ratio of 20%, and pinned boundary conditions at the bottom and top of the models.

The FE analysis included two steps and was similar to the models described in previous sections. The axial load was applied at 20℃ in the first step. In the next step, the thermal load was applied while the axial load was constant. ISO 834 failure criteria for axially loaded elements was investigated (ISO, 1975). The time instant when the axial contraction of walls exceeded $H/100$ (mm), where H is the wall height, was deemed as failure time of the wall. The failure surface temperature presents the faceplate temperature at failure time. Applied fire temperatures followed the ISO 834 standard fire time-temperature curve (ISO, 1975). The wall slenderness and wall thickness were in a range of 5-20 and 200-600 mm, respectively. Wall width (horizontal) was equal to three times the wall thickness in all models. The faceplate thickness was changed accordingly to provide a similar steel plate reinforcement ratio in models. The faceplate thickness is ranged from 4 mm to 12 mm based on wall thickness to provide a steel plate reinforcement ratio of 4%. Tie bar and shear stud (on flanges) with 7 mm to 20 mm diameter were used at a distance equal to 1 and ½ of wall thickness (t_w). The tie bar reinforcement ratio was limited within a range of 0.2-0.6% as recommended in Varma et al. 2014. The steel plate slenderness ratio was limited to 28 ($1.2\sqrt{E / F_y}$) other than two models with plate slenderness ratio of 50 and 75. An axial load equal to 20% and 30 % of the compressive axial capacity of the concrete infill, was applied. Walls were studied with concrete strengths of 40 MPa and 55 MPa and steel yield strength of 345 MPa. The models utilized Pinned-Pinned (P), Fixed-Pinned (FP) and Fixed-Fixed (F) boundary conditions to study the effect of boundary conditions on the behavior of C-PSW/CFs under fire loading.

Table 3-2. The properties, failure time and temperature of C-PSW/CF (Wall sections)

Nomenclature	H/t_w	t_w	W	H	t_p	ρ $(2t_p/t_w)$	d_{tie}	s_{tie}/t_w	ρ_{tie}	s_{tie}/t_p	$P/A_c f'_c$	f'_c	Failure Time	Failure Temperature	Failure Mode
		mm	mm	mm	mm	%	mm		%		%	MPa	min	°C	
CW-200-05-20P	05	200	600	1000	4	4.00	7	0.5	0.38	25	20	40	200	1105	C
CW-200-10-20P	10	200	600	2000	4	4.00	7	0.5	0.38	25	20	40	153	1058	GB
CW-200-15-20P	15	200	600	3000	4	4.00	7	0.5	0.38	25	20	40	128	1025	GB
CW-200-20-20P	20	200	600	4000	4	4.00	7	0.5	0.38	25	20	40	94	968	GB
CW-300-05-20P	05	300	900	1500	6	4.00	10	0.5	0.35	25	20	40	297	1167	C
CW-300-10-20P	10	300	900	3000	6	4.00	10	0.5	0.35	25	20	40	184	1085	GB
CW-300-15-20P	15	300	900	4500	6	4.00	10	0.5	0.35	25	20	40	147	1048	GB
CW-300-20-20P	20	300	900	6000	6	4.00	10	0.5	0.35	25	20	40	140	1041	GB
CW-400-05-20P	05	400	1200	2000	8	4.00	14	0.5	0.38	25	20	40	428	1225	C
CW-400-10-20P	10	400	1200	4000	8	4.00	14	0.5	0.38	25	20	40	242	1131	C
CW-400-15-20P	15	400	1200	6000	8	4.00	14	0.5	0.38	25	20	40	209	1106	GB
CW-400-20-20P	20	400	1200	8000	8	4.00	14	0.5	0.38	25	20	40	173	1074	GB
CW-500-20-20P	20	500	1500	10000	10	4.00	17	0.5	0.36	25	20	40	174	1073	GB
CW-600-20-20P	20	600	1800	12000	12	4.00	20	0.5	0.35	25	20	40	214	1108	GB
CW-200-05-20FP	05	200	600	1000	4	4.00	7	0.5	0.38	25	20	40	202	1107	C
CW-200-10-20FP	10	200	600	2000	4	4.00	7	0.5	0.38	25	20	40	181	1088	C
CW-200-15-20FP	15	200	600	3000	4	4.00	7	0.5	0.38	25	20	40	155	1060	GB
CW-200-20-20FP	20	200	600	4000	4	4.00	7	0.5	0.38	25	20	40	125	1022	GB
CW-300-05-20FP	05	300	900	1500	6	4.00	10	0.5	0.35	25	20	40	328	1183	C
CW-300-10-20FP	10	300	900	3000	6	4.00	10	0.5	0.35	25	20	40	224	1118	C
CW-300-15-20FP	15	300	900	4500	6	4.00	10	0.5	0.35	25	20	40	167	1070	GB
CW-300-20-20FP	20	300	900	6000	6	4.00	10	0.5	0.35	25	20	40	160	1065	GB
CW-200-20-20F	20	200	600	4000	4	4.00	7	0.5	0.38	25	20	40	138	1039	C
CW-300-20-20F	20	300	900	6000	6	4.00	10	0.5	0.35	25	20	40	172	1075	C
CW-400-20-20F	20	400	1200	8000	8	4.00	14	0.5	0.38	25	20	40	316	1175	C
CW-200-20-20P-fc55	20	200	600	4000	4	4.00	7	0.5	0.38	25	20	55	87	953	GB
CW-300-20-20P-fc55	20	300	900	6000	6	4.00	10	0.5	0.35	25	20	55	114	1003	GB
CW-400-20-20P- fc55	20	400	1200	8000	8	4.00	14	0.5	0.38	25	20	55	142	1039	GB
CW-200-05-30P	05	200	600	1000	4	4.00	7	0.5	0.38	25	30	40	93	965	C
CW-300-05-30P	05	300	900	1500	6	4.00	10	0.5	0.35	25	30	40	194	1095	C
CW-300-10-20-ρ133	10	300	900	3000	2	1.33	10	0.5	0.35	75	20	40	154	1059	C
CW-300-10-20- ρ533	10	300	900	3000	8	5.33	10	0.5	0.35	18.75	20	40	215	1115	C
CW-300-10-20-T	10	300	900	3000	6	4.00	20	1	0.35	50	20	40	157	1059	C

C = Crushing

GB = Global Buckling

3.3.1. High-Temperature Distribution

Changing the faceplate thickness between the models causes a slight difference in the wall surface temperatures. For this study, the faceplate thickness was changed to have a similar steel ratio within the cross-section of walls being studied. The comparison of wall surface temperatures for walls with various wall thicknesses is shown in Fig. 3-8(a). The surface temperature of the walls with thicker faceplates is slightly lower than that of the thinner faceplates. The surface temperatures diverge marginally at the early steps of heating. This surface temperature difference between 200 mm and 600 mm thick walls reached to about 170 ℃ at 35 mins. Because the rate of temperature rise decreases in the standard fire curve (ISO 834, 1975), the surface temperatures converged after about 80 min of heating.

The high-temperature distribution through the wall thickness with a thickness of 200 mm, 300 mm and 600 mm at different time points is illustrated in Fig. 3-8(b) to Fig. 3-8(d), respectively. The high-temperature distribution is symmetric through the wall thickness. Also, walls experience nonlinear thermal gradient through the wall thickness. The mid-thickness temperature of walls in Fig. 3-8(b) to Fig. 3-8(d) indicate that the wall mid-thickness temperature is a function of wall thickness. After four hours of heating, the mid-thickness temperature of 200 mm, 300 mm and 600 mm thick walls are 548 ℃, 256 ℃ and 43 ℃, respectively. However, the surface temperatures of these walls are close to each other at different time points.

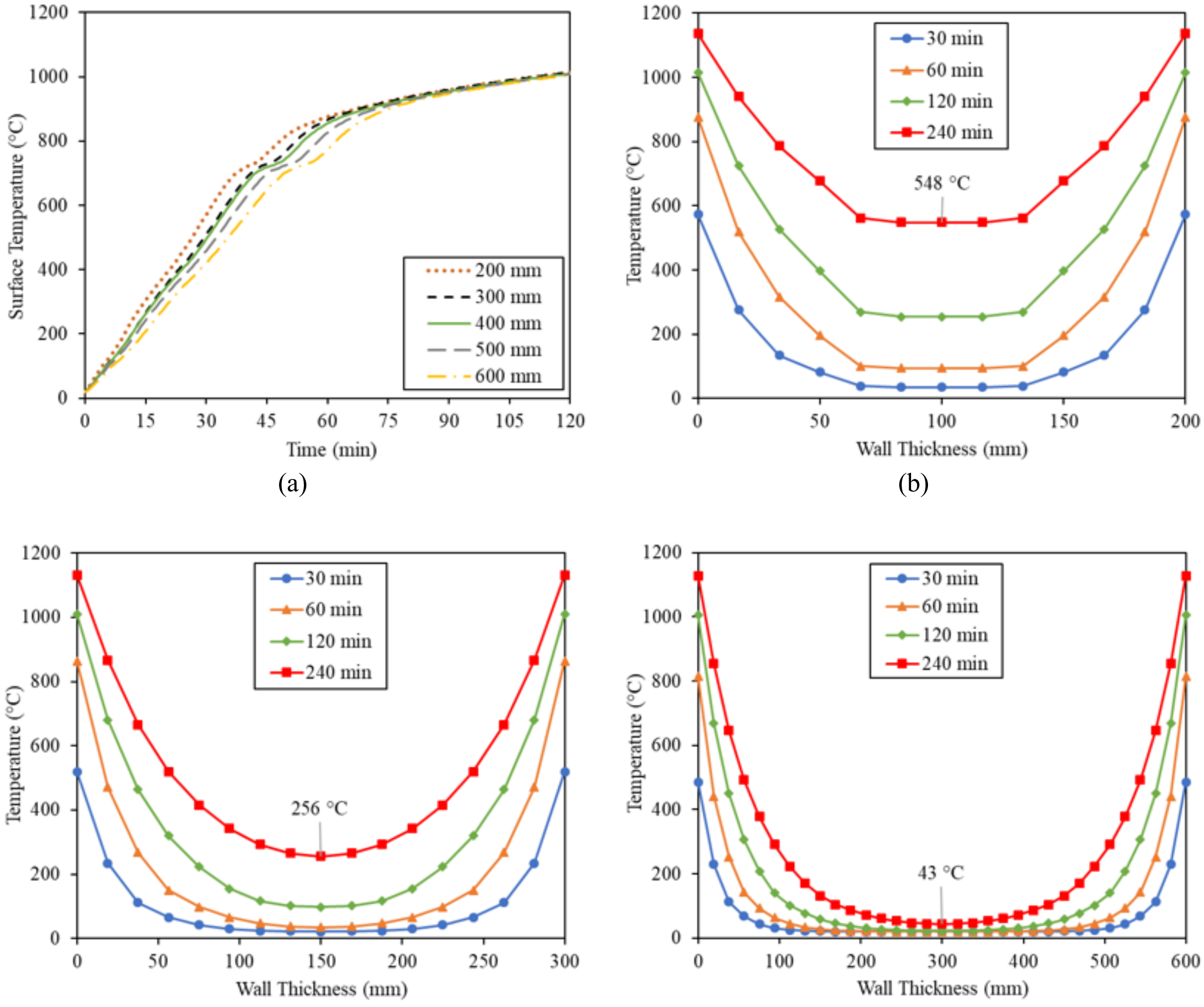

(a) (b)

(c) (d)

Fig. 3-8. (a) Comparison of the surface temperatures. Through-wall thickness temperature of (b) CW-200, (c) CW-300 and (d) CW-600

3.3.2. C-PSW/CF Stress Analysis Results (Wall Sections)

The axial displacement of the walls follows a consistent trend. At early steps of analysis, walls experience thermal expansion. Generally, this expansion takes about 30 mins after the beginning of heating. The amount of thermal expansion depends on the height of the wall. The shorter walls expand less than the taller walls. Eq. (3-1) shows the thermal expansion equation. The surface temperature of the faceplate of walls with various thickness is similar (Fig. 3-8(a)). Therefore, this results in a similar temperature change (ΔT) in Eq. (3-1). Thus, as wall height (H) increases, it causes higher thermal expansion along with the height of the walls.

$$\Delta L = \alpha_L \, \Delta T \, L \tag{3-1}$$

Most of the applied load transfers to the faceplate when walls experience thermal expansion. Also, the force in faceplate can exceed the applied load. As the temperature of the faceplate increases, local buckling occurs in the faceplate. The local buckling of faceplate occurs between the tie bars due to faceplate thermal expansion and degradation of material strength at elevated temperatures. Fig. 3-9(a) shows the buckled faceplate between tie bars. The faceplate loses its load-bearing capacity due to the reduction of material strength and bulging of the faceplate. Therefore, the applied force to faceplate transfers to the concrete core due to degradation stiffness and loadbearing capacity of the faceplate. Concrete core sustains most of the applied axial load until the failure of walls.

Fig. 3-9(b) shows the distribution of the applied load between the faceplate and concrete core for CW-300-20-20FP. The load transferred to faceplate raised abruptly at 5 mins after the beginning of heating due to thermal expansion while the load in concrete core dropped to about -150 kN. Because of the bond between concrete and faceplate, the thermal expansion causes tension in the concrete core of walls. Since the strength of steel degraded at high temperatures and local buckling occurred in the faceplate, the faceplate loses its load bearing capacity. Therefore, the wall undergoes axial shortening. The force in the faceplate dropped to about 10% of the applied load at 55 mins and the concrete infill sustained the rest of the applied load.

When thermal wall expansion reaches its maximum, axial shortening due to the degradation of material strength at elevated temperatures overcomes the thermal wall expansion. Since the strength of material reduces, the axial displacement of the walls drops reduces. Axial shortening of the wall continues gradually. Eventually, since high temperature propagates to most parts of the wall, the strength of material reduces significantly. Thereafter, significant axial shortening occurs abruptly, and the wall undergoes failure.

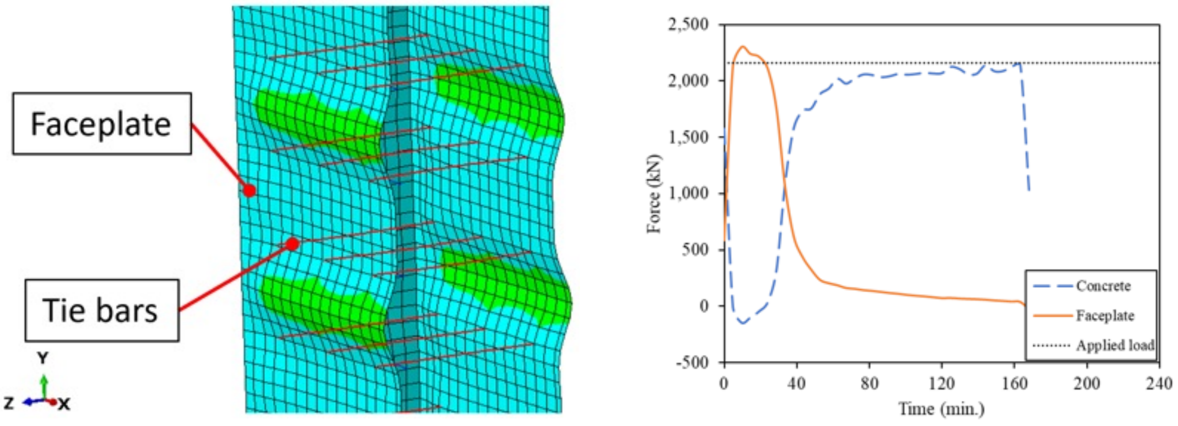

(a) (b)

Fig. 3-9. (a) Local buckling of faceplate between tie bars of CW-300-20-20P (b) Force distribution in CW-300-20-20FP between the faceplate and concrete core

3.3.2.1. The influence of boundary condition

Three different boundary conditions were applied to the walls. The response of walls with pinned-pinned, fixed-pinned and fixed-fixed boundary conditions was studied. The axial displacements of CW-300-20-20 against time with various boundary conditions are compared in Fig. 3-10(a). The axial displacements of walls are close at the early stages of analysis during thermal wall expansion. However, the curves begin to diverge due to the initiation of global instability in the walls. Comparing the response of the wall with a fixed-fixed boundary condition to walls with pinned-pinned or fixed-pinned boundary condition in Fig. 3-10(a) shows that using a fixed-fixed boundary condition improves the fire rating. Table 3-2. presents the failure time of the walls with various boundary conditions. Consistently, walls with pinned-pinned boundary conditions failed earlier than walls with pinned-fixed or fixed-fixed boundary conditions. For example, CW-300-20-20 failed at 140 mins, 160 mins and 172 mins with pinned-pinned, fixed-pinned and fixed-fixed boundary conditions, respectively.

The axial displacements of CW-300-20-20 against the wall surface temperature with various boundary conditions are compared in Fig. 3-10(b). The surface temperature at failure is lower in walls with pinned-pinned boundary conditions. For instance, the wall surface temperature for CW-300-20-20P was about 1041 °C, while CW-300-20-20P failed when the surface temperature reached about 1075 °C with a fixed-fixed boundary condition. Walls with pinned-pinned boundary conditions fail earlier than walls with pinned-fixed or fixed-fixed boundary conditions. Therefore, the next sections are focused on the response of walls with a pinned-pinned boundary condition only.

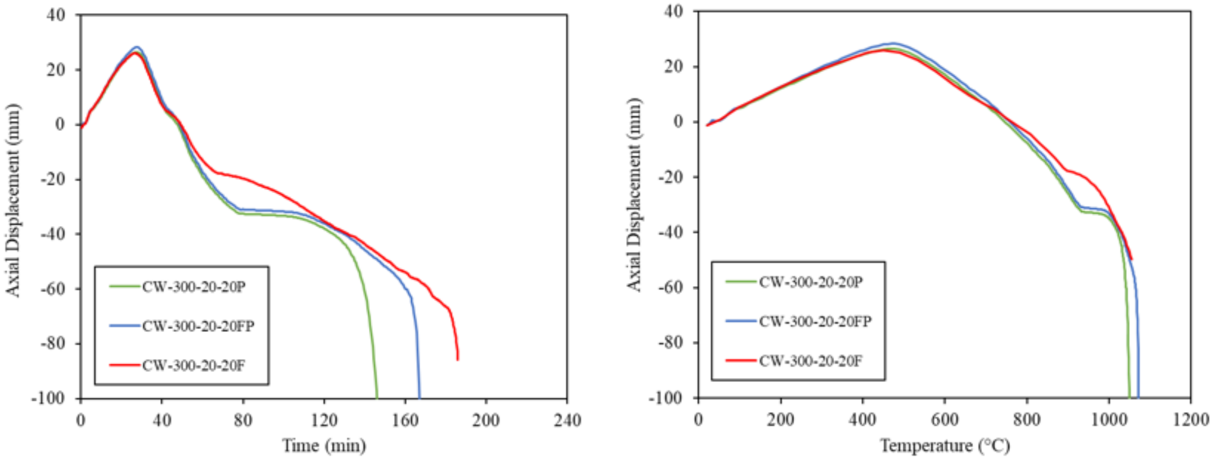

(a) Axial displacement against time (b) Axial displacement against surface temperature

Fig. 3-10. The response of CW-300-20-20 at elevated temperatures with various applied boundary conditions

3.3.2.2. The influence of wall slenderness and wall thickness

The fire resistance of C-PSW/CFs was analyzed with various wall slenderness ratios. The wall slenderness ranged from 5 to 20 and a wall thickness range of 200 mm to 600 mm. The height of the walls varies from 1 m to 12 m to accommodate the specific wall slenderness. The axial displacements against time for four walls with a thickness of 200 mm and 300 mm and wall slenderness of 5 to 20 are shown in Fig. 3-11(a) and (b). The results show that an increase in the wall slenderness results in the reduction of wall fire rating. CW-200-05-20P had a fire rating of 200 mins. However, CW-200-20-20P failed at about 94 mins. CW-200-05-20P failed due to local buckling and losing the wall's load-bearing capacity while CW-200-20-20P failed due to global instability. Similarly, walls fail at higher surface temperatures when the wall slenderness ratios decrease as shown in Fig. 3-11(c) and (d).

The axial displacements of walls with a thickness of 200 mm and 300 mm and wall slenderness ratios of 10 and 15 are compared in Fig. 3-11(e) and (f). CW-300-10-20P failed at 184 min while the fire rating decreased to 153 mins for the wall thickness of 200 mm. The comparison of failure time of walls with various wall thicknesses (Table. 3-2) indicates that reducing the wall thickness leads to an earlier failure of walls. As the high-temperature distribution shown in Fig. 3-8(b) to (c), the concrete in the middle of thicker walls is cooler than the exterior parts of walls. Therefore, the cooler part of the concrete core helps the load bearing capacity of the walls.

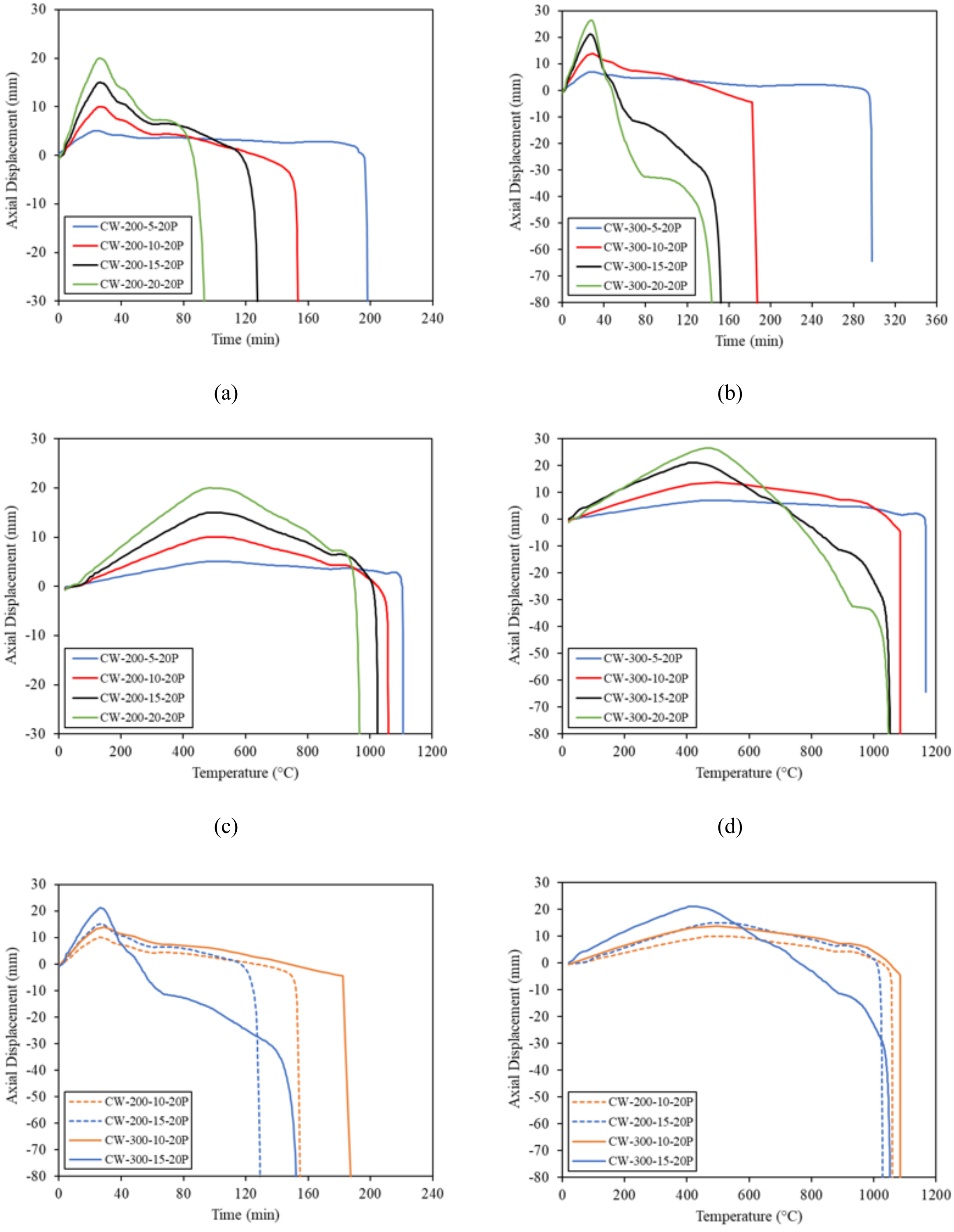

(a) (b)

(c) (d)

(e) (f)

Fig. 3-11. The axial displacement versus time curves of CW-200s (a) and CW-300s (b) and the axial displacement against surface temperature of CW-200s (c) and CW-300s (d) with pinned boundary condition. Axial displacement (e) and surface temperature (f) of 200 mm and 300 mm thick walls

3.3.2.3. The influence of load ratio

To investigate the influence of the load ratio on fire resistance of walls, the behavior of walls was analyzed for 20 and 30 percent of the axial concrete infill compressive capacity at ambient temperature ($A_c f'_c$). The results show that the load level has a major effect on the fire resistance of walls. Fig. 3-12(a) shows the comparison of the axial displacement of the walls induced to 20% $A_c f'_c$ and 30% $A_c f'_c$. For example, CW-200-5-20P and CW-200-5-30P lost their load-bearing capacity at 200 and 93 mins, respectively. Also, at higher load levels, walls experienced smaller thermal expansion at the early stages of fire exposure. Fig. 3-12(b) presents the axial displacements against surface temperature of CW-200-05-XP and CW-300-05-XP. The axial displacement of walls with a lower load ratio was higher at similar surface temperatures. For instance, CW-300-05-20P failed when the surface temperature reached to about 1167 °C. By increasing the applied load to 30% $A_c f'_c$ the failure occurred when the surface temperature reached 965 °C.

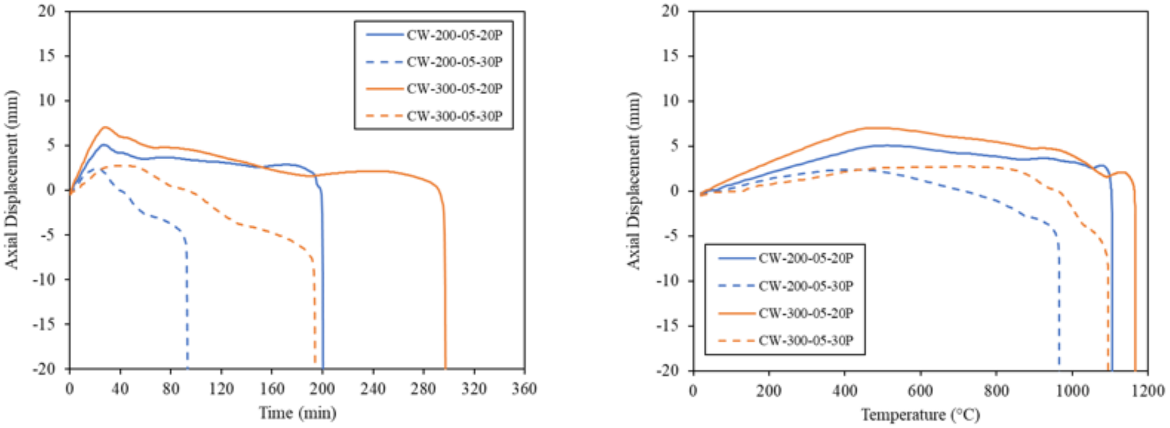

(a) (b)

Fig. 3-12. Axial displacement of walls under three various load ratios CW-200s against time (a) and wall surface temperature (b)

3.3.2.4. The influence of concrete strength

The behavior of walls with two compressive concrete strength of 40 MPa (5.8 ksi) and 55 MPa (8 ksi) were studied in the current parametric study. The fire resistance of walls with a wall thickness range of 200 mm to 400 mm and wall slenderness of 20 with two concrete strength (40 MPa and 55 MPa) was studied. An axial load equal to 20% of the axial compressive capacity of walls concrete core (*20%* $A_c f'_c$) was applied. Hence, the applied axial load to the wall was higher in walls with higher concrete strength (55 MPa). In Fig. 3-13, the axial displacements of CW-400-

20-20 with two different concrete strength against time and surface temperature are compared. Lower axial expansion occurred in walls with higher concrete strength. This is due to the higher axial load application in walls with higher concrete strength. Comparing the fire rating of walls with both concrete strengths shows that walls with higher concrete strength fail earlier with the same load ratio.

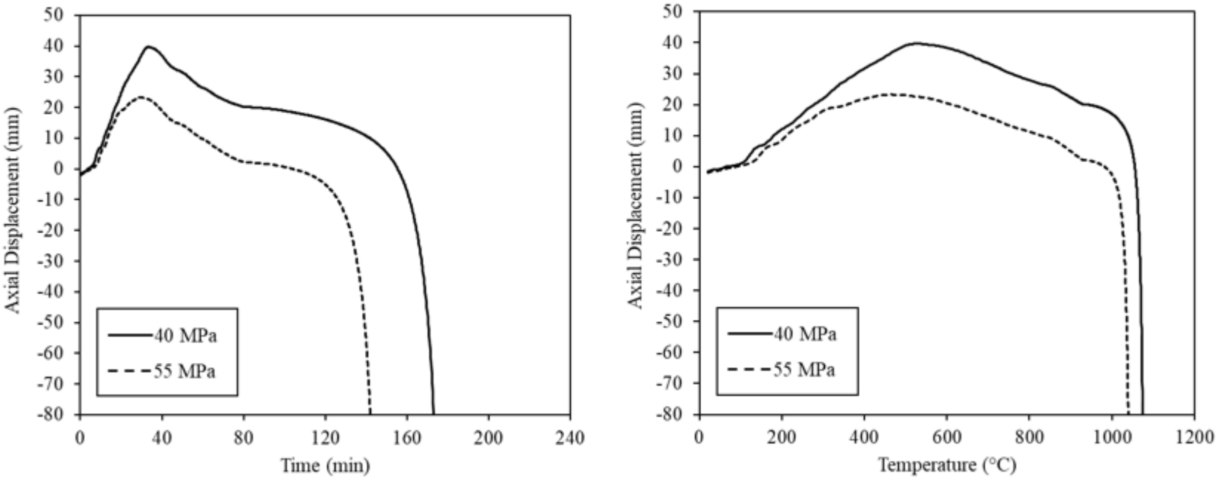

(a) Axial displacement against time (b) Axial displacement against surface temperature

Fig. 3-13. Axial displacement of walls with concrete strength of 40 MPa and 55 MPa

3.3.2.5. Steel plate reinforcement ratio and tie bar spacing

The behavior of CW-300-10-20 under fire loading with plate reinforcement ratios of 1.33%, 4.00%, and 5.33% was studied. The steel plate reinforcement ratio was selected based on the practical ratios (1.5% - 6.0%) recommended in the literature (Varma et al. 2014). The walls had a tie bar spacing equal to half of the wall thickness ($s_{tie} = t_w/2$) and a faceplate thickness (t_p) of 2, 6, and 8 mm resulted in steel plate slenderness ratios (s_{tie}/t_p) of 75, 25 and 19, respectively. Aslo, a wall (CW-300-10-20) with a tie spacing equal to the wall thickness (steel plate slenderness = 50) was modeled. The axial displacements of the walls are compared shown in Fig. 3-14. The legend in Fig. 3-14 is showing the steel plate ratios and the tie bar spacing to wall thickness ratio (s_{tie}/t_w), respectively.

The faceplate of the wall with plate reinforcement of 1.33%, buckled at the early stages of fire exposure due to having lower steel plate slenderness and it did not experience any expansion. Comparing the axial displacement of walls with tie bar spacing of t_w and $t_w/2$ during fire exposure shows that by increasing the tie bar spacing (or steel plate slenderness), the wall experiences lower expansion due to early buckling in the faceplate.

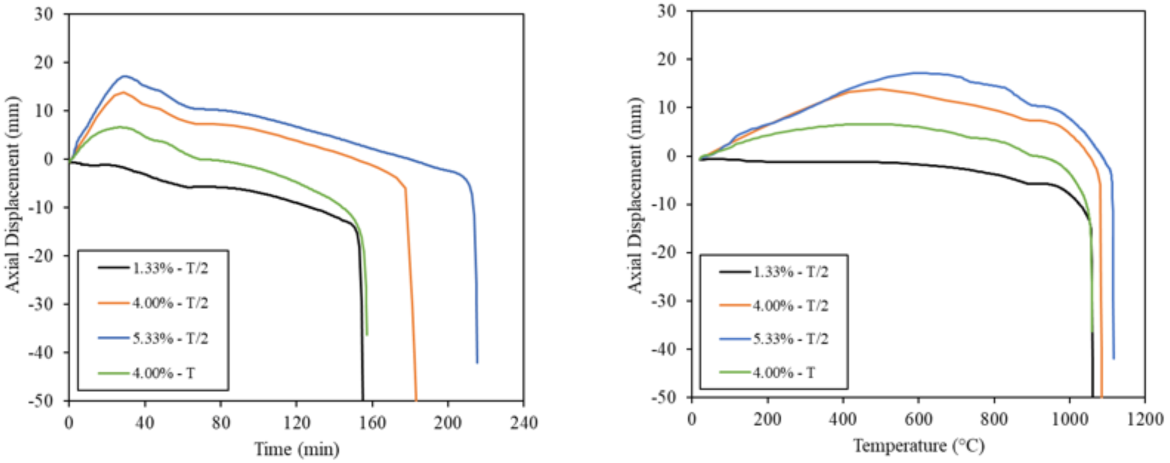

(a) Axial displacement against time (b) Axial displacement against surface temperature

Fig. 3-14. Axial displacement of CW-300-10-20P with different steel ratios and tie bar spacing

3.3.3. C-PSW/CF Unit Width Walls and Stress Analysis Results

C-PSW/CFs for buildings will typically have widths significantly more than wall thickness and be subjected to two-sided (both webs) or one-sided (one web, where the wall may need to design as a fire barrier) fire. C-PSW/CFs may be designed with different configurations like planar walls or C-shaped walls. The interior region can be conservatively modeled as the unit width column representing the whole wall because the regions of the wall closer to boundary elements may have higher axial compression stiffness and strength than the interior regions.

The schematic distribution of critical axial compression capacity of a C-shaped C-PSW/CF is shown in Fig. 3-15(a). This was verified by comparing the axial load distribution in different regions of the walls during exposure to fire loading. A rigid constraint was applied to the top surface of walls in the FE models. The axial load was uniformly applied along the width of the walls. The cross-section of a simulated wall with boundary elements was divided into three regions along the width (middle and ends). The normalized axial reaction (at the base) of the concrete infill and faceplate in the middle and the end parts for SCW4 is compared in Fig. 3-15(b). The axial reactions were almost the same at ambient temperature for both regions. At the beginning of the analysis, the model undergoes thermal expansion leading to concrete cracking. Thus, the axial force in concrete infill dropped and the majority of the applied load was transferred to the faceplate.

However, after about 40 min due to the reduction of stiffness and local buckling of faceplate at elevated temperatures, the applied axial load gradually transferred to the concrete infill. The summation of base reaction forces in the middle region was lower than at the ends throughout the fire loading. Thus, the column strip (a wall with a unit width) taken from the middle region of the wall can be used to conservatively estimate the strength of the wall at elevated temperatures. Also, this offers computationally efficient method to design C-PSW/CF under fire loading.

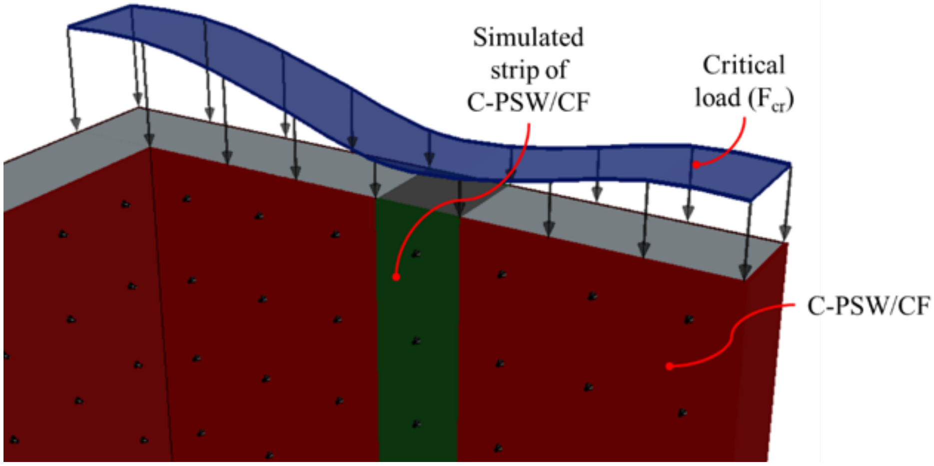

(a)

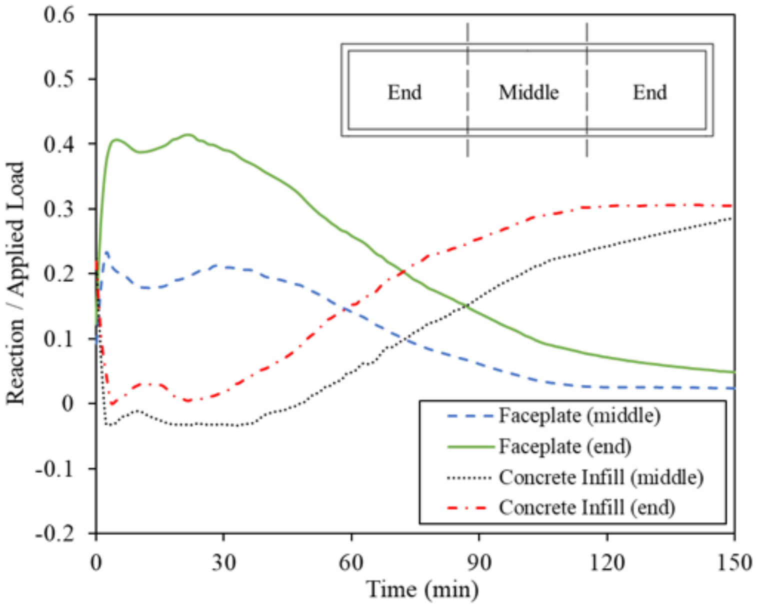

(b)

Fig. 3-15. (a)The variation of critical load of a C-PSW/CF along the width. (b) Distribution of axial load between the middle and end regions in SCW4.

The FE models benchmarked to tests by Wei et al. (2017) and current fire tests were used to simulate a unit width strip of C-PSW/CFs (column) representing the middle region of the wall. The models included a row of tie bars and shear studs. The width of the models was equal to the tie bar spacing. The faceplate was modeled on two sides of the wall. The elevated temperatures were applied to two sides (faceplates) assuming the heat flow is perpendicular to the width of the wall. Symmetric boundary conditions were applied to the edges of the faceplate. The transitional degree of freedom along the wall width was not restrained to allow the column to expand along its width at elevated temperatures. A 3-D view of the developed FE model is shown in Fig. 3-16(a).

The variation of through-thickness temperatures along the width of the wall will be negligible (except corner regions for C-shaped walls). Therefore, the possibility of unit-width analyses of C-PSW/CFs for fire loading needs to be explored. The walls can then be analyzed as unit width column strips, and design strengths can be provided per unit width of the wall.

The axial displacement of the column strip models is compared with the modeled walls and experimental data in Fig. 3-16(b) and 3-16(c). A comparison of the failure times of the benchmarked models is presented in Table 3-3. The columns strip models gave comparable results to the wall models and the experimental results. The failure times for the column strip models are lower than those for the experiments and wall strip models. The failure time of SCW4 (wall) was 155 min which was reduced to 139 mins for the column strip model. The simulated columns have lower axial capacity as was discussed earlier. However, the general behavior is in good agreement with the experimental behavior. The column strip method can be used to conservatively analyze and design C-PSW/CFs with varied configurations and dimensions.

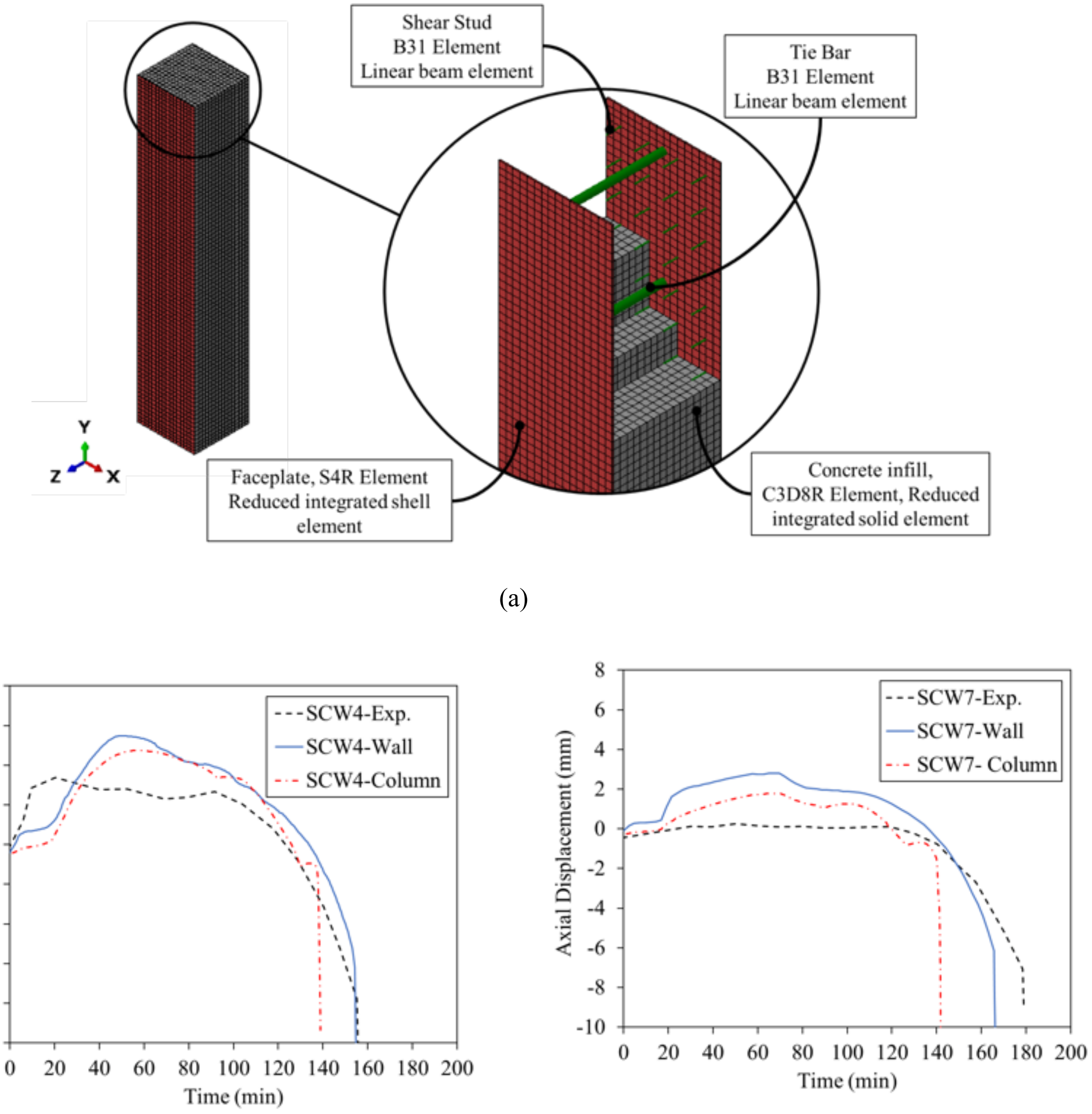

(a)

(b)

(c)

Fig. 3-16. (a) The developed three-dimensional model of a strip of C-PSW/CF (column). The Comparison of numerically obtained axial displacements with experimental data for (b) SCW4 and (c) SCW7

Table 3-3. Summary of finite element and experimental results (specimens tested by Wei et al. 2017)

Specimens	H (mm)	t_w (mm)	t_p (mm)	Shear stud	Tie bar	Load ratio	Failure Time (min)		
							Test	FE (Wall)	FE (Column)
SCW4	1350	150	3	Φ2@40	Φ10@160	0.34	156	155	139
SCW7	850	150	2	Φ2@40	Φ10@160	0.40	178	166	142

All dimensions in mm, unless noted otherwise.

A series of FE analyses was conducted on C-PSW/CF unit width models. This analysis was conducted on models with a wall thickness of 200 mm to 400 mm and a wall slenderness ratio range of 5 to 20. An axial load corresponding to 20% of the compressive capacity of simulated parts of the walls was applied before applying fire loads. Tie bars were located at $t_w/2$ away from each other. Pinned boundary condition was applied to the bottom and top of the model. Table. 3-4 presents the properties, fire rating and failure temperature of studied unit strips of walls in the parametric study.

The failure time and surface temperature of models are presented in Table 3-4. The unit strip wall models failed earlier compare to C-PSW/CF wall sections. As it was mentioned previously, unit width models estimate the capacity of C-PSW/CF conservatively. The axial displacement against time plots for the walls are presented in Fig. 3-17 (a). Similar to C-PSW/CF wall section models, an increase in the wall slenderness ratio results in a lower failure time (CW-300-10-20P failed at 250 mins while CW-300-15-20P failed at about 140 mins). CW-300-10-20P failed due to the crushing of the cross-section, whereas CW-300-15-20P failed due to global instability. Fig. 3-17 (b) shows the axial displacement against surface temperature plots for the models. Models with a higher wall slenderness ratio failed at lower surface temperatures, however, the failure surface temperature was greater than 1000 °C for all the walls.

As was mentioned in section 3.3.2.2 the thickness of C-PSW/CFs had a major influence on the failure time of the walls. A comparison response of 200 mm and 300 mm thick walls (with same slenderness ratios) indicated that reducing the wall thickness led to lower failure times. Due to the low thermal conductivity of concrete, the middle of concrete in thicker walls was cooler than the thin walls. Also, thicker walls failed at higher surface temperatures. The cooler region of the concrete infill delayed the failure time of the wall.

The results of the analytical parametric studies for C-PSW/CF wall sections and unit width walls were utilized to develop a design method to estimate the capacity and fire resistance rating of C-PSW/CFs at elevated temperatures. This is presented in sections 3.4 and 3.5 of current report.

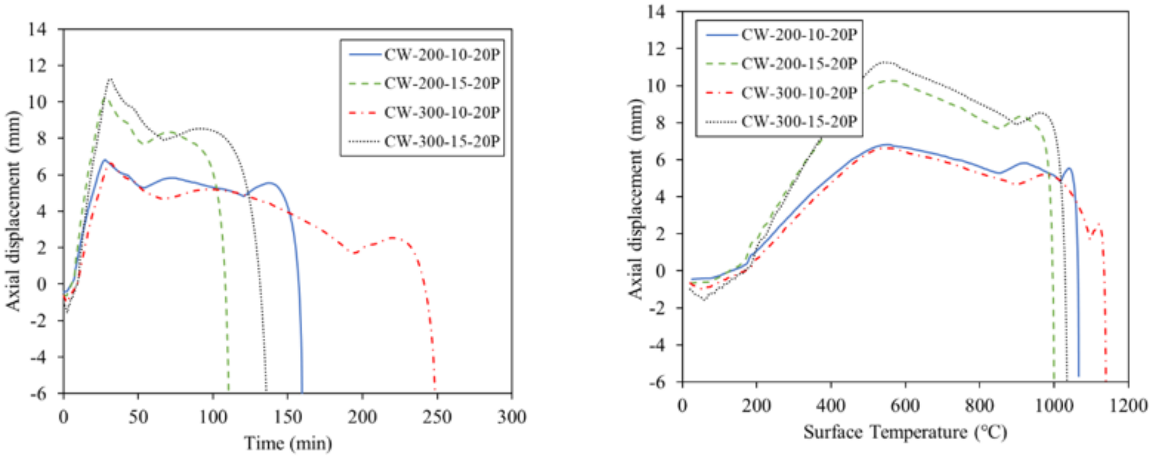

(a) Axial displacement against time

(b) Axial displacement against surface temperature

Fig. 3-17. Axial displacement of CW-300-10-20P with different steel ratios and tie bar spacing

Table 3-4. The properties, failure time and temperature of modeled unit width strip of C-PSW/CF (Columns)

Nomenclature	H/t_w	t_w	W	H	t_p	ρ $(2t_p/t_w)$	d_{tie}	s_{tie}/t_w	ρ_{tie}	s_{tie}/t_p	$P/A_c f'_c$	f'_c	Failure Time	Failure Temperature	Failure Mode
		mm	mm	mm	mm	%	mm		%		%	MPa	min	°C	
CW-200-05-20P	5.00	200	100	1000	4	4.00	7	0.5	0.38	25	20	40	198	1105	C
CW-200-10-20P	10.00	200	100	2000	4	4.00	7	0.5	0.38	25	20	40	160	1068	GB
CW-200-15-20P	15.00	200	100	3000	4	4.00	7	0.5	0.38	25	20	40	112	1004	GB
CW-200-20-20P	20.00	200	100	4000	4	4.00	7	0.5	0.38	25	20	40	81	943	GB
CW-300-05-20P	5.00	300	150	1500	6	4.00	10	0.5	0.35	25	20	40	353	1197	C
CW-300-10-20P	10.00	300	150	3000	6	4.00	10	0.5	0.35	25	20	40	250	1140	GB
CW-300-15-20P	15.00	300	150	4500	6	4.00	10	0.5	0.35	25	20	40	140	1041	GB
CW-300-20-20P	20.00	300	150	6000	6	4.00	10	0.5	0.35	25	20	40	122	1016	GB
CW-400-05-20P	5.00	400	200	2000	8	4.00	14	0.5	0.38	25	20	40	584	1276	C
CW-400-10-20P	10.00	400	200	4000	8	4.00	14	0.5	0.38	25	20	40	446	1234	GB
CW-400-15-20P	15.00	400	200	6000	8	4.00	14	0.5	0.38	25	20	40	209	1110	GB
CW-400-20-20P	20.00	400	200	8000	8	4.00	14	0.5	0.38	25	20	40	171	1075	GB

C = Crushing

GB = Global Buckling

3.4. Proposed Capacity Prediction Design Equations

AISC 360-16 uses Eq. (3-2) to calculate the critical stress of steel columns at elevated temperatures. The nominal compressive stress for flexural buckling of columns at elevated temperatures (F_{cr}) can be calculated using Eq. (3-2) as per AISC 360-16 specification (AISC, 2016). In this equation, $F_y(T)$ is the yield stress at elevated temperatures and $F_e(T)$ is the critical elastic buckling stress at elevated temperatures. $F_e(T)$ can be calculated using Eq. (3-3) where $E(T)$ is the modulus elasticity of steel at elevated temperatures, I is the moment of inertia of the section of the member, L_c is the effective height of the member, and r is the radius of gyration of the cross-section.

$$F_{cr}(T) = \left[0.42^{\sqrt{\frac{F_y(T)}{F_e(T)}}} \right] F_y(T) \tag{3-2}$$

$$F_e(T) = \frac{\pi^2 E(T)}{\left(\frac{L_c}{r}\right)^2} \tag{3-3}$$

This research sought out to develop a design equation similar in form to Eq. 3-2. In order to propose a design equation to estimate the capacity of C-PSWs/CF at elevated temperatures, some modifications were made in the utilized parameters used for steel columns.

Observations from the parametric studies (C-PSW/CF full wall sections and unit width walls) were used to develop a method to calculate the axial compression strength of C-PSWs/CF at elevated temperatures. Two equations (Eqs. 3-4 and 3-5) were proposed to estimate the axial compression capacity of C-PSW/CFs at elevated temperatures [$P_n(T)$]. The method considers temperature dependence of the concrete and steel modulus of elasticity and yield strengths. The comparison of both proposed equations with FE analysis results is described in this section.

Median:

$$P_n(T) = 0.39^{\left(\frac{P_{no}(T)}{P_e(T)}\right)^{0.3}} P_{no}(T) \tag{3-4}$$

Lower bound:

$$P_n(T) = 0.32^{\left(\frac{P_{no}(T)}{P_e(T)}\right)^{0.3}} P_{no}(T) \tag{3-5}$$

Where $P_{no}(T)$ is the cross-section nominal axial compressive strength at elevated temperatures and $P_e(T)$ is the elastic critical buckling load at elevated temperatures. $P_{no}(T)$ and $P_e(T)$ were computed using Eqs. 3-6 and 3-7, respectively.

$$P_{no}(T) = A_s F_y(T) + \sum_{i=elements} 0.85 A_{ci} f_c^{'}(T_i) \tag{3-6}$$

$$P_e(T) = \frac{\pi^2 EI_{eff}(T)}{(L_c)^2} \tag{3-7}$$

Where A_s is the area of steel, A_c is the area of concrete elements, $F_y(T)$is the yield strength of steel material at elevated temperatures and $f'_c(T)$ is the compressive strength of concrete at elevated temperatures. L_c is the effective height of the wall. The effective stiffness of the composite section at elevated temperatures, $EI_{eff}(T)$, can be determined based on the temperature distribution through the thickness by using Eq. 3-8.

$$EI_{eff}(T) = E_s(T) I_s + C_3 \sum_{i=elements} E_c(T_i) I_{ci} \tag{3-8}$$

$$C_3 = 0.45 + 3(A_s / A_g) \leq 0.9 \tag{3-9}$$

Where A_g is the gross area of cross-section, I_s is the moment of inertia of steel (faceplate), I_c is the moment of inertia of concrete, $E_s(T)$ is the modulus elasticity of steel at elevated temperatures, $E_c(T)$ is the modulus elasticity of concrete at elevated temperatures and C_3 is the concrete contribution factor to the stiffness.

The normalized effective stiffness of composite section at elevated temperatures [$EI_{eff}(T)$] to the effective stiffness of composite section at ambient temperatures (EI_{eff}) for two walls' cross-section with a thickness of 200 mm and 300 mm is shown in Fig. 3-18(a) and Fig. 3-18(b), respectively. The contribution of the faceplate and concrete core in the effective stiffness of the composite section of walls is shown separately. Since the faceplate is located at the exterior surface of walls (far from the cross-section's neutral axis), it has a significant contribution to the effective stiffness of walls at ambient temperature. However, the faceplate was directly exposed to elevated temperatures. Therefore, the faceplate temperature raised rapidly and caused a major reduction in steel modulus of elasticity. The flexural stiffness contribution of faceplate reduced from about 68% to less than 10% after about 40 mins of heating. The temperatures through the thickness of thinner walls increase quicker. Therefore, flexural stiffness contribution of thinner walls' concrete core decreases at a quicker rater.

The normalized nominal axial compressive strength (zero height) at elevated temperatures [$P_{no}(T)$] to nominal axial compressive strength (zero height) at ambient temperature [P_{no}] for two walls' cross-section with a thickness of 200 mm and 300 mm is compared in Fig. 3-18(c). Comparing the reduction of $P_{no}(T)$ for walls with various thicknesses shows that $P_{no}(T)$ was diminished at a faster rate in the thinner wall (t_w = 200 mm). In the thicker wall (t_w = 300 mm), the cooler part in the middle of the concrete core helped to maintain the strength capacity of walls.

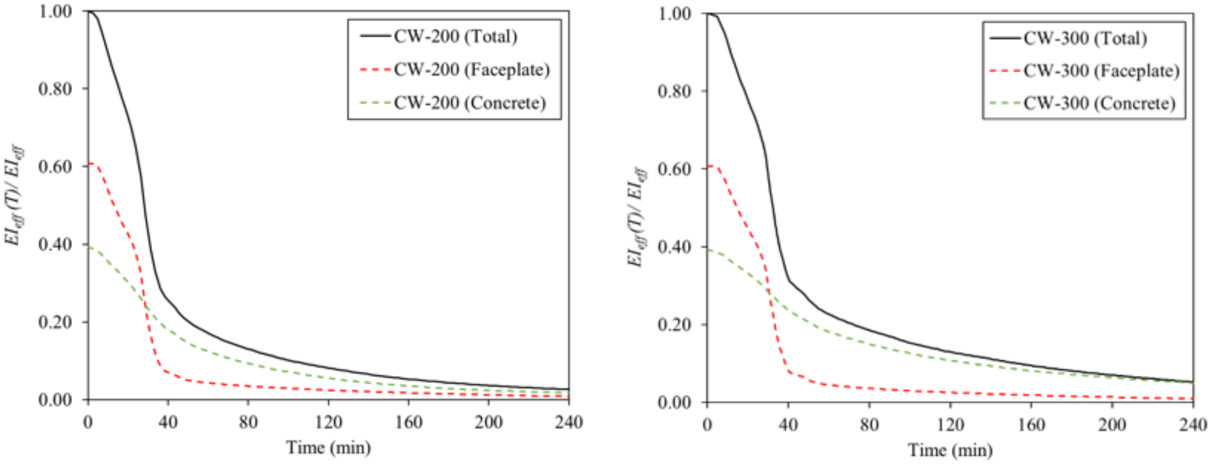

(a) CW-200

(b) CW-300

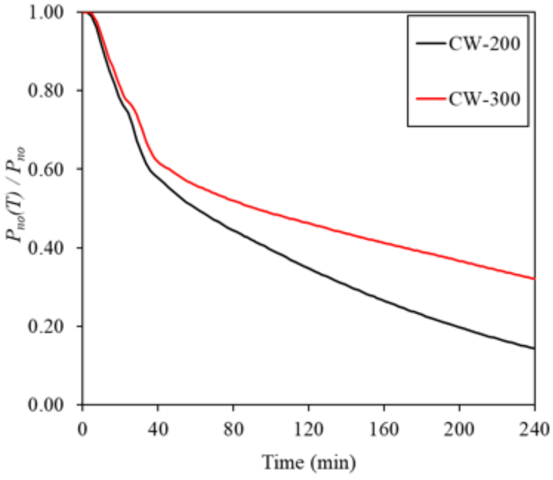

(c) Composite section compressive strength

Fig. 3-18. The reduction of effective stiffness of composite section at elevated temperatures (a, b). The Reduction of nominal axial compressive strength (zero height) at elevated temperatures (c)

All the parameters were calculated based on the temperature of elements at the failure time for the studied cases in the parametric study. The determined axial compression strength of walls $P_n(T)$, was normalized to $P_{no}(T)$. The normalized axial strength loads were plotted against $P_{no}(T)/P_e(T)$ ratios. In Fig. 3-19, $P_n(T)/P_{no}(T)$ ratios against the $P_{no}(T)/P_e(T)$ ratios are plotted for all studied cases. Two equations were fitted to the data points obtained using FE analysis (parametric study). In Fig. 3-19, the proposed strength design equations are compared with FE analysis data points. Eq. 3-5 was defined as the lower bound which passes below all the data points. However, for Eq. 3-4 the average of the data points was considered in the curve fitting process. Therefore, the axial compressive strength of C-PSWs/CF at elevated temperatures can be predicted conservatively by using Eq. 3-5.

It should be noted that the points for walls (with a thickness of 200 mm) were at the top of the rest of the points. 200 mm thick walls are thinner than the practical walls thickness range. Therefore, during the curve-fitting procedure points resulted from 200 mm thick walls were not included. Hence, the proposed equations can conservatively estimate the nominal compressive strength of 200 mm thick walls at elevated temperatures [$P_n(T)$].

The variation of the temperatures along the width of a wall is negligible. Since the temperature of the elements is uniform through the height and width of walls, 1D thermal analysis (through wall thickness) can be performed using 1D heat transfer equations or the developed fiber tool in the current study to determine the temperature profile through the wall thickness. Hence, a 1-D heat transfer analysis can be conducted to calculate the temperatures through the wall thickness at the required fire resistance rating. Accordingly, $P_{no}(T)$ and $P_e(T)$ can be specified based on the determined through-thickness temperatures. Finally, the axial compressive capacity of a wall at the selected fire resistance rating can be computed.

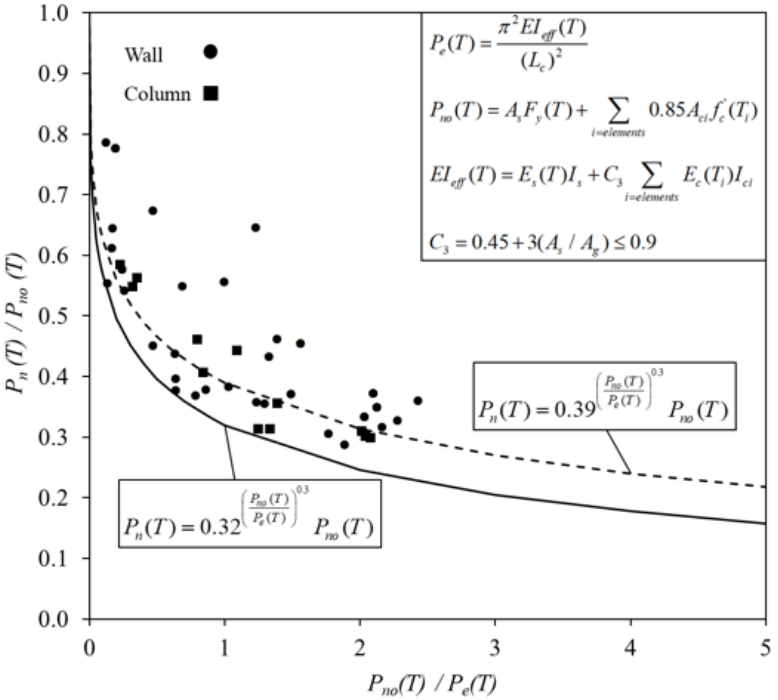

Fig. 3-19. Proposed capacity design equations comparison with FEA results

3.5. Proposed Fire Resistance Rating Equation

In addition to an equation for capacity, this research also sought out to develop equations to calculate the fire resistance rating (FRR), as a unit of time, for C-PSW/CF systems. The process to develop this equation, including assumptions made and limits of its use, are discussed herein. The development of the equation is discussed in several steps as follows.

(i) Estimate $P_n(T)$ and FRR

The axial capacity of walls at elevated temperatures at specific time intervals for a standard fire curve formed the basis for developing the fire resistance equation. The temperature profiles through wall thickness were obtained through thermal FE analysis as discussed in section 3.3.1. Eq. (3-5) was used to calculate the axial capacity of walls under fire loading [$P_n(T)$] at 30 min intervals after the beginning of a fire event. The time instants associated with calculated $P_n(T)$ was considered as the fire resistance rating (R) of the wall. For example, if after one hour a wall had an axial capacity equal to P, it was assumed that the wall has a fire resistance rating of 1 hour under an axial load of P. Therefore, the amount of applied load (P_u) was assumed equal to $P_n(T)$, in next steps of the FRR equation development.

Calculated $P_n(T)$ values were normalized to nominal compressive strength at ambient temperatures (P_n). P_n values were calculated as per section I2-2 of AISC 360-16 (AISC, 2016). P_{no}, EI_{eff} and P_e at ambient temperature can be computed using Eq. (3-10) to Eq. (3-13). The estimated FRR versus load ratio ($P_n(T)/P_n$) for walls with a wall slenderness ratio of 20 is shown in Fig. 3-20.

$$P_{no} = A_s F_y + 0.85 A_c f_c' \tag{3-10}$$

$$EI_{eff} = E_s I_s + C_3 E_c I_c \tag{3-11}$$

$$C_3 = 0.45 + 3(A_s / A_g) \leq 0.9 \tag{3-12}$$

$$P_e = \frac{\pi^2 EI_{eff}}{(L_c)^2} \tag{3-13}$$

$$P_n = 0.658^{\frac{P_{no}}{P_e}} P_{no} \tag{3-14}$$

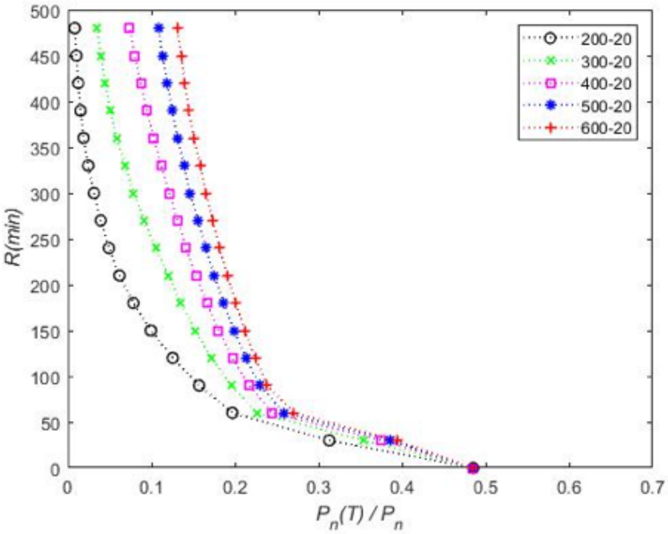

Fig. 3-20. Calculated fire resistance rating versus applied load ratios for C-PSW/CFs with various wall thicknesses and wall slenderness ratio of 20

(ii) Normalize to the wall thickness

The best exponential fit trendlines (FRR versus load ratio) were obtained for walls with a range of 200 to 600 mm, as shown in Fig. 3-21. The trendlines had a general format as Eq. (3-15). The calculated constant (α) for different wall thicknesses are compared in Fig. 3-22(a). The calculated constants were normalized to the 200 mm thick wall's constant. The obtained trendline's equation between "α" and wall thickness ratio (*A*) was modified to Eq. (3-16) for simplification.

$$R = \alpha \left[\exp\left(-12 \frac{P_u}{P_n} \right) \right] \tag{3-15}$$

$$\alpha = \frac{1.9A - 1}{60\,\mathrm{min}} \tag{3-16}$$

$$A = \frac{t_w(mm)}{200mm} \tag{3-17}$$

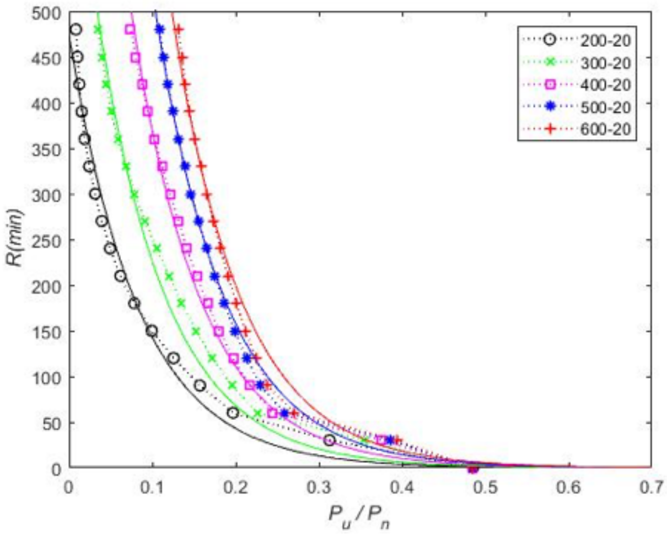

Fig. 3-21. Fitted curves for calculated fire ratings of C-PSW/CFs against applied load ratio.

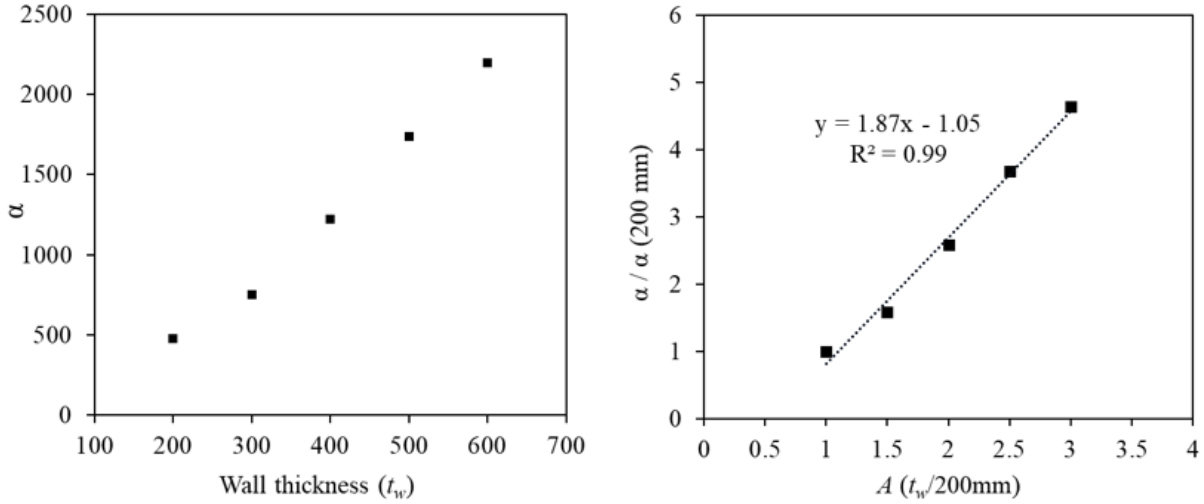

(a)

(b)

Fig. 3-22. The relation of the wall thickness and the constant (α) in Eq. (3-15)

(iii) Normalize to wall slenderness ratio

The estimated FRRs were divided into constant α ($R_{normalized}$ = FRR/ α). The normalized FRR ($R_{normalized}$) versus load ratio is plotted in Fig. 3-23 for. The best fit power trendlines were obtained for walls with a wall slenderness range of 5 to 20. The trendline's equation had a general format as Eq. 3-22. The obtained constants (C) for different wall slenderness ratios are plotted in Fig. 3-24. Constant C can be calculated using Eq. (3-19).

$$R_{normalized} = -18.5\left(\frac{P_u}{P_n}\right)^C + 15 \tag{3-18}$$

$$C = 0.24 - \frac{H/t_w}{230} \tag{3-19}$$

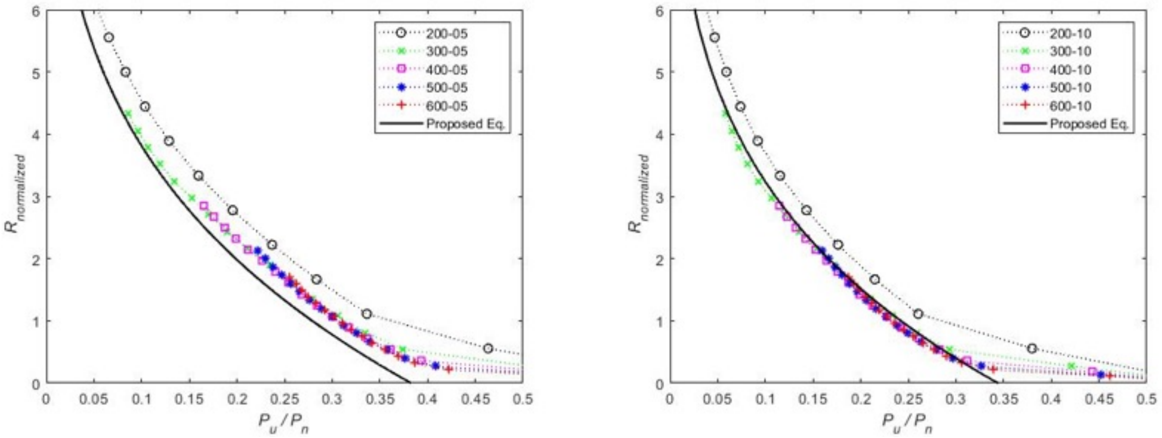

(a) Wall slenderness ratio (H/t_w) = 5

(b) Wall slenderness ratio (H/t_w) = 10

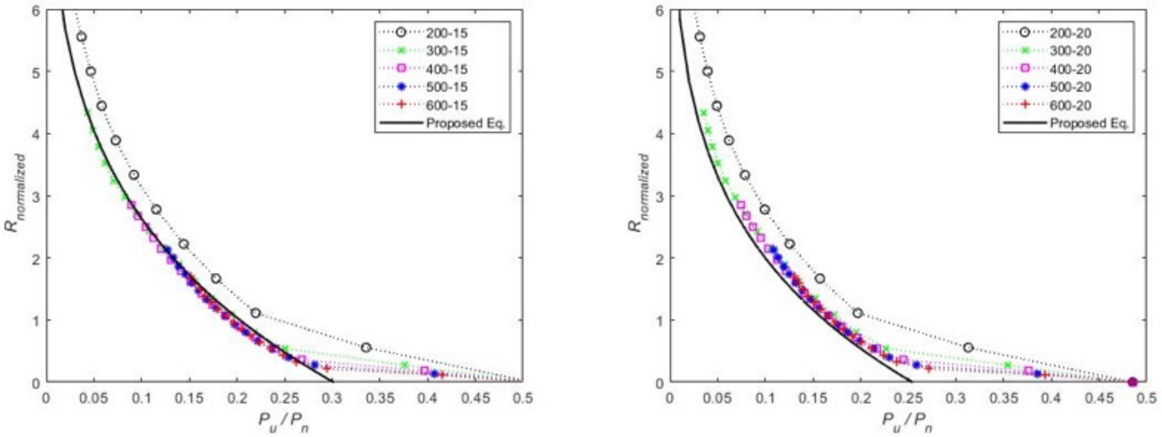

(c) Wall slenderness ratio (H/t_w) = 15

(d) Wall slenderness ratio (H/t_w) = 20

Fig. 3-23. The fitted curve for various wall slenderness ratios (Power format)

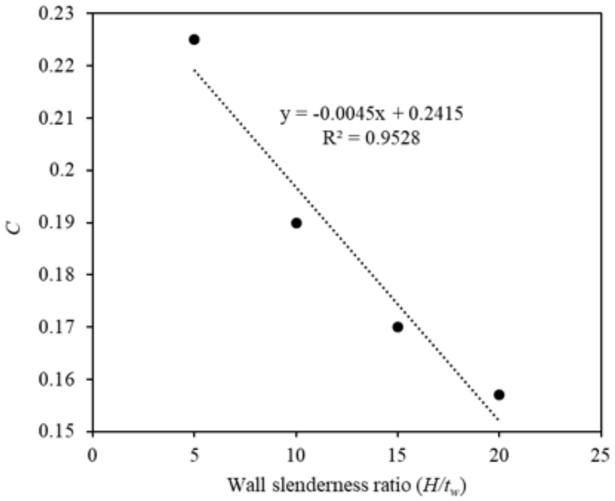

Fig. 3-24. The relation between constant *C* and the wall slenderness ratio

(iv) Substitute the constants equations

The obtained relations for constants α and *C* were substituted into Eq. 3-18. The fire resistance rating of C-PSW/CF can be calculated using Eq. (3-20). The equation is a function of the ratio of applied load to the nominal compressive strength at ambient temperature ($P_u/P_n \leq 20$), wall slenderness ratio (H/t_w) and wall thickness (t_w). The estimated FRR by Eq. (3-20) is compared with the FRR predicted by FE analysis in Fig. 3-25. There is a reasonable comparison between the analytically predicted and the estimated response.

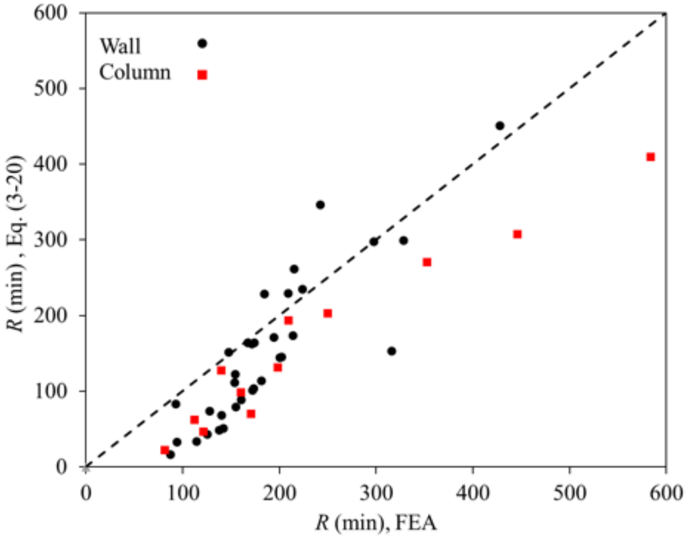

Fig. 3-25. Comparison of fire estimated (Eq. 3-20) and predicted (FEA) fire resistance ratings

$$R = \left[-18.5 \left(\frac{P_u}{P_n} \right)^{\left(0.24 - \frac{H/t_w}{230}\right)} + 15 \right] \left(\frac{1.9 t_w}{200} - 1 \right) \qquad (3\text{-}20)$$

Where

R = Fire rating (hours)

t_w = Wall thickness (mm)

H/t_w = Wall slenderness ratio

P_u = Applied axial load (kN)

P_n = $0.658^{\frac{P_{no}}{P_e}} P_{no}$ (Axial compressive capacity as per AISC 360-16 section I2)

P_{no} = $A_s F_y + 0.85 A_c f_c^{'}$

EI_{eff} = $E_s I_s + C_3 E_c I_c$

C_3 = $0.45 + 3(A_s / A_g) \leq 0.9$

P_e = $\frac{\pi^2 EI_{eff}}{(L_c)^2}$

3.6. Summary and Conclusions

The impetus of the finite element modeling and subsequent analytical studies was to gain insight into the fundamental behavior of C-PSW/CF systems at elevated temperatures. This chapter presented the development of detailed FE models to numerically investigate the behavior of C-PSW/CFs under gravity and fire loading. Further, practical recommendations in the form of design equations were developed based on the studies.

Developed numerical models have been benchmarked with existing experimental data. Due to potential variability associated with experimental data, the conservative failure time and surface temperature estimates from the finite element models were the preferred option to determine the fire resistance of C-PSW/CFs. The surface temperature at the failure of finite element models matches closely with the surface temperatures of specimens at failure (in comparison to time to failure). Therefore, it is recommended to use the surface temperature at failure as a metric to determine the fire resistance of C-PSW/CFs.

The benchmarked FE models were used to conduct parametric studies to evaluate the effect of different parameters on fire resistance of C-PSW/CFs. The temperature of the faceplate (steel plate) increases rapidly due to the direct exposure to fire. Due to the rapid degradation of the mechanical properties of steel plates, most of the axial load transfers to the concrete core. The fire rating of C-PSW/CFs improves with an increase in wall thickness. Concrete has a low thermal conductivity therefore the temperature in the middle of the concrete core increases at a lower rate in thicker walls. The cooler part of the concrete core helps the axial capacity of C-PSW/CFs walls during a fire event.

The analytical parametric study showed that the fire resistance rating of C-PSW/CFs decreases with an increase in the wall slenderness and load ratio. The fire resistance rating of walls reduced by about 55% by increasing the wall slenderness ratio from 5 to 20. The fire resistance rating of 300 mm thick wall reduced by about 160 min (~3 hrs.) with increase in wall slenderness ratio from 5 to 20. Tie bar spacing and steel plate reinforcement ratio had a minor influence on the fire resistance rating of walls. Walls with higher steel plate slenderness ratio (larger tie/stud spacing) had a lower fire resistance rating. The fire resistance rating of 300 mm thick wall with a plate slenderness ratio of 25 reduced by about 7% by increasing the plate slenderness to 50. It is recommended to limit the plate slenderness ratio to $1.2\sqrt{(E/F_y)}$. Due to the higher load level in walls with higher concrete strength (but with equal load ratio), the fire rating of walls with higher concrete strength was lower than geometrically equivalent sections with lower concrete strength.

In buildings the width of the walls can be significantly higher than the wall thickness, the walls would be exposed to two-sided or one-sided fire scenarios. An interior unit width strip of C-PSW/CF representing the whole wall section was studied under fire loading. The unit width strips had a width equal to tie bar spacing. By comparing the normalized parameters of unit width strip and wall models it can be seen that both methods are consistent (Fig. 3-19). 1D heat transfer analysis can be performed to determine the temperature through the wall thickness. The wall cross section properties [$P_e(T)$, $P_{no}(T)$] can be calculated at the time instant equal to the required fire resistance rating to estimate the axial capacity of the wall. The estimated axial capacity can be compared to the applied axial load to the wall. The unit strip method can be used to estimate capacity and fire resistance rating of C-PSWs/CF, conservatively.

An equation to estimate the fire resistance rating of C-PSW/CF was proposed in section 3.5. Based on the proposed lower bound strength equation (Eq. 3-5), the critical axial capacity of walls was calculated. ISO 834 standard time-temperature curve was applied. Wall thickness (t_w), wall slenderness ratio (story height/wall thickness) and load ratio (P_u/P_n) are the input parameters, where P_u is the applied axial load and P_n is the axial capacity as per AISC 360-16, section I2. This equation applies to unprotected walls with a maximum wall slenderness ratio of 20, load ratio (P_u/P_n) of 0.2, plate slenderness ratio of $1.2\sqrt{E/F_y}$ and tie spacing to wall thickness ratio of 1.

Further studies on the performance of C-PSW/CF were conducted using the fiber tool as discussed in Chapter 4 of the current report. The response of the walls under single-sided fire scenario is compared to results two-sided fire exposure. Also, the proposed strength design equations were validated by the developed tool.

Chapter 4. Analytical Studies (Fiber Method Analysis)

4.1. General

FE analysis provided detailed results on the response of C-PSW/CF under fire loading. However, 3D finite-element models are complex and require extensive computational time and effort. As a result, it is difficult to use them in a design scenario. 2D fiber-based models have the advantage of being less resource-intensive, thus requiring reduced computational time and enabling detailed parametric studies. However, the previously developed 2D model (discussed in section 1.1) has a very limited applicability (only applicable to square CFTs with uniform faceplate thickness and all-sided fire) and cannot be effectively used for parametric studies. This fiber model was used as the starting point for the current study, and it was built upon and modified in to a more generic tool having a wider applicability.

A 2D fiber-based analysis tool was developed to carry out the analyses, which was validated and benchmarked using experimental as well as 3D finite-element data. A user interface was also developed to allow easy interaction. This development and validation of the fiber model is presented in detail in 4.2. This numerical tool was then used to conduct parametric studies on CFTs, which included studying the effect of fire protection strategies. The results of these studies were combined into a design equation to predict the capacity and fire rating for CFTs. The details of the parametric studies, their results and proposed equations are discussed in 4.3. Next, the fiber model was used to model C-PSW/CFs using the two approaches (C-PSW/CF wall sections and unit width walls). The obtained results were compared to finite-element models and experimental data. The results from the fiber model were also used to validate the design equations proposed for C-PSW/CFs. These analyses and results are covered in 4.4.

4.2. 2D Numerical Model Development and Benchmarking

A 2D fiber-based numerical model to simulate fire loading of composite axial members was developed. The overarching goal in developing this model was to provide a time efficient and accurate tool that could be used for parametric studies as well as design of composite members under fire loading. MATLAB, a general-purpose computing software, was used as a platform to develop the tool. A user-interface was also developed and implemented to allow more straightforward interaction with the model and conveniently view the results. The following sections presents the development, validation and benchmarking of the fiber model.

4.2.1. Model Algorithm Steps

The basic functionality of this tool was taken from the fiber model developed by Hong (2007) and Hong and Varma (2009). However, the tool was designed to be applicable to a wide range of scenarios, which includes CFTs, composite walls (C-PSW/CFs) and symmetric and non-symmetric heating. Validation of the model was done using experimental and 3D finite-element data. The working, development and validation of the model is presented in this section.

The 2D fiber-model is a fundamental section-based model which involves analyzing a section of the column or wall, typically at its mid-span. For the purpose of analysis, the cross-section is divided into discrete fibers consisting of nodes and elements. A representation on of the section discretized into fibers is shown in Fig. 4-1. The analysis is an incremental analysis wherein the column is analyzed at its present state at each time step and the analysis results used to update the column state for the next time step. At each time step, the procedure can be broadly divided into 3 steps, which are:

(i) 2D Heat Transfer Analysis

(ii) Section Moment-Curvature Analysis

(iii) Non-linear Column Buckling Analysis

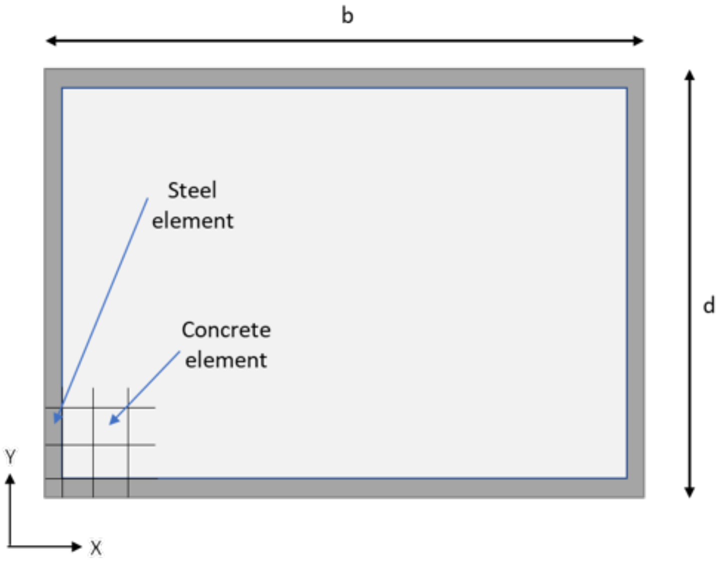

Fig. 4-1. Representative 2D section with steel and concrete fiber discretization

The details of each step, its assumption and simplifications are outlined below:

(i) 2D Heat Transfer Analysis:

The first step in the fiber bases approach is a 2D heat transfer analysis wherein the temperature of each node and element of the section is calculated based on its thermal properties. Heat transfer always occurs from the object at the higher temperature to the object at the lower temperature. Heat can be transferred in three different ways: conduction, convection, and radiation. Conduction is the transmission of heat between two solid objects that are in contact. Convection is the transmission of heat between a solid object and moving fluid that are in contact with each other. Radiation is the heat transfer between any two objects (solid, fluid, or gas) in the form of electromagnetic waves. These three modes of heat transfer are represented in Fig. 4-2. The heat balance equations between objects can be setup by considering all the contributions of energy. These equations in their finite difference form can be solved numerically.

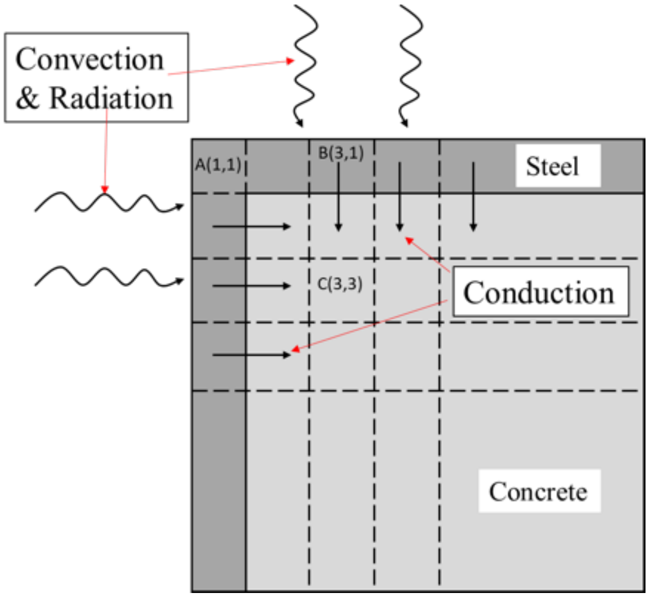

Fig. 4-2. Representation if the three modes of heat transfer: convection, conduction & radiation

The first step of this heat transfer analysis is defining the surface temperatures, which are assumed constant along the length of the column. Thus, the calculated section temperatures are true for the entire column. For the developed model, multiple time-temperature curves are programmed into the model to specify the surface temperature, thus providing flexibility of analysis. Also, the user can choose to directly specify the surface temperature or specify a gas temperature and calculate the surface temperature considering convection and radiation. The modelling of thermal conductivity, specific heat and other equations related to heat transfer are covered in Hong et al. (2009) and are not repeated here. A layer of fire protection can also be modeled outside the steel surface. A schematic flowchart of the algorithm is shown in Fig. 4-3. If modeled, the thermal properties of fire protection are assumed to remain constant with temperature.

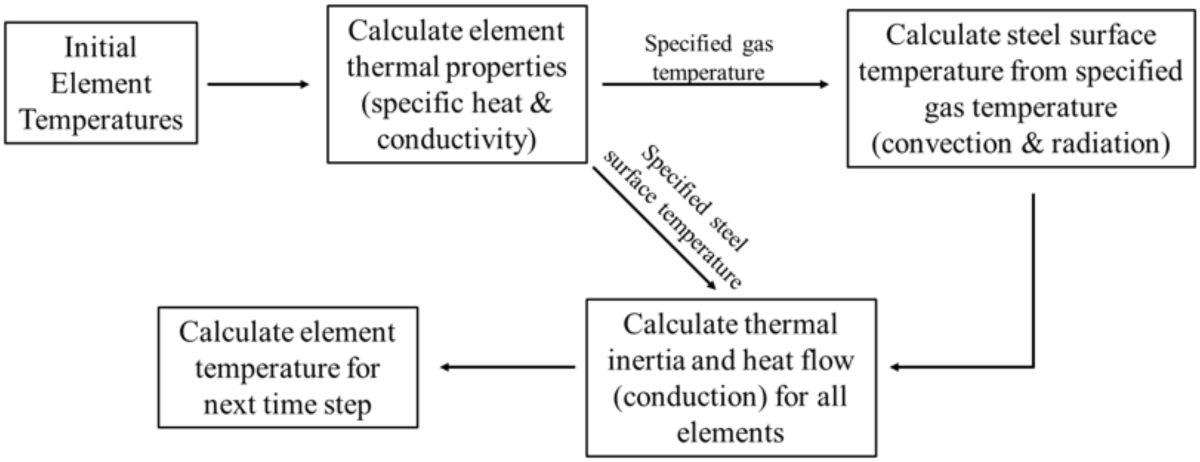

Fig. 4-3. Schematic flowchart of algorithm for 2D heat transfer

There are two heat-transfer algorithms, one of which is called depending on the model being run. The symmetric heat-transfer algorithm considers all four sides of the column to be heated, thus heat transfer within the section is doubly symmetric and there is no heat loss from the member to the air. The non-symmetric heat-transfer algorithm is called for one or three-sided heating. In this case, heat is absorbed by the column from the heated surfaces and the unheated surfaces lose heat to the atmosphere. The extent of heat loss can be controlled by adjusting the convection coefficient, which is a user-defined parameter. The element temperatures obtained are used to determine material properties as outlined in the next steps.

(ii) Section Moment-Curvature Analysis:

The next step of the analysis involves generating a moment-curvature plot of the section at its current temperature state and axial load level. In this step, the curvature is started from 0 m^{-1} and increased in small increments to 0.35 m^{-1}. The section moment for each curvature value is calculated using an iterative process. An initial centroidal strain is assumed and its value adjusted based on section equilibrium (i.e. summation of element forces equals the applied axial load). Element total strains are calculated from curvature and centroidal strain based on the plane sections assumption (plane sections remain plane). Thermal strain is also calculated for each fiber from its coefficient of thermal expansion and temperature change. The mechanical strains are then obtained by subtracting thermal strain from total strain, which are provided as input to the material stress-strain-temperature (σ-ε-T) models to get stresses in the elements. Once force equilibrium is established, net moment of the section is calculated by summing up the moment contribution of each element.

Multiple stress-strain-temperature material models are programmed in the model to allow flexibility of analysis and allow the comparison of different proposed models. In all these models, concrete strength in tension is assumed zero and strain hardening of steel in tension is also ignored. Different material models and their combinations are discussed further in this chapter. Further detailed steps and equations to obtain strains and stresses and moment are detailed in Hong (2007) and Hong et al. (2009). The obtained moment-curvature plot is then used in column buckling analysis as outlined in the next step. A pictorial flowchart showing the algorithm to get moment-curvature curves is given in Fig. 4-4.

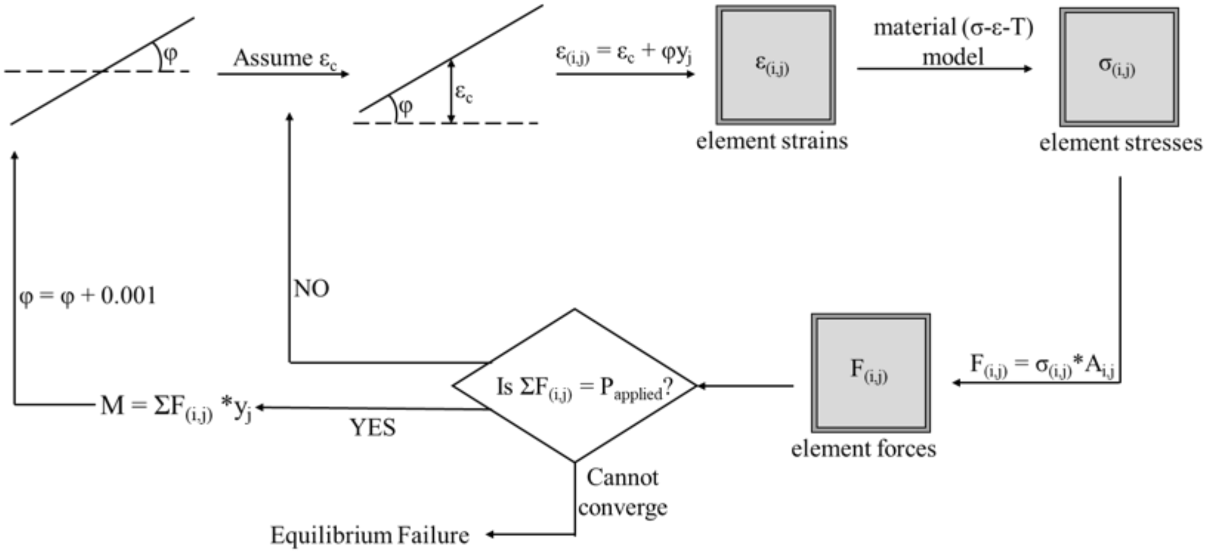

Fig. 4-4. Pictorial flowchart for calculating section moment-curvature response

(iii) Non-linear Column Buckling Analysis:

The above calculated station moments are used to get the curvatures using the moment-curvature plot obtained in Step 2. An updated deflected shape (lateral displacement) is then found by numerical double integration of these curvatures ($M=EIv''=EI\phi$). This updated shape is compared to the assumed shape at the beginning of the time step and iterations are carried out till convergence. Detailed procedure and equations for this step are given in Hong (2007) Hong et al. (2009). The column is said to have failed in global inelastic buckling when maximum station moment along the column length (typically at mid-span) exceeds the maximum moment that can be developed in the section (maximum moment in M-ϕ curve).

The model checks for two modes of failure for the column, one of which (global buckling failure) is mentioned above. Apart from this, the column is said to have failed in yielding or crushing if axial force equilibrium cannot be established at any step while generating the moment-curvature plot. This failure mode is checked in Step 2 of the above-mentioned procedure. It implies strength degradation of steel and concrete (due to elevated temperatures) to the extent that the member cannot support the axial load. This failure mode governs for short columns whereas longer columns typically fail in global buckling. A pictorial flowchart of the overall inelastic buckling algorithm is given in Fig. 4-5.

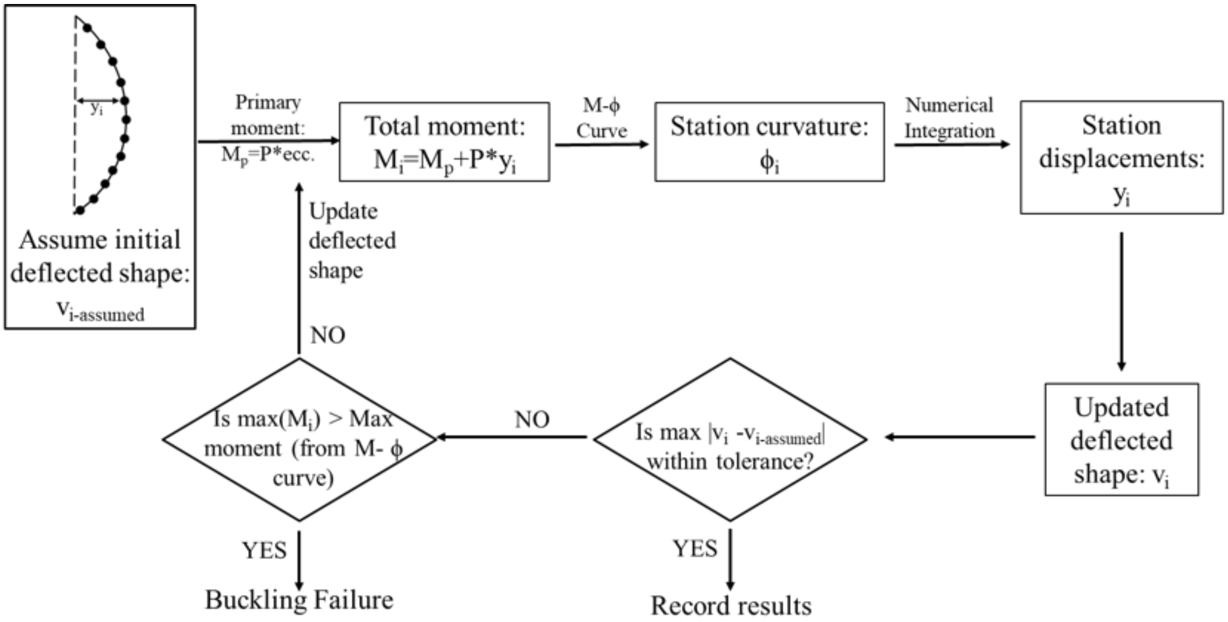

Fig. 4-5. Pictorial flow chart for predicting the overall behavior of a composite axial member

4.2.2. Material Stress-Strain-Temperature Models

Material stress-strain relationships at elevated temperatures are complex and difficult to model exactly. However, several researchers have developed simplified stress-strain-temperature models for steel and concrete based on experimental studies. Several of the relevant material models used in this study are discussed here.

4.2.2.1. Lie's stress-strain model for concrete (1992)

Lie (1992) developed a mathematical stress-strain relationship for steel and confined concrete at elevated temperatures. Lie's expression assumes that concrete compressive strength remains constant from 20°C to 400°C but the elastic modulus falls to about 40% or 50% of the original value. After 400°C, concrete compressive strength and elastic modulus both decrease. This model ignores any strength of concrete in tension. The equations for the material model are given in Lie (1992) and the stress-strain curves at various temperatures are shown in Fig. 4-1(a).

4.2.2.2. Poh's stress-strain model for steel (2001)

Poh (2001) proposed a mathematical relationship for the stress-strain-temperature ($\sigma-\varepsilon$-T) behavior of structural steel. Poh (2001) based his equations on experimental results of stress-strain ($\sigma-\varepsilon$) responses of conventional steel at elevated temperatures. The experimental background and development of equations is covered in Poh (2001) and Fig. 4-7 presents the stress-strain curves at different temperatures.

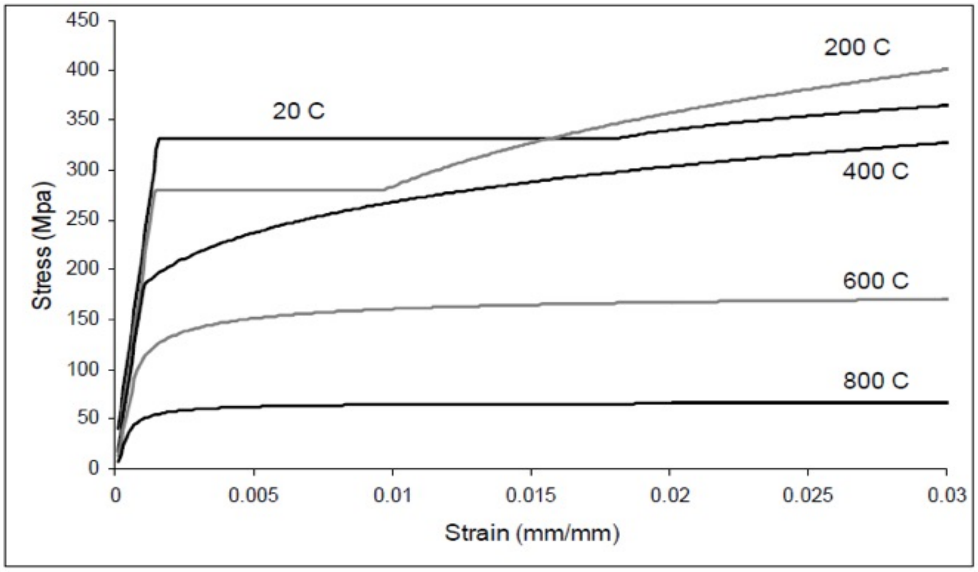

Fig. 4-6. Stress-strain curves for 330 MPa steel developed using Poh's model. Ref: Hong (2007)

4.2.2.3. Lie's stress-strain model for steel (1995)

Lie and Irwin (1995) proposed a mathematical stress-strain relationship for steel at elevated temperatures based on their experimental results. Their model for steel is symmetric in tension and compression, while softening and strength reduction at elevated temperature is accounted for by reducing Young's modulus and yield strength with temperature. The equations for the material model are given in Lie (1992) and the stress-strain curves at various temperatures are shown in Fig. 4-6.

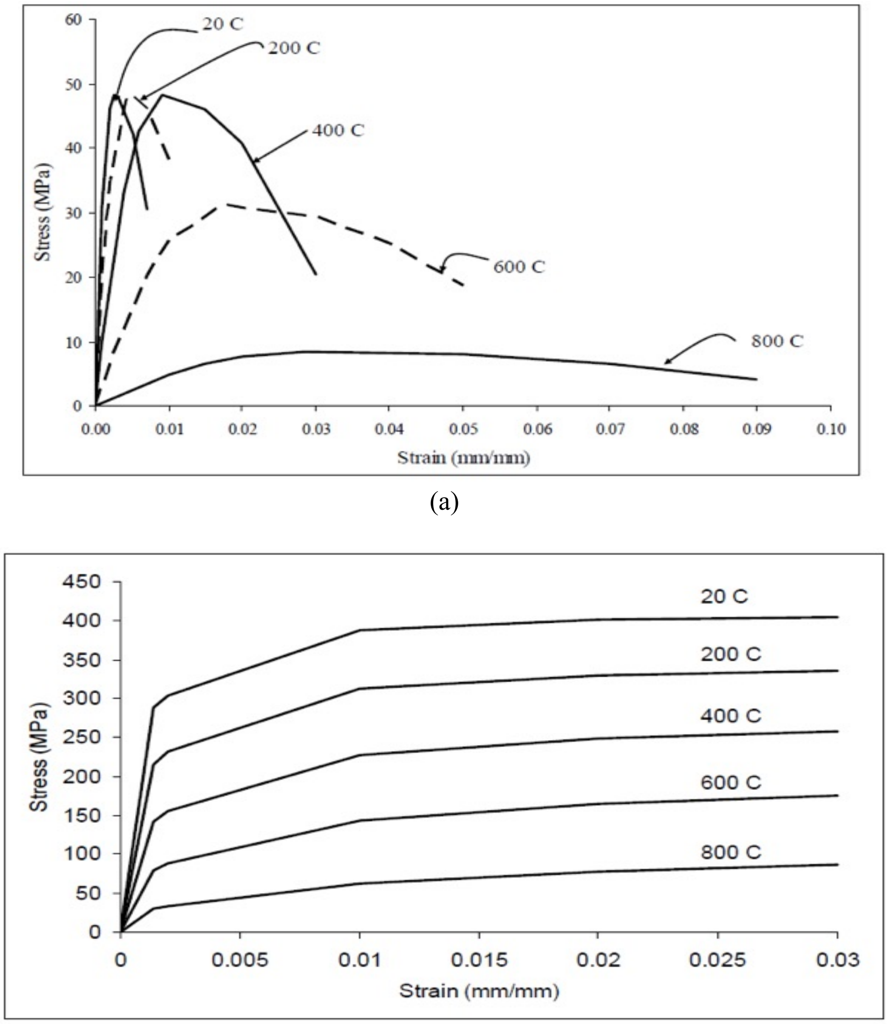

(a)

(b)

Fig. 4-7. Concrete (a) and steel (b) stress-strain curves at elevated temperatures developed by Lie. (Hong, 2007)

4.2.2.4. Eurocode proposed stress-strain curves (1994)

Eurocode 1994-1-2 proposes stress-strain curves for steel and concrete at elevated temperatures. These curves have also been programmed in the fiber model. Eurocode assumes steel behavior to be symmetric in tension and compression (i.e. ignores local buckling in compression and strain hardening in tension), assumes zero strength of concrete in tension and neglects the effect of concrete confinement (i.e. assumes conservative post-peak behavior). Detailed equations and discussion on the curves can be found in Section 3 of Eurocode 1994-1-2 (Eurocode 2005). Fig. 4-8 shows the stress-strain plots for steel and concrete at elevated temperatures.

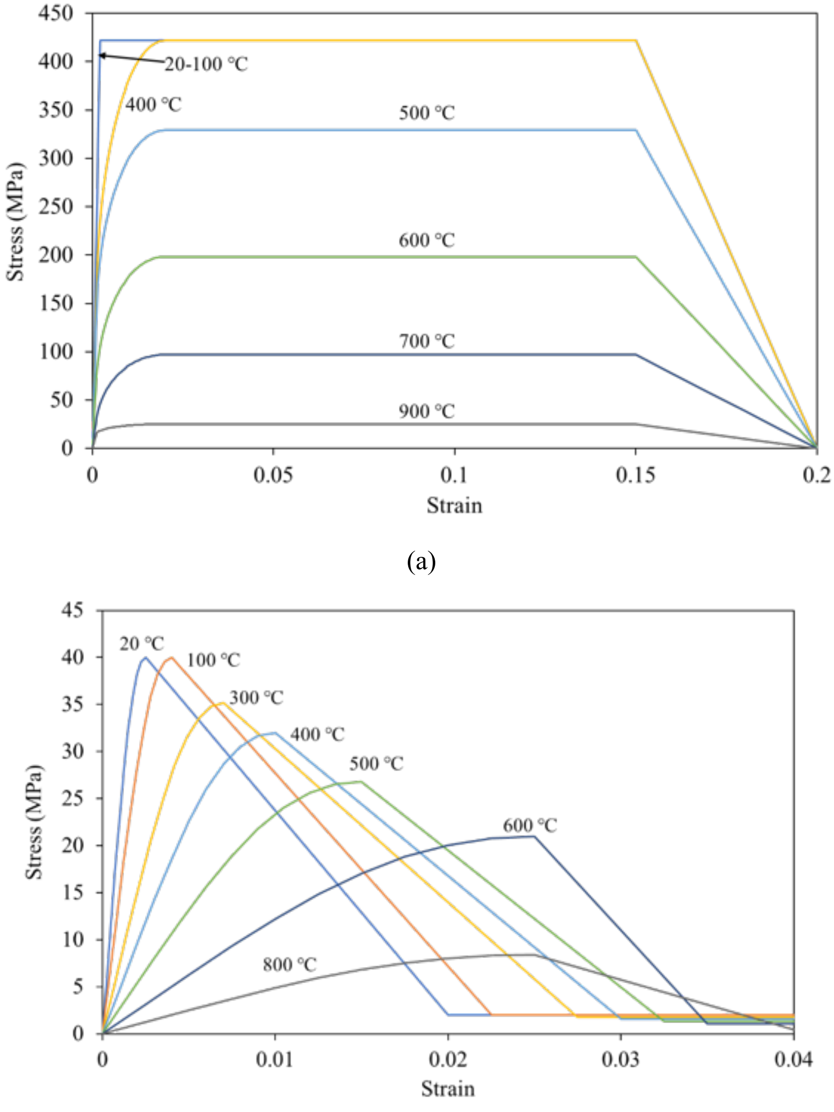

(a)

(b)

Fig. 4-8. Eurocode stress-strain-temperature curves for (a) 420 MPa steel and (b) 40 MPa concrete

All the material models described to this point are symmetric in tension and compression. Therefore, they do not account for local buckling and in the case of C-PSW/CF systems would not account for this behavior in the outer steel plates and the associated strength reduction. A material model accounting for local buckling of the outer steel plates is desired especially in more slender sections where this behavior is more predominant. Lai et al. (2016) developed an effective stress-strain model for steel that considered strength degradation due to local buckling in compression and strain hardening in tension. This model was developed for steel at ambient temperatures and validated using experimental data. Further details of its development and validation are given in Lai et al. (2016). The above-mentioned material model was modified to account for temperature effects, which is explained in the next chapter, and was compared with other existing steel material models.

Material stress-strain-temperature models form a crucial part of the 2D fiber-based analysis tool and have a significant effect on the behavior of the member as discussed further in this thesis. Additionally, material behavior at elevated temperatures is complicated as discussed previously and thus the material models are at best an approximation of true material behavior. Some of the relevant material models developed by researchers have been discussed in previous sections and have been programmed into the fiber model. The user can select the model to be run, which allows for flexibility of analysis and parametric studies.

4.2.2.5. Modification of Lai et al (2016) model for elevated temperature

Most of the material models utilized in the fiber method are taken directly from literature. However, the effective stress-strain model for steel developed by Lai et al (2016) was modified by the authors to work for elevated temperatures. This modification and different material model combinations available to the user are discussed herein. Lai et al. (2016) developed effective stress-strain curves for steel for non-compact and slender CFTs which accounted for local buckling of steel faceplates in compression and strain hardening in tension. The development and validation of these equations is given in detail in Lai et al. (2016). Fig. 4-9 shows the stress-strain curves for compact, non-compact and slender sections at ambient temperature.

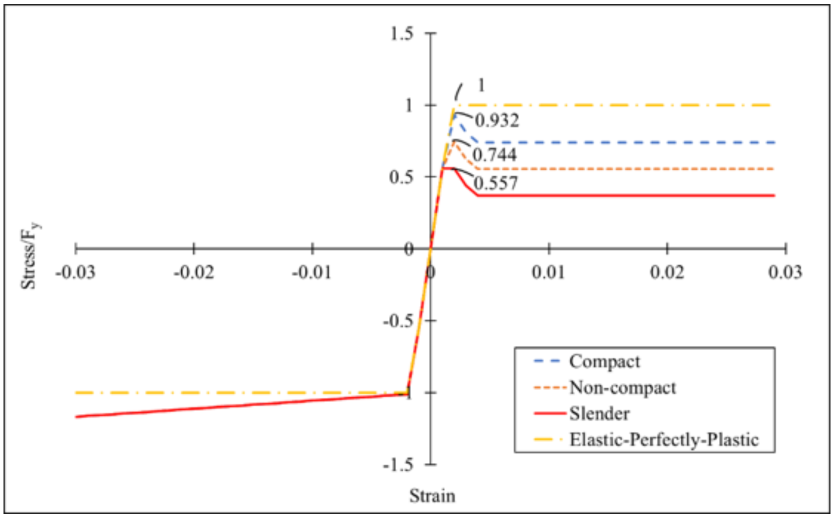

Fig. 4-9. Effective stress-strain curves for compact (λ=50), non-compact (λ=67) and slender (λ=100) sections for steel (F_y=358 MPa) at ambient temperature

As these equations were developed for ambient temperatures, they were modified by the authors to work for elevated temperatures. The modifications involved updating the stiffness, yield strength, and post-buckling strength in compression as a function of temperature. The equations for temperature dependence of yield strength (σ_y) and Young's modulus (E_s) were taken as recommended by Poh (2001). The stress-strain-temperature curves obtained using these equations are given in Fig. 4-10. The relative behavior of different combination of material models was explored and is covered in the sub-section discussing the benchmarking of the fiber model.

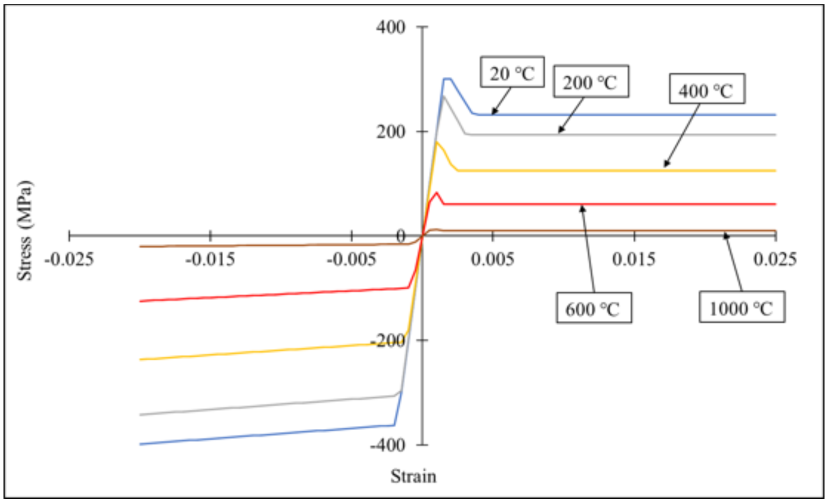

Fig. 4-10. Effective stress-strain curves for 330 MPa steel at elevated temperatures

4.2.3. Fiber-Model Validation and Benchmarking

The fiber model, which was modified for this research, developed by Hong et al. (2009) was extensively validated at the time of its development. The validation process involved comparison with experimental and finite-element data. The detailed validation of the model is covered in Hong (2007) and Hong et al. (2009) and a representative comparison graph generated by Hong et al (2009) is given in Fig. 4-11. The figure shows the temperature vs time and axial displacement vs time for a square CFT specimen, with plots obtained from experiment, 3D FEM model and the fiber model plotted together. It can be seen that the fiber model is reasonably accurate in predicting the failure time and axial displacement.

4.2.3.1. Validation and benchmarking to capacity equations

For the fiber model developed by the authors, validation was carried out at both ambient and elevated temperatures. The results obtained from the fiber-model were compared with the capacity equations given in AISC 360 Specification (Chapter-I, Eq. I2-2 to I2-13). Fig. 4-12 shows the normalized load versus axial displacement plots for compact, non-compact and slender CFT sections for conventional and effective steel models. Results obtained using conventional (elastic-perfectly-plastic) and effective (Lai et al. 2016) steel models are shown in Fig. 4-12(a) and Fig. 4-12(b), respectively. The load is normalized against the predicted column capacity per AISC 360 (Chapter I). Fiber model predicted buckling of columns close to the AISC predicted critical load. Hence the capacity predicted by the fiber model (at ambient temperature) has good agreement with the capacity estimated per AISC 360.

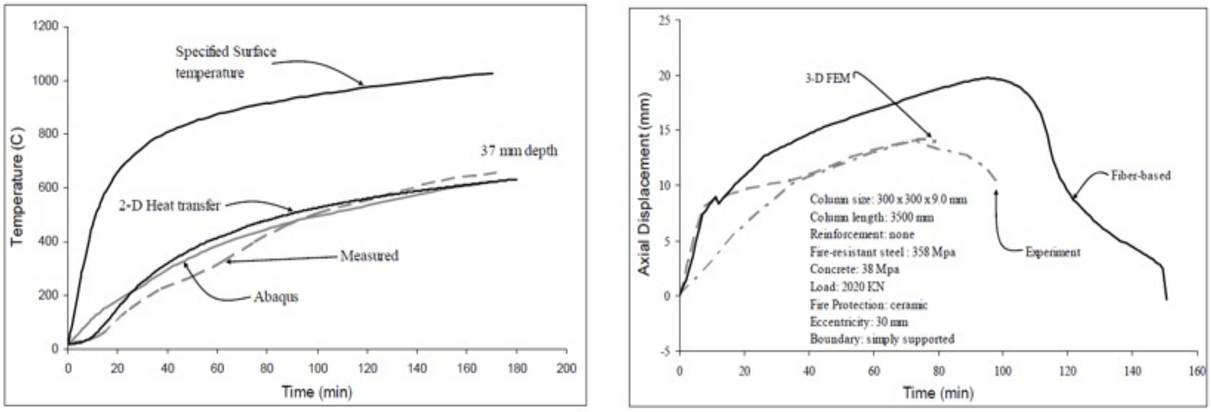

(a)

(b)

Fig. 4-11. Validation of Existing Fiber Model. Ref: Hong (2007)

The predicted capacity given in AISC 360 was used for comparison in benchmarking the developed fiber model(s) and the comparisons are shown in Fig 4-12. Comparing Fig. 4-12(a) and (b) shows that the Lai et al. 2016 effective stress-strain curves utilized compare more favorably for capacity prediction than conventional elastic-perfectly plastic for non-compact and slender sections. However, for compact sections, the effective stress-strain model seems slightly overly-conservative. This is because local buckling of steel faceplates is significant only for non-compact/slender sections. Thus, conventional (elastic-perfectly-plastic) stress-strain model gives better results for compact sections, as it does not consider local buckling. Eurocode models also do not consider local buckling and hence should be used only for compact sections.

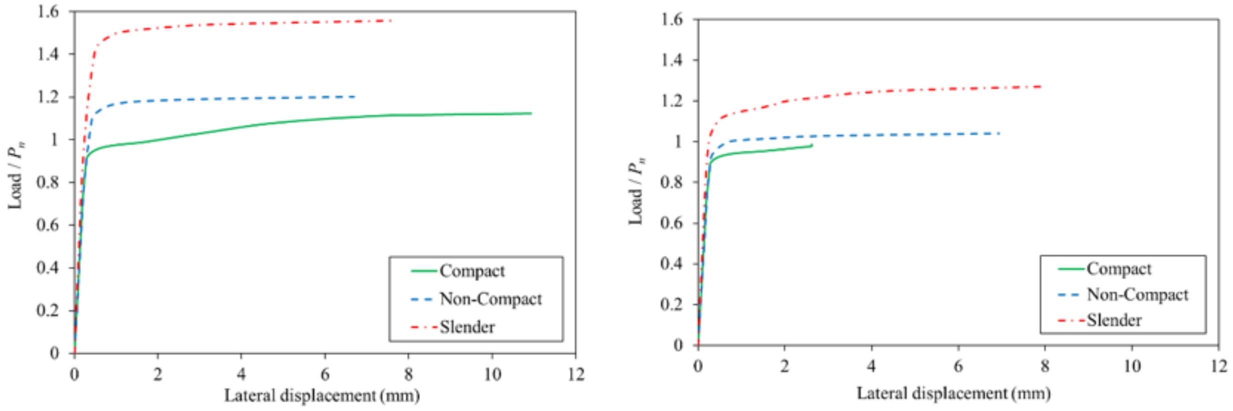

(a) (b)

Fig. 4-12. Comparison of compressive strength (load vs. displacement) for (a) conventional (elastic-perfectly-plastic) and (b) effective (Lai et al. 2016) steel models versus AISC predicted strength

4.2.3.2. Validation and benchmarking to experimental data

The fiber model was also validated against the experimental data of Lue et al. (2006). They tested a total of 30 CFT column specimens at ambient temperature with varying concrete strength. Details of all the specimens tested and the obtained results are given in Lue et al. (2006). The comparisons of experimental, fiber-model predicted and AISC Specification (2016) predicted strengths for select specimens are shown in Table 4-1.

Table 4-1. Comparison of experimental, fiber-model predicted and AISC 2016 predicted compressive strengths at ambient temperature

Specimen No.	Notation	Average experimental strength (kN)	Model predicted compressive strength (kN)	Nominal compressive strength per AISC Manual 2016 (kN)
1	C4K 4-1–4	1328.5	1075	1004.1
2	C9K 6-1–6	1722.3	1425	1323.8
3	C10K 6-1–6	1885.5	1500	1388.3
4	C12K 6-1–6	2089.8	1625	1516.2

At elevated temperature, model validation was aimed at verifying the heat transfer algorithms and material stress-strain-temperature models. The temperature profiles across the section of C-PSW/CF specimens were compared with experimental data and 3D FE results (Varma et al., 2019). This comparison was done for both symmetric and non-symmetric heating. The steel surface temperature at failure of different wall specimens as predicted by the fiber model and by 3D FE analysis was also compared (Bhardwaj et al. 2019b). Fig. 4-13(a) shows the comparison of temperature profile through the thickness of a 200 mm thick wall at two instants obtained from FE analysis and the fiber model. Fig. 4-13(b) shows the comparison of temperature variation with time for non-symmetric heating as obtained from experimental data and as predicted by the fiber model. Table 4-2 presents the failure surface temperature predicted by FEM and the fiber model for 6 wall specimens.

Table 4-2. Comparison of failure surface temperature for 6 wall specimens from FE analysis and fiber-model

Nomenclature	Height (mm)	Wall slenderness ratio (H/t_w)	FEM predicted failure surface temperature (°C)	Fiber model predicted failure surface temperature (°C)
CW-300-10-20	3000	10	1084	1171
CW-300-15-20	4500	15	1048	1100
CW-300-20-20	6000	20	1041	1033
CW-200-10-20	2000	10	1058	1073
CW-200-15-20	3000	15	1025	1000
CW-200-20-20	4000	20	968	938

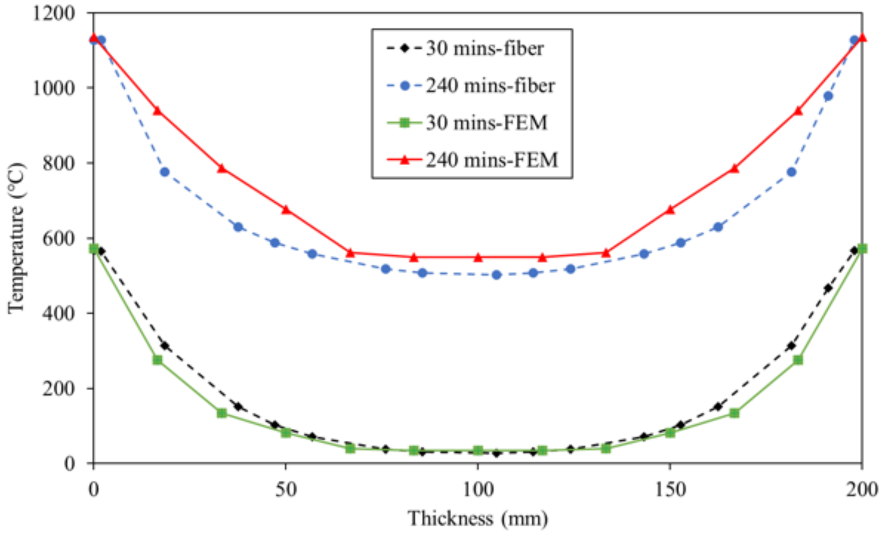

(a)

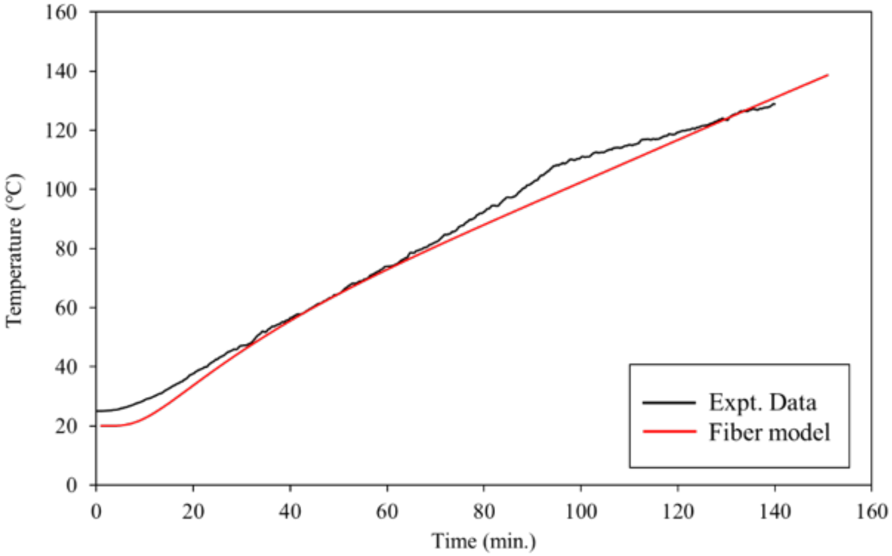

(b)

Fig. 4-13. (a) Temperature profiles across the section at various time instants; Comparison of fiber model predicted and FEM data. (b) Surface temperature vs time for 3-sided heating: comparison of experimental data and fiber model. The plot shows the temperature of a point on the un-heated surface

4.2.3.3. Comparison of material models at elevated temperatures

The effect of different material models was also considered when benchmarking the fiber model. Six different combinations of material models for steel and concrete were tested for CFTs and C-PSWs/CF. They were compared with finite-element data to study how different material models influence behavior with respect to finite-element models. The combinations tested are shown in Table 4-3 and the obtained comparisons are presented and discussed below.

Wall Specimen CW-200-10-20 was used for comparing different material models. The obtained plots for axial displacement vs. time and axial displacement vs. temperature are shown in Fig. 4-14(a) and (b). Similar plots for specimen CW-200-20-20 are shown in Fig. 4-14 (c) and (d). It is evident that the 6 material model combinations show a similar trend for both walls. The peak axial displacement is seen to be primarily dependent on the steel material model. As concrete strength in tension is ignored in all material models, it does not influence wall behavior for positive axial displacements. The concrete material model does have a significant effect on the post-peak behavior of the wall, demonstrated by a clear increase in time to failure for Lie's confined concrete model. However, the confined concrete model overestimates the wall capacity compared to FE results. Thus, the effect of confinement of concrete is not very prominent in C-PSWs. This is being concluded along with the conclusion that Eurocode model for concrete is better for CPSWs. The reason that the confined concrete model over-predicts C-PSW/CF strength (and gives less conservative results as compared to the Eurocode model) is because the effect of concrete confinement is not significant in C-PSW/CFs. It is recommended to use Eurocode defined material model for concrete for walls.

Further, a CFT column having overall dimensions 300 mm × 300 mm with steel faceplate thickness 9 mm and height equal to 3.5m was modeled. Axial load equal to 2020 kN was applied. The obtained axial displacement against time and temperature plots for the six material model combinations are shown in Fig. 4-15. Similar behavior was observed for the CFT column, with steel material model governing the peak axial displacements and the steel and concrete models influencing the time to failure. However, concrete material model has a lesser impact on CFT post-peak behavior as compared to walls. The difference in time to failure for Eurocode's concrete model and Lie's concrete model is not as significant, as observed for C-PSW/CFs. Comparing these results with experimental data for the same specimen (Hong, 2007) it is observed that Poh's steel model gives axial displacements which are closest to the experimental data. Although concrete model does not have a high impact on CFT behavior, the Eurocode concrete model shows better agreement with experimentally observed failure times.

Table 4-3. Various combinations of material models tested

Model ID	Steel model	Concrete Model
Model 1	Eurocode	Eurocode
Model 2	Eurocode	Lie Confined
Model 3	Effective σ-ε	Lie Confined
Model 4	Poh	Lie Confined
Model 5	Poh	Eurocode
Model 6	Effective σ-ε	Eurocode

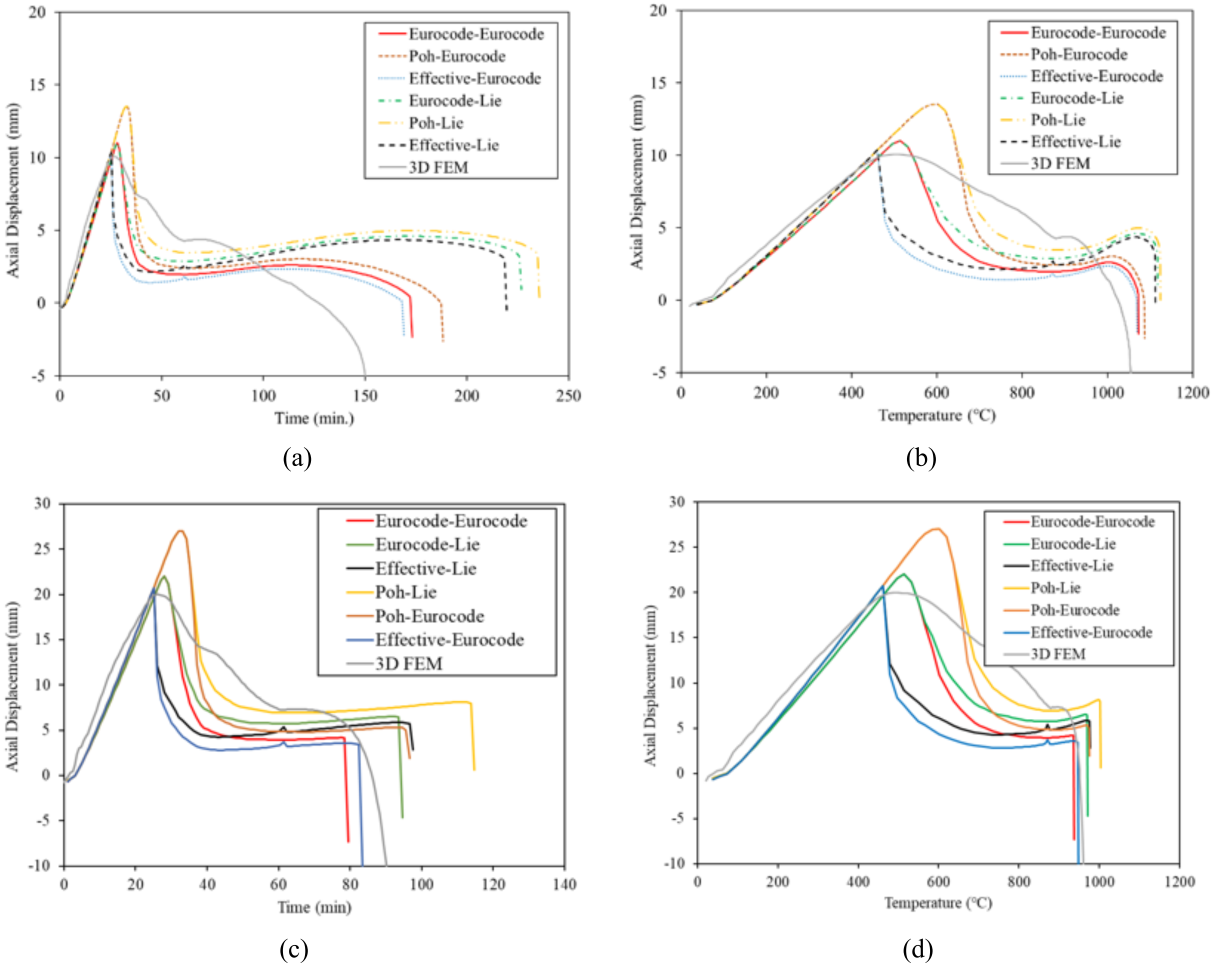

(a) (b)

(c) (d)

Fig. 4-14. (a,c) Axial displacement vs time and (b,d) Axial displacement against temperature for the wall specimen for different combinations of material models, plotted with the FE analysis obtained curve. The curves are labelled by the steel and concrete model, respectively.

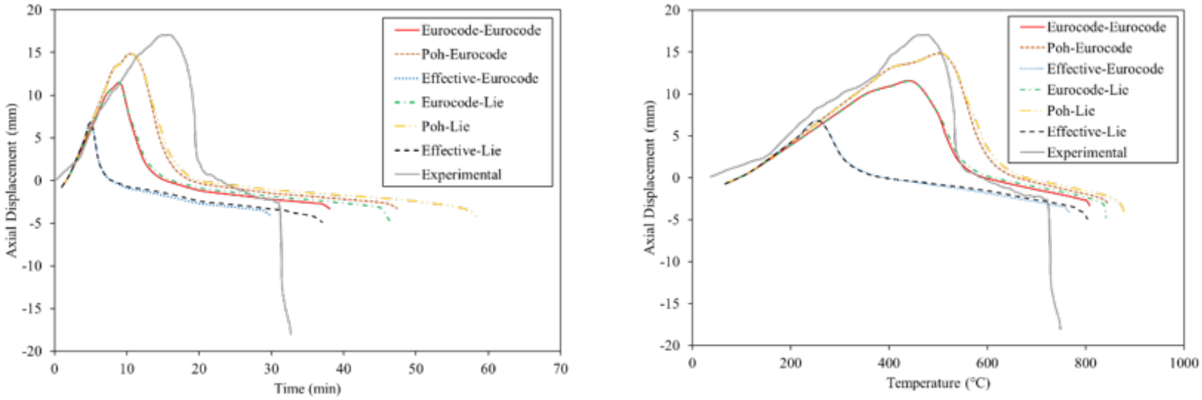

(a) (b)

Fig. 4-15. (a) Axial displacement vs time and (b) Axial displacement against temperature for the CFT specimen for different combinations of material models, plotted with the FE analysis obtained curve. The curves are labelled by the steel and concrete model, respectively.

4.2.4. Development and Functioning of User Interface

A Graphical User Interface (GUI) was developed for the fiber model with the main aim of enhancing its usability and giving designers the ability to better manipulate the inputs and visualize the results. The GUI was developed using MATLAB App Designer, R2018b. The interface was designed with the ability to run the model in multiple ways depending on user preferences and input and display the results as interactive plots. The structure of the interface can be divided into two main components, namely, a pre-processor and a post-processor. This structure and displays are explained below.

(i) Pre-Processor:

The pre-processor is the first step of the UI implementation. The user inputs key parameters including geometric and material properties of the column/wall, loading conditions and fiber discretization. Most of the inputs have in-built default values, which are utilized if the user does not provide anything. The pre-processor also determines how to run the fiber model, based on the inputs of the user. The UI provides the option of using the model as a simple analysis tool, using the model for parametric studies, or using it as a design tool. A section for advanced options is also provided if the user wants to change other details of the model. The pre-processor interface and advanced options tab are shown in Fig. 4-16 (a) and (b).

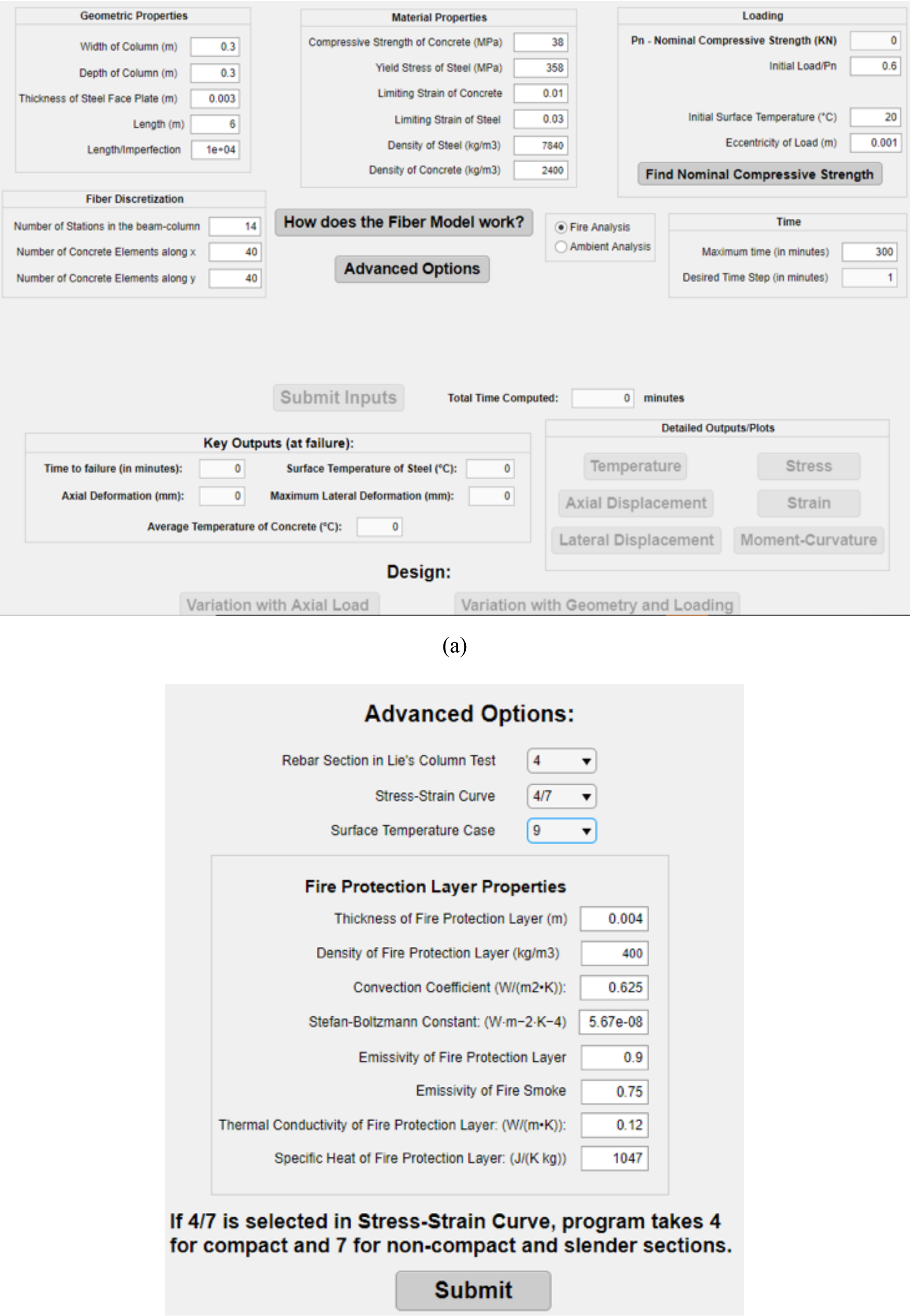

Geometric Properties

Width of Column (m) 0.3

Depth of Column (m) 0.3

Thickness of Steel Face Plate (m) 0.003

Length (m) 6

Length/Imperfection 1e+04

Material Properties

Compressive Strength of Concrete (MPa) 38

Yield Stress of Steel (MPa) 358

Limiting Strain of Concrete 0.01

Limiting Strain of Steel 0.03

Density of Steel (kg/m3) 7840

Density of Concrete (kg/m3) 2400

Loading

Pn - Nominal Compressive Strength (KN) 0

Initial Load/Pn 0.6

Initial Surface Temperature (°C) 20

Eccentricity of Load (m) 0.001

Fiber Discretization

Number of Stations in the beam-column 14

Number of Concrete Elements along x 40

Number of Concrete Elements along y 40

● Fire Analysis

○ Ambient Analysis

Time

Maximum time (in minutes) 300

Desired Time Step (in minutes) 1

Total Time Computed: 0 minutes

Key Outputs (at failure):

Time to failure (in minutes): 0

Surface Temperature of Steel (°C): 0

Axial Deformation (mm): 0

Maximum Lateral Deformation (mm): 0

Average Temperature of Concrete (°C): 0

(a)

Advanced Options:

Rebar Section in Lie's Column Test 4

Stress-Strain Curve 4/7

Surface Temperature Case 9

Fire Protection Layer Properties

Thickness of Fire Protection Layer (m) 0.004

Density of Fire Protection Layer (kg/m3) 400

Convection Coefficient (W/(m2•K)): 0.625

Stefan-Boltzmann Constant: (W·m−2·K−4) 5.67e-08

Emissivity of Fire Protection Layer 0.9

Emissivity of Fire Smoke 0.75

Thermal Conductivity of Fire Protection Layer: (W/(m•K)): 0.12

Specific Heat of Fire Protection Layer: (J/(K kg)) 1047

If 4/7 is selected in Stress-Strain Curve, program takes 4 for compact and 7 for non-compact and slender sections.

(b)

Fig. 4-16. (a) Pre-processor interface of the UI, with all input variables (b) Advanced options interface of the UI

(ii) Post-Processor:

The post processor provides the user with various options to view the results. This part of the UI is called after the simulations have been run, and it takes the output variables from the main code. The post-processor then generates interactive visual outputs of Temperature, Axial and Lateral Deformations, Stress, Strain and Moment-Curvature. For each plot, the user has multiple options of viewing the results, and while running the program in design mode, the post-processor allows the user to visualize the allowable design values such as wall or column dimensions and material properties. A few examples of the post-processor outputs are shown in Fig. 4-17.

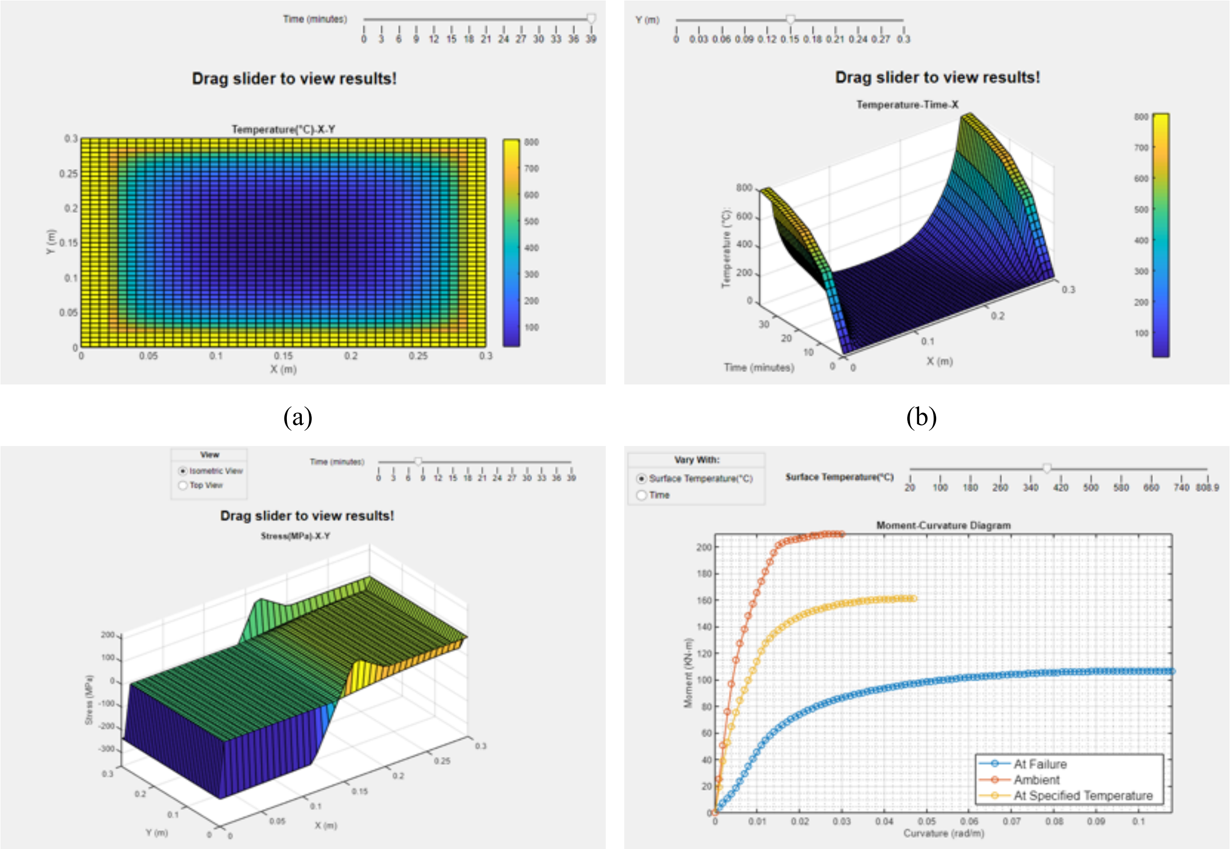

(a) (b)

(c) (d)

Fig. 4-17. Examples of post-processor output interfaces

4.2.5. Limitations of the Fiber Model

The 2D fiber model provides a quick and accurate tool for analysis and design of composite axial members. However, the tool faces certain limitations as a result of the simplifying assumptions made. These major limitations and assumptions are discussed as follows:

- The fiber model provides only 2 degrees of freedom for strains, i.e. centroidal longitudinal strain and curvature, making it more restrictive than 3D models.

- The fiber model assumes plane sections remain plane and perpendicular to the neutral axis at every discrete location (station) along the length. Between two discrete points, the section curvature is assumed to be interpolated, which is a major limitation.

- The fiber model uses uniaxial stress-strain-temperature models for steel and concrete. The multiaxial stresses and strains are not accounted and are assumed to have no influence on the longitudinal (uniaxial) stress-strain-temperature behavior.

- As a result of the previous assumption, the effect of concrete infill applying a lateral pressure on steel faceplates (thus increasing their tendency to buckle outwards) is not accounted for.

- In the case of C-PSW/CFs, the effect of ties and shear studs causing local variations in heat transfer is ignored and they are not modeled. Tie bar spacing is considered only to determine section slenderness

4.3. CFT Parametric Studies and Capacity Prediction

The fiber model discussed in the above section was used to carry out parametric studies on CFT columns. The goal of these studies was to understand how different parameters influence CFT behavior and to develop an equation for capacity prediction. In all the studies a constant axial load was applied while the column surface was subjected to increasing temperatures following the ASTM E119 time-temperature curves on all or some sides.

Four parameters were considered in the parametric study namely aspect ratio of the column section (ratio of width to depth), reinforcement ratio/section slenderness (steel faceplate thickness), steel yield strength and concrete compressive strength. For each case, simulations were run for column slenderness of 5, 10, 15, 20, 30 and 50 and the axial load was increased from 10% to 100% of ambient nominal capacity in increments of 10%. The nominal axial capacity of CFTs was calculated per AISC 360-16, Chapter I. Based on the parameters to be studied, a parametric study matrix was developed. This matrix is given in Table 4-4. The nomenclature of the models presents the properties of the models in the order of aspect ratio, section slenderness, steel yield strength and concrete compressive strength. All cases were without fire protection as the effect of fire protection was separately studied. Plots form the four series and the results are further discussed in detail in the following sub-sections.

Table 4-4. Parametric studies matrix for CFTs at elevated temperature

Nomenclature	Cross section dimensions (mm × mm)	Aspect ratio	Steel tube thickness (mm)	Cross section slenderness	Steel yield strength F_y (MPa)	Concrete strength $f'c$ (MPa)
C-1.0-50-358-38	300 × 300	1	6	50	358	38
C-1.5-50-358-38	250 × 360	1.5	7.2	50	358	38
C-2.0-50-358-38	210 × 420	2	8.4	50	358	38
C-1.0-33-358-38	300 × 300	1	9	33	358	38
C-1.0-50-358-38	300 × 300	1	6	50	358	38
C-1.0-66-358-38	300 × 300	1	4.5	66	358	38
C-1.0-100-358-38	300 × 300	1	3	100	358	38
C-1.0-50-358-38	300 × 300	1	6	50	358	38
C-1.0-50-413-38	300 × 300	1	6	50	413	38
C-1.0-50-482-38	300 × 300	1	6	50	482	38
C-1.0-50-358-27	300 × 300	1	6	50	358	27
C-1.0-50-358-38	300 × 300	1	6	50	358	38
C-1.0-50-358-48	300 × 300	1	6	50	358	48

4.3.1. Section Aspect Ratio

The column aspect ratio (ratio of column depth to width) was studied as a variable parameter. The cases were taken such that aspect ratio increased from 1 (C-1.0-50-358-38) to 2 (C-2.0-50-358-38) while section area and section slenderness remained nearly constant. The results are presented in a critical load against slenderness plot at two surface temperatures, which is shown in Fig. 4-18. In the figure, the curves are plotted for surface temperatures of 400 °C and 900 °C and the curves are identified by their aspect ratio in the legend.

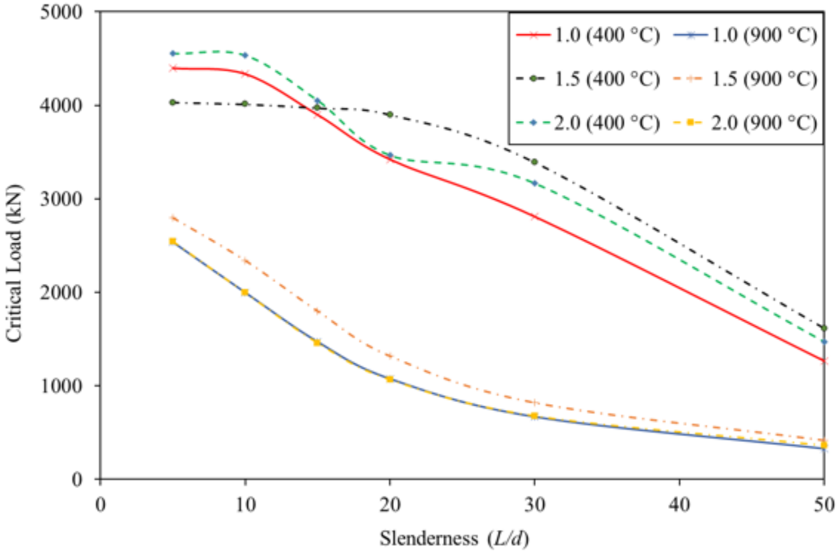

Fig. 4-18. Critical load versus slenderness at two surface temperatures for various aspect ratios

The aspect ratio does not have a very significant effect on column capacity at 400 °C and 900 °C (Fig. 4-1)8. While the column capacity increased slightly going from a ratio of 1 to 1.5 (for both 400 °C and 900 °C), it dropped again when the aspect ratio was further increased to 2. This is because as the depth of the column decreases (increasing aspect ratio), both moment of inertia ($I = bd^3/12$) and length (L = slenderness × d) reduce for a given column slenderness. As critical buckling load is a function of the ratio of effective stiffness to length, it is unaffected. However, increasing the aspect ratio further would bring down the capacity as the effect of concrete confinement would reduce. In this study, the aspect ratio was limited to 2 as columns in practice rarely have higher aspect ratios.

4.3.2. Cross Section Slenderness

A range of section slenderness was considered by varying the thickness of steel faceplates while keeping the overall dimensions constant. The effective stress-strain model for steel was used for non-compact and slender sections, to account for local buckling of steel. The obtained critical load against slenderness plots are shown in Fig. 4-19, which has plots for 400 °C and 900 °C with the curves identified by section slenderness and temperature in the legend.

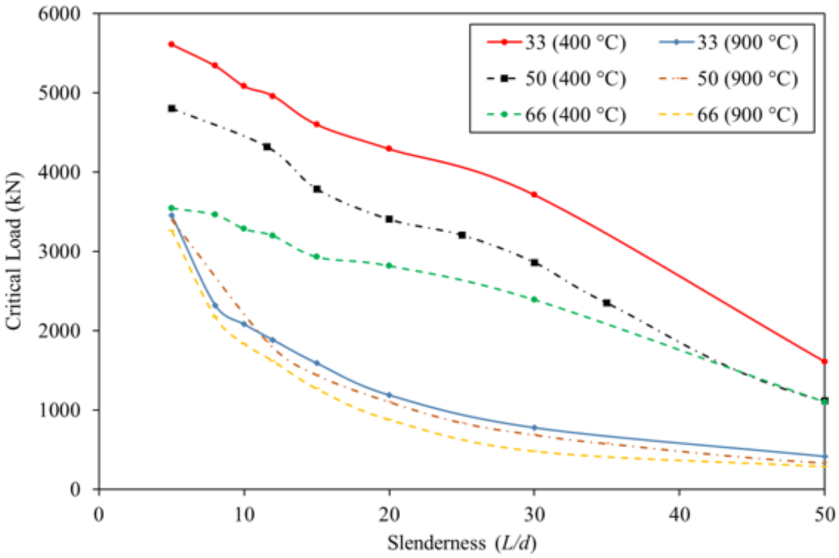

Fig. 4-19. Critical load versus slenderness curves at two surface temperatures for varying section slenderness (reinforcement ratio)

Section slenderness has a significant effect on the critical load. The critical load decreased by nearly 40% for a non-compact section compared to a compact section. This is because local buckling for non-compact and slender sections prevents the steel from achieving its full yield strength. Thus, the column fails at lower axial loads. However, the effect of section slenderness decreases with increasing surface temperature, as the plots for 900°C are nearly coinciding. This is due to steel carrying lower fraction of the axial loads at higher temperatures, minimizing the effect of local buckling on overall capacity.

4.3.3. Steel Yield Strength

Steel yield strength was ranged from 358 MPa to 482 MPa to study its effect on column behavior. The results from these models are shown in Fig. 4-20, the plots identified by steel yield strength and temperature in the legend.

The figure shows that steel yield strength does not significantly affect the load capacity of CFTs. The capacity of columns increased slightly at 400 °C by increasing steel strength. However, the effect of steel yield strength was negligible at 900 °C and the results were close. This occurred due to strength degradation of steel at high temperatures, which resulted in concrete carrying most of the applied axial load.

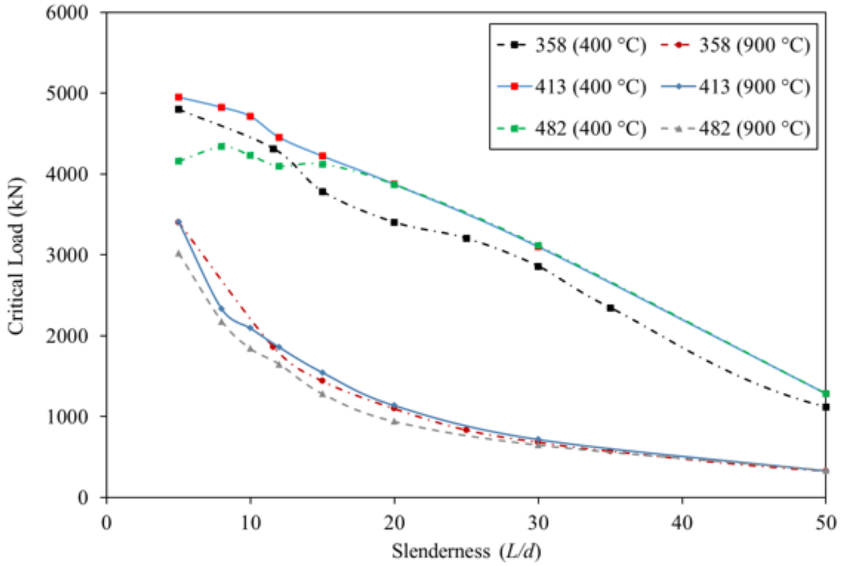

Fig. 4-20. Critical load versus slenderness curves at two surface temperatures for varying steel yield strength

4.3.4. Concrete compressive strength

Concrete compressive strength (f'_c) was varied from 27 - 48 MPa (3.9 -7 ksi), to study its effect on column capacity. The obtained results are compared in Fig. 4-21. The plots are identified by concrete compressive strength and surface temperature in the legend.

Fig. 4-21 shows that the load capacity of CFTs increases with increasing concrete compressive strength for a surface temperature of 400 °C. However, the capacity shows a smaller increase when the surface temperature is 900 °C. Concrete compressive strength has a significant influence on the CFT capacity as most of the concrete remains at relatively low temperatures due to its low thermal conductivity. At elevated temperatures, concrete carries most of the applied axial load and changing its strength affects column capacity.

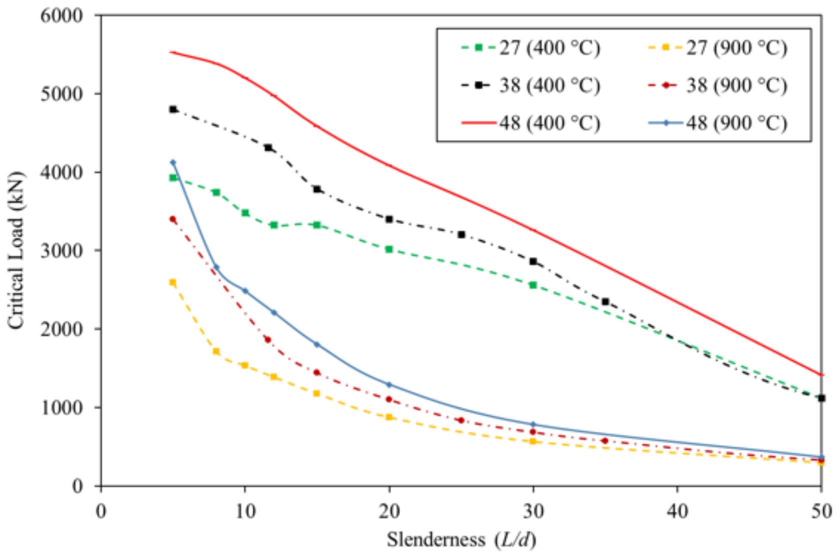

Fig. 4-21. Critical load versus slenderness curves at two surface temperatures for varying concrete compressive strength

4.3.5. Effect of Fire Protection

The fiber model was developed to be able to model a layer of fire protection on the steel surface. Studies were thus conducted to analyze the effect of fire protection on CFT column behavior. Applying a layer of fire protection is a common practice in the industry to increase the fire resistance of structural components.

The fire protection used in these studies was a 4 mm thick layer of gypsum with specific heat capacity C = 1047 J/(kg K) and thermal conductivity k = 0.120 W/(m K). The column was a 300mm × 300 mm square section with 6mm steel faceplates. 358 MPa steel and 38 MPa concrete was considered. Critical load vs. slenderness vs. temperature (P_n *vs. L/d vs. T*) plots were generated similar to those generated for parametric studies above.

Fig. 4-22(a) shows the comparison of load versus slenderness versus temperature plots for the specimen with and without fire protection. For a given temperature and slenderness ratio, the specimen with fire protection has a lower capacity as compared to the specimen without fire protection. This is because, for a given steel surface temperature, concrete is at a higher average temperature in the specimen with fire protection, due to a shallower temperature gradient. This occurs because there is a temperature drop across the layer of fire protection, which is not accounted for meaning steel is at a lower temperature compared to the surrounding air temperature.

Fig. 4-22(b) shows this comparison of temperature profiles across the section which shows concrete at higher temperatures in the specimen with fire protection.

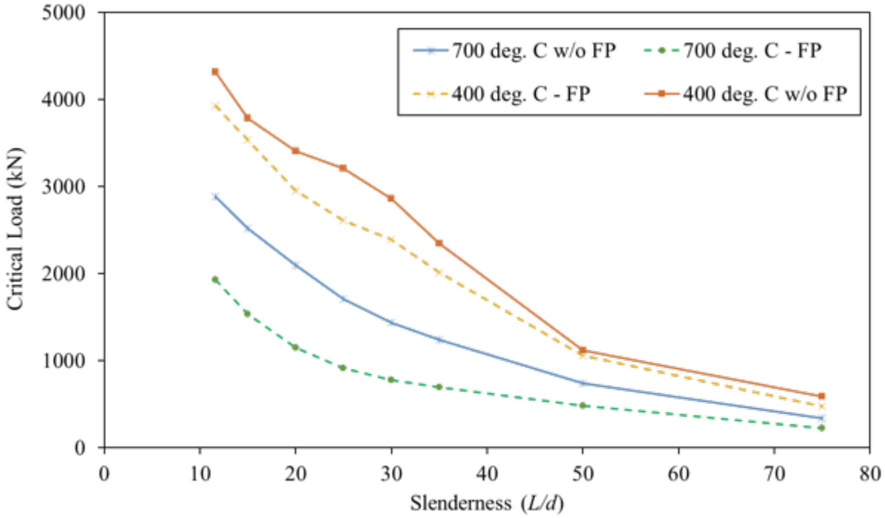

(a)

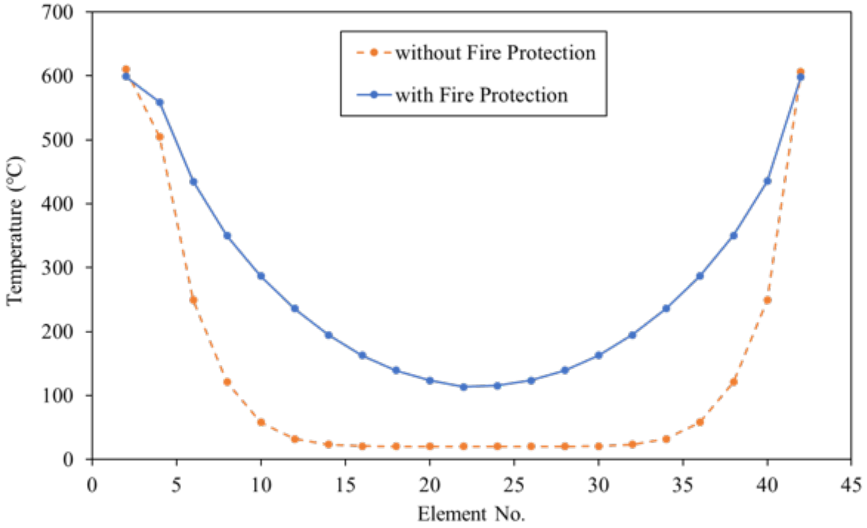

(b)

Fig. 4-22. (a) Critical load vs Slenderness comparison for a column with and without fire protection. (b) Temperature profiles for a column at failure with and without FRP for steel surface temperature = 600 ℃

The effect of fire protection on steel surface temperature and fire resistance (time to failure) of CFTs is shown in Fig. 4-23(a), which plots axial displacement against surface temperature and time. While axial displacements are similar in both cases, steel gets heated to significantly higher temperatures (~1000 ℃) in the absence of fire protection as compared to ~700 ℃ with fire protection. Similarly, Fig. 4.23(b) shows that application of fire protection increases the time to failure by nearly 2.5 times. This is because fire protection significantly delays the heating of steel and restricts steel to temperatures around 700 °C.

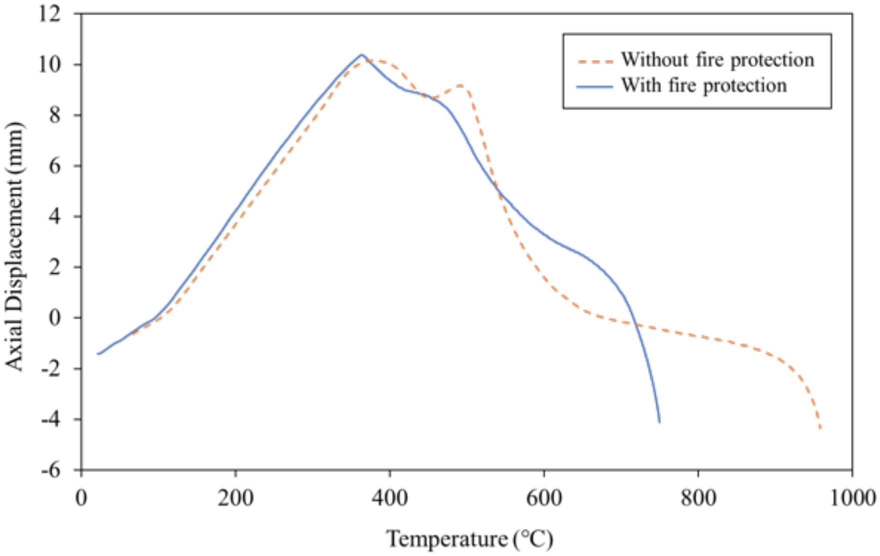

(a)

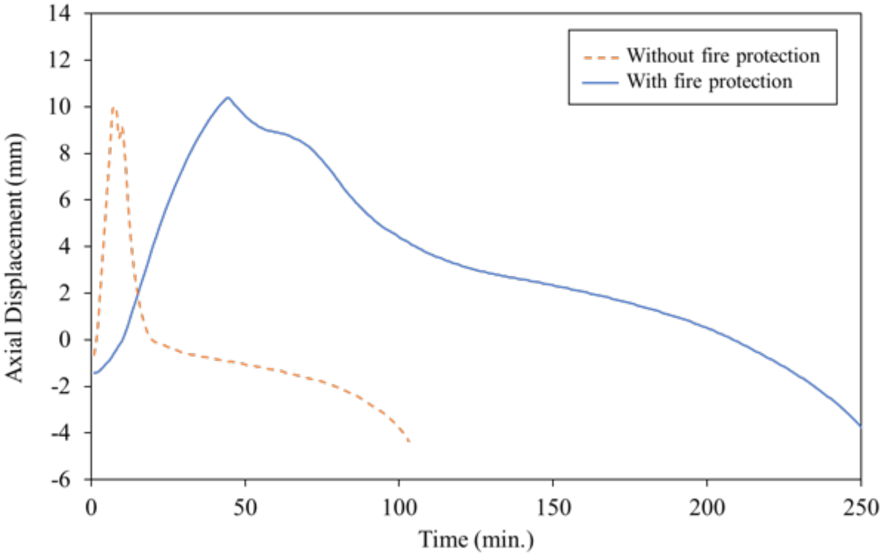

(b)

Fig. 4-23. (a) Axial displacement versus surface temperature and (b) axial displacement versus time comparisons for a column with and without fire protection

4.3.6. Concrete Contribution Factor to Stiffness

As further studies to develop a capacity prediction equation, the variation of concrete contribution to effective stiffness of the CFT was explored. As per AISC 360-16, the effective stiffness of filled composite axial members is given by Eq. (4-1a) at ambient temperature. In this equation, the factor C_3 accounts for cracking of concrete, as cracked concrete is assumed not to contribute to effective stiffness.

$$(EI)_{eff} = E_s I_s + C_3 E_c I_c \tag{4-1a}$$

$$C_3 = 0.45 + 3\left(\frac{A_s}{A_g}\right) \leq 0.9 \tag{4-1b}$$

where,

A_s: area of steel faceplates

A_g: gross section area

E_s: modulus of elasticity of steel

E_c: modulus of elasticity of concrete

I_s: moment of inertia of steel about the section centroid

I_c: moment of inertia of concrete about the section centroid

From Eq. (4-1b), C_3 is a function of reinforcement ratio/section slenderness. The authors investigated the validity of this formula at elevated temperatures using the fiber-model. For this, the contribution factor was calculated at failure as the ratio of *EI* of uncracked concrete elements to the total concrete elements, as given in Eq. (4-2).

$$C_3 = \frac{\sum_{compression} E_c(T) I_c}{\sum_{uncracked} E_c(T) I_c} \tag{4-2}$$

In the above equation, the modulus of elasticity for each element was taken as a function of its temperature according to the values given in Table A-4.2.2 of AISC 360-16. Moment of inertia for each element was taken about the section centroid. The specimen was analyzed with varying section slenderness, axial loads and column slenderness. The axial load was maintained at 20%, 40% and 60% of the ambient nominal capacity for each case. The obtained results are plotted in Fig. 4-24.

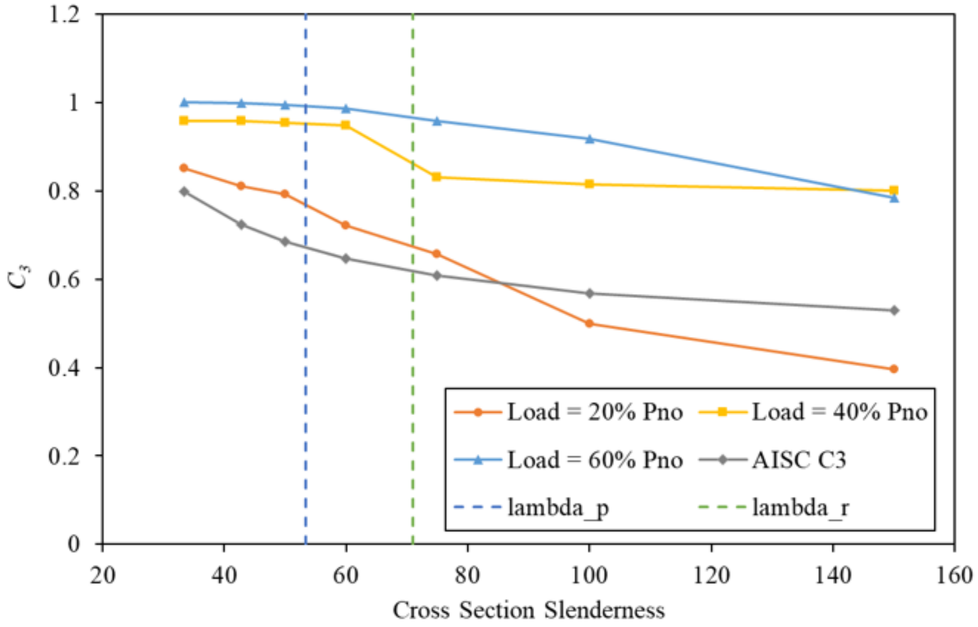
1.2
1
0.8
0.6
0.4
0.2
0
C_3
20
40
60
80
100
120
140
160
Cross Section Slenderness
Load = 20% Pno
Load = 40% Pno
Load = 60% Pno
AISC C3
lambda_p
lambda_r

(a)

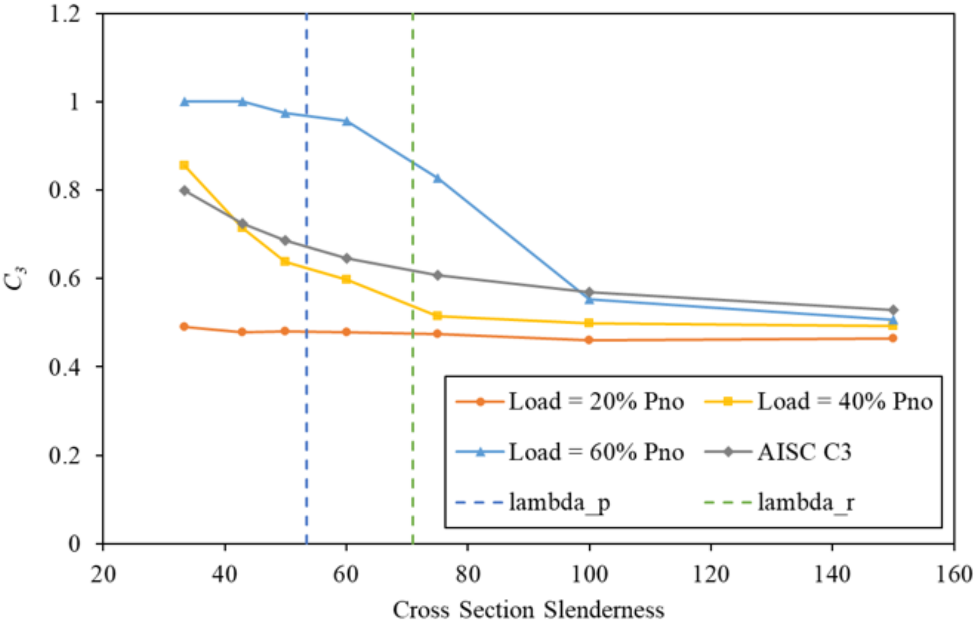
1.2
1
0.8
0.6
0.4
0.2
0
C_3
20
40
60
80
100
120
140
160
Cross Section Slenderness
Load = 20% Pno
Load = 40% Pno
Load = 60% Pno
AISC C3
lambda_p
lambda_r

(b)

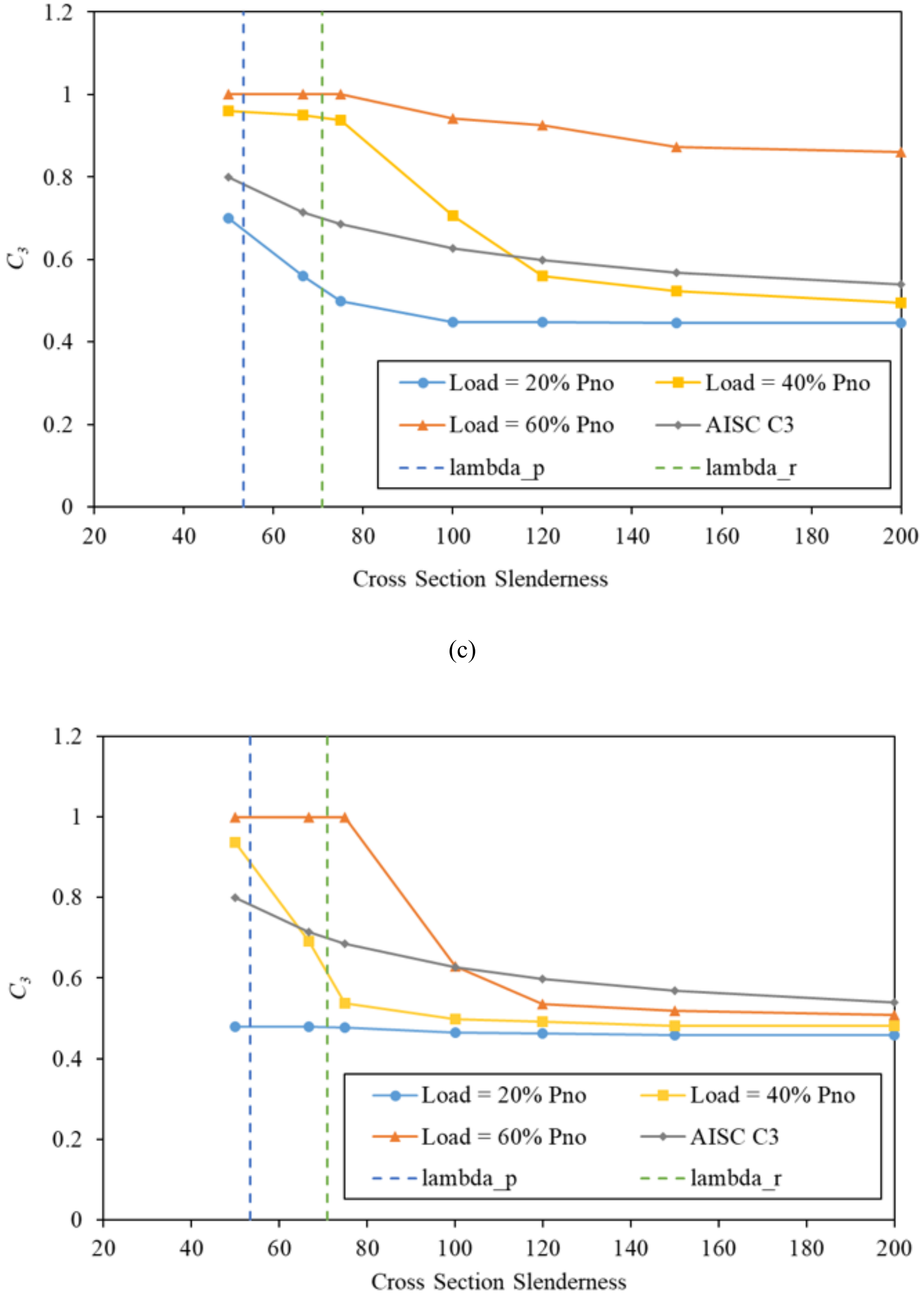

(c)

(d)

Fig. 4-24. Variation of concrete contribution factor to stiffness (C3) with section slenderness and axial load for (a) aspect ratio = 1 & column slenderness = 5, (b) aspect ratio = 1 & column slenderness = 15, (c) aspect ratio = 2 & column slenderness = 5, (d) aspect ratio = 2 & column slenderness = 15

It can be seen from Fig. 4-24 that C_3 initially decreases with increasing section slenderness, then approaching a constant value of 0.45. Also, at elevated temperatures, C_3 is a function of the axial load as well as column slenderness. This is because at higher axial loads, more concrete is uncracked as compressive stresses are higher. Comparing with the AISC 360-16 curve, it is observed that the AISC 360-16 equation is conservative for axial loads greater than 50% of the nominal capacity, but it gets unconservative for high slenderness and low axial loads.

4.3.7. Capacity Prediction Equation for CFTs at Elevated Temperature

Based on the observations discussed in the above sections and the results of the parametric studies, an equation to predict the capacity of CFTs at elevated temperatures was developed and proposed, which is discussed here. For this purpose, the results from the parametric studies were normalized and plotted on a single graph.

The obtained critical load from the fiber analysis [$P_n(T)$] was normalized with the calculated nominal capacity of the column at the failure temperature [$P_{no}(T)$]. This was calculated based on the steel surface temperature at failure and the temperature of all the concrete elements. This non-dimensional ratio [$P_n(T)/ P_{no}(T)$] was plotted on the y-axis. The equations used for its calculation are given below:

For compact sections ($\lambda < \lambda_p$),

$$P_{no}(T) = A_s F_y(T) + 0.85 \sum_{i=conc\_elements} f'_c(T_i) A_{ci} \tag{4-3}$$

For non-compact sections ($\lambda_p < \lambda < \lambda_r$),

$$P_{no}(T) = P_p - \frac{P_p - P_y}{\lambda_r - \lambda_p}\left(\lambda - \lambda_p\right)^2 \tag{4-4a}$$

where $P_p(T) = A_s F_y(T) + 0.7 \sum_{i=conc\_elements} f'_c(T_i) A_{ci}$ (4-4b)

For slender sections ($\lambda > \lambda_r$),

$$P_{no}(T) = A_s F_{cr}(T) + 0.7 \sum_{i=conc\_elements} f'_c(T_i) A_{ci} \tag{4-5a}$$

where $F_{cr}(T) = \dfrac{9E_s(T)}{\left(\dfrac{b}{t_s}\right)^2}$ (4-5b)

Here, slenderness ratio (λ) is defined as b/t_s where b and t_s are the larger column dimension and steel faceplate thickness respectively. A_s is the area of steel faceplates and $F_y(T)$ is the yield strength of steel at failure surface temperature. For concrete, summation is carried out over all concrete elements where $f'_c(T)$ is the compressive strength for the given element temperature and A_{ci} is the area of the element. Steel and concrete strengths as a function of temperature are calculated from Tables A-4.2.1 and A-4.2.2 of AISC 360-16, respectively. This normalized critical load is plotted against the ratio of nominal capacity [$P_{no}(T)$] to elastic buckling strength [$P_e(T)$] at the failure temperature [$P_{no}(T)/P_e(T)$] on the x-axis. The elastic buckling capacity at failure temperature is calculated as follows:

$$P_e(T) = \frac{\pi^2 (EI)_{eff}}{L^2} \tag{4-6a}$$

$$(EI)_{eff} = E_s(T) I_s + C_3 \sum_{i=conc\_elements} E_c(T_i) I_{ci} \tag{4-6b}$$

Here, $EI_{eff}(T)$ is the effective section stiffness, which is calculated as shown in Eq. (4-6b). L is the effective length of the column, which depends on the support conditions. In Eq. (4-6b), $E_s(T)$ is the steel modulus of elasticity at failure surface temperature, and $E_c(T_i)$ is the modulus of elasticity of concrete elements at their temperature. The moments of inertia I_s and I_c are calculated about the centroid of the section. C_3 is calculated as given in Eq. (4-1b). Based on the data points, curve-fitting was done to obtain a lower-bound curve, a median curve and a simplified bi-linear curve. These equations are given below:

Lower bound:

$$P_n(T) = 0.45^{\left(\frac{P_{no}(T)}{P_e(T)}\right)^{0.3}} P_{no}(T) \tag{4-7}$$

Median:

$$P_n(T) = 0.80^{\left(\frac{P_{no}(T)}{P_e(T)}\right)^{0.8}} P_{no}(T) \tag{4-8}$$

Simplified bi-linear:

$$P_n(T) = \left[1 - 0.4\left(\frac{P_{no}(T)}{P_e(T)}\right)\right] P_{no}(T), \text{ if } \frac{P_{no}(T)}{P_e(T)} < 1 \tag{4-9a}$$

$$P_n(T) = 0.06\left[11 - \frac{P_{no}(T)}{P_e(T)}\right] P_{no}(T), \text{ if } \frac{P_{no}(T)}{P_e(T)} \geq 1 \tag{4-9b}$$

Here, *$P_{no}(T)$* is the nominal column capacity at failure temperature, calculated as given in Eq. (4-3) to Eq. (4-5) and *$P_e(T)$* is the elastic buckling strength of the column, calculated using Eq. (4-6a). Plotting the equations on the normalized curve discussed above, they can be reduced to $y = C_1^{x^{C_2}}$. Fig. 4-25 plots all the experimental normalized data points, and the proposed design curves.

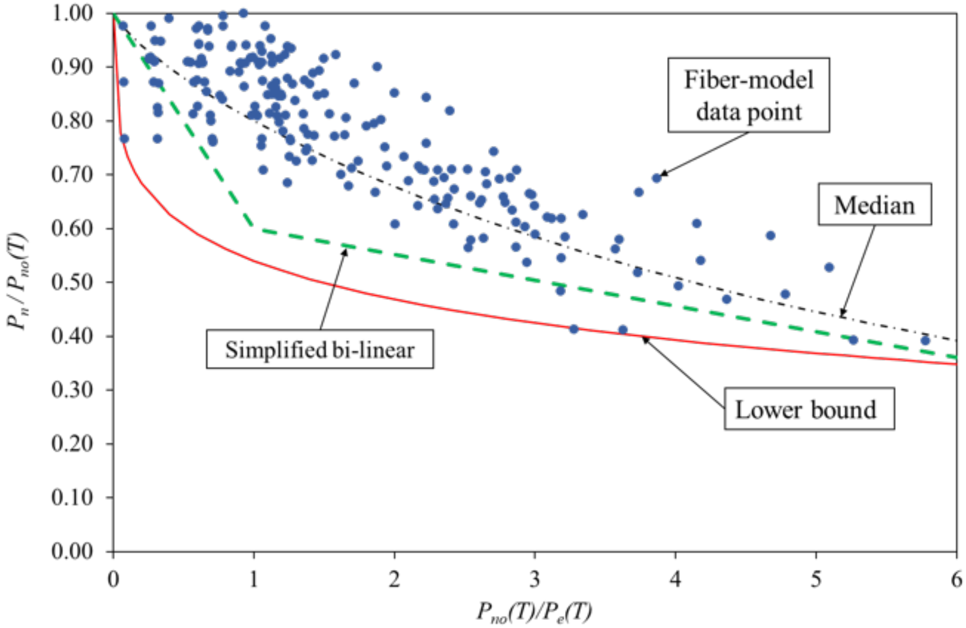

Fig. 4-25. Normalized results of the parametric studies plotted with the proposed theoretical capacity curves (lower-bound, median and simplified bi-linear)

The lower-bound curve is conservative in predicting CFT capacity comparing to the fiber model results as shown in Fig. 4-25. This equation can be used to estimate the axial load capacity of CFTs, given its properties and the targeted fire resistance rating. A 2D heat transfer needs to be conducted up to the required time (fire rating). Based on the steel and concrete temperatures obtained, *$P_{no}(T)$* and *$P_e(T)$* can be calculated. The lower bound critical load can then be obtained using Eq. (4-7).

A modified equation for *C_3* was not proposed in the study as the proposed design curves were seen to be conservative. This was done to simplify the calculation process, as any over-estimation of *C_3* was compensated by the proposed capacity equation (Eq. 4-7), which is conservative.

4.4. C-PSW/CF Modelling and Analysis

In the next step of this study, composite-plate shear walls were modelled using the fiber-based tool. The objective was to compare their performance with the results obtained from finite-element models and thus validate their behavior. For this purpose, eight wall specimens with varying parameters such as wall thickness, overall slenderness and applied load were compared. The details of the wall specimens used in the study are given previously in Table 3-2. The results of 3D finite-element modelling of these specimens are covered in Chapter 3 and results for comparison are taken from there.

Two different modelling techniques were used for walls, which were: (i) modelling the entire wall cross-section and (ii) modelling a strip of the wall section. Results from both these techniques were compared with each other and with FEM results from the corresponding modelling techniques. Further explanation of these techniques and the obtained results are discussed in this section.

Single-sided heating of walls was also modeled using the strip method, in which only one face of the wall was assumed exposed to fire. As it can be expected to have situations where only one side of the walls is exposed to fire, the fiber-model was developed to be able to model the same. These results were also compared with finite-element data.

4.4.1. Wall Section Models

In this modelling technique, the entire wall cross-section in modelled. As discussed previously, ties and shear studs are not modelled as the fiber model cannot account for them. The principle and algorithm of modelling of walls is similar to that of CFTs. The only consideration is that the wall section needs to be oriented such that its minor (weak) axis is horizontal, as the fiber model can simulate buckling along the horizontal axis only. For each specimen, the normalized wall capacity, axial displacement and section temperatures were compared. These values are compared with experimental data and finite-element models.

Fig. 4-26. shows the normalized critical load versus slenderness plots for all the tested specimens. They are plotted with FEM data for comparison. In the plot, green data points are fiber model results while red points are FEM results. The same shapes on the plots corresponds to the same specimen (for example square represents CW-200-15). Both the fiber model and FEM data points follow the similar trend. However, there are differences in both the results, which are evident as both points of a same specimen are not coinciding. These discrepancies arise as a result of differences in temperature distribution, and other simplifying assumptions of the fiber model, listed in section 4.3.

Data points obtained from the fiber model are also plotted with the proposed capacity equation for C-PSW/CFs [see Eq. (3-5)] in Fig. 4-26 for comparison and further validation of the equation. It can be seen from the figure that all the data points are above the proposed lower bound curve, and follow the trend highlighted by the median curve. Also, the proposed equation is adequate and validated by the fiber model.

For further comparison of C-PSW/CF performance, axial displacement versus time and axial displacement versus temperature curves obtained from the fiber model and finite-element models were also compared. Fig. 4-27(a) shows the plots for axial displacement versus time while Fig. 4-27(b) shows the plots for axial displacement against the surface temperature for 4 specimens. It is evident from the graphs that there is a reasonable agreement in FEM data and fiber model. The position of peak axial displacements nearly coincides in the fiber model and FEM data. The discrepancies again can be explained by the simplifying assumptions made in the fiber model.

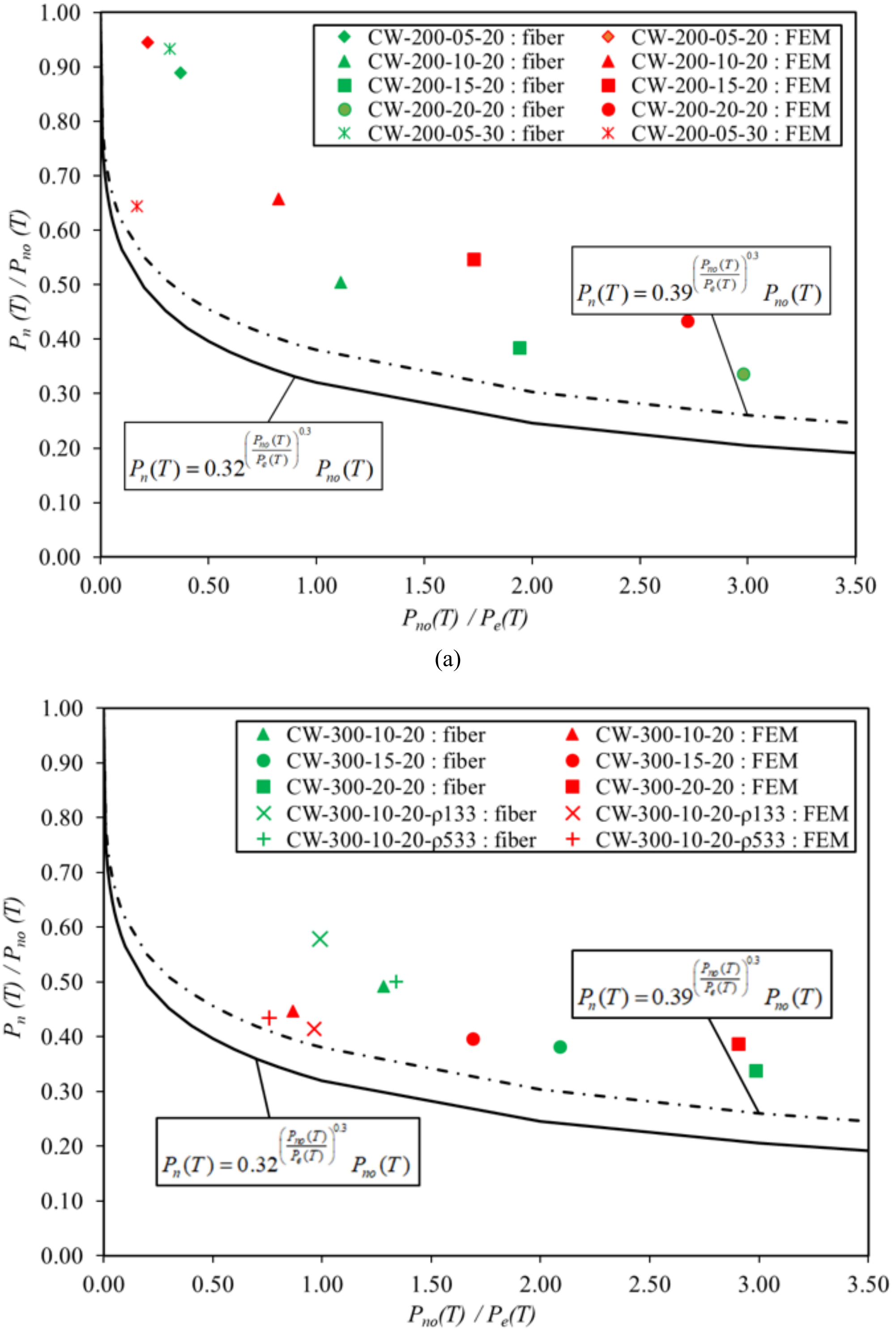

(a)

(b)

Fig. 4-26. Normalized results of the comparison between fiber-model and FE analysis for wall specimens using section method for (a) 200 mm wall thickness and (b) 300 mm wall thickness

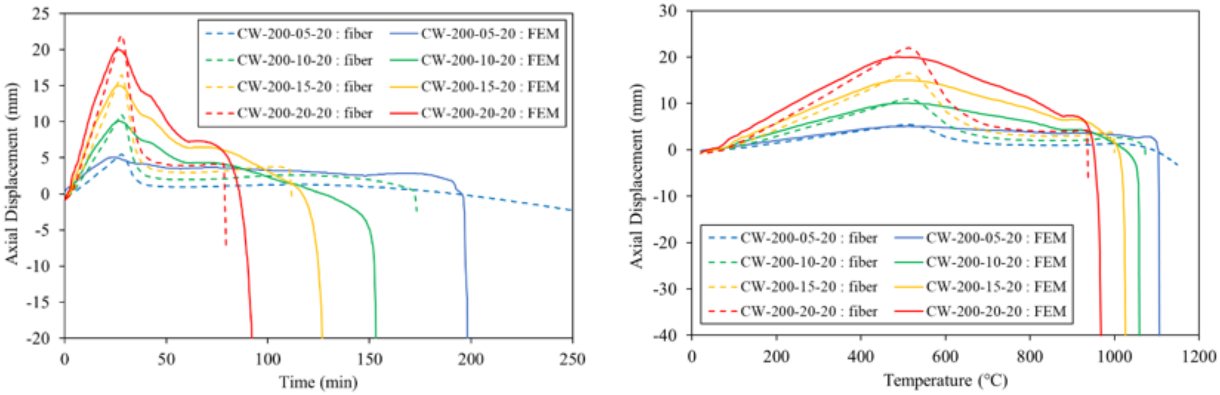

(a) (b)

Fig. 4-27. Comparison of fiber-model and FE analysis predicted axial displacements for CW-200 specimens using section method; (a) axial displacement vs time and (b) axial displacement vs surface temperature

4.4.2. C-PSW/CF Unit Width Models

In this modelling technique, the wall cross-section is divided down into strips perpendicular to the wall direction. A single strip of the wall is then modelled. A strip is defined by half the tie spacing on each side of a tie bar. Thus, the width of the strip modelled equals the tie bar spacing. For these models, steel faceplates are modelled only on two sides of the specimen, while the other two sides are assumed to have symmetric boundary conditions. The detail of the unit width model is discussed in section 3.3.3.

4.4.2.1. Two-sided heating

Heat is assumed to flow only perpendicular to the wall, as width of the wall is considered infinite. Hence heat transfer is done only in one direction and temperature along the wall width is assumed to be constant. The remaining analysis principles are similar to those of CFTs, the only difference being that steel elements are only on two edges, instead of four. The symmetric boundary condition for the concrete edges is implicitly modelled, and hence need not be specifically accounted for.

Similar to the section method, for each specimen, the normalized wall capacity, axial displacement and section temperatures were compared. These values are compared with FE analysis results. The temperature profile across the section is plotted and compared for the 200mm thick wall specimen in Fig. 4-28. Bhardwaj et al. (2019b) recommended to use the surface temperature at failure as a metric to study the fire resistance of C-PSW/CFs. The failure surface temperatures as predicted by the fiber model and FE analysis are compared in Fig. 4-29. The figure shows a close match in the predicted surface temperatures at failure.

Fig. 4-30 shows the axial displacement versus time plots while Fig. 4-31 shows the normalized critical load vs slenderness plots. The normalized load versus slenderness plot shows that the FE analysis is generally more conservative, as it predicts slightly lower critical loads as compared to the fiber-based approach. From Fig. 4-30, it is observed that while there is a general agreement in predicted axial displacement, there are some differences in the axial displacement predicted by the fiber model and the FE analysis.

These differences in part can be explained by the difference in heat transfer algorithms, which generate slightly different temperature profiles across thee section, as is evident from Fig. 4-28. Fiber model predicted temperatures are lower than the finite element predicted ones beyond 200 minutes, and hence the lower predicted strengths by the finite-element models can be explained. Apart from this, the simplifying assumptions of the fiber model would also explain the differences.

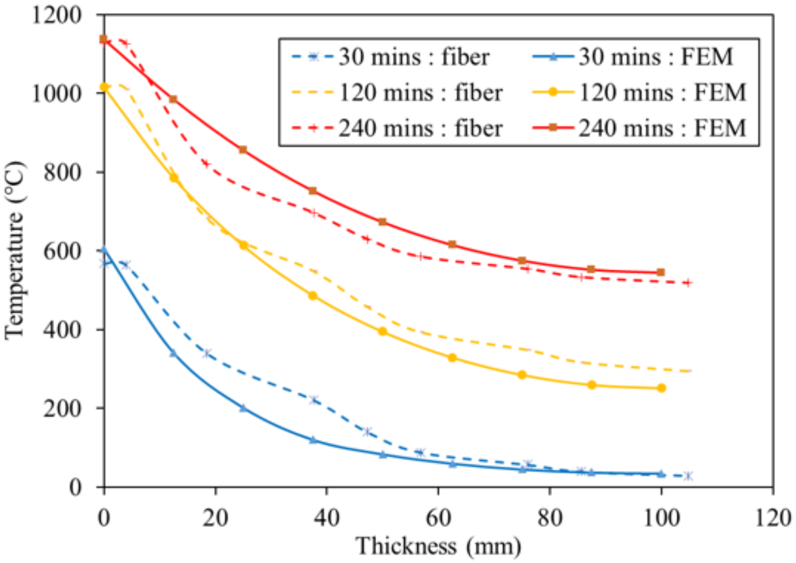

Fig. 4-28. Temperature profiles comparison (half-section) between fiber-model and FE analysis for 200mm wall thickness at three time instants- strip method

Similar to the section method, the proposed equation using the strip method for finite-element models [see Chapter 3, Eq. (3-5)] was validated using the fiber method. Fig. 4-31 shows the data points from several specimens plotted on the normalized load vs slenderness plot with the proposed equation. It is evident that the proposed equation is significantly conservative when compared to the fiber model results. Hence, the proposed curve can be used as a conservative lower bound to estimate wall capacity.

As a last step, the results from section method and strip method (unit width walls) for the fiber model were compared with each other. This comparison was done in terms of the normalized critical load vs slenderness data points. Fig. 4-32 shows this comparison where both the data points are plotted together. It can be seen from the plot that the strip method is generally more conservative, as its data points are slightly lower on the curve. Also, because the strip method is independent of the width of the wall, it is recommended to be used for modelling C-PSW/CFs.

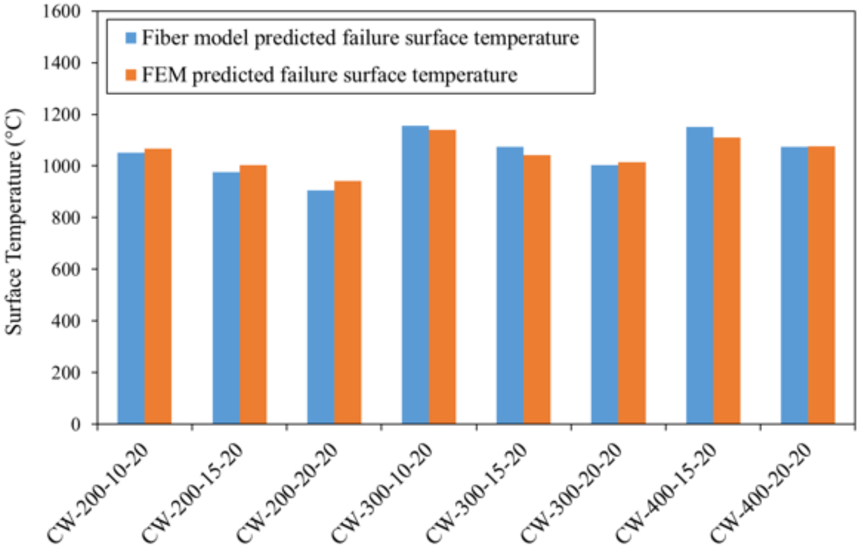

Fig. 4-29. Comparison of failure surface temperatures as predicted by fiber model and FE analysis- strip method

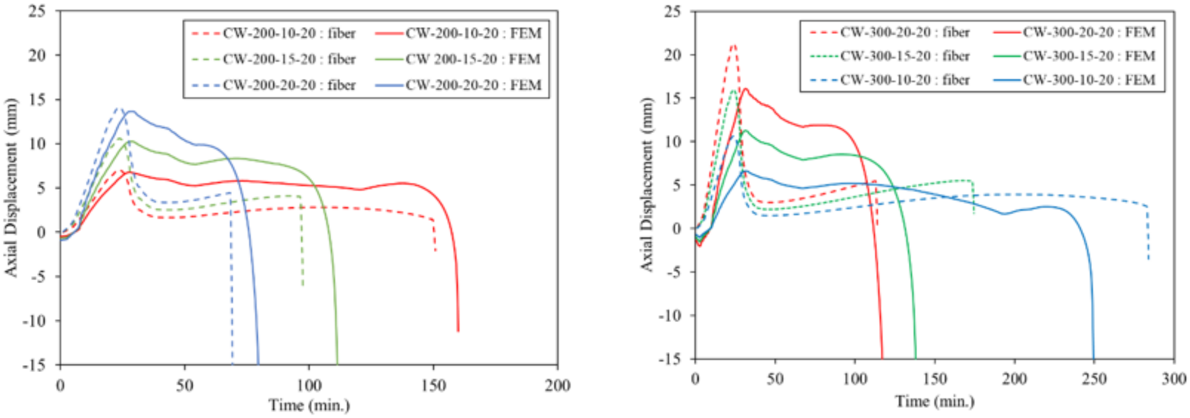

(a) (b)

Fig. 4-30. Comparison of fiber-model and FE analysis predicted axial displacements for (a) CW-200 specimens and (b) CW-300 specimens using strip method

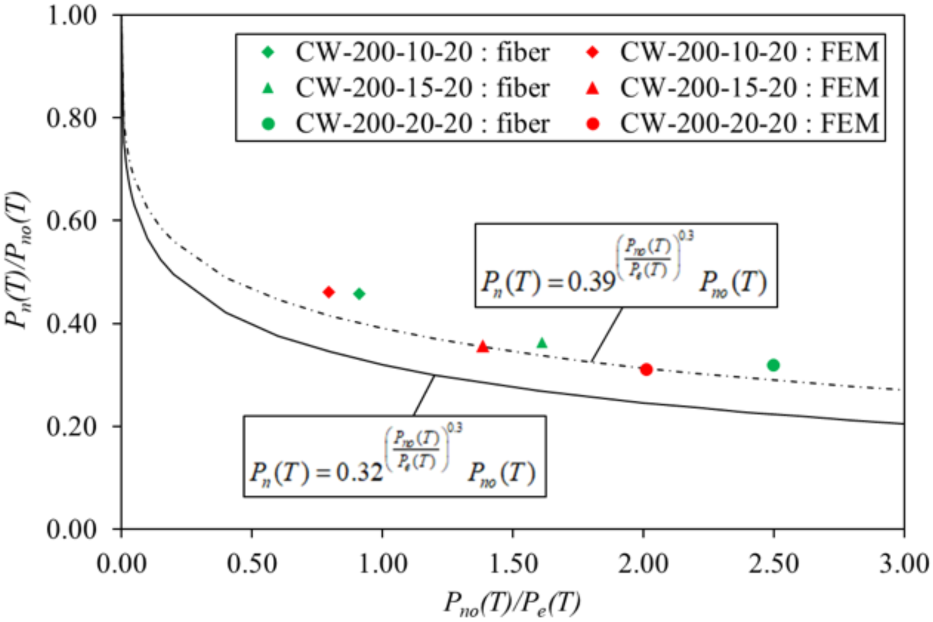

(a)

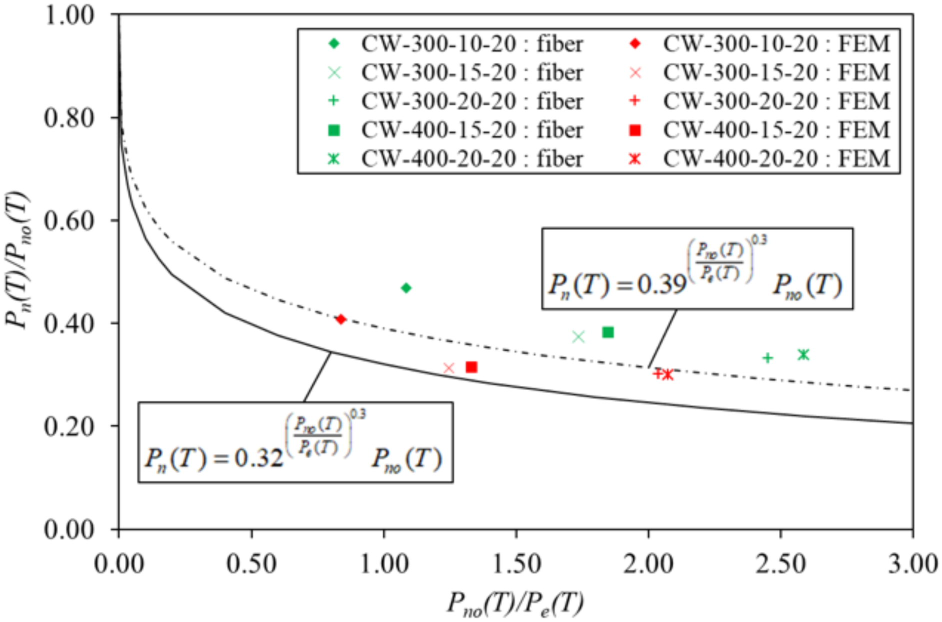

(b)

Fig. 4-31. Normalized results of the comparison between fiber-model and FEM data for wall specimens using strip method

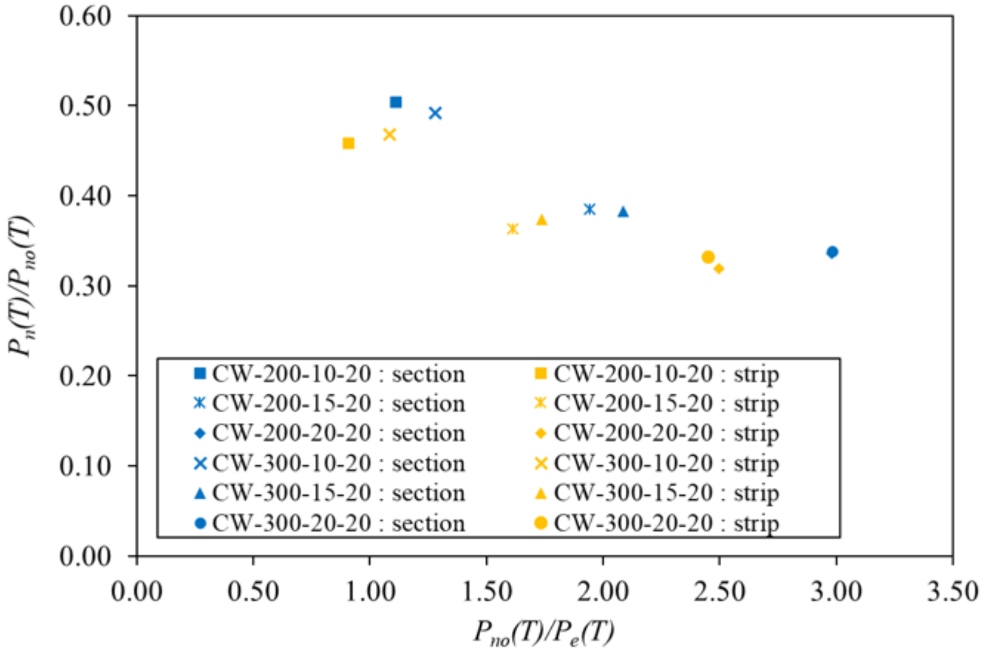

Fig. 4-32. Comparison of normalized load versus slenderness data for section method and strip method for fiber model

4.4.2.2. Single-sided heating

As the last step of the study, single-sided heating of C-PSW/CFs were modeled. In this study, fire was assumed to be present only on one side of the wall. Only one face of the wall was exposed to fire loading while the other face remained at ambient temperature. The fiber-model was designed to be able to model single-sided heating for walls using the strip-based approach.

Heat transfer was modeled in one direction, perpendicular to the width of the wall. The unexposed face of the wall was assumed to remain at room temperature (20 °C). Heat loss to the atmosphere through the unexposed face was calibrated by adjusting the value of the convection coefficient. The variation of temperature across the wall thickness was compared with FE analysis and is shown in Fig. 4-33. The graph shows the temperature at various nodes across the section at different time instants as obtained from the fiber model and FE analysis. There is a good agreement in the temperature profiles obtained from the two models.

Further steps of analysis involve developing a cross-section moment-curvature curve for the calculated temperature states. Newmark's modified method is implemented to obtain a converged deflected shape, as outlined in 4.2.1. As material stiffness of steel and concrete reduces with increasing temperatures, center of stiffness of the section will vary with time for non-symmetric heating. Hence center of stiffness of the section and load eccentricity are calculated at each time step, and the primary moment due to eccentricity is updated in modified Newmark's method. Lateral displacement and curvature in the direction of the heated face are taken as positive. A comparison of out-of-plane displacements obtained from the fiber model and FE analysis for the CW-300-10 strip model is shown in Fig. 4-34. The graph shows the variation of out-of-plane displacement against the temperature of the steel surface exposed to fire. There is a good agreement in the displacements, with both the models predicting comparable peak out-of-plane displacement.

Wall sections with varying height (wall slenderness) were modeled for single-sided fire to study the effect of height on the direction of global buckling. A wall section with overall thickness 300 mm, width of 150 mm and steel faceplate thickness of 6 mm was modeled. Steel and concrete strengths were taken as 345 MPa and 40 MPa respectively. Axial load equal to 20% of $A_c f'_c$ was applied. Wall sections with overall slenderness of 10, 15, 20, 22, 25 and 30 were considered. Fig. 4-35 plots the out-of-plane displacement for the six models against temperature of the exposed steel surface.

All the walls were observed to initially buckle in the positive direction (direction of heated face). This is because of thermal bowing due to asymmetric heating, which caused the heated steel faceplate to expand more than the remaining section. The shorter walls ($H/t_w < 20$) were seen to buckle in the opposite direction (towards the unexposed face) after a period of heating. The asymmetric heating resulted in steel and concrete near the exposed face losing more stiffness compared to the material near the unexposed face. Center of stiffness thus shifted towards the unexposed face. As load was assumed to act at the geometric center of the section, a primary moment was generated which was opposite to the moments imposed due to the expansion of material on the heated face (thermal moments). A representation of the two types of moments generated is shown in Fig. 4-36. The wall section buckled towards the unexposed face when the primary moment overcame the thermal moment.

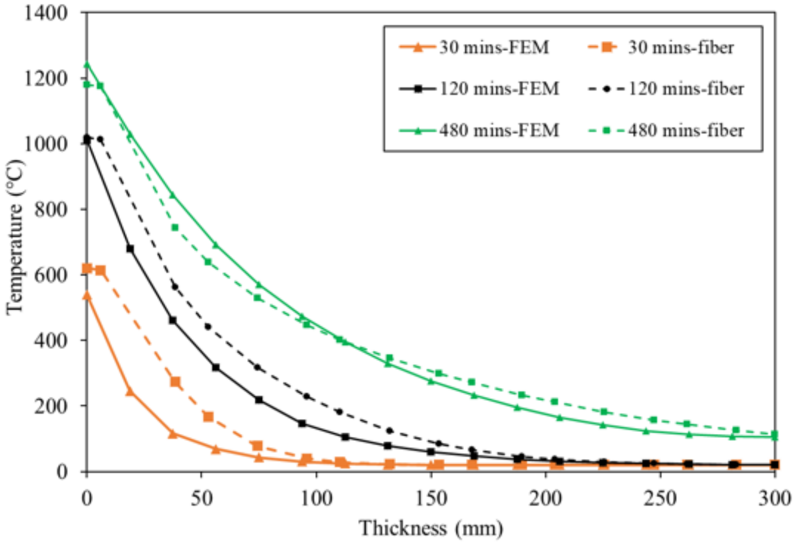

Fig. 4-33. Comparison of cross-section temperature profiles for one-sided heating at three time instants for fiber model and FE analysis

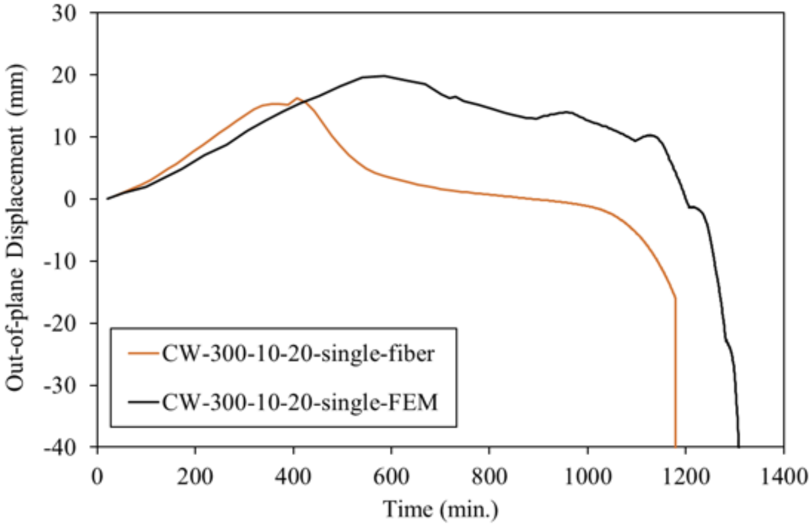

Fig. 4-34. Comparison of fiber model and FE analysis predicted out-of-plane displacement against temperature of the exposed steel surface for CW-300-10 specimen

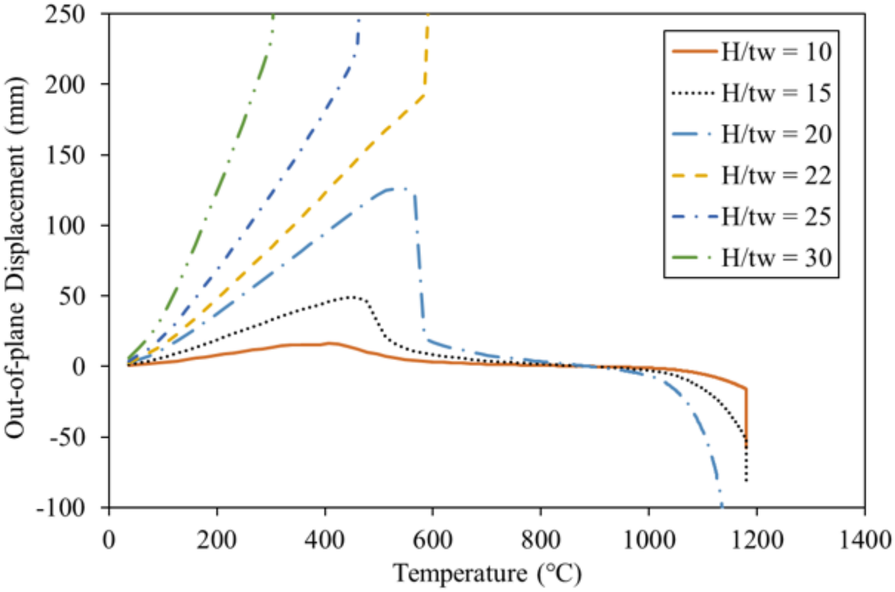

Fig. 4-35. Out-of-plane displacement against temperature of the exposed steel surface for 6 wall slenderness ratios (*H/t_w*) for CW-300-xx-20 wall section with single-sided heating

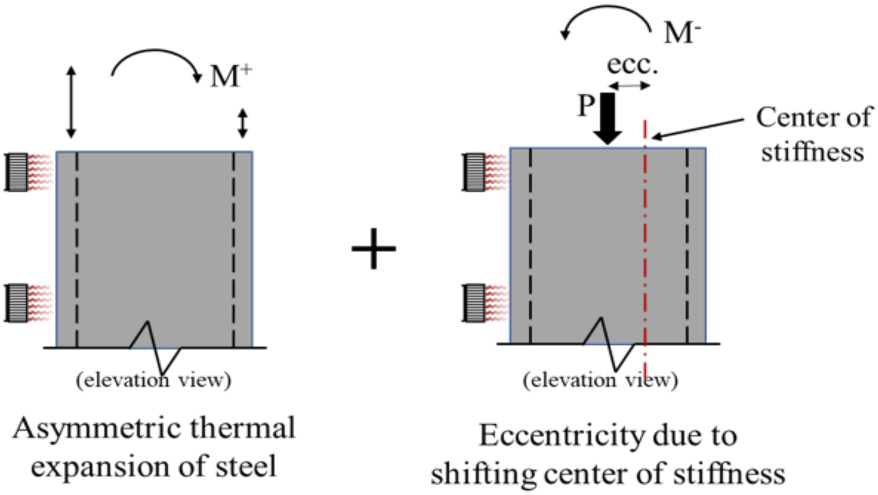

Fig. 4-36. Representation of the two types of moments generated in a wall section exposed to asymmetric heating

Another observation from Fig. 4-35 is the difference in failure surface temperature (and failure time) for different wall sections. Walls with slenderness greater than 20 failed at low surface temperatures (relatively smaller time to failure) while short walls were stable for longer a longer duration. This is because for high slenderness, the moments arising from the asymmetric thermal gradients were enough to cause instability even at lower temperatures. Slender wall sections were seen to fail quickly even for low applied axial loads. This is represented in Fig. 4-37 which shows the failure time and temperature at failure of the exposed steel face for different applied load ratios. The figure shows the behavior of the wall section with overall slenderness of 25. Load was applied as a fraction of the ambient nominal capacity of the wall section (AISC, 2016). Even for low load ratios of 10%, the wall section failed at 41 minutes, or at a surface temperature of 725 °C. Wall sections with slenderness less than 20, however, were seen to be stable for a significantly longer duration (240 minutes to 600 minutes). Such a difference in behavior is not observed for symmetric fire loading as thermal effects do not produce thermal bowing when a member is heated symmetrically. In such cases, moments arise only because of imperfections in the member.

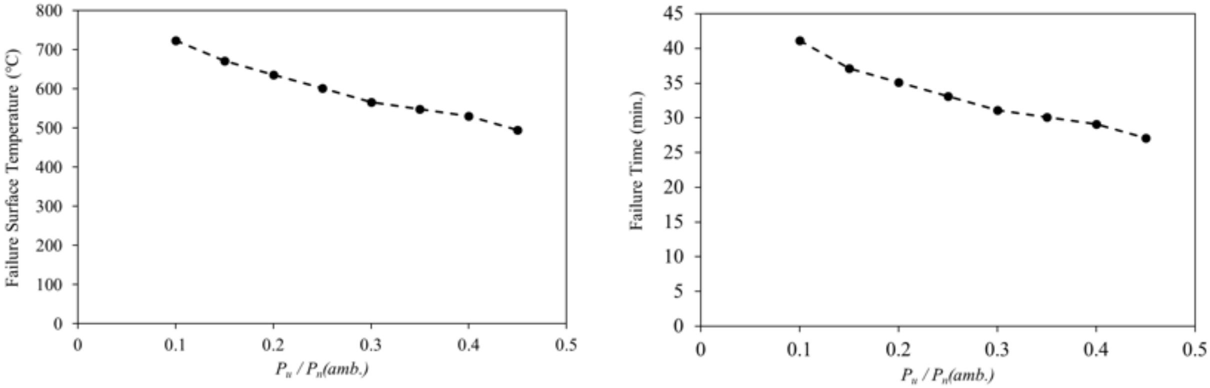

(a) (b)

Fig. 4-37. (a) Failure surface temperature and (b) Failure time against axial load ratio for wall slenderness = 25 for single-sided heating

The wall models were also studied for an applied load ratio of 30% $A_c f'_c$ to understand the relative effect of applied axial load and wall slenderness. The time to failure (fire resistance) of the six models for 20% and 30% applied axial load was plotted and is shown in Fig. 4-38. Fire resistance decreases rapidly as wall slenderness goes beyond 20, and it is seen to be independent of the applied load. This is as the plots for 20% and 30% $A_c f'_c$ are nearly coinciding for $H/t_w > 20$. For wall slenderness less than 20, the applied axial load has a significant effect on fire resistance. Further, these results were plotted on the normalized load versus slenderness plot, shown in Fig. 4-39. The proposed lower-bound Eq. (3-5) is also plotted for comparison. The figure shows four series of data points, with wall slenderness less than and greater than 20, and applied axial load of 20% and 30% $A_c f'_c$. This plot also shows that wall sections with $H/t_w > 20$ are below the proposed capacity curve, hence having inadequate capacity. Shorter walls ($H/t_w < 20$) are seen to have adequate capacity compared to the proposed design curve.

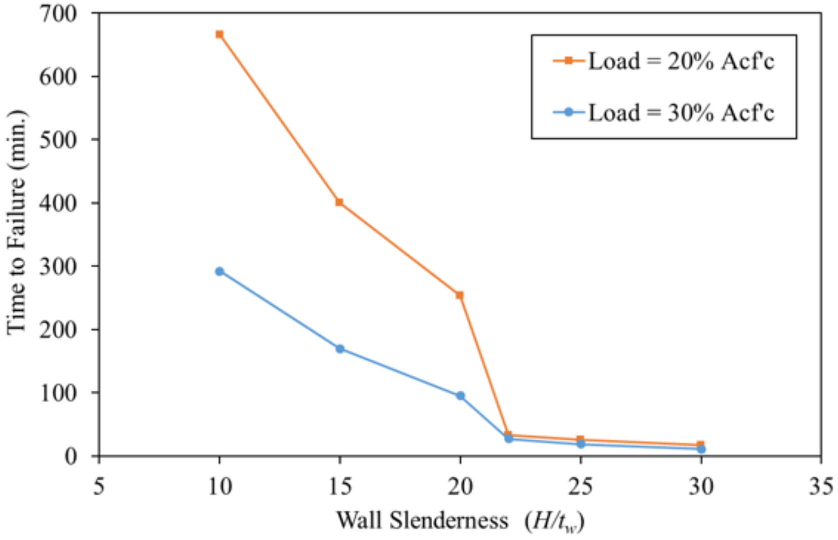

Fig. 4-38. Variation of time to failure (fire resistance) with wall slenderness (single-sided heating) for applied axial load equal to 20% and 30% $A_c f'_c$

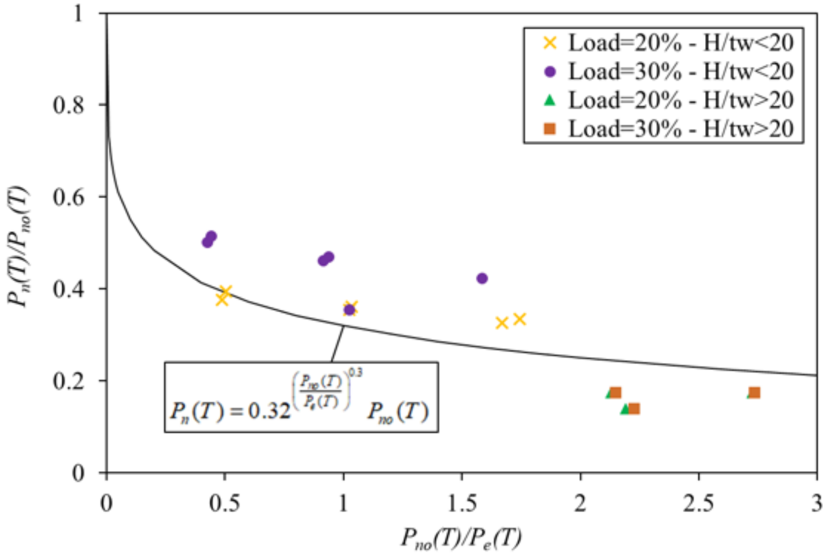

Fig. 4-39. Normalized critical load against slenderness data points for single-sided heating

From the above observations, it is evident that wall slenderness ratio has a significant effect on the behavior and stability of C-PSW/CFs under asymmetric fire loading. More slender wall sections ($H/t_w > 20$) have relatively poor fire resistance (~40 mins.) irrespective of the applied axial load. For short walls ($H/t_w < 20$), the proposed capacity equations [Eq. (3-12) and Eq. (3-13)] were adequate for predicting axial load capacity. Based on the results of these studies, it is recommended to limit the wall slenderness ratio, or the story height-to-wall thickness ratio to 20 for walls without fire protection. For walls with $H/t_w > 20$, it is recommended to apply fire protection. Additional experimental and numerical studies are recommended to determine the dependency of wall stability on other wall parameters such as thickness, reinforcement ratio and material properties.

4.5. Summary and Conclusions

A cross-section behavior based 2D fiber model was developed to simulate composite axial members under fire loading. This model incorporated algorithms of heat transfer, calculation of moment-curvature response and inelastic buckling. The fiber model was validated at ambient and elevated temperatures using experimental data and 3D FE results. Multiple time-temperature curves, material models and heating scenarios were programed to provide the flexibility of analysis. A graphical user interface was developed for the fiber model, that would allow the user better interaction with the model. The user interface allows the fiber model to be run as an analysis or design tool and provides various options to visualize the results.

Using this fiber model, the effect of various parameters on the stability of CFTs under uniform fire loading was investigated. A capacity equation for CFTs at elevated temperatures was also developed and proposed. C-PSW/CFs were modeled using the fiber model and the results compared to FE analysis. Fiber model results were also compared against the proposed capacity equations for C-PSW/CFs. Two modeling techniques of C-PSW/CFs were explored: the section-based approach and the strip-based approach. Single-sided heating of C-PSW/CFs was also modeled and studied using the strip-based approach.

Results of the parametric study on CFTs indicated that concrete compressive strength and section slenderness have a significant influence on the capacity of CFTs. Load capacity of CFTs was seen to decrease with decreasing concrete strength and increasing cross section slenderness. However, steel yield strength and aspect ratio had a minor effect on the load capacity. Also, it was observed that column capacity was nearly independent of all the four parameters at high temperatures (~900 °C).

A layer of fire protection was seen to significantly increase (about 2.5 times) the fire resistance rating (time to failure) of CFTs by restricting steel temperatures to ~700 °C. However, for a given steel surface temperature, columns with fire protection had a lower axial load capacity due to a higher average concrete temperature. For instance, the critical load of unprotected CFTs with a slenderness of 20 and 50 was about 80% and 50% higher than protected CFT at a surface temperature of 700 °C. Design equations were proposed to calculate the capacity of CFTs at elevated temperatures. Three equations were proposed based on the parametric analysis results: (a) lower bound, (b) median, and (c) simplified bi-linear equation. Lower bound equation is recommended for the design purposes.

C-PSW/CF modeled using the two approaches gave results consistent with FE analysis and the proposed capacity equations. The strip-based approach was seen to be more consistent with FE models and more conservative as it neglected the additional strength due to wall boundary elements. It is recommended to use the strip-based approach for modeling C-PSW/CF. Single-sided heating of walls was modeled and studied using the strip-based approach. It was observed that walls with wall slenderness ratios greater than 20 have low fire resistance to asymmetric heating, irrespective of the applied axial load. This is due to second-order moments resulting from thermal bowing caused by the asymmetric temperature gradient. Walls with slenderness less than 20 have a significantly higher fire resistance rating, with specimens remaining stable up to 600 minutes. For instance, the fire resistance rating of walls ($t_w = 300$ mm – 20% load) with a wall slenderness ratio of 20 and 25 was reduced from 254 min to 26 min. Additionally, the proposed capacity equations for C-PSW/CFs were seen to be adequate for walls with wall slenderness ratio less than 20 exposed to asymmetric fire loading. It was recommended based on these observations to define wall slenderness ratio limit of 20 for unprotected walls that would be exposed to asymmetric heating.

4.6. Recommendations for Future Work

As future work, a study to develop equations for predicting fire resistance (time to failure) of composite axial members is recommended. A detailed parametric study (similar to the study on CFTs) is recommended for C-PSW/CFs exposed to asymmetric fire loading, to better characterize the effect of various parameters. Detailed studies are also recommended to specify limits on slenderness and the applied axial load for asymmetric fire conditions. Similar studies can also be performed for CFTs exposed to asymmetric fire loading (one-sided or three-sided heating) and design equations developed for the same.

Chapter 5. Vent Holes

5.1. General

The existing water in the concrete infill of C-PSW/CF systems evaporates at elevated temperatures. During fire tests of C-PSW/CF (Chapter 2) a significant amount of vapor and water was released from the vent holes. The faceplate surrounding the concrete infill can trap vapor between faceplate and concrete during a fire event and a C-PSW/CF system can act like an enclosed vessel. The temperature rise builds up pressure between the faceplate and concrete. This pressure can create stresses that may result in the yielding of the steel plate or fracture at welds. Providing vent holes can help to release the built-up pressure. The vent holes should not be blocked by any structural or non-structural elements. A rational method has been developed based on using spring-operated relief pressure devices design methods. The details of the developed method to design the vent holes sizes with a sample example are provided in this chapter.

5.2. Methodology

The faceplate of a C-PSW/CF is assumed to behavior as a pressure vessel and the vapor can travel freely. The design method of sizing spring-operated relief pressure devices is employed with the following assumptions to design vent holes for the composite walls:

- It is assumed the C-PSW/CF acts like an enclosed vessel as shown in Fig. 5-1.
- The water content (free and bonded) of concrete evaporates when the temperature of concrete exceeds 100 ℃.
- The generated vapor rate is equal to the vapor discharge rate.
- An allowable pressure build-up is calculated based on the maximum allowable concrete pouring height (Bhardwaj et al., 2018b).
- The temperature of vapor does not exceed 200 ℃ during traveling inside the wall until it reaches a vent hole.
- The flow of vapor through vent holes is reversible and isentropic.

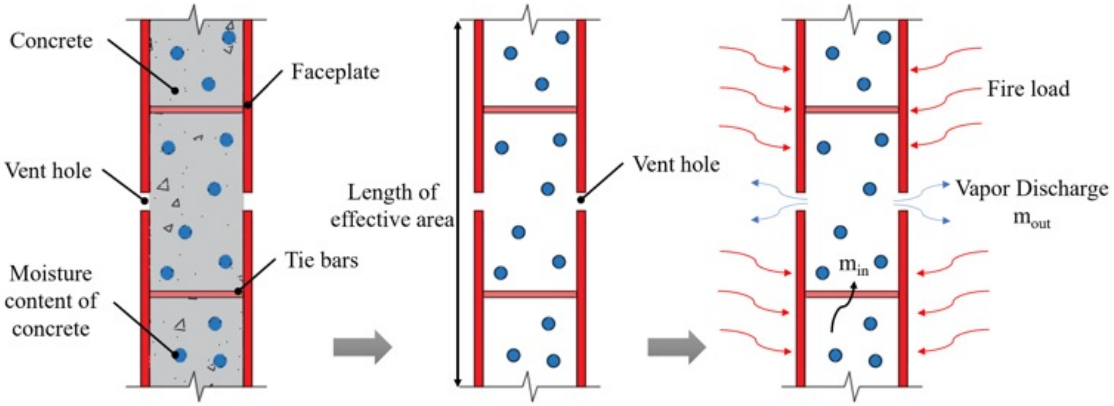

Fig. 5-1. Assumptions for the proposed method for sizing vent holes

Eq. (5-1) is employed to calculate the required vent hole for a designated effective area. Vent holes are in the middle of the effective area. The maximum allowable pressure should be calculated based on the maximum concrete pour height that does not significantly affect the compressive strength of C-PSW/CFs (Bhardwaj et al. 2018). The vapor generation rate (*m*) can be determined based on the rate of the concrete thickness that is heating or drying. This can be calculated by dividing the amount of evaporated water content to the duration (time) associated with the dry concrete thickness (t_{dc}). The discharge rate of every vent hole can be taken equal to the vapor generation rate (*m*), conservatively. The effective area (A_{eff}) for every vent hole can be calculated based on the vent hole spacing. At least one vent hole at the top and bottom of the wall, on every floor, should be provided. Based on the height of the wall additional vent holes should be provided between the top and bottom vent hole if needed (Fig. 5-2).

$$A = \frac{m}{K_d P \sqrt{\frac{\gamma M_m}{\overline{R}T}\left(\frac{2}{\gamma+1}\right)^{\left(\frac{\gamma+1}{\gamma-1}\right)}}} \tag{5-1}$$

where:

m	Vapor generation rate	$\overline{R}$	Ideal gas constant
A	Vent hole area	T	Temperature
γ	Specific heat ratio	M_m	Molar weight
P	Allowable pressure	K_d	Discharge coefficient

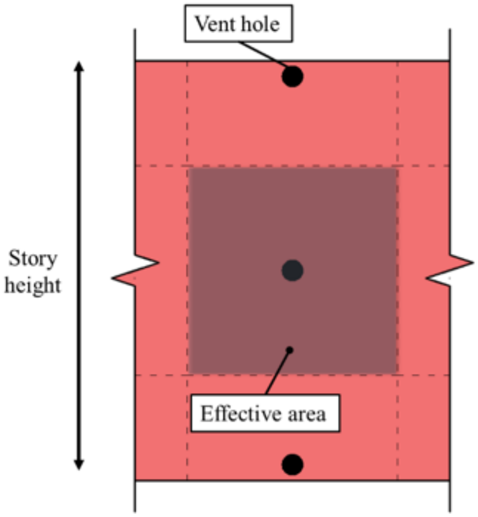

Fig. 5-2. Vent holes located at the center of effective area, bottom and top of walls at every floor

The moisture content of concrete infill can travel to cooler regions. The moisture migration within the concrete can increase pressure in the concrete pores. In the absence of vent holes, the moisture of concrete may travel to cooler regions during exposure of C-PSW/CFs to fire. Several studies have been performed to predict the moisture migration in concrete at elevated temperatures (Choe et al. 2018, Heijden et al. 2007, Khoylou 1997). Mathematical models have been developed to predict the moisture (Ichikawa and England 2003). However, due to the complexity of the mathematical models and lack of clarity in the material properties used in the models, more studies are needed to investigate the moisture migration in the concrete infill in walls without vent holes.

5.3. Water-Cement Ratio

The vapor generation rate can be defined based on the dry concrete volume during exposure to fire loading. The volume of evaporated water (based on the dry concrete volume) can be calculated based on the moisture content of the concrete. The moisture content (w) is defined as the volume of water in a unit volume of concrete. No water loss is assumed. Conservatively, all water in concrete (free and chemically bonded) was assumed to be evaporable.

The vent hole sizes for a range of water-cement ratios (0.30 to 0.38) were calculated. In Fig. 5-3 the size of the vent holes against the effective area size for C-PSW/CFs (examples) with various water-cement ratios is shown. The maximum calculated rate in the examples was used to calculate the vent hole sizes conservatively. The concrete mix in Table 2-2 was used to compute the amount of water for water-cement ratios. The amount of water was altered to achieve the selected water-cement ratio. In Table 5-1, calculated moisture contents for various water-cement ratios are presented. Using lower water-cement ratio results in smaller vent hole diameter (for the same effective area) or larger effective area (for the same vent hole size). As an example, for a vent hole with a 25 mm diameter, the effective area increased from 11.6 m^2 to 14.8 m^2 when the water-cement ratio decreased from 0.38 to 0.30.

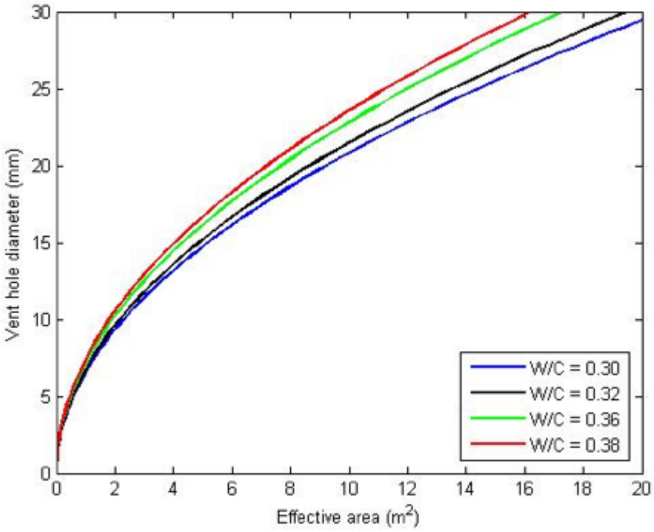

(a) Without fire protection

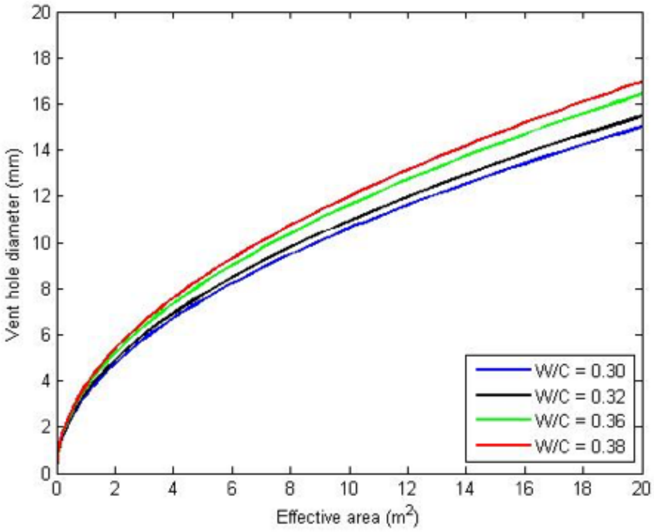

(b) With fire protection

Fig. 5-3. Size of vent holes against the effective area for 4 water-cement ratios

Table 5-1. Calculated moisture contents associated with water-cement ratios

W/C	Water (*lb./cf*)	Moisture content (%)
0.30	210	12.5
0.32	224	13.3
0.36	252	15.0
0.38	267	15.9

5.4. Maximum Vent Holes Spacing

The spacing between vent holes should not exceed the floor height (approximately 3-3.6m or 10-12 ft). At least one vent hole should be provided in the top and bottom of a C-PSW/CF panel at every story.

5.5. Minimum Vent Hole Size

The vent holes have a minimum diameter of 25 mm (1 in) to assure that the vent hole would not get clogged by concrete aggregates. Fig. 5-4 shows a general relationship between the vent hole size and the effective area for a C-PSW/CF system. The highlighted region in Fig. 5-4, shows the range of the effective areas for a single vent hole (with a minimum diameter). The range of the effective areas in the highlighted region depends on the heating rate (Fire protected or unprotected), water-cement ratio and the allowable pressure. For effective areas larger than the highlighted region (larger than A in Fig. 5-4), the required vent hole size should be calculated using Eq. 5-1.

Table 5-2 shows the effective areas for a vent hole with a minimum diameter (25 mm diameter). The considered parameters in Table 5-2 are water-cement ratio (w/c = 0.35-0.40) or moisture ratio (w =0.14 -0.16), the allowable pressure (10 – 15 psi) and the fire protection thickness (0 - 19mm). It should be noted that the spacing between the vent holes should not exceed the maximum vent hole spacing as mentioned in section 5.4. Assuming a maximum effective area of 13 m^2 (3.6 m × 3.6 m), vent holes with 25 mm would be adequate for protected walls as shown in Table 5-2. However, larger vent holes may be required for the same effective area size (highlighted in grey cases in Table 5-2).

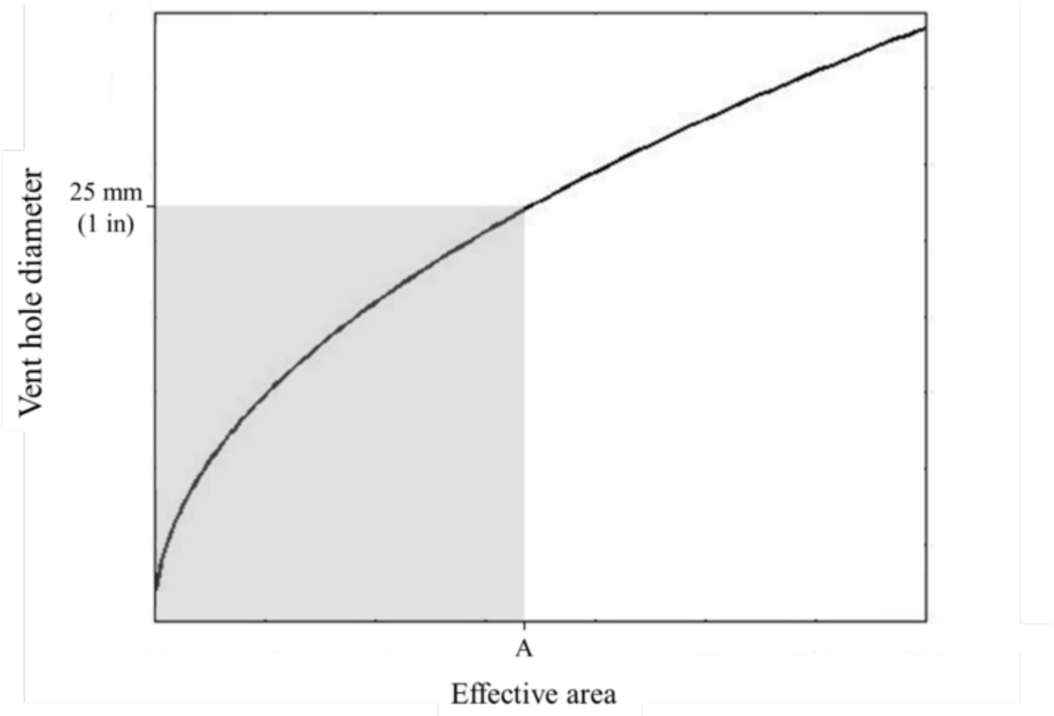

Fig. 5-4. The covered range of effective area by using a minimum vent hole size

Table 5-2. Calculated effective areas (A_{eff}) for various wall properties with a vent hole size of 25 mm diameter

Effective area (m^2) Vent hole size = 25 mm			Unprotected		Protected		Protected		Protected		Protected	
					9.5 mm (3/8 in)		12.7 mm (1/2 in)		15.9 mm (5/8 in)		19.05 mm (3/4 in)	
Allowable Pressure		w	16%	14%	16%	14%	16%	14%	16%	14%	16%	14%
MPa	Psi	w/c	0.40	0.35	0.40	0.35	0.40	0.35	0.40	0.35	0.40	0.35
0.069	10.00	A_{eff} (m^2)	8.8	10.0	19.8	22.6	23.0	26.3	26.0	29.7	28.9	33.0
0.103	15.00		13.2	15.1	29.6	33.9	34.6	39.5	39.0	44.5	43.3	49.5

5.6. Examples

Two examples are provided in this section for designing vent holes for C-PSW/CF with fire protection and without fire protection. The design procedure is based on the recommended method in the current chapter. These examples are provided for a C-PSW/CF with a wall thickness of 609.6 mm (24 in). The details of the wall are presented in Table 5-3.

Table 5-3. Properties of archetype C-PSW/CF

Wall thickness	609.6 mm (24 in)
Faceplate thickness	12.7 mm (0.5 in)
Tie bar spacing	457.2 mm (18 in)
Tie bar diameter	25.4 mm (1 in)
Steel plate slenderness ratio	36
Fire protection thickness	23.81m (15/16 in)

Example 1. Sizing vent holes for a C-PSW/CF without fire protection

Step 1. Perform transient thermal analysis (without fire protection)

Perform thermal analysis to calculate the maximum vapor generation rate. A finite element thermal analysis was performed to determine the dry concrete thickness. Table 5-4 shows the time different parts of wall temperature had achieved to 100°C. The rate of vapor generation is calculated for all locations and the maximum rate would occur was selected. The rate was calculated by dividing the dry concrete thickness to the associated time for a unit area.

Table 5-4. Calculation of maximum vapor generation rate

Locations (Through Thickness) (mm)	**0**	**19.05**	**38.1**	**57.15**	**76.2**	**95.25**	**114.3**	**133.35**	**152.4**	**171.45**
Time (min)	6.51	15.86	29.90	47.15	67.80	92.85	122.37	156.74	193.88	236.69
Rate	0.00	1.20	1.27	1.21	1.12	1.03	0.93	0.85	0.79	0.72

Step 2. Calculate maximum allowable pressure

$\rho = 1000\ {}^{kg}\!/_{m^3}$	Water density
$g_c = 9.81\ {}^{m}\!/_{s^2}$	Acceleration of gravity
$h = 9\,m$	Maximum concrete pouring height (Bhardwaj et al. 2018b)
$P = \rho . g_c . h = 88290 Pa$	Maximum allowable build-up pressure

Step 3. Calculate vapor generation rate (without fire protection)

$\rho = 1000\ {}^{kg}\!/_{m^3}$	Water density
$\omega = 16\%$	Moisture content (%-By volume)
$L_{eff} = 1m$	Effective area dimension (length)

$A_{eff} = L_{eff}^2 = 1m^2$	Vent hole effective area
$T_{dc} = 38.1mm$	Dry concrete thickness
$t_{dc} = 29.9\min$	Time (associated with dry concrete thickness)
$V_{dc} = T_{dc}.A_{eff} = 0.038m^3$	Dry concrete volume (for effective area)
$V_w = V_{dc}.w = 0.006m^3$	Evaporated water volume
$m = \frac{V_w \rho}{t_{dc}} = 3.4 \, {}^{gr}\!/_{\min}$	Vapor discharge rate

Step 4. Calculate vent hole size

$T = 200^{\circ}C$	Vapor temperature (Conservatively)
$\gamma = 1.315$	Heat capacity ratio at 200 °C
$K_d = 0.62$	Discharge coefficient
$R = 8.424 \frac{kg\, m^2}{s^2\, K\, mol}$	Universal gas constant
$M_m = 0.018 \, {}^{kg}\!/_{mol}$	Molar weight of water
$A = \frac{m}{K_d P \sqrt{\frac{\gamma M_m}{\overline{R}T} \left(\frac{2}{\gamma+1} \right)^{\left(\frac{\gamma+1}{\gamma-1} \right)}}} = 43.58mm^2$	Vent hole area
$d = 2.\sqrt{{}^{A}\!/_{\pi}} = 7.45\, mm$	Vent hole diameter

Use a minimum vent hole size with 25 mm diameter.

Step 5. Calculate vent hole size for different effective areas

The steps above can be repeated for a range of effective areas. In Fig. 5-5 the size of the vent hole for various effective areas and allowable pressure equal to P/2, P and 2P is shown.

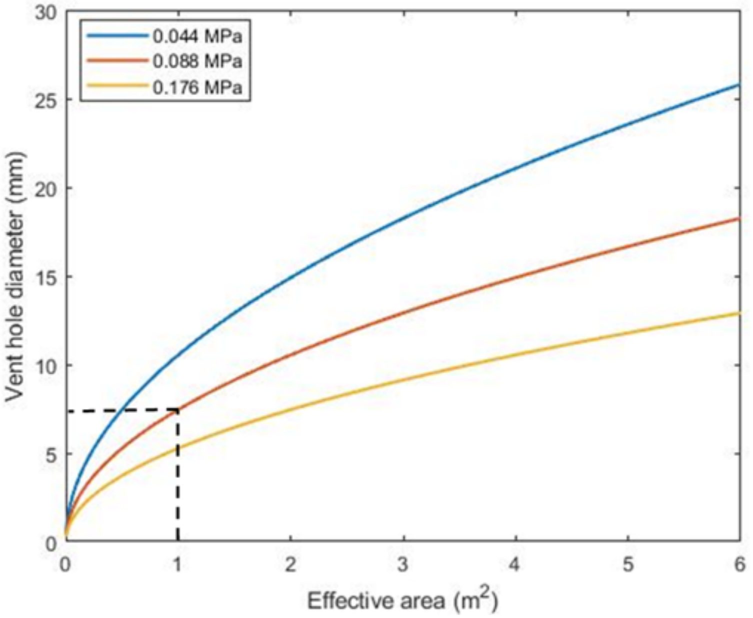

Fig. 5-5. Vent hole sizes for various effective areas and allowable pressures (Without fire protection)

Example 2. Sizing vent holes for a C-PSW/CF with fire protection

Step 1. Perform transient thermal analysis (With fire protection)

Perform thermal analysis to calculate the maximum vapor generation rate. An FE thermal analysis was performed to determine the dry concrete thickness. Table 5-5 shows at what time different parts of wall temperature had achieved to 100°C. The rate of vapor generation is calculated for all locations and the maximum rate would occur was selected. The rate was calculated by dividing the dry concrete thickness to the associated time for a unit area.

Table 5-5. Calculation of maximum vapor generation rate

Locations (Through Thickness) (mm)	**0**	**19.05**	**38.1**	**57.15**	**76.2**
Time (min)	62.40	92.88	132.72	178.56	230.40
Rate	0.00	0.21	0.29	0.32	0.33

Step 2. Calculate maximum allowable pressure

$\rho = 1000 \, {}^{kg}\!/_{m^3}$	Water density
$g_c = 9.81 \, {}^{m}\!/_{s^2}$	Acceleration of gravity
$h = 9\,m$	Maximum concrete pouring height (Bhardwaj et al. 2018b)
$P = \rho . g_c . h = 88290 Pa$	Maximum allowable build-up pressure

Step 3. Calculate vapor generation rate

$\rho = 1000 \, {}^{kg}\!/_{m^3}$	Water density
$\omega = 16\%$	Moisture content (%-By volume)
$L_{eff} = 1m$	Effective area dimension (length)
$A_{eff} = L_{eff}^2 = 1m^2$	Vent hole effective area

$T_{dc} = 76.2mm$	Dry concrete thickness
$t_{dc} = 230.40\min$	Time (associated with dry concrete thickness)
$V_{dc} = T_{dc}.A_{eff} = 0.076m^3$	Dry concrete volume (for effective area)
$V_w = V_{dc}.w = 0.0012m^3$	Evaporated water volume
$m = \frac{V_w \rho}{t_{dc}} = 0.88 \, {}^{gr}\!/\!_{\min}$	Vapor discharge rate

Step 4. Calculate vent hole size

$T = 200^\circ C$	Vapor temperature (Conservatively)
$\gamma = 1.315$	Heat capacity ratio at 200 °C
$K_d = 0.62$	Discharge coefficient
$R = 8.424 \frac{kg\, m^2}{s^2\, K\, mol}$	Universal gas constant
$M_m = 0.018 \, {}^{kg}\!/\!_{mol}$	Molar weight of water
$A = \frac{m}{K_d P \sqrt{\frac{\gamma M_m}{\overline{R}T}\left(\frac{2}{\gamma+1}\right)^{\left(\frac{\gamma+1}{\gamma-1}\right)}}} = 11.31mm^2$	Vent hole area
$d = 2.\sqrt{{}^{A}\!/\!_{\pi}} = 3.8\,mm$	Vent hole diameter

Use a minimum vent hole size with a 25 mm diameter.

Step 5. Calculate vent hole size for different effective areas.

The steps above can be repeated for a range of effective areas. In Fig. 5-6 the size of the vent hole for various effective areas and allowable pressure equal to P/2, P and 2P is shown.

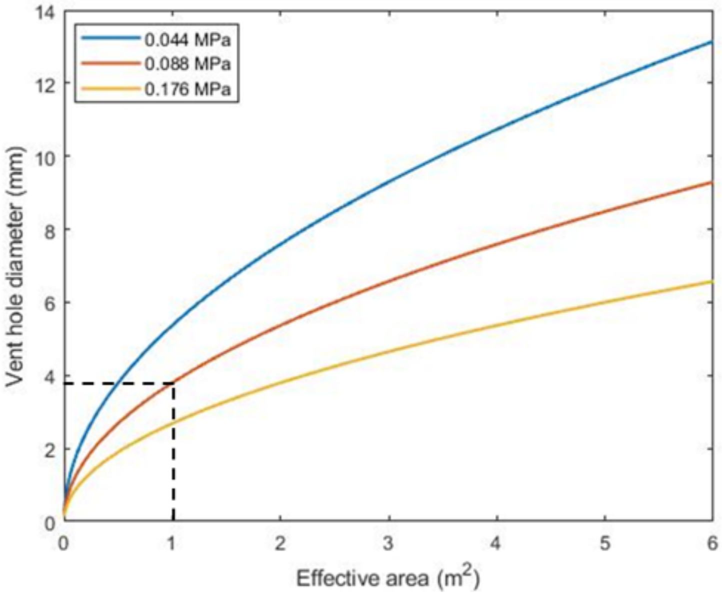

Fig. 5-6. Vent hole sizes for various effective areas and allowable pressures (With fire protection)

5.7. Summary and Conclusions

The free and bonded water in concrete evaporates at elevated temperatures. The vapor can be trapped between the faceplate and concrete. By increasing the temperature of the vapor, the pressure builds up behind the faceplate. Vent holes can reduce built-up pressures by letting steam / vapor escape. Prescriptive methods have not been developed to design the vent holes for composite members. Therefore, a rational method was developed to size the vent holes. In the developed method, it is assumed that the maximum allowable pressure does not exceed the pressure associated with the maximum concrete pouring height (9 m) or any specified allowable pressure by the designer. The vent hole sizes for allowable pressure equivalent to 4.5 m and 18 m of concrete pouring height were calculated. The vent hole diameter increased by about 30% and decreased by about 40%, respectively, compared to the vent hole sizes associated with pressure equivalent to 9 m concrete pouring height.

Vent hole size can be calculated based on the effective area for a single vent hole, which depends on the vent hole spacing. The comparison of vent holes size for different moisture contents (0.30 - 0.38) showed that smaller vent hole sizes can be used for concrete mixes with lower water-cement ratios. The diameter of vent holes reduced around 13% by decreasing the moisture ratio from 0.38 to 0.30. A minimum vent hole diameter of 25 mm is recommended to avoid vent hole closure by concrete aggregate during a fire event. To further investigate the developed method, experimental studies can be conducted to study the effect of buildup vapor pressure on C-PSW/CFs and to provide detailed recommendations for concrete properties and detailing of vent holes.

Chapter 6. Summary and Conclusions

Composite-Plate Shear Wall/Concrete Filled (C-PSW/CF), also known as SpeedCore walls, are being considered for commercial high-rise buildings. C-PSW/CF system is an efficient lateral load resisting system. However, understanding the behavior and performance of C-PSW/CF system under fire loading is also essential. During a fire event, the steel faceplate at the exterior surface of the wall (around the concrete core) would be directly exposed to fire and a non-linear thermal gradient can develop through the wall thickness. The mechanical properties of steel and concrete materials undergo degradation at elevated temperatures. Consequently, composite walls can lose their load bearing capacity under combined fire loading. There is a need to experimentally and numerically evaluate the fire behavior and resistance of C-PSW/CF and to develop structural performance based design recommendations. This study consisted of the following steps:

- Experimental studies were conducted to evaluate the behavior of C-PSW/CF system at elevated temperatures. Five C-PSW/CF specimens were tested under combined axial and fire loading. Axial load ratio, steel plate slenderness ratio, using shear studs between tie bars and two fire scenarios (Uniform vs single-sided heating) were considered in the design of the specimens for current fire tests. The results of previous experimental studies (from the literature) were compiled with the current fire tests, in which the wall slenderness ratio, wall thickness, steel plate reinforcement ratio, and fire scenario (Uniform vs single-sided heating) were considered as the main parameters. The comprehensive results of fire tests were used to benchmark numerical models developed in this study.

- Two numerical approaches namely Finite Element Analysis (FEA) and Fiber Analysis were used to perform analytical parametric studies. A fiber-based tool was developed in the current study. This tool can be used to evaluate thermal and structural behavior for standard and non-standard fire scenarios. A user graphical interface was developed for this tool to make users' interaction simple and efficient. The fiber-based tool was validated using experimental and analytical (FEA) results. Composite columns and walls can be analyzed under standard and user input fire time-temperature curves. Various temperature-dependent material models can be selected by the user.

- The results from experimental investigations were utilized to benchmark the FEA models. Eurocode material properties at elevated temperatures and ISO 834 standard fire time-temperatures were applied. The effect of wall slenderness ratio, wall thickness, load ratio, plate slenderness ratio, concrete strength, steel plate reinforcement ratio, boundary conditions and fire scenario (uniform vs single sided heating) were studied in the parametric study as described in section 3.3 and 4.4. A conservative and computationally efficient method (unit width columns) was developed to design walls under fire loading. The results of the parametric studies led to the development of equations to estimate the strength and the load bearing capacity of C-PSW/CFs.

- Concrete filled steel tube (CFT) columns are popular in practice since they combine the structural properties and advantages of concrete and steel material. However, there are no mechanics-based approaches or equations to calculate the load capacity of CFTs at elevated temperatures. A parametric study was conducted on the fire performance of CFTs using the fiber-based tool developed in the current study. Section aspect ratio (column depth/width), cross section slenderness (steel plate slenderness), steel yield stress, concrete compressive strength and effect of fire protection were considered in the parametric study. The detail results of the parametric study are discussed in section 4.3. The results obtained from the parametric study were used to develop equations to estimate the axial capacity of CFTs at elevated temperatures.

- The existing bound and unbound water in concrete (concrete core in C-PSW/CF) evaporates at elevated temperatures. During a fire event, the water vapor can be trapped by the steel faceplate. The imposed pressure on the faceplate increases as the temperature of the trapped water vapor rises. The trapped water vapor can escape through the appropriately sized vent holes. A rational method was developed (as discussed in Chapter 5) to limit the produced pressure by designing the vent holes.

The key conclusions from the experimental and numerical investigation of C-PWS/CFs and CFTs under combined fire and gravity loads are as follows:

- The cooler region in the middle of the concrete core helps maintain the load bearing capacity of composite walls. Increasing the wall thickness can improve the fire resistance rating of C-PSW/CFs, significantly.

- The observations (from experimental and numerical analysis) showed that the local buckling of the steel faceplates occurred between tie bar locations. However, this local buckling did not lead to failure or significant loss of load capacity at elevated temperature.

- Limiting the plate slenderness (s/t_p, tie spacing / plate thickness) ratio improves the fire resistance of the C-PSW/CF. It is recommended to limit the plate slenderness ratio to $1.2\sqrt{E/F_y}$, where E is the modulus of elasticity of the steel plate and F_y is the steel plate yield strength.

- Increasing wall slenderness ratio (story height/ wall thickness) can have a detrimental effect on the fire resistance of composite walls. The fire resistance rating of walls reduced by around 55% when the wall slenderness ratio was increased from 5 to 20.

- Composite walls subjected to one-sided heating have much longer fire resistance (time) than walls subjected to two-sided heating. This is related to the contribution of the steel faceplate and concrete on the unheated side. However, this conclusion is limited to composite walls with slenderness ratio less than or equal to 20.

- For composite walls with slenderness ratio greater than 20, the thermal gradient and bowing resulting from one-sided heating leads to early onset of global instability. This reduces the fire resistance (time) significantly. Consequently, walls with slenderness ratio greater than 20 should have fire protection / insulation at least on the side that may be exposed to fire.

- Vent holes are required and recommended for composite walls to relieve the build-up of steam or vapor pressure caused by water evaporation from heated concrete. Vent hole design depends on the thermal gradient through the concrete, rate of moisture evaporation, and the allowable pressure on the steel faceplate. The water-to-cement ratio in the concrete mix design has a minor influence on the design of vent holes.

- Vent hole diameter and spacing can be designed using the method and equations presented in this report. However, a minimum vent hole diameter of 25 mm is recommended with at least two vent holes along the story height at each floor.

- CFTs with higher cross-section slenderness (non-compact or slender sections) have lower fire resistance since steel cannot reach its yield strength in slender sections. A higher fraction of axial load was resisted by the concrete core at the early stages of fire exposure. The capacity of CFTs reduces significantly by reducing the concrete compressive strength. Protected CFTs had lower axial capacity at the same surface temperature however fire protection can increase the fire resistant rating (time) of CFTs by around 2.5 times.

The findings and data from the experimental and numerical analysis were used to develop design equations for C-PSW/CFs and CFTs subjected to combined axial and fire loading:

- The axial capacity of C-PSW/CF and CFTs at elevated temperatures can be estimated using the following proposed equations:

  C-PSW/CF: $$P_n(T) = 0.32^{\left(\frac{P_{no}(T)}{P_e(T)}\right)^{0.3}} P_{no}(T)$$

  CFT: $$P_n(T) = 0.45^{\left(\frac{P_{no}(T)}{P_e(T)}\right)^{0.3}} P_{no}(T)$$

  Where $P_{no}(T)$ is the section axial load capacity and $P_e(T)$ is column elastic buckling capacity at elevated temperatures.

  The equation for C-PSW/CFs is to be used along with the unit width method for conservatively calculating the axial capacity of the composite wall at elevated temperature. In this method, 1D thermal analysis is conducted to calculate the properties of a unit with of the wall cross section [$P_{no}(T)$, $P_e(T)$] at elevated temperatures (as discussed in section 3.3.3) to be used with the proposed design equations.

- The fire resistance rating (time) of unprotected C-PSW/CF (exposed to standard ISO 834 time-temperature curve) can be estimated using the following proposed equation:

$$R = \left[-18.5 \left(\frac{P_u}{P_n} \right)^{\left(0.24 - \frac{H/t_w}{230}\right)} + 15 \right] \left(\frac{1.9 t_w}{200} - 1 \right)$$

Where P_u is the applied axial load, P_n is the axial capacity at ambient temperature based on AISC 360-16 section I2.2. H/t_w is the wall slenderness ratio and t_w is wall thickness. This equation is limited for C-PSW/CF walls with a steel plate slenderness less than $1.2\sqrt{(E/F_y)}$, tie spacing-to-wall thickness, $s_{tie}/t_w \leq 1.0$, load ratio, $P_u/P_n \leq 0.2$ and wall thickness, t_w between 200 and 600 mm.

The findings in the current research are limited to the range of considered parameters. The proposed equations and recommendations for the design of C-PSW/CFs and CFTs under fire loading can be used in the development of design guidelines and specifications. A code change proposal to AISC 360-22, Appendix 4 is presented in Appendix A of the current report.

Appendix A. Proposal to AISC 360-22 Appendix 4.

The findings of the current research including proposed design and fire resistance rating equations will be proposed to AISC to be considered in the next AISC 360-22 specification (Appendix. 4). This appendix presents the code change proposal (Appendix 4 and commentary) based on the current research. It should be noted that this proposal may be changed in the future. AISC 360-16 was used to cite sections (or equations) in other chapters of the specification.

1. Structural Design Requirement

1.1. General Structural Integrity

(a) Vent Holes

The requirement for steam vent holes in concrete-filled columns and concrete-filled composite plate shear walls shall be evaluated. Any rational method that considers heat transfer through the cross-section, water content in concrete, fire protection, and the allowable pressure build up in the member is permitted for calculating the size and spacing of vent holes.

2. Design by Simple Methods of Analysis

(a) Design for Compression in Concrete-Filled Composite Columns

For concrete-filled composite columns, the nominal strength for compression shall be determined using the provisions of Section I2.2 with steel and concrete properties as stipulated in Section A-4.2.3b. Equation A-1 shall be used in lieu of Equations I2-2 and I2-3 to calculate the nominal compressive strength for flexural buckling:

$$P_n(T) = 0.45^{\left(\frac{P_{no}(T)}{P_e(T)}\right)^{0.3}} P_{no}(T) \tag{A-1}$$

where $P_{no}(T)$ is calculated at elevated temperature using Equations I2-10, I2-11, and I2-12. $P_e(T)$ is calculated at elevated temperature using Equations I2-5, I2-13, and I2-14. $F_y(T)$, $f'_c(T)$, $E_s(T)$, and $E_c(T)$ are obtained using coefficients from Tables A-4.2.1 and A-4.2.2.

(b) Design for Compression in Concrete-Filled Composite Plate Shear Walls

For concrete-filled composite plate shear walls, the nominal strength for compression shall be determined using the provisions of Section I2.3 with steel and concrete properties as stipulated in Section A-4.2.3b and Equation A-4-2 used in lieu of Equations I2-2 and I2-3 to calculate the nominal compressive strength for flexural buckling:

$$P_n(T) = 0.32^{\left(\frac{P_{no}(T)}{P_e(T)}\right)^{0.3}} P_{no}(T) \tag{A-2}$$

where $P_{no}(T)$ is calculated at elevated temperature using Equation I2-16. $P_e(T)$ is calculated at elevated temperature using Equations I2-5 and I1-1. $F_y(T)$, $f'_c(T_c)$, $E_s(T)$, and $E_c(T_c)$ are obtained using coefficients from Tables A-4.2.1 and A-4.2.2.

User Note: For composite members, the steel temperature is determined using heat transfer equations with heat input corresponding to the design-basis fire. The temperature distribution in concrete infill can be calculated using one- or two-dimensional heat transfer equations. The regions of concrete infill will have varying temperatures and mechanical properties. Concrete contribution to axial strength and effective stiffness can therefore be calculated by discretizing the cross-section into smaller elements (with each concrete element considered to have a uniform temperature) and summing up the contribution of individual elements.

3. Structural Steel Assemblies

Composite Plate Shear Walls

For unprotected composite plate shear walls meeting the requirements of Chapter I, the fire resistance rating is permitted to be determined in accordance with Equation A-3.

$$R = \left[-18.5\left(\frac{P_u}{P_n}\right)^{\left(0.24-\frac{H/t_w}{230}\right)} + 15\right]\left(\frac{1.9t_w}{8} - 1\right) \tag{A-3}$$

$$R = \left[-18.5\left(\frac{P_u}{P_n}\right)^{\left(0.24-\frac{H/t_w}{230}\right)} + 15\right]\left(\frac{1.9t_w}{200} - 1\right) \tag{A-3M}$$

where R is the fire rating in hours, P_u is the applied axial load in kips (kN), and H, t_w, and P_n are as defined in Chapter I.

The use of Equation A-1 shall be limited to walls satisfying all the following conditions:

- Wall slenderness ratio (H/t_w) is less than or equal to 20
- Axial load ratio (P_u/P_n) is less than or equal to 0.2
- Wall thickness, t_w, is between 8 in. and 24 in. (200 mm and 600 mm)

Commentary

1c. General Structural Integrity

Concrete filled composite columns and shear walls subjected to fire loading will experience internal pressure build-up due to the steam emanating from concrete at elevated temperatures. The steam needs to be vented out to prevent the pressure build-up and its adverse effects on the members. The magnitude and rate of internal pressure build-up for a design-basis fire depends on the fire protection and moisture content of concrete infill. In current research a rational method was developed that considers these factors and can be used to calculate the size and spacing of vent holes required to limit the internal pressure build-up to a specified value.

2c. Design by Simple Methods of Analysis

Simple methods may suffice when a structural member or component can be assumed to be subjected to uniform heat flux on all sides and the assumption of a uniform temperature is reasonable as, for example, in a free-standing column surrounded by fire. For composite shear walls, the simplified analyses can be conducted per unit width of the wall and one-dimensional heat-transfer equations can be used to model the thermal response. The unit width method for shear walls is conservative and can be used for different configurations of the walls, including planar walls and C-shaped walls.

The equations for compression strength of composite columns and composite plate shear walls at elevated temperatures have been developed based on parametric studies conducted in current research. A numerical tool developed and benchmarked to evaluate the fire performance of concrete-filled columns. The authors conducted a study to evaluate the effect of parameters such as the aspect ratio (length-to-width ratio), section slenderness, and concrete and steel strengths on the strength degradation at elevated temperatures. Figure A1 shows the comparison of Equation A-1 with the parametric study data from the tool. Equation A-1 provides a lower-bound estimate of composite columns compression strength.

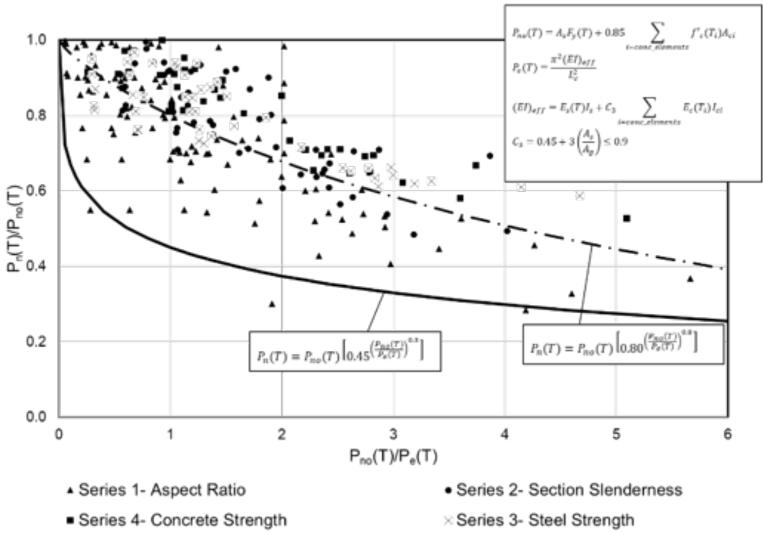

Fig. A1. Comparison of compression strength of concrete-filled composite columns with Equation A-1

In current research a detailed finite element analyses for composite plate shear walls was conducted, using models validated against experimental data. Fig. A-2 shows the comparison of Eq. A-2 with the finite element data. The data plotted includes planar walls with length-to-thickness ratio of 3 and corresponding unit width column strips (with no flange plates). Equation A-2 provides a lower-bound estimate of composite shear wall compression strength.

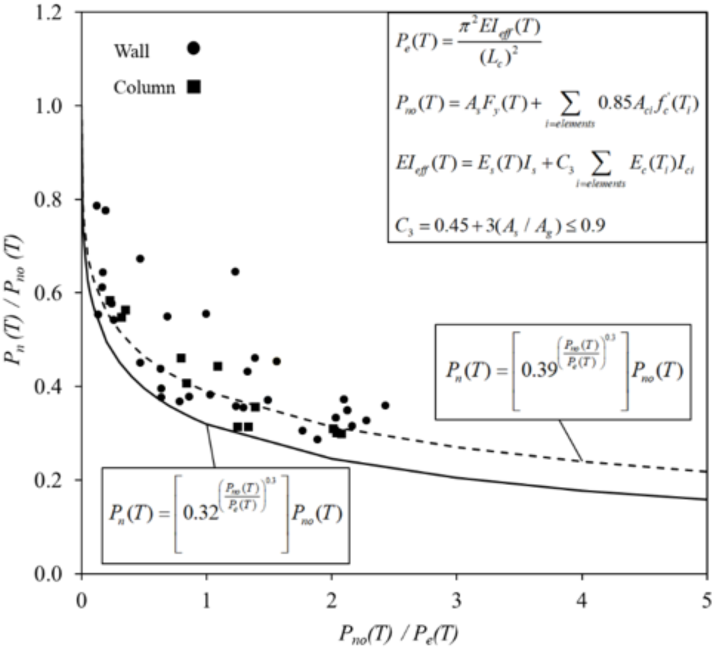

Fig. A-2. Comparison of compression strength of composite shear walls and unit strip columns with Equation A-2.

3.c Composite Plate Shear Walls

Equation A-3 for determining the fire resistance rating of composite plate shear walls is based on current research. The equation provides conservative failure times for walls subjected to standard ISO or ASTM fire scenarios. The equations are based on data obtained from experiments and benchmarked numerical models. The equation can be used for composite plate shear walls that meet the detailing and design requirements of Chapter I, namely the steelplate slenderness and tie spacing requirements. The limits for applicability of Equation A-2 are based on the range of parameters considered in the study. For walls with slenderness greater than 20, one-sided fire scenarios may start controlling the failure of the wall and additional fire-protection may need to be provided. Typical axial load ratios for composite plate shear walls are in the range of 10-20%.

Appendix B. Axial Displacement Correction

This appendix presents the method used to calculate the axial displacements on the exposed and unexposed surface of the specimen. To protect the sensors against high temperatures, the string potentiometers were located 475 mm (18.5 in) away from the web of the C-PSW/CF specimen (Points A’ and B’ in Fig. B1). The specimen CW2 was bent due to the thermal expansion of the exposed side of the wall. To calculate the axial displacements on the exposed and unexposed surface of the specimens (points A and B, respectively), the error in the measured displacements (at points A’ and B’) were deducted.

A schematic plan view of the deformed specimen is shown in Fig. B1. The angle section on the specimen with the string potentiometers and the location of the string potentiometers are shown in Fig. B1(a). The axial displacements on the exposed and unexposed surfaces (a and b) were calculated based on the measured displacements (a’ and b’) as follows:

L_a = The distance of SP2 from the exposed surface

L_b = The distance of SP4 from the unexposed surface

a' = (Measured displacement by SP2)/2

b' = (Measured displacement by SP4)/2

$L = L_a + t_w + L_b$	The distance of sensors from each other
$\arcsin(\theta) = {}^{(a'+b')}\!/_{L}$	Rotation of the angle
$Error_a = L_a \sin(\theta)$	Calculated error in SP2
$Error_b = L_b \sin(\theta)$	Calculated error in SP4
$a = a' + 2(a' - Error_a)$	The correct axial displacement on the exposed surface
$b = b' + 2(b' - Error_b)$	The correct axial displacement on the unexposed surface

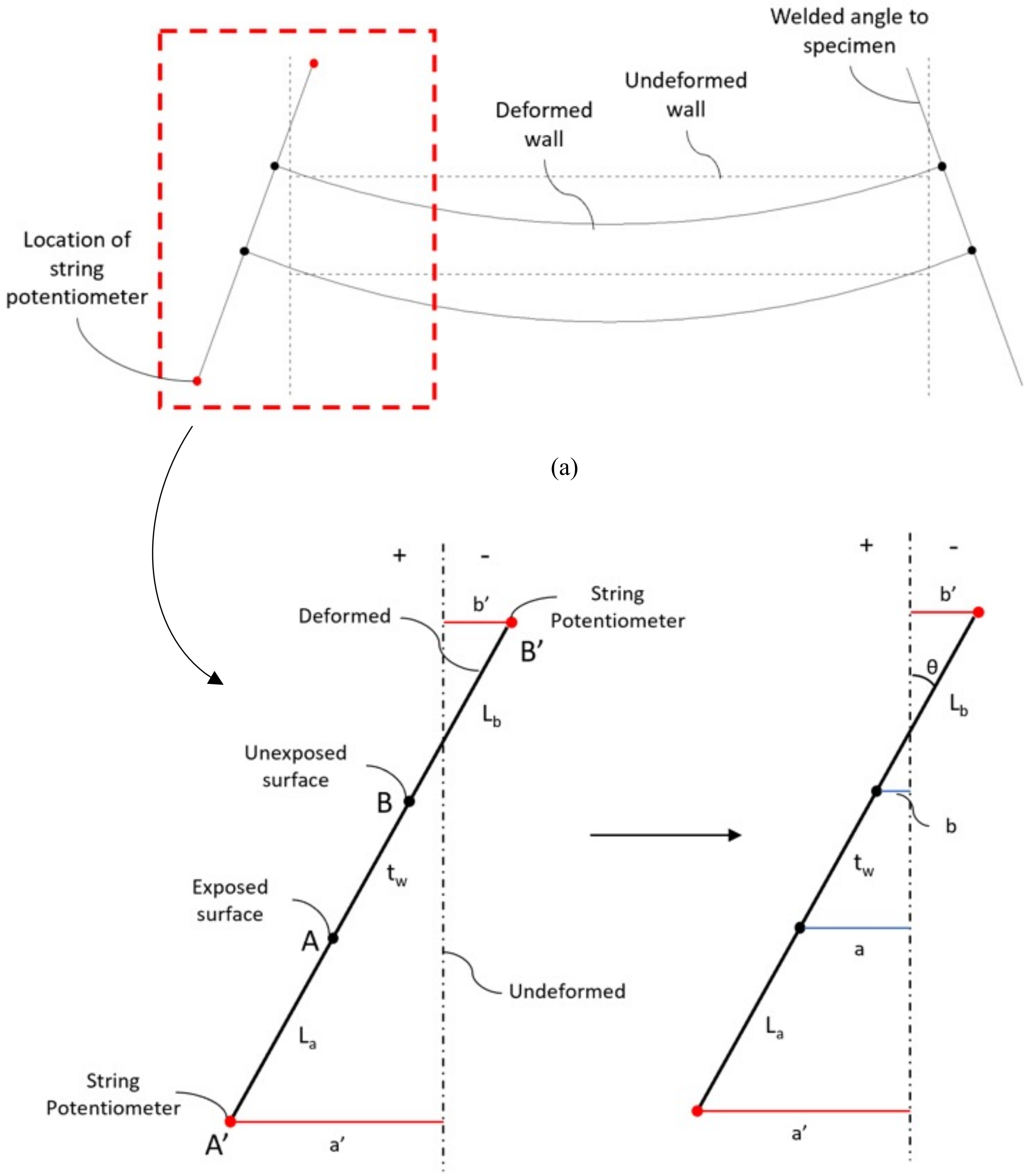

(a)

(b)

Fig. B1. Schematic plan view of deformed shape of CW2 specimen with the detail

References

AISC (American Institute of Steel Construction). (2016). "Specification for structural steel buildings." AISC 360-16, Chicago, IL.

AISC (American Institute of Steel Construction). (2016). "Seismic Provisions for Structural Steel Buildings." AISC 341, Chicago, IL.

ASTM (American Standards of Testing and Materials). (2000). "Standard Test Methods for Fire Tests of Building Construction and Materials." ASTM E-119,

Alzeni, Y. and Bruneau, M. (2014). "Cyclic Inelastic Behavior of Concrete Filled Sandwich Panel Walls Subjected to In-Plane Flexure," *Technical Report MCEER-14-0009*, MCEER, University at Buffalo, Buffalo, NY.

ASCE *(*American Society of Civil Engineers). (2016). "*Minimum Design Loads for Buildings and Other Structure"ASCE 7.* Reston, VA.

Bhardwaj, S.R., and Varma, A.H. (2016). "Effect of Imperfections on the Compression Behavior of SC Walls." *Proceedings of the Annual Stability Conference*, Structural Stability Research Council, Orlando, FL. April 12-15, 11 pp

Bhardwaj, S.R., and Varma, A.H. (2017a). "SC Wall Compression Behavior: Interaction of Design and Construction Parameters." *Proceedings of the Annual Stability Conference*, Structural Stability Research Council, San Antonio,Texas, March 2017, 14 pp.

Bhardwaj, S.R., and Varma, A.H. (2017b). "Design of Modular Steel-plate Composite Walls for Safety-related Nuclear Facilities." *AISC Design Guide 32*. American Institute of Steel Construction, Chicago, IL, USA

Bhardwaj, S.R., Varma, A.H., Orbovic, N. (2018). "Behavior of Steel-plate Composite Wall Piers under Biaxial Loading." *Journal of Structural Engineering*, ASCE, Vol. 145, Issue 2, Feb. 2019. https://doi.org/10.1061/(ASCE)ST.1943-541X.0002247

Bhardwaj, S.R., Varma, A.H., Wazalwar, P. (2019). "Axial Force-Biaxial Moment-Vector Shear (P-M-V) Interaction for Steel-plate Composite (SC) Wall Piers." *Nuclear Engineering and Design* 349 (April):162–73. https://doi.org/10.1016/j.nucengdes.2019.04.022.

Bhardwaj, S.R., Wang, A.Y., Varma, A.H. (2018b), "Slenderness Requirements for CF-CPSW: The Effects of Concrete Casting" in *Proceedings of Eighth International Conference on Thin-Walled Structures*, Lisbon,Portugal, 15 pp

Bruneau, M., Alzeni, Y., and Fouché, P. (2013). "Seismic behavior of concrete-filled steel sandwich walls and concrete-filled steel tube columns." *Steel Innovations 2013 Conf.*, Christchurch, New Zealand.

Cedeno, G., Varma, A.H., and Agarwal, A. (2009). "Behavior of Floor Systems under Realistic Fire Loading." *Proceedings of the 2009 Structures Congress, ASCE*.

Choe, G., Kim, G., Yoon, M., Hwang, E., Nam, J., & Guncunski, N. (2019). Effect of moisture migration and water vapor pressure build-up with the heating rate on concrete spalling type. *Cement and Concrete Research*, *116*, 1-10.

Eurocode (2005). "Eurocode 4: Design of Composite Steel and Concrete Structures–Part 1-2: General Rules Structural Fire Design." EN 1994-1-2, Brussels, Belgium.

Epackachi, S., Nguyen, N., Kurt, E., Whittaker, A. and Varma, A.H. (2015). "In-Plane Seismic Behavior of Rectangular Steel-Plate Composite Wall Piers." *Journal of Structural Engineering*, ASCE, Vol. 141, No. 7.

Fischer, E. C., & Varma, A. H. (2017). Fire resilience of composite beams with simple connections: Parametric studies and design. *Journal of Constructional Steel Research*, *128*, 119-135.

Heinisuo, M., & Jokinen, T. (2014). Tubular composite columns in a non-symmetrical fire. *Magazine of Civil Engineering*, (5).

Hong, S. (2007). *Fundamental behavior and stability of CFT columns under fire loading* (Doctoral dissertation, Purdue University).

Hong, S., & Varma, A. H. (2009). Analytical modeling of the standard fire behavior of loaded CFT columns. *Journal of Constructional Steel Research*, *65*(1), 54-69.

Hong, S., Varma, A. H., (2009). Predicting Fire Behavior of Composite CFT Columns Using Fundamental Section Behavior, Journal of ASTM International, Vol. 7, No. 1

Hou, X., Kodur, V. K., & Zheng, W. (2015). Factors governing the fire response of bonded prestressed concrete continuous beams. *Materials and structures*, *48*(9), 2885-2900.

Hu, B., Huang, J. Q., & Lou, G. B. (2018). "Degradation of Out-of-plane Initial Stiffness of Steel-concrete Walls Exposed to Fire." *International Journal of Steel Structures*, *18*(1), 51-67.

Ichikawa, Y., & England, G. L. (2004). Prediction of moisture migration and pore pressure build-up in concrete at high temperatures. *Nuclear Engineering and design*, *228*(1-3), 245-259.

Khoylou, N. (1997). Modelling of moisture migration and spalling behaviour in non-uniformly heated concrete.

Kodur, V. K., & MacKinnon, D. H. (2000). Design of concrete-filled hollow structural steel columns for fire endurance. *Engineering Journal-American Institute of Steel Construction*, *37*(1), 13-24.

Kurt, E.G., Varma, A.H., Booth, P.N. and Whittaker, A. (2016). "In-plane Behavior and Design of Rectangular SC Wall Piers Without Boundary Elements." *Journal of Structural Engineering*, ASCE, Vol. 142, No. 6.

Lai, Z., & Varma, A. H. (2016). Effective stress-strain relationships for analysis of noncompact and slender filled composite (CFT) members. *Engineering Structures*, *124*, 457-472.

Lee, J., & Fenves, G. L. (1998). Plastic-damage model for cyclic loading of concrete structures. *Journal of engineering mechanics*, *124*(8), 892-900.

Lie, T., ed., (1992). Structural Fire Protection" Manual and Reports on Engineering Practice No. 78, ASCE, New York, N.Y.

Lie, T. T., & Irwin, R. J. (1995). Fire resistance of rectangular steel columns filled with bar-reinforced concrete. *Journal of structural engineering*, *121*(5), 797-805.

Lue, D. M., Liu, J. L., & Yen, T. (2007). Experimental study on rectangular CFT columns with high-strength concrete. *Journal of Constructional Steel Research*, *63*(1), 37-44.

Moon, I, Jee, N, Kim, W, Lee, C.S., Yoo, S.T. (2009). "Performance-based design of Stiffened Steel Plate Concrete Wall in Fire.". *Transactions of International Conference on Structural Mechanics in Reactor Technology*, *SMiRT 20*, Div. 6, Paper 1675, Espoo, Finland.

ISO-834 (*International Standard ISO 834*). (1975). "Fire resistance tests-elements-elements of building construction*."* Geneva, 1975.

Ji, X., Cheng, X., Jia, X., and Varma, A.H. (2017). "Cyclic In-Plane Shear Behavior of Double-Skin Composite Walls in High-Rise Buildings." *Journal of Structural Engineering*, Vol. 143, No. 6, ASCE, Reston,VA. https://doi.org/10.1061/(ASCE)ST.1943-541X.0001749

Jia-Qi Liu, Lin-Hai Han, Xiao-Ling Zhao. (2018) "Performance of concrete-filled steel tubular column-wall structure subjected to ISO-834 standard fire: analytical behavior." *Thin-Walled*

Structures, Volume 129, 2018, Pages 28-44, ISSN 0263-8231, https://doi.org/10.1016/j.tws.2018.03.027.

Ollgaard, J. G., Slutter, R. G., & Fisher, J. W. (1971). “Shear strength of stud connectors in lightweight and normal weight concrete.” *AISC Eng'g Jr.,* April 1971 (71-10).

Poh, K. W. (2001). Stress-strain-temperature relationship for structural steel. *Journal of materials in civil engineering*, *13*(5), 371-379.

Rodrigues, J. P. C., Laím, L. M., & Korzen, M. (2014). Fire behaviour of circular concrete columns with restrained thermal elongation. *Journal of Advanced Concrete Technology*, *12*(9), 289-298.

Selden, K. L. (2014). “Structural behavior and design of composite beams subjected to fire.”

Selvarajah, R. (2013). “Behavior and design of earthquake-resistant dualplate composite shear wall systems.” Ph.D. dissertation, Purdue Univ., West Lafayette, IN.

Seo, J., Varma, A. H., Sener, K., & Ayhan, D. (2016). “Steel-plate composite (SC) walls: In-plane shear behavior, database, and design.” *Journal of Constructional Steel Research*, *119*, 202-215.

Shafaei S., Wang A., Varma A.H., and Morgen B. (2018a). “Stability of Steel Modules during Construction.”*Proceedings of the Annual Stability Conference-Structural Stability Research Council.* Baltimore, Maryland, April 10-13, 2018.

Shafaei S., Wang A., Varma A.H., and Morgen B. (2018b). “Shear Buckling of Thin-Walled Built-Up Steel Modules Before Composite Phase.” *Eighth International Conference on Thin-Walled Structures-ICTWS*, Lisbon, Portugal, July 24-27.

Simulia (2016). *ABAQUS 2017 Documentation*, Dassault Systemes Simulia Corporation Providence, RI.

Van Der Heijden, G. H. A., Van Bijnen, R. M. W., Pel, L., & Huinink, H. P. (2007). Moisture transport in heated concrete, as studied by NMR, and its consequences for fire spalling. *Cement and concrete research*, *37*(6), 894-901.

Varma, A. H., Hong, S., & Choe, L. (2013). “Fundamental behavior of CFT beam-columns under fire loading.” *Steel Compos. Struct. Int. J*, *15*(6), 679-703.

Varma, A.H., Lai, Z., and Seo, J. (2017). “An Introduction to coupled composite core wall systems for high-rise construction.” *Proceedings of the 8th International Conference on Composite Construction in Steel and Concrete*, Wyoming, USA.

Varma, A. H., Malushte, S. R., Sener, K. C., & Lai, Z. (2014). Steel-plate composite (SC) walls for safety related nuclear facilities: Design for in-plane forces and out-of-plane moments. *Nuclear Engineering and Design*, *269*, 240-249.

Varma, A., Zhang, K., & Malushte, S. (2013). “Local Buckling of SC Composite Walls at Ambient and Elevated Temperatures.” In *Transactions of the 22nd International Conference on Structural Mechanics in Reactor Technology (SMiRT 22)* (pp. 1-10).

Wang A., Seo J., Shafaei S., Varma A.H., and Klemencic, R. (2018). “On the Seismic Behavior of Concrete-Filled Composite Plate Shear Walls.” *Eleventh U.S. National Conference on Earthquake Engineering*. Los Angeles, California, June 25-29, 2018.

Wei, F., Fang, C., & Wu, B. (2017). “Fire resistance of concrete-filled steel plate composite (CFSPC) walls.” *Fire Safety Journal*, *88*, 26-39.

Yang, H., Liu, F., Zhang, S., & Lv, X. (2013). Experimental investigation of concrete-filled square hollow section columns subjected to non-uniform exposure. *Engineering structures*, *48*, 292-312.

Zheng, W., & Hou, X. (2008). Experiment and analysis on the mechanical behaviour of PC simply-supported slabs subjected to fire. *Advances in Structural Engineering*, *11*(1), 71-89.